University of Southampton
Faculty of Engineering and Physical Sciences
School of Engineering

Tip gap noise mechanisms in ducted marine propellers due to unsteady flow features

by

Adam D. Higgens

ORCID ID 0000-0001-6871-2854

A thesis submitted for the degree of
Doctor of Philosophy

April 2019

UNIVERSITY OF SOUTHAMPTON

ABSTRACT

Faculty of Engineering and Physical Sciences

School of Engineering

Thesis for the degree of Doctor of Philosophy

TIP GAP NOISE MECHANISMS IN DUCTED MARINE PROPELLERS DUE TO UNSTEADY FLOW FEATURES

by Adam D. Higgens

Ducted propellers exist in both aerodynamic and hydrodynamic contexts, and the former has received significantly more attention than the latter. This thesis is aimed at identifying the key noise mechanisms in marine ducted propellers. The properties of the fluid media have a significant impact on the relative importance of noise producing flow features and the differences in likely noise sources for aerodynamic and hydrodynamic propellers are discussed.

This thesis uses time-resolved simulations to investigate the unsteady flow features in the tip gap region of a ducted propeller. By inferring the important noise mechanisms it is possible to identify specific criteria which can be used to produce noise mitigating designs. A variety of simplified geometries have been investigated beginning with an open tipped foil to provide a base line case. The complexity of the case is progressively increased to investigate the impact of the tip gap height, the inclusion of a no slip condition on the boundary surface above the tip, and the impact of foil thickness and camber. The numerical simulations have been carried out using an open source computational fluid dynamics software with both time-averaged, and time-resolved simulations conducted. Post processing techniques such as vortex identification criteria and an acoustic analogy have been used to infer the primary noise sources in the tip gap region. Non-dimensional quantities have been used to investigate the flow features and have shown good agreement with previous numerical and experimental work.

The studies found that the most likely cause of noise within the tip gap region is due to the unsteady flow structures being shed through the tip gap and scattered over the sharp edge of the tip. The size and strength of these structures is highly dependent on the tip gap size, and explains why reduced tip gaps are associated with reduced rotor tip noise. The vortex structures are shown to be an accurate indicator of the hydrodynamic surface pressure variations leading to a more intuitive metric to use for improved designs.

A simple design modification is made to the blade with the aim of removing the vortex structures within the tip gap region in order to reduce the strength of the unsteady pressure fluctuations. This improved design reduced the surface pressure spectra by greater than 30dB at certain, key frequencies.

Table of Contents

List of Figures

List of Tables

Declaration of Authorship

I, Adam D. Higgens, declare that this thesis entitled *Tip gap noise mechanisms in ducted marine propellers due to unsteady flow features* and the work presented in it are my own and have been generated by me as the result of my own original research.

I confirm that:

1. This work was done wholly or mainly while in candidature for a research degree at this University;
2. Where any part of this thesis has previously been submitted for a degree or any other qualification at this University or any other institution, this has been clearly stated;
3. Where I have consulted the published work of others, this is always clearly attributed;
4. Where I have quoted from the work of others, the source is always given. With the exception of such quotations, this thesis is entirely my own work;
5. I have acknowledged all main sources of help;
6. Where the thesis is based on work done by myself jointly with others, I have made clear exactly what was done by others and what I have contributed myself;
7. Either none of this work has been published before submission, or parts of this work have been published as:
    - A. Higgens, A. Lidtke, P. Joseph, S. Turnock, *Investigation into the Tip Gap Flow and its Influence on Ducted Propeller Tip Gap Noise Using Acoustic Analogies*, In Journal of Ship Research (under review) [1]
    - A. Higgens, P. Joseph, S. Turnock, *Improvements in the Methodology for Identifying Noise Sources in Ducted Marine Propellers*, In Proceedings of the 21st Numerical Towing Tank Symposium - NuTTS '18 [2]
    - A. Higgens, A. Lidtke, P. Joseph, S. Turnock, *Investigation into the Tip Gap Flow and its Influence on Ducted Propeller Tip Gap Noise Using Acoustic Analogies*, In Proceedings of the 32nd Symposium on Naval Hydrodynamics (2018) [3]
    - A. Higgens, P. Joseph, S. Turnock, *Investigation into the Tip Gap Flow and it's Influence on Ducted Propeller Tip Gap Noise Using CFD*, In Proceedings of the 20th Numerical Towing Tank Symposium - NuTTS '17 [4]

Signed:

Date:

Acknowledgements

Thanks firstly to DSTL and EPSRC for providing the funding for this work. I'd also like to acknowledge the use of the IRIDIS High Performance Computing Facility, and associated support services at the University of Southampton, in the completion of this work.

I'd like to thank Professors Anthony Molland and Stephen Turnock for access to their experimental data and Dr Charles Badoe for his simulation data based on the same experiments and multiple questions fielded by all regarding the initial simulations carried out in this work. I'd particularly like to thank Artur Lidtke for his mentorship through the very steep learning curve that is `OpenFOAM`.

Thanks to my supervision team, Professors Stephen Turnock and Phillip Joseph, whose openness and endless enthusiasm has been a great source of energy. Thanks to the whole Fluid Structure Interactions group for maintaining such a warm and sociable working environment, and the Post Graduate Seminar series for providing us with a more formal platform for sharing our research interests.

Nomenclature

Symbol	Description	Units
A	Foil camber	$[m]$
B	Camber location	$[m]$
C_m	LES model constant	$[-]$
C_D	Coefficient of drag	$[-]$
C_L	Coefficient of lift	$[-]$
C_p	Coefficient of pressure	$[-]$
c	Foil chord	$[m]$
c_0	Speed of sound	$[m\,s^{-1}]$
$\mathbf{D}$	Stress tensor	$[kg\,m^{-1}\,s^{-2}]$
d	Distance from foil surface	$[m]$
h	Tip gap height	$[m]$
f	Frequency	$[s^{-1}]$
F	Generalised acoustic source	$[kg\,m^{-3}\,s^{-2}]$
k	Turbulent kinetic energy	$[m^2 s^{-2}$
$\mathbf{I}$	Identity matrix	$[-]$
I	Integral	$[-]$
l	Source length scale	$[m]$
L	Characteristic length	$[m]$
$\mathbf{n}$	Normal vector	$[-]$
N	Number of cells	$[-]$
p	Pressure	$[kg\,m^{-1}\,s^{-2}]$
Q	Q-criterion	$[s^{-1}]$
$\mathbf{r}$	Vector to receiver	$[m]$
$\mathbf{S}$	Strain rate tensor	$[s_{-1}]$
S	Surface area	$[m^2]$
s	Velocity gradient tensor	$[m\,s^{-2}]$
$\mathbf{T}$	Lighthill stress tensor	$[kg\,m^{-1}\,s^{-2}]$
t	Time; foil thickness	$[s; m]$
$\mathbf{U}$	Velocity	$[m\,s^{-1}]$
U_∞	Free-stream velocity magnitude	$[ms^{-1}]$
u^*	Friction velocity	$[ms^{-1}]$
V	Volume	$[m^3]$
$\mathbf{x}$	Receiver location vector	$[m]$
$\mathbf{y}$	Source location vector	$[m]$

Δx , Δy, Δz	Grid spacing in the chord-wise, wall-normal and span-wise directions	$[m]$

Greek Symbols

α	Angle of attack	$[degrees]$
Γ	Source acceleration	$[s^{-1}]$
Δ	Filter; Grid spacing	$[m; m]$
δ	Boundary layer thickness	$[m]$
η	Kolmogorov length scale	$[m]$
ϵ	Turbulence dissipation rate	$[m^2\, s^{-3}]$
λ	Wavelength	$[m]$
λ_2	λ_2-criteria	$[s^{-1}]$
μ	Dynamic viscosity	$[kg\, m^{-1}\, s^{-1}]$
ν	Kinematic viscosity	$[m^2\, s^{-1}]$
ρ	Density	$[kg\, m^{-3}]$
$\boldsymbol{\tau}$	Stress tensor	$[m^2\, s^{-2}]$
τ	Retarded time	$[s]$
ϕ	Arbitrary variable	$[-]$
$\mathbf{\Omega}$	Vorticity tensor	$[s^{-1}]$
ω	Vorticity	$[s^{-1}]$

Mathematical Operators

$\nabla\times$	Curl
$\nabla\cdot$	Divergence
∇	Gradient
∇^2	Laplacian operator
$\Box^2$	d'Alembertian
ϕ^T	Transpose
∂	Partial derivative
$\otimes$	Tensor product
$\Box^2$	d'Alembertian

Dimensionless Groups

C	Courant number	$\frac{u\Delta t}{\Delta x}$
M	Mach number	$\frac{u}{c_0}$
Re	Reynolds number	$\frac{UL}{\nu}$
St	Strouhal number	$\frac{fL}{U}$

Abbreviations

CAA	Computational aero acoustics
CFD	Computational fluid dynamics

DES	Detached eddy simulation
DILU	Diagonal incomplete lower upper
DNS	Direct numerical simulation
FSI	Fluid structure interaction
FV	Finite volume
FW-H	Ffowcs Williams and Hawkings acoustic analogy
GAMG	Generic algebraic multigrid
HVAC	Heating ventilation and air conditioning
LBM	Lattice Boltzman Method
LE	Leading edge
LES	Large eddy simulations
MRI	Matched refractive index
NACA	The National Advisory Committee for Aeronautics
NASA	The National Aeronautical and Space Administration
OSV	Offshore supply vessel
PBiCG	Preconditioned bi-conjugate gradient
PDE	Partial differential equation
PIMPLE	PISO and SIMPLE algorithms combined
PISO	Pressure implicit split operator
PIV	Particle imaging velocimetry
PS	Pressure side
PSD	Power spectral density
QHSF	Quiet High Speed Fan
RANS	Reynolds-averaged Navier Stokes
rms	Root mean square
RO-PAX	Roll on passenger ferry
SGS	Sub-grid scales
SIMPLE	Semi-implicit pressure linked equations
SPL	Sound pressure level
SS	Suction side
SST	Shear stress transport
TE	Trailing edge
TLV	Tip leakage vortex
URANS	Unsteady RANS
WALE	Wall adapting local eddy
WSV	Windfarm support vessel

Subscripts and superscripts

ϕ_f	On the cell face
ϕ_n	Component normal to the surface
ϕ_t	Component tangential to the surface
ϕ_w	At the wall
ϕ_0	Mean component
$\overline{\phi}$	Spatial filtering
ϕ'	Fluctuating component
ϕ_σ	Cavitation limit
$\hat{\boldsymbol{\phi}}$	Unit vector

Chapter 1

Introduction

1.1 Motivation

Sound is acoustic energy which is transferred through a medium by pressure waves. Noise is the name given to a form of sound which can be described as one which is loud, unpleasant or generally unwanted. Noise is an important design consideration in all areas of the marine industry: high noise and vibration levels can cause discomfort and even health issues for crew members on board vessels, achieving low noise for high levels of comfort is important in yacht design, and for military vessels low noise can increase the operability of a vessel by reducing the likelihood of detection. The effect of anthropogenic noise on marine life is also an area which has traditionally not received much attention but now is increasingly being investigated from an ecological perspective [5] [6] [7] [8].

This research is focussed on investigating the noise sources of ducted marine propellers used on submarines, focussing in particular on the tip vortex, and the effect of changing the size and shape of the gap between the ducting and the propeller tip. Ducted propellers are also seen on other vessels such as Offshore Supply Vessels (OSVs) and Windfarm Support Vessels (WSVs) where the propeller operates inside of a continuous annular shroud such as the Voith Linear Jet shown in Figure 1.1.

Propeller noise can be classified into several components including: turbulence ingestion, trailing edge noise, cavitation and tip gap interaction noise. While there has been extensive research into the first three mechanisms, the noise mechanisms related to the tip gap are less well understood. The noise generated by an aerodynamic fan in a duct has been the focus of a significant amount of research for aircraft engines, wind turbines and Heating Ventilation and Air Conditioning (HVAC), due in part to requirements near airports for maximum sound levels for the comfort of people near to these systems. However, the research into the noise of marine propellers has been far less extensive, perhaps because the effect of marine

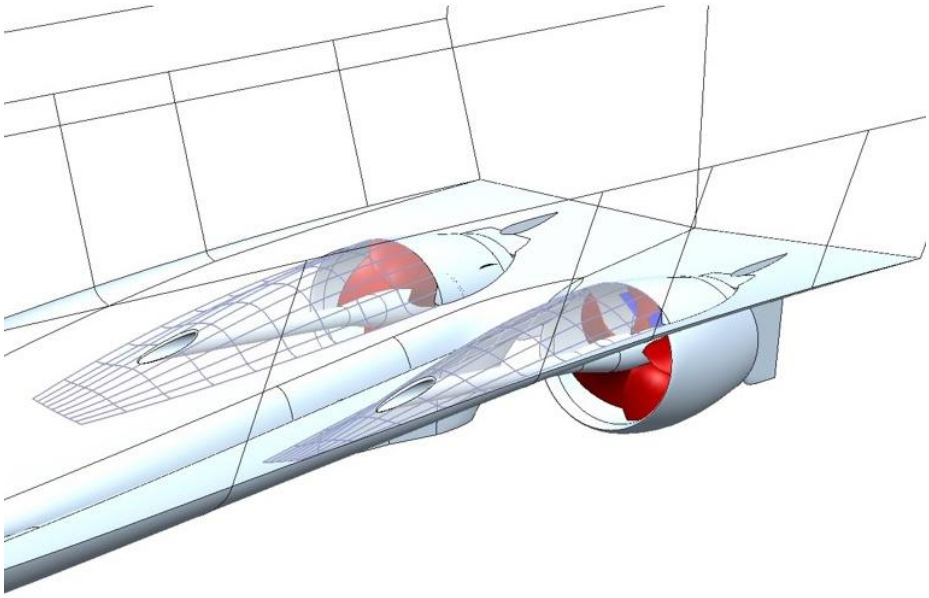

Figure 1.1: The Voith Linear Jet - an example of a ducted marine propeller used on Windfarm Support Vessels (WSVs).

noise is not felt by the majority of the human population, the research regarding marine propeller noise is driven mainly by the military.

In the aviation industry, the problem of tip leakage flow noise is generated by the large by-pass fan at the front of a turbo-fan engine. Typically these fan blades are manufactured to sufficiently high tolerances that the usual approach is to simply minimise the tip gaps to $h/c \ll 1\,\%$, where h is the tip gap height and c is the foil chord.

In the marine industry the use of ever decreasing tip gap heights causes several problems. The primary concern regarding noise production in a marine context is cavitation, a phenomena experienced when the local pressure in a liquid drops below the vapour pressure of that liquid causing small cavities to form filled with the vapour of the liquid. When the local pressure increases again, these cavities collapse violently producing efficient noise sources which propagate to the far-field, as well as causing erosion and wear if they collapse on a solid surface such as the propeller blade or duct. As the tip gap is made smaller the tip flow inevitably increases its speed and therefore the pressure drops following Bernoulli's equation, increasing the likelihood of cavitation occurring. This effect is suppressed as the operational depth increases because the local ambient pressure increases. However, relying on using greater depth to suppress cavitation can not be relied upon in a military context as it would imply a minimum operating depth above which the operating noise would sharply increase. Figure 1.2 shows a schematic representation of the impact of cavitation caused by a reduced tip gap. It can be seen that the noise level in the far-field reduces with the

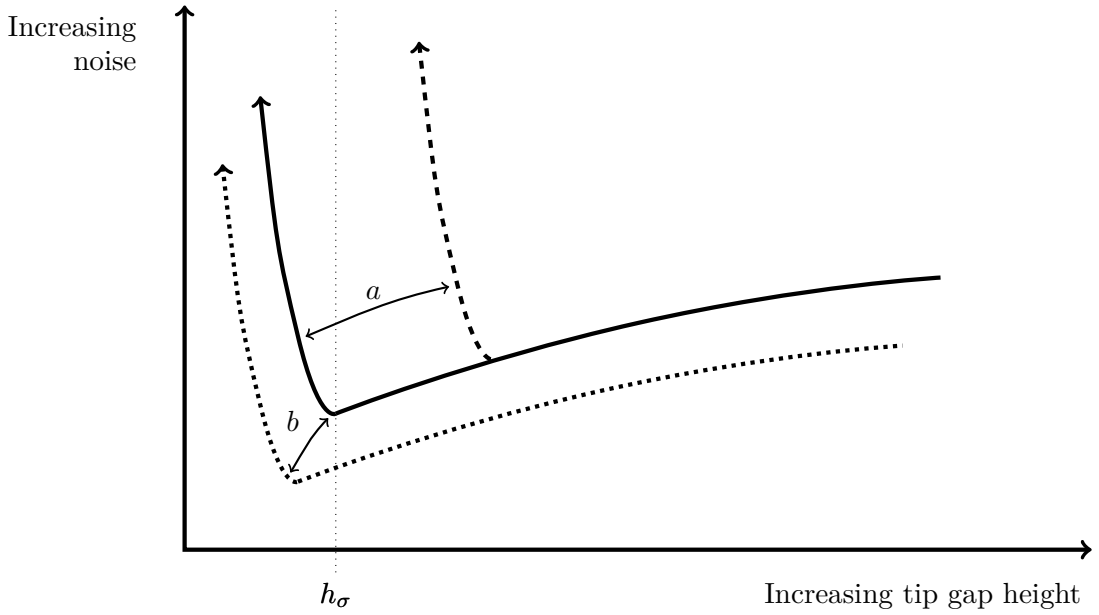

Figure 1.2: The cavitation problem - simply reducing the tip gap height in marine propellers increases the likelihood of cavitation, with drastic implications for far-field noise. Transition a illustrates the effect of operating at a shallower depth and inducing cavitation faster. Transition b shows the potential impact of an improved tip design, producing lower noise overall and allowing a closer tip gap.

reducing tip gap with the base case shown as the solid line. However, at a critical point, h_σ the gap reduces to a point which causes cavitation in the tip gap region. This causes the rapid increase shown in the far-field noise. The implications of operating at a shallower depth are shown by transition a, to the dashed line, showing that the increase in noise would occur at a larger tip gap height due to the reduced ambient pressure at that depth. Finally, transition b, to the dotted line shows the potential improvements made by an improved tip design which could reduce the noise production at larger gap heights, improving the operating depth range for a given noise performance profile.

The sources of noise of interest in the tip gap region can be classified into three main categories and a summarised in Figure 1.3:

1. The interaction of the blade tip and the boundary layer of the duct. As the tip gap reduces the tip of the blade moves deeper into the boundary layer of the duct which causes a change in the local inflow velocity and turbulence.

2. Tip leakage flow from the high to low pressure sides of the propeller blade over the tip. This flow happens over the tip of any lifting surface but in this arrangement it also interacts with the duct boundary layer, and as the gap reduces the tip leakage flow becomes restricted, changing the velocity and impacting on the formation of the tip vortex.

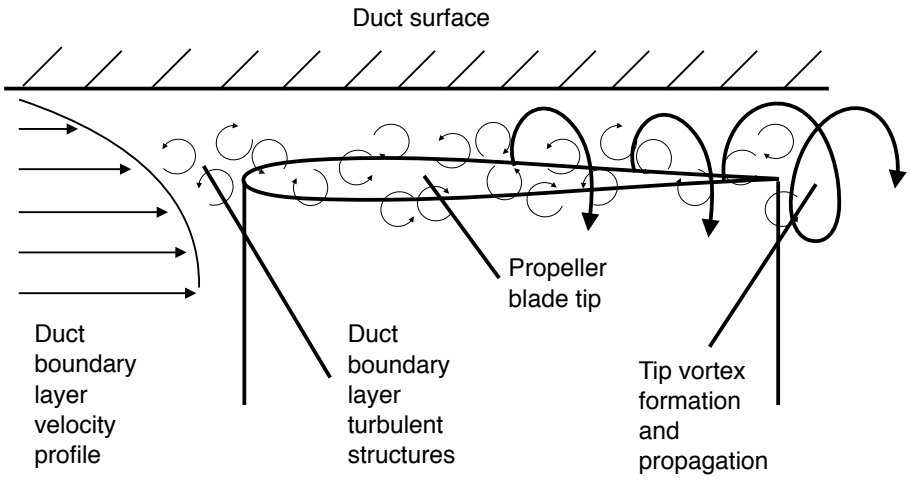

Figure 1.3: Schematic representation of the tip vortex interaction with the duct boundary layer.

3. As the tip leakage flow reaches the trailing edge of the blade the tip vortex is shed and convects downstream. This vortex interacts with the duct boundary layer and causes unsteady pressure fluctuations on the surface of the duct which may generate noise.

The impact of the tip gap on the noise produced by ducted propellers has been researched both numerically and experimentally as will be discussed later in Section 2.4. However, the mechanisms responsible for the noise in the tip region and the impact of the tip gap size are still poorly understood. Experimentally, the lack of insight is at least in part due to the difficulty of assessing the unsteady flow mechanisms within the very small tip gap region, particularly in engines in the aviation industry. In a full propeller arrangement the tip gap is difficult to access with sensors or optical methods to quantify the flow in that region. A number of studies have simplified the arrangement to stationary blades, either by investigating a single blade or a cascade comprising multiple blades, allowing easier access to the tip gap. Difficulties remain however in the physical size limitations of experimental equipment and therefore the size of the flow structures involved.

Numerical studies offer a better capability to observe the flow features within the tip gap and have been used to further the understanding of this region in aerodynamic engines. However, Mach number scaling will be shown to be important in the efficiency of radiated sound and the combination of lower flow speeds and a higher sound speed in marine applications results in different source mechanisms dominating the acoustic radiation.

1.2 Aim & objectives

The aim of this work is to investigate the unsteady flow mechanisms within the tip gap in order to improve the understanding of the important structures which influence the noise production in this region. The source mechanisms involved are currently poorly understood and identifying the unsteady flow features responsible would allow the production of improved, noise-mitigating propeller designs, as well as providing suggestions for retro actively improving propellers which are currently in use.

The objectives of this thesis required to achieve this aim are listed below:

- Outline the current state of the art for ducted propeller tip gap noise by reviewing the literature surrounding fluid structure interaction noise in general, how it is applied to to ducted propellers, and how it can be simulated numerically.
- Discuss the available methods regarding numerical acoustic modelling, before identifying the most viable option for ducted marine propeller noise.
- Undertake initial studies: form a good understanding of the formation of a tip vortex on an open tipped foil to provide a baseline case to compare against when investigating the tip gap flow; conduct time-averaged simulations on a simplified arrangement across a variety of tip gap heights and foil thicknesses; give an indication of the most influential factors affecting tip gap flow; carry out time-resolved simulations on a reduced test matrix to offer further insight into the unsteady flow features.
- Simulate realistic geometries following previous experimental and numerical works and focus understanding on the complex tip gap flow mechanisms and far-field noise predictions. Identify the dependency of these flow mechanisms and noise predictions on tip gap height and duct boundary conditions.
- Infer the noise production mechanisms in the tip gap region, along with suggested design improvements to help suppress noise production and investigate the effectiveness of a design modification to make final recommendations for design improvements and further work.

1.3 Foil terminology and axis orientation

The simulations carried out in this work use the NACA 4-digit foil series as they present a series of foils which have been widely researched, offering the chance for validation and comparison of the current work with previous studies. The foils follow a mathematical description for their shape and so offer good repeatability between different works without the need for direct collaboration. They will be referred to in this work using their 4-digit

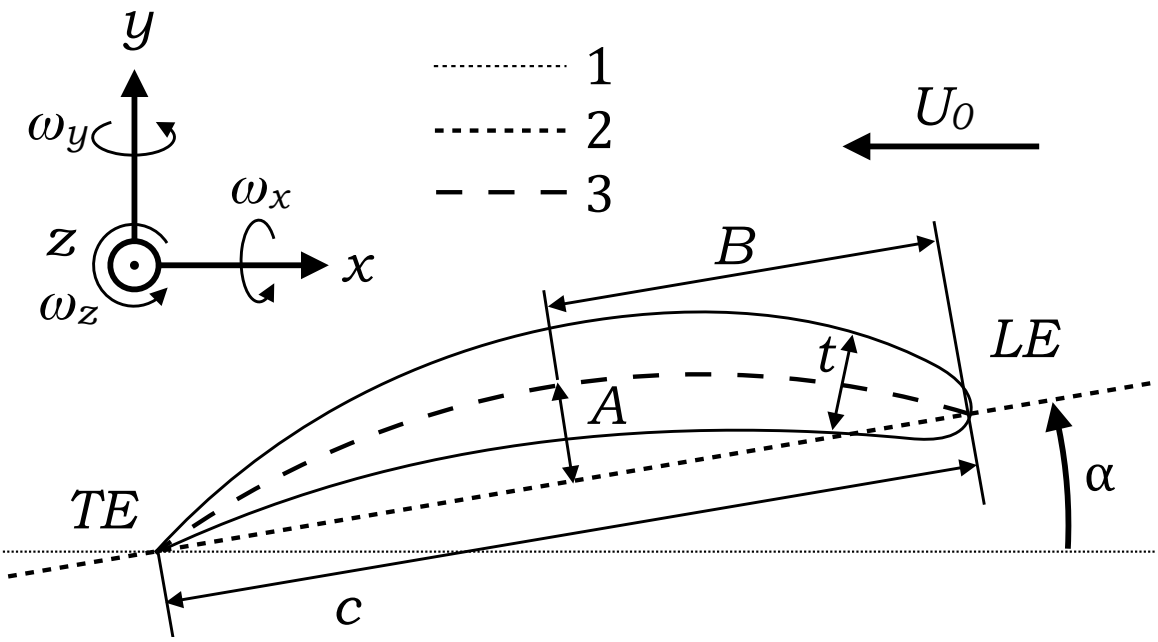

Figure 1.4: The Anatomy of a Foil - Schematic diagram of the terminology used in this work to describe a NACA 4-digit foil along with the axes orientation and positive angle of attack.

naming convention and so the meaning of each digit and the terminology used for foil dimensions will be explained here. Figure 1.4 shows the two dimensional representation of the NACA 4-digit foil which represents the constant cross-section of the foils used in this work. The NACA 4-digit foils were first created using a parametric spline based on three parameters given by the four digits which will be explained here. The axes used in this work are right handed as shown, defining the z-axis coming out of the Figure, denoted by the circle with a dot, and the rotational direction ω rotating clockwise about the axis when viewed in the positive direction of that axis.

In Figure 1.4 Line 1 shows the base line, in line with the x-axis, and the mean flow, U_0. Given this mean flow, the leading edge LE, and trailing edge TE, become intuitive as the forward and aft ends of the foil. Line 2 is a straight line which connects the LE and TE and is referred to as the chord line and the length between the LE and TE is the chord, c. The angle of attack, α is defined as the angle between the chord line and the base line. Line 3 is the mean camber line and joins the LE and TE taking into account the amount of camber, or curve of the foil. The maximum camber is given by dimension A, and A/c, taken as a percentage gives the first NACA digit. The location of this maximum camber, shown as the distance, B aft of the LE is given in 10^{th}s of chord as the 2nd NACA digit. The thickness of the foil, t is given as the maximum value divided by the chord as a percentage, two give the last two NACA digits. For example, the NACA5510 foil has a 5% camber, located 50% aft of the LE, with a maximum thickness of 10%.

1.4 Important assumptions and simplifications

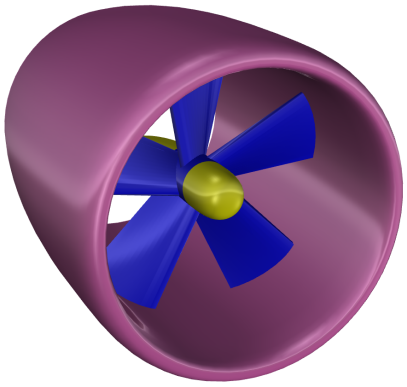

(a) Realistic ducted propeller with stators removed

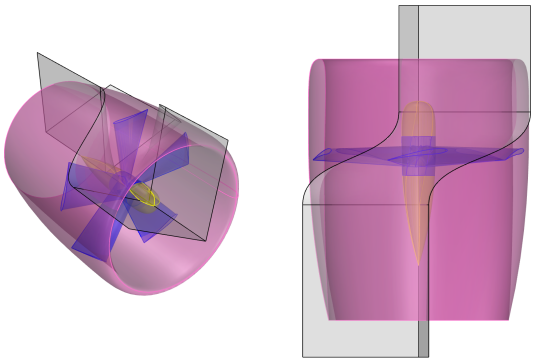

(b) Single blade, wedge domain. Grey surfaces show the domain "wedge" shape and the propeller and duct outside of these surfaces would be removed.

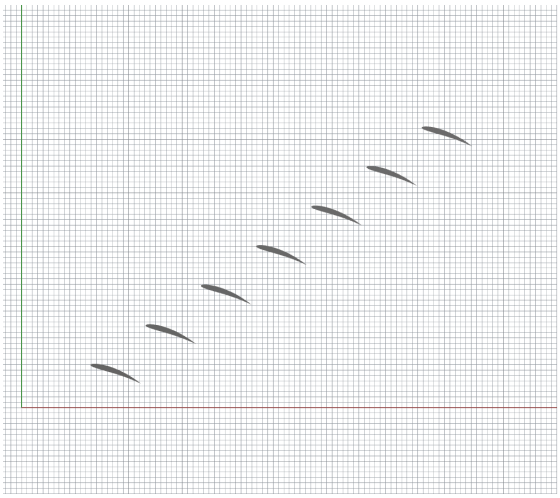

(c) Multiple blade cascade

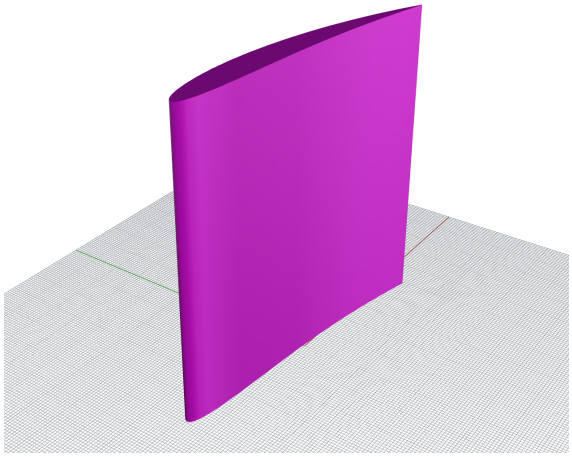

(d) Single stationary blade

Figure 1.5: Comparison between realistic ducted propeller and simplified test cases

Although performing simulations and experiments with full geometries is possible, simplifications are often made to improve either the practicality or efficiency of both experimental and numerical studies. It is important to be aware of the impact of such simplifications and they will be discussed here, with four typical arrangements found in the literature shown in Figure 1.5.

There are several ways that rotating propellers are simplified in both numerical and experimental studies, and the review of the current literature presented in Chapter 2 will reflect this. Experimentally, the options are to use a stationary blade, with either a cascade of blades, or

just a single blade. The cascade of blades provides the benefit of blades downstream having to operate in the wake of those upstream, therefore presenting the flow characteristics of the real problem. In aeroacoustic problems, it is often required that experiments are carried out within an anechoic wind tunnel. These facilities use an open jet configuration within an anechoic chamber where the working section is usually of limited size. For this reason, previous experimental works by Grilliant et al. [9] on ducted propellers have used a single blade set-up, to maximise the size of the blade that can be studied.

Numerical techniques allow greater flexibility as the computational domain does not have to mimic reality exactly, instead special boundary conditions can be applied to recreate the periodic nature of a rotating propeller or linear cascade. Using periodic boundary conditions allows a propeller with, for example, 5 blades can be divided into a $\frac{1}{5}$ domain with a wedge shape. The boundary conditions using a wedge domain can be set such that the outflow of one of the wedge boundary of the domain can be used for the inflow condition on the opposite boundary. A schematic of a wedge domain used with a single blade is shown in Figure 1.5b showing the full arrangement being split by the domain limits shown in grey, which would have the periodic boundary conditions applied to them. The dividing faces can be seen to twist as they pass through the propeller plane which is necessary when using propeller blades which have overlapping regions. Furthermore, the domain and blade can be fixed in space, instead using a moving wall boundary condition for the duct surface, combined with a rotating inflow, so that the relative motion of a rotating propeller is maintained, without having to use difficult over-set mesh techniques. This technique is popular within the turbo machinery industry [10] [11] [12].

In this thesis the realistic design condition of a ducted propeller was simplified to reduce the computational expense and thus allow an increased fidelity grid to be used. The simulations carried out herein use a single, straight blade, in a non-rotating set-up, with no upstream or downstream stator blades as shown in Figure 1.5d. Cavitation will be neglected in the simulations during this work, assuming that the operational depth of the propeller would be sufficient to suppress cavitation, but the impact that cavitation could have will be discussed qualitatively. Neglecting cavitation restricts the study to a single phase flow which allows a simplified computational set-up, and so the effect of gravity can be neglected and all pressures are relative. This idealisation permitted a more methodical development from initial simulations to investigate the formation of the tip vortex through a parametric analysis of a single foil, whilst also allowing detailed comparison with previous experimental and numerical studies [9] [13] [14]. In deciding on the arrangement which would be applied to the simulations presented in this thesis, the individual simplifications, and the possible impact they have on the flow physics are listed below:

- A rotating blade has a faster tip speed than root speed, meaning that the relative speed between the blade and the fluid is different at the root and the tip, as is the

relative angle of attack. To account for the span-wise variation in relative flow speed and angle, rotating propeller blades are twisted, to avoid having large areas of the foil operating in either with such a small angle of attack that they do not contribute significantly to the lift, or such high angles of attack that they induce stall. This effect can be recreated to a certain extent by using a twisted foil to change the angle of attack at different span locations [15] and [16].

- In a ducted propeller arrangement, the duct is usually fixed, thus creating a relative motion between the blade tip and the duct surface, in the same direction as the tip leakage flow driven by the pressure difference across the tip of the blade. This could be recreated both numerically by using a moving wall boundary condition and experimentally by using a moving surface such as a belt.
- The inflow to a blade in a rotating propeller is affected by the wake of the preceding blade. Using a non-rotating blade configuration removes this effect but it can be recreated by using a blade cascade, such that individual blades are staggered on a flat surface to generate a similar interaction mechanism as would be experienced in the rotating frame [17] [18]. A schematic sketch of a linear cascade is shown in Figure 1.5c. The use of a blade cascade in numerical simulations requires either an increased domain size within which all the blades are simulated, or the use of periodic boundary conditions such that the downstream out flow can be used to define the upstream inflow, thus creating the effect of an infinite cascade, similar to that of a rotating propeller. This requires complex fluid flow to be captured at the outflow boundary and mapped on to the inflow boundary, as well as requiring a high grid resolution to be maintained throughout the entire domain to accurately simulate the structures between periods. Previous works have combined the effects of blade cascade and moving end walls to recreate some of the effects of rotation in a Cartesian experimetnal setup [19], [20], [21].

1.5 Thesis structure

Four parts are used to structure the thesis, collated to illustrate key areas of attention throughout this study. Part 1 will establish the methodology and assess the state of the art regarding ducted propeller noise generation. Part 2 investigates the most simplified cases to provide a baseline case with which to draw comparisons and help establish general flow behaviour as the tip gap height is reduced. Part 3 will apply the methodology to a more realistic test case with similarities to previous experimental work and offering new insight allowed by the chosen methodology. Part 4 will provide recommendations for improved blade designs, propose future research and summarise the conclusions of this thesis.

- **Part 1 - Establishing the methodology:** The theory surrounding fluid dynamics will be discussed in Chapter 2, with particular attention paid to turbulence, noise generation, and vortex identification. Chapter 3 will discuss the finite-volume method used by the selected CFD software to allow a numerical approach to solving the equations discussed in Chapter 2. Chapter 4 will discuss the available approaches regarding numerical noise prediction and the reasons behind the chosen method.
- **Part 2 - Parametric analysis of NACA0020:** Chapter 5 will investigate the formation of a tip vortex around an open tipped foil to present a baseline case in the flow mechanics which will be of importance later in the thesis. Chapter 6 will investigate the influence of varying the tip gap height, h, on the formation of the tip vortex. This study uses a simplified methodology with a slip boundary condition on the surface near the tip, allowing a more rapid initial parametric study. Time-resolved simulations are presented which reveal the unsteady flow features within the tip gap region. The potential fundamental noise sources in the tip gap region are inferred from the unsteady flow features.
- **Part 3 - Application to practical geometries:** Chapter 7 describes a case study on a NACA5510 foil, based on previous experimental and numerical works. This study includes the more realistic shape of the aerofoil, including reduced thickness and higher camber, as well as including the no-slip condition on the boundary surface near the foil tip, and a boundary layer profile on this surface. Chapter 7 investigates the effects of the simplifications by running comparison cases with and without the no-slip and boundary layer profiles by comparing the lift and drag performance, as well as visualising the vortical structures in the flow, and predicting the far-field noise with the use of the chosen acoustic analogy.

  Investigation of the complex flow features within the tip gap region led to the hypothesis that an important noise generation mechanism in the tip gap region may be the scattering of these turbulent structures as they interact with the suction side edge of the tip and are shed into the free stream. This proposed mechanism is likely to be similar to trailing edge noise which involves the scattering of turbulent structures back upstream in the form of acoustic waves with long wave length. This noise source can not be considered compact with respect to the acoustic wavelength and therefore the incompressible solver is unlikely to accurately predict the source terms which the acoustic analogy requires.

  Chapter 8 conducts further analysis of the NACA5510 foil to identify the noise sources responsible for the far-field noise predictions from the acoustic analogy and investigates the flow features to infer the regions which will be likely to produce noise via the scattering mechanism. Chapter 9 analyses the impact of varying the tip gap height on the noise sources identified in the previous chapter. This discussion includes the

hydrodynamic sources and explains the variation observed in far-field noise predictions.

- **Part 4 - Recommendations and conclusions:** Chapter 10 discusses a number of proposed design improvements to reduce the far-field noise. These suggestions draw inspiration from existing research being done to reduce trailing edge noise, as well as more intuitive responses to the unsteady flow features seen in Part 3. One design is chosen and analysed, showing the removal of coherent structures within the tip gap and reducing the surface pressure fluctuations in key areas. Chapter 11 summarises the conclusions drawn from this work. It also lists the contributions made through published works, and outlines a recommended path for future investigations.

Part I

Establishing the methodology

Chapter 2

Ducted propeller noise

2.1 Introduction

Ducted propellers are situated within an annular duct with the aim of modifying the flow over the propeller to enhance certain performance characteristics. In the marine context these ducts as generally split into two categories, accelerating or decelerating ducts referring to the effect that the foil shaped cross-section of the duct has on the flow through it [22]. A schematic representation of these two duct types is given in Figure 2.1 showing the foil shaped cross-section. It is apparent that the lift produced by the accelerating duct produces lower pressure and therefore higher flow speed inside the duct. The converse is true for the decelerating duct.

Accelerating ducts have the advantage of increasing the advance coefficient of the propeller at low speed as well as increasing the thrust produced by the duct adding to the thrust produced by the propeller and hence improving the efficiency in a high thrust application [23]. At zero speed this is known as the bollard pull and has applications for tugs or offshore support vessels required to manoeuvre heavy loads, potentially also in heavy seas. Whilst operating in any condition away from this application of low speed and high thrust,

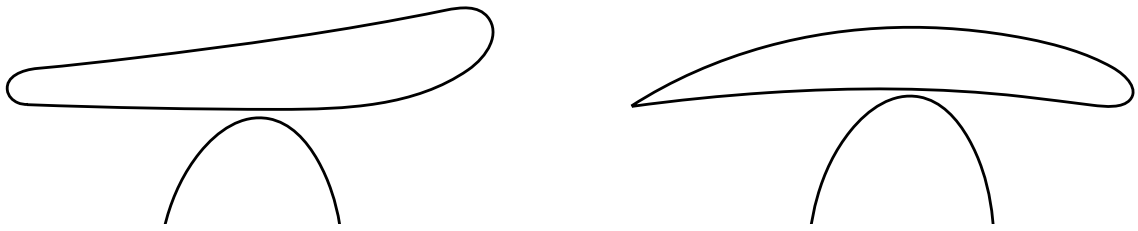

(a) Accelerating duct **(b)** Decelerating duct

Figure 2.1: Two main duct types used in marine propulsion, with flow from right to left, showing the location of the propeller near the mid chord of the duct.

these ducts see an increase in drag and generally are less efficient than open propellers. Decelerating ducts slow the speed and so increase the local pressure at the propeller which delays the onset of cavitation. Cavitation creates an efficient noise source and so reducing the likelihood of cavitation is of interest to vessels that have stringent noise requirements, such as research vessels operating in protected areas or military vessels trying to avoid detection. Decelerating ducts tend to experience an increase in drag, with no useful work being done by the lift. The principle of a decelerating duct can be extended to use a higher number of propeller blades with square tips and small tip gaps, coupled with stator vanes either upstream or downstream of the propeller to use the swirling wake to produce extra thrust. This is known as a pump jet and is used on military vessels [22] due to the noise reduction aided by the reduced cavitation caused by the increased pressure and the reduced tip vortex intensity.

Aerodynamic engines also include ducts to increase the performance of the compression stage of the engine cycle and reduce the noise emitted from the bypass fan. Several works have investigated the control of the tip leakage flow with a view to improving performance in the compressor [24] [25]. While marine propellers use mostly the lift generated by the propellers for thrust, aerodynamic engines such as turbojets, turbofans and turboprops, augment the thrust from the fan by employing combustion to accelerate the inflowing air and produce thrust from the resultant jet. Aerodynamic engines require a number of stages to achieve the compression necessary and so the arrangement of aerodynamic and hydrodynamic ducted propulsors appear different, as shown in Figure 2.2. Despite the differences in these two arrangements, the area of interest for this thesis is similar in both, square tipped propeller blades operating close to the duct surface.

This chapter will introduce the theory governing the fluid flow involved in ducted propellers, how turbulence is governed and how it generates noise in general, and is based on previous works simulating propeller noise in the marine environment [26] and [27]. The classification of noise sources, and how these relate to ducted marine propellers including the behaviour of vorticity and vortices will then be discussed.

2.2 Fluid dynamics

All fluid flows must obey the conservation of mass equation, stating that matter cannot be created or destroyed, also known as the continuity equation,

[1] http://www.voith.com/en/products-services/power-transmission/voith-linear-jet-40389.html

[2] https://www.rolls-royce.com/products-and-services/civil-aerospace/airlines/trent-1000.aspx#technology

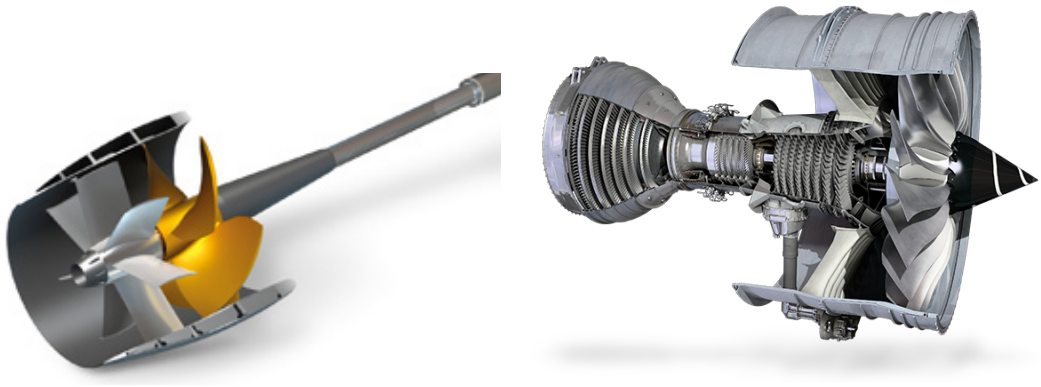

(a) Linear Jet marine propulsor produced by Voith GmbH[1]

(b) Trent 1000 aerodynamic turbo fan engine produced by Rolls-Royce[2]

Figure 2.2: Comparison of ducted propulsors in the marine and aviation industry. Marine propellers use fewer blades with higher loading on each blade and so the material thickness is high, while the turbo fan uses a high number of thin blades using composite materials.

$$\frac{\partial \rho}{\partial t} + \nabla \cdot (\rho \mathbf{U}) = 0, \tag{2.1}$$

where $\rho(\mathbf{x}, t)$ and $\mathbf{U}(\mathbf{x}, t)$ are the fluid density and velocity respectively.

All fluids also must obey the conservation of momentum, known as the Navier-Stokes equation,

$$\frac{\partial (\rho \mathbf{U})}{\partial t} + \nabla \cdot ((\rho \mathbf{U}) \otimes \mathbf{U}) = -\nabla p + \mu \mathbf{D}, \tag{2.2}$$

where p is the pressure, μ is the dynamic viscosity and $\mathbf{D}$ is the stress tensor of the fluid. This equation describes the effect of Newton's second law of motion, that applying a force to a mass results in an acceleration.

The stress tensor $\mathbf{D}$ may be written as

$$\mathbf{D} = 2\left(\mathbf{S} - \frac{1}{3}(\nabla \cdot \mathbf{U})\mathbf{I}\right), \tag{2.3}$$

where $\mathbf{I}$ is the identity matrix and $\mathbf{S}$ is the symmetric part of the strain rate tensor,

$$\mathbf{S} = \frac{1}{2}\left(\nabla \mathbf{U} + (\nabla \mathbf{U})^T\right). \tag{2.4}$$

where T denotes the transpose of the matrix. These equations of motion d include the effect of compressibility and therefore still allow for variable density. If the fluid is assumed to be

incompressible then Equations 2.1 and 2.2 can be reduced to:

$$\nabla \cdot \mathbf{U} = 0, \tag{2.5a}$$

$$\frac{\partial \mathbf{U}}{\partial t} + \nabla \cdot (\mathbf{U} \otimes \mathbf{U}) = -\frac{1}{\rho}\nabla p + \nu \mathbf{D}, \tag{2.5b}$$

where ν is the kinematic viscosity of the fluid.

Analytical solutions to the equations of motion discussed only exist for a handful of cases [28]. For most flows, therefore, a numerical solution must be found. This work uses computational fluid dynamics (CFD) implemented through the use of `OpenFOAM` and the finite volume method to discretise these equations for discrete regions of fluid and solve for pressure and velocity to maintain the conservation of mass and momentum. This will be discussed further in Chapter 3.

2.3 Turbulence

Turbulent structures develop due to the instabilities controlled by the inertial forces within a fluid, and is damped by the viscous properties of that fluid. The ratio between these forces is defined as the Reynolds Number,

$$Re = \frac{UL}{\nu}, \tag{2.6}$$

where U and L are the characteristic velocity and length scales respectively, and $\nu = \mu/\rho$ is the kinematic viscosity, defined as the ratio between the dynamic viscosity, μ and the density ρ of the fluid. The Reynolds Number can be used to predict the behaviour of the flow such that below a certain threshold the flow is likely to be smooth or laminar and above the threshold it is likely to transition to turbulence. For the boundary layer on a flat plate it is expected that this transition occurs at $Re_x \approx 5 \times 10^5$

The seemingly random nature of turbulent structures within a flow requires a statistical approach to be taken to describe them, separating the properties into their slowly varying mean and rapidly fluctuating components,

$$p(\mathbf{x}, t) = p_0(\mathbf{x}) + p'(\mathbf{x}, t) \tag{2.7a}$$

$$\mathbf{U}(\mathbf{x}, t) = \mathbf{U}_0(\mathbf{x}) + \mathbf{U}'(\mathbf{x}, t) \tag{2.7b}$$

The left hand side represents the total value, the subscript 0 represents the mean component, and the primed terms are the fluctuating components.

Turbulence is a random phenomenon and there are a range of scales of structures, or eddies, within the flow as hypothesised by Kolmogorov [29] [30]. Kolmogorov suggests that the range of eddy sizes in the flow will vary from the significant length scale, L, with the size of the smallest eddies being dependent on the Reynolds Number and the turbulent energy dissipation rate, ϵ. The size of these small eddies is described by the Kolmogorov Length Scale which is defined as

$$\eta = \left(\frac{\nu^3}{\epsilon}\right)^{3/4}. \tag{2.8}$$

The eddies of scale η can be assumed to behave isotropically, such that they are independent of spatial changes. With regards to marine engineering problems, the high Reynolds Numbers involved are beyond the turbulent transition range and so turbulence will always be involved in the flow. This means that turbulent boundary layers will develop on any body within the flow and within the context of this work it means that the boundary layer of both the duct and the propeller blades will mostly be turbulent. The modelling of their interaction will therefore depend heavily on the behaviour of turbulent structures.

2.4 Noise generated by ducted marine propellers

The noise generated by ducted propellers has been a subject of importance in the aviation industry since turbo-fan engines were introduced in the 1950's, with the primary motivation of improving passengers comfort or reducing the noise for those under flight paths or near airports. The field sound produced aerodynaimcally is known as aeroacoustics but it's principles can be applied to all fluid media including water, in the case of this work. The fundamentals of aeroacoustics were first proposed and formulated by Lighthill [31] [32] which were later extended by Curle to take into account the effect of surfaces [33].

A ducted propeller can be broken down into its individual components to identify the different noise sources which contribute to the overall noise. By first taking the propeller blade and treating it as an open ended foil, the following sources have been identified as the major components in self-noise generation, as shown in Figure 2.3 [34]. These are:

(a) Turbulent boundary layer: trailing edge noise,

(b) Laminar boundary layer: vortex shedding noise,

(c) Separation noise at low angle of attack,

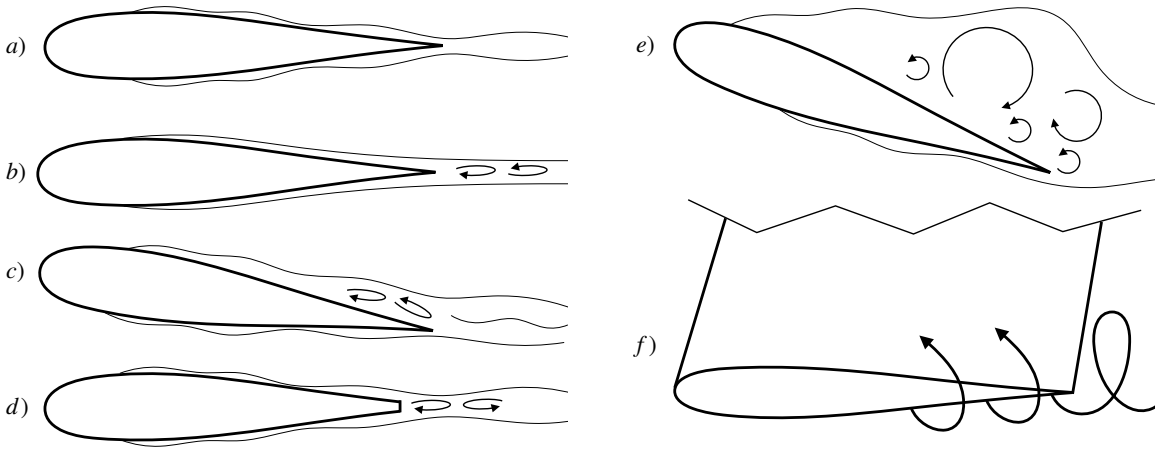

Figure 2.3: Noise components on a foil, adapted from [34].

(d) Trailing edge bluntness: Vortex shedding noise,

(e) Separation: stall noise at high angle of attack,

(f) Tip vortex formation noise.

A blade encountering a turbulent inflow, causes pressure fluctuations along the surface which behave as dipole sources, shown schematically in Figure 2.4. Due to the large pressure differential generated on either side of a lifting surface, in a marine context the local pressure can drop below the vapour pressure of the surrounding water. This causes small bubbles of vapourised water to be generated in the fluid, and on the surface of the foil, where the lowest pressures are likely to occur in a process known as cavitation. The collapse of these bubbles can be a very strong source of noise and has been the subject of a growing area of research recently [35] [36] [26] and [37]. The noise generated by cavitation is outside the scope of this thesis, as the primary motivation is to investigate propeller noise on submarines, it will be assumed that the operating depth of the propeller is such that the ambient pressure is sufficient to prevent cavitation from occurring.

When the blade is placed within a duct, the effect is analogous to introducing a wall close to the tip of this foil. This wall will have a boundary layer region where the velocity goes to zero at the surface. In a marine propeller it is highly likely that the boundary layer will be turbulent due to the high Reynolds numbers involved. The interaction between the duct boundary layer and the blade tip presents a combination of sound sources, from the non uniform and turbulent inflow velocity at the tip, turbulent boundary layer noise from the blade, tip vortex formation noise, and interaction noise between the tip vortex and the duct boundary layer. A schematic representation of the important flow features has been presented in Figure 1.3.

In 2011 Berdanier observed that although FSI noise has been known about and considered

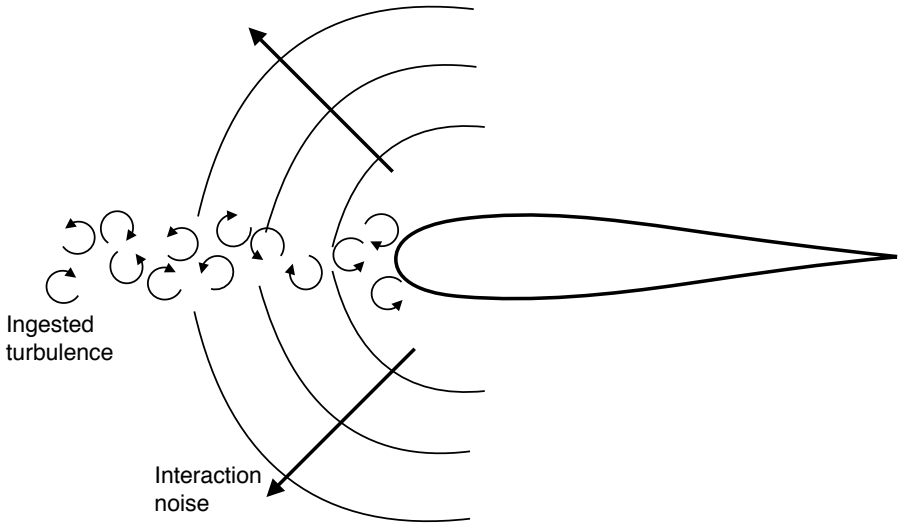

Figure 2.4: Schematic representation of ingested turbulence noise.

since the late 1800s, it's use in understanding tip gap flows, and the associated noise sources was a relatively new area of research, and not very well understood [38]. In the drive for quieter turbofan engines as the commercial aerospace industry continues to grow, the amount of research has increased. Studies of ducted fan noise have included general noise measurements of full arrangements [39] [40] [41] [42] [43] [44] [45] [46], as well as simplified arrangements to try and isolate individual noise sources [47], [48], [49].

Figure 2.5 shows the major noise sources in a ducted fan as proposed by Berdanier. Berdanier concludes that two major sources of tip gap dependent noise are due to the interaction between the trailing tip vortex and the stators which are downstream and the rotational instability which occurs in front of the fan, first proposed by Liu et al [50]. Both of these mechanisms are the result of tip leakage flow and the resultant vorticity created. A propeller or fan uses the same principles as a wing to generate lift by creating a pressure gradient across the blade. At the tip of any wing or blade therefore there is a point where the pressure side (PS) meets the suction side (SS) and there is a pressure gradient in the free fluid. This causes a flow around the tip known as tip leakage, and subsequently a spanwise flow velocity component on both sides of the wing. When the tip leakage flow is combined with the incident flow a vortex is produced which wraps up along the SS of the blade and is shed from the trailing edge (TE) [9]. The span-wise component of flow on either side of the wing is in opposite directions and so at the TE there is a shearing of the two flow directions, causing a sheet of vorticity in the wake of the wing. The vortex which has formed along the tip of the wing and the vorticity of this sheet are caused by the same pressure gradient and have the same rotational direction, and so the vortex sheet rolls up into the existing tip vortex causing it to strengthen.

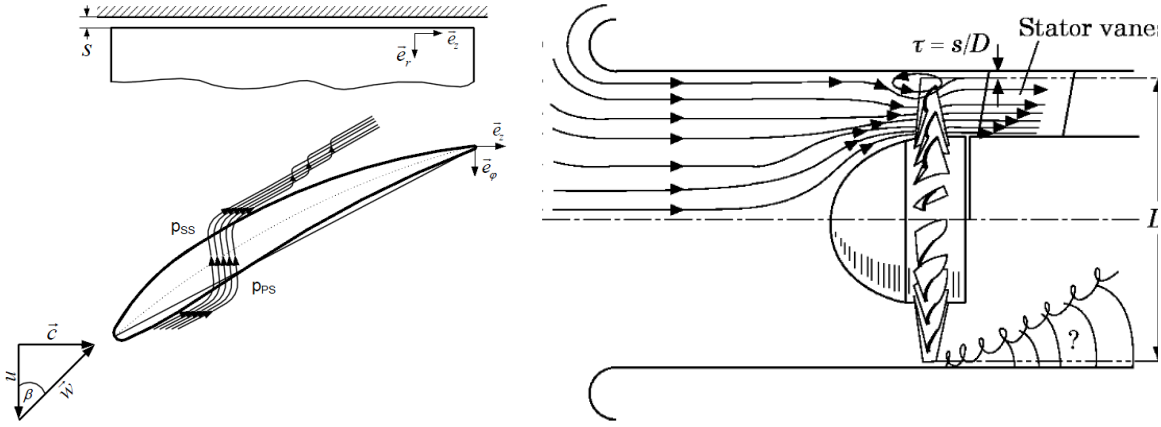

Figure 2.5: Tip leakage and vortex production, and rotational instabilities and downstream vortex growth [38].

In a propeller the blades are usually fixed and so the angle of attack of the blade is dependent on the flow velocity. If this angle of attack is too great then the blade will stall, causing separated flow on the SS which will contain strong turbulence. Coupled with the tip vortex also on the SS, this can cause a strong vorticity on the SS which is usually shed from the TE. The stalling of the fan blades causes regions of air which rotate with the fan rather than moving downstream and are a source if noise [51]. It has been found that fans using a forward sweep have a lower sound pressure level (SPL) than those with a backwards sweep [41]. San et al. showed that a stationary forward swept wing can achieve a higher angle of attack before stall occurs [52], which could explain the lower noise in the forward swept fan, due to the reduction in rotational instability noise. This principle was incorporated into the design of the Quiet High Speed Fan (QHSF) [53] which showed a significant reduction in fan noise.

An open propeller without a duct will shed its tip vortex towards the TE of the propeller blade. When combined with the rotation of a propeller, this vortex creates a helical structure downstream of an open propeller which contracts as the streamlines contract in the faster flow region of the wake [54]. However in a ducted propeller, this contraction of the streamlines still occurs and causes a stretching of the outer wake where the tip vortex is, as the fluid from outside the wake is blocked by the duct. As this propagating vortex interacts with the duct boundary layer, it will create a swirling region of unsteadiness, which will in turn produce pressure fluctuations on the surface of the duct. This source of noise is currently not well understood [55]. Empirical predictions have been made for the broadband noise radiated from ducted fans [56]. Glegg suggested that the tip vortex interaction with the duct boundary layer may produce a broadband noise source and could be the dominant source of high frequency noise. The effect of the boundary layer on ducted fan noise was further investigated on a test rig which attempted the removal of the boundary layer by the

use of suction, allowing a comparison of the noise generated with and without the boundary layer of the duct [57].

2.5 Challenges in identifying noise source mechanisms

In the marine industry, sea trials and full scale acoustic tests of propellers are well established and allow an accurate measurement of far-field noise radiation [58] [59]. However there are a number of drawbacks in the understanding of the noise generated by specific mechanisms of propeller noise when limited to full scale experimental analysis. One major problem is cavitation, which is not considered in this thesis. If cavitation occurs on a marine propeller it generates highly efficient sound sources that propagate strongly to the far-field. Cavitation noise may mask any of the weaker sound sources such as those caused by surface pressure fluctuations or vorticity and shear strains within the fluid, which are of more interest when discussing submarine propellers operating at depth. Finally, undertaking design development cycles which are based on using full scale propellers and experiments is costly and time-consuming and therefore impractical.

Some of these issues can be avoided by using smaller scale experiments such as towing tanks, flow channels, or flumes to investigate the propeller flow. The problem with these methodologies is that noise measurement becomes very difficult as these environments contain high levels of reverberation, making it challenging to distinguish the propagating signal from the reverberations reflecting off the walls and equipment within the experimental space. Some of these effects can be negated by the use of anechoic or hybrid wind tunnels [9] [60] [61]. A high proportion of the aerodynamic research to date has involved experimental procedures such as these [9] [60] [61]. These studies can produce far-field noise predictions, as well as allowing in depth analysis into the flow physics using techniques such as hot-wires, surface pressure taps, and particle image velocimetry (PIV) measurements. However, these methods still have limitations in the sampling resolution that can be reasonably taken. For example, the clustering of surface pressure measurements is limited by the physical size of the taps or sensors, PIV measurements are limited by the number of laser sheets and cameras that are available for each run, and hot-wire measurements are limited by the physical size of the hot-wire accessing small areas such as tip gaps, and the size of the structures of interest relative to the wire.

These restrictions have led to a gap in the knowledge regarding tip gap noise reduction, with the primary method being to infer improvements based on large flow regimes and the flow mechanisms involved in the acoustic sources are still not well understood. As such, design improvements are largely reactive and can be slow to evolve.

Use of numerical methods to study marine propeller noise

Given the challenges regarding experimental analysis, this research will use numerical methods to gain further insight into areas which have been prohibitive in previous studies. This research aims to analyse the flow regime between the tip of the blade and the duct, and understand the flow geometry in this region, allowing the prediction of effective noise mitigating designs. As the computational power available grows, CFD is used more frequently in the analysis of complex flow geometries regarding noise production by propellers. In fans, interest lies in exploring the noise produced by turbo machines, ducted fans in Heating Ventilation and Air Conditioning (HVAC) systems, as well as in large scale turbo-fan engines for aircraft as previously mentioned. In the marine industry, ducted propellers are less common as they are usually used to achieve specific goals, such as accelerating the flow to produce better efficiency at low speeds to increase bollard pull power for vessels which require high manoeuvrability. Such operations occur for relatively short time durations and so noise reduction is not a high priority in these vessels. More recently, noise prediction for commercial vessels is gaining importance [6] [7] [8] and so CFD is being used in this environment to predict far-field noise production and offer design improvements. Due to the importance of cavitation in noise production the majority of studies regarding marine propellers have focussed on predicting cavitation noise. Such studies include work by Lidtke et al [36] [26] [16], Bensow et al. [62] [35] which all use time resolved simulations to capture the sound sources on an integration surface before using an acoustic analogy to infer the propagation to the far-field.

A small number of studies have investigated shipping noise in non-cavitating conditions. Ianniello et al. have compared the noise predicting capability of CFD simulations with those of experiments [58] [63] [64] [65] based on a full scale RO-PAX vessel. Viitanen et al. [66] compared the noise production for wetted and cavitating conditions of a propeller compared with the predictions from experiments. Lloyd et al. [37] demonstrated the use of acoustic analogies when looking at propeller noise, compared RANS predictions from Ianniello et al. [58] and showed their effectiveness. Furthermore, Lloyd [27] used Large Eddy Simulation (LES) combined with an inlet turbulence generator and an acoustic analogy to predict the far-field noise of tidal turbines subject to a turbulent inflow.

Recent experimental works have shed light on the complex nature of the fluid mechanics in the tip gap region of a ducted propeller. Li et al. [67] used Matched Refractive Index (MRI) techniques to investigate the flow characteristics in the tip gap region of two axial turbo machines. The study concluded that the flow in this region was highly turbulent, and that the turbulence was spatially inhomogeneous. As such, computational methods such as Reynolds Averaged Navier Stokes (RANS) methods which makes models the turbulence in flows by assuming that it behaves in a predictable way rather than resolving it directly. The impact of either resolving or modelling the turbulence will be discussed in more detail in

Chapter 3. Li et al. concluded that higher resolution techniques which directly calculated at least the larger scales of the turbulence would be required to simulate tip gap flows.

2.6 Simplification of geometry to investigate fundamental flow features

It has been discussed that large scale experimental set-ups in the marine environment present significant complications regarding an insight into the noise sources of interest in this work. Model scale experiments using rotating propellers alleviate some of these difficulties but still hold difficulties in the acquisition of data with sufficient resolution in physically small spaces without impacting the flow of interest. The use of numerical methods allows the sampling of data from any location in the flow with the benefit of post-processing allowing the analysis of a single data set a number of times using different techniques as new insights lead the investigation in new directions. The limiting factor with numerical investigations is computational cost, which has different limitations depending on the spatial and temporal resolution of the simulations, as well as the equipment which is used, and the accuracy of the selected the solvers. Further discussion regarding the numerical methods is given in Chapter 3, while a more qualitative discussion will be presented here with examples of the impact this has had on the literature.

Numerical flow simulations rely on discretising the flow into finite quantities, and applying the Navier Stokes equations to determine the behaviour of the fluid accounting for viscous effects, turbulence, and the geometry of the flow. In reality the computational power available for the simulations will also have an impact but for this discussion it will be assumed that the computational power available remains constant. The relative expense of the simulation is fundamentally determined by the amount of turbulence which is resolved within the fluid domain, therefore, broadly speaking, in order to resolve a higher proportion of the turbulence, the physical size of the flow domain must be reduced to maintain the same computational effort.

The impact of this limitation can be seen in the literature where simulations using complete models of the fans of interest are limited. Previous work using complete models has almost exclusively been aimed at using the turbulent wake field predicted by time averaged simulations to predict the modes which will be propagated within a duct such as the noise prediction codes developed by NASA, [68], [69], [70] and [71]. These papers show that the code can give a general indication of the far-field noise generation of different turbo fan arrangements including tonal noise dominated by blade passing frequencies [72] but do not allow the identification of individual sources.

Noise generation is by definition an unsteady process and so understanding the source

mechanism induced by unsteady flow requires a higher resolution of turbulence. For this reason most studies maintain the computational effort by reducing the volume of flow resolved while increase the resolution on the turbulence. In a rotating frame this can be done by simulating a single propeller blade and using periodic boundary conditions [73] [10] [74] .

2.7 Invesitgation of a single non-rotating blade

In order to understand the fundamental behaviour of tip leakage flow, a number of experimental and numerical studies have simplified the geometry significantly by using a single blade in a non-rotating frame. Such studies have aimed at better understanding the onset of cavitation based on the tip gap size [75], and a number of studies developed based on experimental work by Grilliat et al. [9] to investigate the aeroacoustics of tip gap flow. This work used an experimental approach with NACA5510 foil at various angles of attack and tip gap heights in an anechoic wind tunnel. The advantage of simplifying the case in this way is that it offers the opportunity to interrogate the fundamental unsteady flow mechanisms involved. Subsequent studies have revisited this arrangement, illustrating the wealth of information that is available from a relatively simple test case [49] [13] [14] [76] [77] [78]. As discussed previously in this chapter, such simplifications also benefit numerical simulations, allowing higher spatial and temporal resolutions to be used, and thus resolve a high proportion of the turbulence.

2.8 Summary

This Chapter has introduced the use of ducted propellers in the marine environment, and highlighted the similarities and differences they have with aerodynamic fans. The current literature is largely based on aerodynamic fans used in the aviation industry and HVAC systems with little attention being devoted to hydrodynamic ducted propellers. Two important features of operating in water are: the risk of cavitation due to localised pressure drops; a significant decrease in the Mach number due to the speed of sound being greater and typical flow speeds being lower in a marine context. This thesis assumes that cavitation is suppressed by the operating depth of the propeller and so the key difference between this work and the literature is the difference in the Mach number. This has impacts for the efficiency of different noise mechanisms due to Mach number scaling which will be discussed further in Chapter 4.

A summary of the literature surrounding both marine and aerodynamic studies has been presented, and has found that while it is widely agreed that using tight tip gap clearances

reduces the noise produced and experimental studies of aerodynamic fans have tried to quantify the noise due to the boundary layer interaction, the mechanisms by which noise is generated in this area is not well understood.

To gain an understanding of the noise sources, the unsteady flow features that occur in the region in question must be understood. At present experimental techniques either do not have the sampling frequency required as with PIV, or the spatial resolution required, as with pressure taps or hot-wire measurements, to allow a fundamental understanding of the flow features. With the increasing power available for computational studies, it is likely that numerical simulations of the problem will be able to produce high fidelity investigation of the unsteady flow. This simulation of the flow features allows better visualisation of the unsteady flow mechanisms, and therefore a more complete understanding of the fundamental sources of the noise.

Chapter 3

Fluid modelling

3.1 Introduction

The investigation of ducted propeller tip gap noise can be split into two key stages, the understanding of the flow over the propeller, with particular focus given to the tip gap vortex flow, and the subsequent modelling of the noise produced by this flow, and it's propagation to the far field. To gain an understanding of the flow geometries within this problem, computational fluid dynamics (CFD) will be used to simulate the flow allowing the analysis of the most important flow mechanisms involved. Computational fluid dynamics allows the use of numerical methods to solve the Navier Stokes equations, by discretising them with respect to both space and time. This spatial discretisation is known as a finite-volume method, meaning that the solution domain is split into discrete cells or control volumes. The CFD program being used for this research is `OpenFOAM`, an open source CFD software based on finite volume methods using unstructured grids. `OpenFOAM` offers the ability to split, or decompose, jobs across multiple processors and therefore is easy to use with high powered computing clusters for greater efficiency in simulation time. The open source nature of `OpenFOAM` also offers greater flexibility in the set up of simulations. This felxibility is the primary reason for using `OpenFOAM` in the current study because as the investigations develops, different implementations of the basic code may become necessary and the open source nature allows the creation of new modules by editing the original source code.

This chapter will discuss the numerical methods for the discretisation of the flow domain with respect to space and time. It will cover the different methods of accounting for turbulence as mentioned and the merits and costs of each method with respect to the simulation of noise. The numerical techniques available for the identification of vortex structures which are of interest to the current problem will then be presented.

3.2 Turbulence modelling

Since the late 1970's CFD has proven itself to be a time and cost effective tool with regard to the design of fluid dynamic systems when compared with physical testing using apparatus such as wind tunnels. As computational power has increased, so too has the fidelity of the simulations which can be carried out in CFD on realistic engineering problems, including more accurate modelling of turbulent structures. The required resolution of turbulent structures plays a key role in choosing a solution method within CFD. Whether the turbulence is calculated directly (resolved) or modelled has implications of the grid resolution and time step required. The technique of removing the turbulence from the calculation and modelling it is done by averaging the flow parameters with respect to time, a method referred to as Reynolds Averaged Navier Stokes (RANS) and the different methods of modelling the turbulence will be discussed further in this chapter. This approach proves to be generally reliable for simulations involving steady flow regimes, as any result which is averaged over time will become a steady version of the true flow. For this reason, flows with unsteady characteristics will lose accuracy with the use of a RANS simulation, and may not even be able to be resolved sufficiently if the flow is highly unsteady. An unsteady version of RANS exists, known as uRANS, which uses the same time averaging approach as RANS but allows for the simulation to progress in time to capture some of the unsteady characteristics. The time-averaging of the Navier Stokes equations used in uRANS means that none of the turbulence is resolved therefore making the approach incapable of capturing the eddies which are the primary objective of this work.

More direct methods of calculating the turbulence exist and the extent to which it is calculated is dependent on a spatial filter which is governed by the mesh density. This spatial filter is used so that only the largest turbulent structures, or eddies, are resolved, with scales smaller than the grid, sub grid scales (SGS) being modelled, is known as Large Eddy Simulation (LES). This technique is computationally more expensive than RANS since the simulations requires a higher resolution in both time and space. There are non-dimensional values which can be calculated to define the spatial and temporal resolutions which will be discussed further in Section 3.2.2.

For very high accuracy applications the turbulence can be entirely resolved within a simulation using a method called Direct Numerical Simulation (DNS). The spatial and temporal resolution requirement is much higher again than LES, with eddy sizes including the Kolmogorov scale (see Equation 2.8) needing to be resolved by the grid. This resolution increase has a significant effect on the simulation time for a given domain as not only are there more cells which therefore require more calculations per time-step, meaning more time to solve each time step, but also more time steps to solve the same total time for the flow. When interested in frequency content of flows a certain time sample is required such

that the lower frequencies can be resolved with sufficient resolution, while at the same time a sufficiently low time-step must be used so that the sampling frequency can satisfy the Nyquist criteria where the sampling frequency required is equal to double the frequency of the highest frequency content to be investigated. In this work however, the limiting factor on the time-step for the simulations was the numerical stability rather than satisfying the Nyquist criterion, based on the assumption that the frequencies of interest were below $20kHz$.

3.2.1 Reynolds Averaged Navier-Stokes - RANS

The RANS method uses a time filter by averaging the flow properties over ever-increasing time steps to give a quasi-steady flow regime which allows for simplification of the simulations. As such, all of the turbulence in RANS simulations must be modelled, and there are several systems which do that by adding transport equations to be solved. In the marine industry, a common method is the $k-\omega$ SST model, developed by Menter et al. [79], which introduces two additional variables, turbulent kinetic energy k and the specific dissipation rate ω, that are used to infer a scalar variable for the eddy viscosity, ν_t. The SST model has been shown to be more robust in simulations that involve separated flow, which is important to this work, where the formation of the tip vortex is dependent on flow separation.

3.2.2 Large Eddy Simulation - LES

Large Eddy Simulation (LES) provides a more accurate computation of the flow properties as the larger eddies are directly resolved. The filtering of LES simulations is spatial and defined by the local grid size, with eddies that are smaller than the grid size being modelled using the sub-grid scale (SGS) stress tensor where,

$$\boldsymbol{\tau}_{ij} = \overline{\mathbf{U} \otimes \mathbf{U}} - \overline{\mathbf{U}} \otimes \overline{\mathbf{U}}. \tag{3.1}$$

As with RANS there are many options available for accounting for the sub grid scales in LES and how they interact with the large turbulent eddies which are resolved. Most are formed based on the assumption that τ_{ij} is proportional to the resolved rate of strain tensor, $\overline{\mathbf{S}}_{ij}$, following [80] and [81]:

$$\boldsymbol{\tau}_{ij} - \frac{1}{3}\boldsymbol{\tau}_{ij} \cdot \mathbf{I} = -2\,\nu_{sgs}\,\overline{\mathbf{S}}_{ij} \tag{3.2}$$

where,

$$\overline{\mathbf{S}}_{ij} = \frac{1}{2}\left(\frac{\partial \overline{\mathbf{u}}_i}{\partial x_j} + \frac{\partial \overline{\mathbf{u}}_j}{\partial x_i}\right). \tag{3.3}$$

The over-line represents the spatial filtering which is imposed by the local grid resolution. The general formulation for the eddy viscosity for most models can be shown to be:

$$\boldsymbol{\nu}_{sgs} = C_m^2\, \Delta^2\, \overline{OP}(\mathbf{x}, t) \tag{3.4}$$

where C_m is a constant defined by the model, Δ is the filter length which is implicitly taken from the local grid resolution, and $\overline{OP}$ is and operator defined from the resolved fields.

A variety of sub grid models are available for use with LES and within the `Openfoam` framework. One of the most popular is the Smagorinsky model, later updated to the Dynamic Smagorinsky model, and has been used in previous works using LES to predict far-field noise with the help of an acoustic analogy [27] [36] [16]. However, it has been suggested that the Smagorinsky models do not correctly predict the sub grid scale viscosity in the near wall region [80]. In the case of wall bounded flows, a Wall-Adapting Local Eddy-viscosity (WALE) model has been proposed [80] and a number of studies have compared the use of the different sgs models available for use in LES [82] [81] [83] [84] [85]. While it could be argued that the differences between the models are minor, the studies conclude that when combined with a sufficiently fine mesh [81] the WALE model performs better than the Smagorinsky models whilst also showing a more efficient use of computational effort [85]. The WALE model will be used in this work given the tip gap flow is highly analogous to the wall bounded flow for which the model was created, along with the increased computational efficiency and robust application to both structured and unstructured grids.

The WALE model uses an operator which is based on the traceless symmetric part of the square of the velocity gradient tensor, s_{ij}^d, leaing to [81]:

$$\overline{OP}(\mathbf{x}, t) = \frac{\left(s_{ij}^d s_{ij}^d\right)^{2/3}}{\left(\overline{\mathbf{S}}_{ij}\overline{\mathbf{S}}_{ij}\right)^{5/2} + \left(s_{ij}^d s_{ij}^d\right)^{5/4}}. \tag{3.5}$$

Applying this filter to the equations of mass and momentum conservation leads to

$$\nabla \cdot \overline{\mathbf{U}} = 0 \tag{3.6a}$$

$$\frac{\partial\left(\overline{\mathbf{U}}\right)}{\partial t} + \nabla \cdot \left(\overline{\mathbf{U}} \otimes \overline{\mathbf{U}}\right) = -\frac{1}{\rho}\nabla p + \nu \nabla^2 \overline{\mathbf{U}} - \nabla \cdot \boldsymbol{\tau}_{ij}. \tag{3.6b}$$

The assumption that the sub-grid scales are sufficiently small that they can be modelled rather than resolved places strict requirements on the grid as discussed by [86] leading to the condition:

$$x^+ \approx 50 - 150, \tag{3.7a}$$
$$y^+ \approx 1 - 3, \tag{3.7b}$$
$$z^+ \approx 15 - 30, \tag{3.7c}$$

where x is aligned with the flow, y is perpendicular from the wall, and z is parallel with the wall and transverse to the flow.

The superscript + indicates a non-dimensional distance defined by the local friction velocity u^*, distance from the first grid point to the wall y and kinematic viscosity of the fluid ν such that

$$y^+ = \frac{u^* y}{\nu}, \tag{3.8a}$$
$$u^* = \sqrt{\frac{\tau_w}{\rho}}, \tag{3.8b}$$
$$\tau_w = \mu \left.\frac{du}{dy}\right|_{y=y_w}. \tag{3.8c}$$

where τ_w is the wall shear stress, ρ is the fluid density, μ is the dynamic viscosity, and du/dy is the velocity gradient at the wall. The calculation of x^+ and z^+ follow similarly using Equations 3.8b and 3.8c such that:

$$x^+ = \frac{u^* \Delta x}{\nu}, \quad z^+ = \frac{u^* \Delta z}{\nu}, \tag{3.9}$$

using the stream-wise grid spacing, Δx and transverse grid spacing Δz.

The stability of the simulation is also governed by the relationship between the cell size, Δx, the local flow speed, u and the time step Δt, given by the Courant number, C,

$$C = \frac{u \Delta t}{\Delta x} < C_{max}. \tag{3.10}$$

A ,maximum Courant number of unity is usually required to ensure stability of unsteady simulations and is physically equivalent to the fluid moving through a single cell in a single time step. As discussed, with the PIMPLE algorithm this requirement can be relaxed

somewhat and this work found Courant numbers of $C \approx 5$ were achievable to allow faster simulation times.

The use of these grid refinement requirements can be alleviated somewhat by removing some of the cells in the inner most layers of the boundary layer, assuming that the flow near the wall behaves in a predictable way and therefore can be modelled. These models are referred to as wall functions and allow the y^+ requirement to be significantly increased which can greatly reduce the number of total cells and therefore the computational cost, given that wall resolved LES requires a very large proportion of the cells be used to resolve the inner boundary layer [87]. Wall modelling is therefore a popular resource for reducing the cell count of LES simulations and discussions regarding different models have been presented by [88] and [87]. However, caution must be taken when using these models as by definition they make assumptions about the inner layers of the boundary layer flow. For this reason this work used wall functions for the boundary surface above the tip as it is flat and continuous and capturing the exact flow characteristics when the flow meets the edges of the surface are not important. The foil surface did not use wall functions but maintained the $y^+ < 1$ criteria as the flow within the tip gap region is expected to be complex and with thin boundary layer profiles.

Both RANS and LES have their uses in this field of research as RANS modelling allows new simulations to be tested to give approximate results, rather than using an LES solver and having to wait for the full simulation to run before checking for errors. RANS modelling can also be useful in setting up a case for LES. When the developed flow is expected to be very complex, running a full LES simulation can require a very long time for the flow to fully develop into its converged state, meaning a large proportion of computational time is spent on something which has little or no relevance. For this reason RANS simulations are often used to develop the flow fully but approximately, before using the higher accuracy methods. This resolved flow can then be used to initiate the solution with an LES solver so the computational time is used more efficiently.

3.3 Solution algorithms

3.3.1 Pressure velocity coupling

There are two variables to be solved in the Navier Stokes equations, namely pressure and velocity, and so they must be coupled in order to solve them simultaneously. `OpenFOAM` relies on the semi-implicit method for pressure linked equations (SIMPLE) [89], pressure-implicit split-operator (PISO) [90] or a combined algorithm (PIMPLE) to iteratively link the pressure and velocity solutions. The SIMPLE algorithm is used in this work to solve the time averaged RANS simulations, while PIMPLE is used for the time resolved simulations. PIMPLE is

used over PISO because it allows several iterations to be carried out within each time step. This allows for Courant numbers which are greater than unit and can therefore improve simulation time by reducing the required time-step.

3.3.2 Equation discretisation

In order to solve the partial differential equations (PDEs) which define the fluid flow, they must first be discretised in such a way that they can be described in matrix form as

$$\mathbf{A}\ \mathbf{x} = \mathbf{b}. \tag{3.11}$$

Here, $\mathbf{A}$ is a square matrix, which stores coefficients for fluid properties and grid parameters, $\mathbf{x}$ is a column vector containing the dependent variables and $\mathbf{b}$ is the source vector containing the boundary conditions.

In order to solve the discretised equations there are a number of solvers which can be implemented within `OpenFOAM`. Following previous works using acoustic analogies with incompressible LES solvers [27] [16], this work uses the multi-grid (`GAMG`) solver with a `GaussSeidel` smoother to solve for pressure as this combination has been shown to work well on unstructured grids [27]. Velocity is solved for using the preconditioned bi-conjugate gradient solver (`PBiCG`) in conjunction with the diagonal incomplete lower upper (`DILU`) preconditioner.

3.3.3 Finite volume method

The finite volume method divides the flow domain into a series of discrete volumes or cells, bounded by flat faces, allowing the governing flow equations to be solved over each cell ensuring that the conservation of mass and momentum across the cell. Equation 2.5a can be integrated over a cell of volume V to give:

$$\int_V \nabla \cdot \mathbf{U} dV = 0. \tag{3.12}$$

Gauss' theorem may be used to rewrite Equation 3.12 as

$$\int_S \mathbf{U} \cdot d\mathbf{S} = 0 \tag{3.13}$$

where S is the surface area of the volume, and $\mathbf{S}$ represents the surface area vector. This theorem can similarly be used with the conservation of momentum equation, Equation 2.5b.

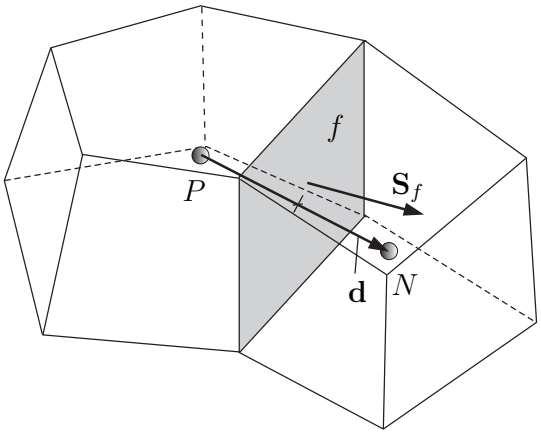

Figure 3.1: "Parameters in finite volume discretisation" taken from the `OpenFOAM` Programmers Guide [91].

3.3.4 Numerical schemes

Figure 3.1 shows the representation of two neighbouring cells, P and N along with their connecting face, f, and the corresponding surface area vector, $\mathbf{S}_f$. Flow properties are usually stored at the cell centres, and their movement from one cell to the next is shown by $\mathbf{d}$. The numerical solution of the differential equations requires the flow properties to be known at the cell face centres, to allow the integral over the cell faces. One simple way to calculate the face values given the cell centre values would be to use linear interpolation.

If Figure 3.1 were simplified so the cells were aligned with centroids on the x-axis, an arbitrary variable ϕ would be calculated on the face by

$$\phi_f = \frac{\phi_N - \phi_P}{x_N - x_P}(x_f - x_P) + \phi_P \tag{3.14}$$

where the subscripts P and N denote cell centres and f is at the face. For a uniform grid along the x-axis this expression reduces to the mean value of the two cell centre values,

$$\phi_f = \frac{\phi_N + \phi_P}{2}. \tag{3.15}$$

Calculation of the gradients of flow variables at the cell faces are also important and this can be done by taking the Taylor expansion of the face value using both cells P and N,

taking the distance between cell centres as Δx which yields

$$\phi_N = \phi\left(x_f + \frac{\Delta x}{2}\right) = \phi(x_f) + \frac{\Delta x}{2}\phi'(x_f) + \frac{(\frac{\Delta x}{2})^2}{2!}\phi''(x_f) + \mathrm{O}\left[\Delta x^3\right], \tag{3.16a}$$

$$\phi_P = \phi\left(x_f - \frac{\Delta x}{2}\right) = \phi(x_f) - \frac{\Delta x}{2}\phi'(x_f) + \frac{(\frac{\Delta x}{2})^2}{2!}\phi''(x_f) + \mathrm{O}\left[\Delta x^3\right]. \tag{3.16b}$$

Subtracting Equation 3.16b from Equation 3.16a gives

$$\phi_N - \phi_P = \phi'_f \Delta x + \mathrm{O}\left[\Delta x^3\right] \tag{3.17}$$

and rearranging for the gradient at the face, ϕ'_f leaves

$$\phi'_f = \frac{\phi_P - \phi_N}{\Delta x} + \mathrm{O}\left[\Delta x^2\right]. \tag{3.18}$$

It can be seen that this scheme is of second order accuracy and uses cells on either side of the face to determine the face value. It is therefore known as the second-order central difference (CD) scheme. The second order CD scheme can produce non-physical results in certain conditions and therefore can impact the stability of the simulation. Stability can be improved by using first order schemes such as an upwind differencing (UD) scheme, which takes the face value to be equal to the cell centre value upstream,

$$\phi_f = \begin{cases} \phi_P, & \text{if } F \geq 0 \\ \phi_N, & \text{if } F < 0. \end{cases} \tag{3.19}$$

Intuitively it is obvious that UD schemes sacrifice some numerical accuracy for increased stability, and often blended differencing (BD) schemes will be used which allow the use of a limited amount of the transition effects of upwinding to increase stability whilst retaining most of the accuracy of a CD scheme.

3.4 Meshing strategy

There are two main methods for generating the grid for a CFD simulation; structured and unstructured and their advantages and disadvantages will be discussed here and are summarised in Table 3.1.

Table 3.1: Key features of structured, cartesian unstructured and tetrahedral unstructured grid generation.

Attribute	Structured	Unstructured	
		Cartesian	Tetrahedral
Labour intensity	High	Low	Low
Resolution control	High	Low	High
Resolution flexibility	None	High	High
Cell orientation	Controllable	Fixed	Free
Maximum Volume Ratio	Low	High	Low
Mesh Non-orthogonality	Low	Very low	High

Structured grids are time-consuming to create but offer the highest amount of control over cell spacing and orientation and therefore have great benefit when flow is aligned with the cell orientation but have limitations in their strict structure. As a structured grid requires the same number of points on opposing grid edges, areas which require dense grid resolution such as areas of high curvature of complex flow structures, this high density is projected to the limits of the domain, meaning fine grid refinement is wasted in areas of little interest or which have little impact on the general solution. Structured grids also lose their advantage when the flow is highly irregular or unsteady. In these regions the flow through the cells is no longer aligned with the axis of the cell and passes through the faces at an angle.

Different meshing software generate unstructured grids in different ways, using mostly either Cartesian or tetrahedral grids consisting of 6 quadrilateral and 4 triangular faces respectively. Cartesian grids uses hexahedral cells maintain cell faces which are parallel with the axes of the domain, which can be an advantage if the flow is aligned with the grid. However, at the intersection between different levels of grid resolution, two problems occur, on is that the volume ratio from one layer to the next is very high. The transition from one layer to the next in hexahedral meshes requires the edge length of the cell to be halved, resulting in a volume ratio between layers of $2^3 = 8$. This volume ratio means that layers of refinement have to be added in stages, so there are regions of similar cell size, separated by large jumps at the interface. There is now a hanging node in the middle of a cell face, which is not directly connected to the edges of the larger cell, meaning that the faces of four cells connect to a single face of the larger cell.

Tetrahedral grids use four triangular faces to make each individual cell. This means that the problems encountered with Cartesian grids are avoided, as there are no hanging nodes and the faces between neighbouring cells are never split. This allows cell size growth to be much smoother, without needing large volume ratios. The disadvantage of tetrahedral grids is that the cell faces are much less likely to be aligned with the flow direction. However in areas of very complex, turbulent flow, Cartesian grids also lose this alignment and so also

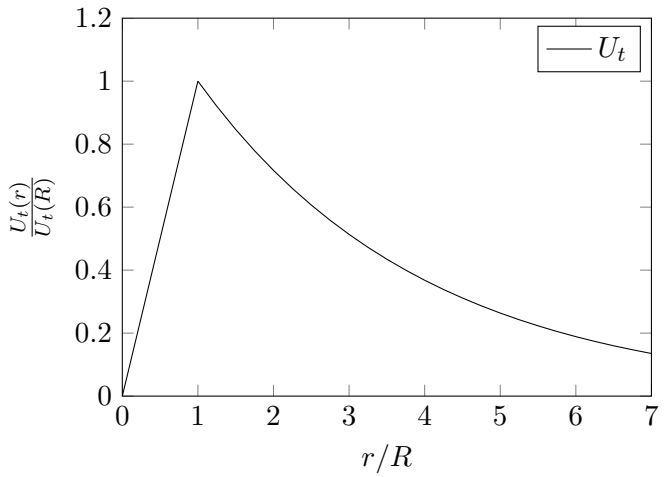

Figure 3.2: Rankine vortex tangential velocity, U_t, based on core radius, R.

lose their advantage.

3.5 Vortex identification methods

Due to the central role vortices have in this research it is important to discuss how they are formed, and how they can be objectively identified within a flow field. Vortices are present in most flows, from the very small scales where they form the basis of turbulence, to the very large scales affecting global weather patterns and cosmic structures. Vortices in real flows can be approximated by a Rankine vortex [92] which has two components of different vortical structures. The inner core behaves like a solid object of radius R, equivalent to a rotating cylinder where the tangential velocity at the centre is zero but at the edge is a maximum, with a linear relationship between the two points. If this cylinder is immersed in a fluid, the fluid behaves like a potential vortex, where the tangential velocity will be maximum at the surface of the cylinder due to viscosity, and will decrease with an inverse square relationship with distance from the cylinder as the viscous effects reduce. If the cylinder itself is then replaced by fluid which behaves on a solid body rotation then a Rankine vortex is produced which gives a good representation of a real vortex [54]. This representation is shown in Figure 3.2 where r is the distance from the centre, $r = R$ is the location of the edge of the viscous core region, and U_t is the tangential velocity.

The centre of this vortex has a constant vorticity, as the solid body rotation means that the angular velocity throughout the core is constant. However, using vorticity alone to identify a vortex is not always reliable. Vorticity gives a measure of the rotation at a location within a fluid, however, there is no threshold value which defines a vortex core. A clear vortex could exist within an area of slow rotation which is beneath the threshold set, equally a highly

turbulent region could contain areas of high vorticity but with a random distribution of different sized eddies. Vortex definitions can be split into three different classifications:

- Classification 1: Region or Line. Regional algorithms find groups of cells which are all bound by a vortex region, which can be used to infer the size of the vortex core, while line algorithms describe the path of the centre of the vortex. Regional algorithms tend to less expensive computationally and can be applied to a volume domain, while line algorithms need to find precise points on a series of planes which are close to perpendicular to the vortex path. These points are joined to form the line and so linking lines with multiple vortices requires an appropriate spacing of the sampling surfaces. The most suitable algorithm would be one which identifies a region, rather than a line and this region would define the limit of the grid refinement required to capture the vortex behaviour.
- Classification 2: Galilean Invariance. Vortices only exhibit swirling motion if the reference frame moves with the vortex. Schemes which are Galilean invariant produce the same result if a uniform flow is applied to the flow field. given the variety of flow directions in and around the tip region, Galilean invariance will be an important attribute in the selected algorithm.
- Classification 3: Local or Global: Local algorithms use the information in individual cells, regardless of their neighbours, while global algorithms require a regional view of several cells to identify the presence of a vortex. Local algorithms are advantageous for this work as they can be applied to the whole flow domain for computational ease, as well as the option of being processed at each time step within `OpenFOAM`.

Based on these definitions, the two options considered here for vortex identification algorithms are Q and λ_2 criteria as they are included as part of the `OpenFOAM` software and have been shown to perform well describing the shape of vortices within a flow field [93] [94] [95].

The Q criterion is defined as a spatial region where

$$Q = \frac{1}{2}\left(|\mathbf{\Omega}|^2 - |\mathbf{S}|^2\right) > 0, \tag{3.20}$$

where $\mathbf{\Omega} = \frac{1}{2}\left[\nabla \boldsymbol{v} - (\nabla \boldsymbol{v})^T\right]$ is the vorticity tensor, and $\mathbf{S} = \frac{1}{2}\left[\nabla \boldsymbol{v} + (\nabla \boldsymbol{v})^T\right]$ is the rate of strain tensor, where $\boldsymbol{v}(\boldsymbol{x}, t)$ is the velocity field. The criteria $Q > 0$, implies that a point is within a vortex if the vorticity is greater than the rate of strain.

The λ_2-criterion considers the three eigenvalues of the sum of $\mathbf{S}^2$ and $\mathbf{\Omega}^2$, and defines a pressure minimum due to vortical motion as being a connected region with two negative eigenvalues, thus the definition is,

$$\lambda_2 \left(\mathbf{S}^2 + \mathbf{\Omega}^2 \right) < 0. \tag{3.21}$$

stating that if the second eigenvalue, λ_2 is negative, then that point lies within a vortex.

The open source nature of `OpenFOAM` would allow packages to be written which could achieve other vortex definitions such as the Δ and the M_z-criterion [96], [95], the latter is suggested by Haller to be the most robust criteria for identifying vortices in complex flows. However the benefit of this would be relatively low with regard to the prediction of noise generation, and would require significant additional work.

In most cases it should be noted that the λ_2 and Q criteria produce similar, if not identical results[94]. However in the cases investigated during the development of the λ_2-criterion [96], it has been shown to produce more reliable results and further studies have agreed it is more robust than the Q-criterion [95]. For this reason the λ_2-criterion will be used in this work. The initial test case in Chapter 5 will use both criteria as well as using the magnitude of vorticity as a further comparison of the two systems.

3.6 Summary

This chapter has discussed the discretisation of a fluid domain into finite volumes and of the governing equations to allow the use of numerical methods to resolve the flow. The selection of `OpenFOAM` has been justified due to its open source nature making it readily available and cost effective whilst also allowing the manipulation the dictionaries which control the simulations and the post processing.

Different CFD techniques have been discussed and their usefulness and limitations has be shown, both with respect to resolving the turbulence within the flow, and predicting noise. The least computationally expensive technique, RANS, offers an indication of the general flow features, but due to its time-averaged approach, it may not be of use for simulating highly unsteady flows. The prediction of noise has been shown to require unsteady approaches by definition and so RANS alone will not be used for noise source investigation. The unsteady RANS approach, URANS, has been shown in the literature to not resolve the turbulent structures sufficiently which are of interest to this work with regard to their noise generation and so will not be used.

LES has been shown to be the most promising technique to develop the understanding of the effect of tip gap flow on noise generation. This has been determined by inspection of the methodology of LES as well as by reviewing the literature regarding FSI noise investigations. The drawback of LES with regard to computational expense has been discussed and so RANS will still be used in preliminary investigation work as well as early simulations. The

use of RANS to produce a starting condition for LES simulations has been shown to reduce the simulation time required by an LES simulation. The selected LES sub-grid model has been presented following previous studies demonstrating its accuracy in resolving flows with similar features to those expected in this thesis.

Chapter 4

Acoustic modelling

4.1 Introduction

In order to further the understanding of the noise sources in the tip gap region, the far-field noise has been predicted numerically to allow comparison with the flow features. This chapter discusses the different methodologies which are available, comparing their relative merits and shortcomings, before explaining the chosen method in greater detail.

4.2 Noise generation and classification

Noise can be described as a pressure wave of small longitudinal amplitude fluctuations travelling through a compressible fluid. The fluid in question must obey the linearised mass continuity equation

$$\frac{\partial \rho}{\partial t} + \nabla \cdot (\rho \mathbf{U}) = 0, \tag{4.1}$$

which is the same as equation 2.1, and the conservation of momentum equation which may be written as

$$\frac{\partial (\rho \mathbf{U})}{\partial t} + \nabla \cdot (\rho \mathbf{U} \otimes \mathbf{U}) = -\nabla p + F(\mathbf{y}, t), \tag{4.2}$$

where $F(\mathbf{y}, t)$ represents an generalised source with position within the sound generation region, y, and tends to zero in the far field. The variables of interest are pressure and density which can be related using $p = c_0^2 \rho$ where c_0 is the speed of sound. This relationship allows the momentum equation to be linearised and rewritten as

$$\frac{\partial(\rho\mathbf{U})}{\partial t} + c_0^2\nabla p = F(\mathbf{y}, t). \tag{4.3}$$

The fluctuating components of pressure and velocity is the difference between the total value and mean value as

$$p' = p - p_0 \tag{4.4a}$$
$$\rho' = \rho - \rho_0. \tag{4.4b}$$

Taking the spatial derivative of Equation 4.3 and subtracting it from the time derivative of Equation 4.1 yields the inhomogeneous wave equation

$$\left(\frac{1}{\partial t^2} - c_0^2\nabla^2\right)\rho' = c_0^2\Box^2\rho' = F(\mathbf{y}, t), \tag{4.5}$$

where $\Box^2$ is the d'Alembertian or wave operator, which governs sound propagation due to an external force, which corresponds to the acoustic source term.

Lighthill [31] proposed that the acoustic sources in a fluid could be represented by the non-linear components in the Navier-Stokes equations, such that by subtracting the linearised momentum equation (Equation 4.3) from the full momentum equation (Equation 4.2) an exact expression can be made for the acoustic source and equations 4.3 and 4.5 can be re-written as

$$\frac{\partial(\rho\mathbf{U})}{\partial t} + c_0^2\nabla p = -\nabla\cdot\mathbf{T} \tag{4.6a}$$
$$c_0^2\Box^2\rho' = \nabla^2\mathbf{T} \tag{4.6b}$$

where the turbulent stresses throughout the fluid which represent sources of noise are described by the Lighthill stress Tensor,

$$\mathbf{T} = \rho\mathbf{U}\otimes\mathbf{U} - p\mathbf{I} + \mathbf{D} - c_0^2\rho'\mathbf{I}, \tag{4.7}$$

which for low Mach numbers can be simplified to

$$\mathbf{T} \approx \rho_0\mathbf{U}\otimes\mathbf{U}, \tag{4.8}$$

which is justified for marine propellers $M < 0.03$ as discussed by [35] [97] [22],

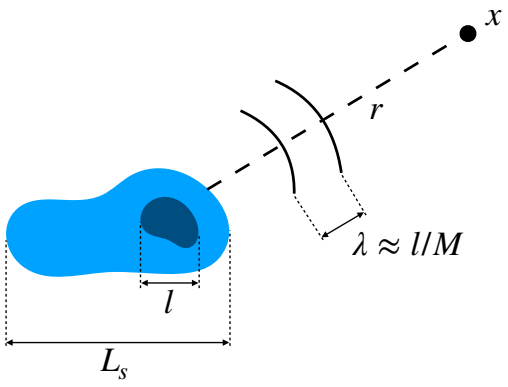

Figure 4.1: Acoustic length scales and definitions, adapted from [98].

If there is a solid body within the flow then there must be no flow across the wall of the body, so then $\mathbf{U} \cdot \hat{\mathbf{n}} = 0$ where $\hat{\mathbf{n}}$ is the wall normal unit vector. This implies that the Reynolds stress tensor at the wall is zero, allowing the wave equation to be written as [33]

$$c_0^2 \Box^2 \rho' = \nabla^2 \mathbf{T} + \nabla(p\mathbf{I} \cdot \hat{\mathbf{n}}). \tag{4.9}$$

The length scales which describe the relative sizes of an acoustic source and far-field are shown in Figure 4.1. The source region (such as rigid bodies in the flow) has size L_s, a compact source (such as an individual eddy) has length l. The acoustic wavelength is λ and the distance is r, to the receiver location, x. The receiver is said to be in the acoustic far-field if the distance to the receiver is much larger than the acoustic wavelength such that $r \gg \lambda$. The far-field relative to the source region is dependent on the distance to the receiver being much larger than the source size, $r \gg L_s$. The source is said to be compact if the characteristic source length is much shorter than acoustic wavelength $\lambda \gg l$ and similarly for the source region $\lambda \gg L_s$ [98].

The types of noise source can be split into three distinct categories, collectively known as multipoles which exhibit different characteristic behaviours [99]. These are:

- Monopole sources represent a fluctuating change of mass inside a finite volume,
- Dipoles are created by a force exerted on the fluid by a surface moving relative to the fluid,
- Quadrupoles are created by turbulent stresses with the fluid volume.

Under the assumption that the Mach number is small and the sources are compact, the far-field root mean square (rms) pressure, p, due to the n^{th} multi-pole can be shown to be,

$$p \approx \frac{1}{c_0^n |\mathbf{r}|} \frac{u^n}{l^n} \cdot O(F_{ijk\ldots}) \tag{4.10}$$

where $n = 0, 1, 2$ for monopole, dipole and quadrupole sources respectively, u and c_0 are the flow and sound speed of the fluid respectively and $\mathbf{x}$ is the location vector of the receiver which is at a distance $|\mathbf{r}|$ from the source, as shown in Figure 4.1.

Order of magnitude estimates can be made for F based on the type of source. The eddy source size and flow speed for each multi-pole, and therefore that the pressure contribution of each is ultimately dependent on Mach number, M:

$$p_{monopole}(\mathbf{x}, t) \propto \frac{\rho_0}{|\mathbf{r}|} l u^2, \tag{4.11a}$$

$$p_{dipole}(\mathbf{x}, t) \propto \frac{\rho_0}{|\mathbf{r}|} l u^2 M, \tag{4.11b}$$

$$p_{quadrupole}(\mathbf{x}, t) \propto \frac{\rho_0}{|\mathbf{r}|} l u^2 M^2 \tag{4.11c}$$

$$\text{where} \quad M = \frac{u}{c_0}, \tag{4.11d}$$

i.e. that the pressure contribution for multipoles scales by M^n. It has been shown that for marine propellers $M < 0.03$ [35] [97] [22], and therfore the quadrupole sources offer a much smaller contribution than the other two and have been discounted in previous works [27]. This implies that dipole sources are likely to be the primary noise source in this problem.

4.3 Numerical methods for acoustics

Problems involving both flow and sound present particular features which need special consideration to be solved numerically. The difficulty simulating fluids and acoustics simultaneously is largely due to the very different scales of the fluctuating components of fluid properties contained in the problem. Fluid flow typically contains large pressure and velocity fluctuations caused by both large and small, slow moving eddies within the flow. Acoustic waves have relatively small pressure and density fluctuations that propagate at high speed compared with the flow speeds of interest [98]. The result is that small inaccuracies in the unsteady flow calculation, which would usually be negligable, can produce very large errors in the predicted acoustic propagation. Any spatially discretised domain will have the tendency to cause numerical dissipation and dispersion, as a smooth wave is discretised into distinct sections and a proportion of the information is lost. Numerical dissipation and dispersion applies to both the fluid flow and the acoustic propagation and the errors induced are minimised by reducing the discretisation length scales [98]. Due to the importance of aeroacoustics in many engineering problems, the various methods availble to predict them are well discussed within the literature [100] [98]

This section will compare the different methods which can be used to numerically model aeroacoustic problems, often referred to as Computational Aero Acoustics (CAA). Their

strengths and weaknesses will be presented, and their suitability to predicting tip gap noise will be discussed.

4.3.1 Direct compressible simulation

Direct compressible simulations are used to simulate the propagation of sound directly through the fluid medium. Directly resolving the acoustic propagation offers advantages in certain situations. For example, it will capture the sound being reflected from solid surfaces, as well as sound waves which are refracted through shear layers. In order to accurately capture the propagation of sound to the desired receiver locations, the numerical and spatial resolution have to be high in order to minimise the numerical dissipation and dispersion. Studies using this methodology require high resolution Large Eddy Simulation (LES) [101] [102], or Lattice Boltzman Method (LBM) [14] simulations, or fully resolved Direct Numerical Simulation (DNS) [103]. It was suggested by Choi and Moin [86], following initial estimates from Chapman [104], that the number of grid points required for wall resolved LES, N_{wr}, and DNS, N_{DNS}, are given by:

$$N_{wr} \sim Re_{L_x}^{13/7} \tag{4.12a}$$

$$N_{DNS} \sim Re_{L_x}^{37/14}. \tag{4.12b}$$

The flows of interest to this work have Reynolds numbers of order of magnitude $10^5 < Re < 10^6$, meaning that the minimum number of cells required for a wall resolved LES simulation would be of the order 10^{14}. The mesh requirements of these types of simulation make them impractical using the computational power available, with practical cell counts roughly limited to the order of 10^7 cells.

4.3.2 Acoustic analogy

An acoustic analogy is a method of calculating the propagation of sound based on the motions of a fluid [105]. First the sound sources are found by calculating the fluid flow, before the propagation of the source is calculated to a known receiver location. This allows these methods to be used as a post processing tool, and does not require simulating the propagation of sound directly. This also means that receiver locations can be placed outside of the simulation domain allowing the method to be flexible if additional receivers need to be added and reducing the size of the domain to only contain the flow of interest, further reducing the computational effort. Recent works towards the prediction of aeroacoustics and hyrdroacoustics have used this methodology for its versatility and computational efficiency.

Part of the reason for its success is that it can be implemented using both compressible and incompressible solvers [106], as the solution to the hydrodynamic problem is used only to generate the sound sources, and not to propagate the sound directly. However, the use of an incompressible solver for calculating the sound sources requires the assumption that the sources are acoustically compact [27]. For an acoustic source to be considered compact its characteristic length must be significantly shorter than the acoustic wavelength, as discussed in Section 4.2. The implication of using the compact source assumption is that source mechanisms which involve large surfaces can not be predicted by an incompressible solver as the acoustic waves are not captured [107].

- **Lighthill's acoustic analogy** - Lighthill pioneered the work of aeroacoustics by rearranging the equations of motion of a fluid into a wave equation, given in Equation 4.6b [31]. Lighthill's method requires the integration of the acoustic sources present within a flow and deducing their contribution to the acoustic pressure fluctuations at a known receiver in the far-field. At the time the primary interest was in the reduction of jet noise, and so this volumetric approach was necessary to capture the sources of interest. This formulation is still used effectively to predict jet noise, although the FW-H analogy offers a more computationally efficient option by using a porous integration surface to avoid the use of a volumetric integral. However, Lighthill's formulation does not account for the presence solid objects within the flow and so can not be applied to the problem investigated here.

- **Curle's acoustic analogy** - Lighthill's analogy was extended by Curle [33] to account for the presence of solid bodies within the flow, with the result shown in Equation 4.9. Acounting for solid bodies within the flow made Lighthill's work applicable to a wider range of external flow problems, including tip gap noise investigated in this work [48].

- **Ffowcs Williams-Hawkings acoustic analogy** - The work by Lighthill and Curle was further developed by Ffwocs Williams and Hawkings to account for the motion of the body within the flow [108]. This approach offers considerably greater flexibility than the other analogies mentioned as the sound sources are integrated over a surface which can be bound to one of the physical boundaries, or can be arbitrarily located within the fluid flow. If the boundary is chosen to be within the fluid then considerable care must be taken to place the surface such that it captures all of the sources of interest and is not penetrated by strong voritces which cause spurius noise predictions as they pass through the integration surfaces [109] [110] [111]. When used with an integration surface which is within the fluid, this analogy can include a volumetric integral to capture quadrupole noise sources, similar to Lighthill's original analogy. Due to its flexibility this analogy has found favour in the prediction of aeroacoustics [13] as well as hydroacoustics [62]. As the analogy simply radiates the sound from distinct sources it can also be used with pressure samples taken from experimental

inveistigations [112]. The use of this analogy relies on the fluid solver capturing all of the relevant sound sources. Care must be taken when using the FW-H analogy in conjunction with an incompressible fluid solver as source mechanisms which rely on compressibility will not be captured [107]. Noise generation due to trailing edge mechanisms, for example, has been shown to require a compressible flow solver [113] [114].

4.3.3 Acoustic-viscous splitting

Acoustic-viscous splitting methods divide the problem into two distinct problems; the viscous fluid motions and the acoustic propagations, as first proposed by Hardin and Pope [115]. Firstly, the fluid motions are solved using an incompressible solver, which establishes the motions of the fluid and leads to velocity and pressure fluctuations within the fluid. This requires the same grid refinement methodology which has been discussed in Chapter 3, such that all of the important flow features can be captured accurately. In a simulation looking to resolve the incompressible flow features and surface pressure fluctuations, the density fluctuations are considered negligible at low Mach numbers. As has been discussed, these hydrodynamic density fluctuations when considered relative to the acoustic density fluctuations can be quite large. This method uses the speed of sound, c_0 to infer the density fluctuations based on the calculated pressure fluctuations.

Acoustic-viscous splitting allows advantages over the direct compressible simulations as the viscous and acoustic grids can be designed specifically for their purpose, allowing more efficient calculation of the propagating acoustic waves. Similarly to the direct compressible simulations this method includes the requirement that the receiver locations must be known ahead of time, reducing the possibility for further analysis of different locations. There is also the need for two separate simulations to run concurrently, with the fluctuating fields transferred between grids and alternating between acoustic and viscous simulations at each time step. In the literature it appears that this technique is still limited in its applications and is under development [116], and only currently applied to simple, usually two-dimensional geometries[117] [118] [119].

4.3.4 Analytical and empirical methods

Analytical and empirical methods exist for the prediction of inlet turbulence and trailing edge noise based on idealised geometries. Inlet turbulence noise and trailing edge noise can be reasonably well predicted, assuming that the turbulence properties in the inlet velocity or boundary layer are well known [120] [121]. Analytical methods are usually based on flows over flat plates with sharp leading or trailing edges [122] [123]. Empirical models have been generated using experimental investigations of simple aerofoils such as the NACA0012 [124].

The advantage of using simplified models is that the turbulence properties required are usually the turbulence intensity and the characteristic integral length scale which can be obtained either experimentally or numerically. Once the turbulence properties are known the far-field broadband noise can be inferred with little computational effort.

In the case of scattered turbulence over sharp edges, an accurate acoustic source term can be problematic to resolve. This problem can be overcome by using a Green's function which acts as a transfer function allowing the surface pressure fluctuations to be used to infer the far-field propagation [125]. For simple geometries this can be done analytically and for more complex geometries the Green's function can be found numerically. However, determining the appropriate Green's function requires the knowledge of both the surface pressure fluctuation and the far-field propagation, and so a direct numerical simulation is needed. This involves the use of high fidelity computational methods as discussed earlier in this chapter, as well as a simplified geometry.

The use of analytical models is limited by the assumptions of idealised flow conditions, which differ from the complex three dimensional arrangement in this thesis. Empirical models are similarly limited due to the simplifications which are required to obtain them, using aerofoils with large end plates which remove any tip leakage flow and so they can not be used to predict far-field noise from tip gap flows.

4.4 Selection of appropriate CAA method

For this work, the chosen method had to be computationally efficient, and ideally to use post processing techniques for the acoustic propagations to have the flexibility to change the receiver locations and be selective about the region of the foil investigated. Due to the low flow speeds involved and the high speed of sound in water, the Mach numbers typical of a ducted marine propeller are $M \approx 0.03$ and so the assumption of flow incompressibility is valid. As the flow can be assumed to be incompressible, an incompressible solver can be used to solve for the fluid flow which reduces the complexity of the solver as it has fewer variables to solve at each time step. The use of an incompressible solver helps with the stability of the simulation as compressible simulations require special treatment of the boundaries to ensure that pressure waves are allowed to pass out of the domain without being reflected. For this reason the chosen acoustic modelling method should be capable of using an incompressible solver for the fluid flow. The use of direct compressible simulations would not be feasible due to computational expense. The acoustic-viscous splitting method was also ruled out for the lack of flexibility but also because its implementation and validation for cases such as those being studied are still in their early stages. The use of an acoustic analogy suits the requirements of this project and it was decided to use the Ffowcs Williams-Hawkings analogy as it offered the greatest flexibility. The FW-H analogy also has been well documented in

the literature and an implementation strategy was available to the author as presented in [16] with little adaptation required.

4.5 Ffowcs Williams-Hawkings acoustic analogy

The advantage of the FW-H approach is that all of the noise sources are calculated before applying the acoustic analogy for radiation. The difficulty is that the surface therefore has to be selected carefully to include all of the important sources [26]. Once the surface has been selected and defined the pressure fluctuations in the far field due to turbulent flow within its region V and exterior to an impenetrable moving surface S, can be shown to be

$$p'(\mathbf{x},t) = I_1(\mathbf{x},t) + I_2(\mathbf{x},t) + I_3(\mathbf{x},t) + p'_Q(\mathbf{x},t), \tag{4.13}$$

where p'_Q represents sources within the flow but outside of S and the three integral terms, following [35], are given by

$$4\pi I_1(\mathbf{x},t) = \frac{\partial}{\partial t}\int_S \left[\frac{\rho_0 U_n(t)}{r}\right]_\tau dS_\mathbf{y}, \tag{4.14a}$$

$$4\pi I_2(\mathbf{x},t) = \frac{1}{c_0}\frac{\partial}{\partial t}\int_S \left[\frac{L_r(t)}{r}\right]_\tau dS_\mathbf{y}, \tag{4.14b}$$

$$4\pi I_3(\mathbf{x},t) = \int_S \left[\frac{L_r(t)}{r^2}\right]_\tau dS_\mathbf{y}. \tag{4.14c}$$

here $\mathbf{x}$ is the location of the observer, $\mathbf{y}$ is the location of the source and $r = |\mathbf{y} - \mathbf{x}|$ is the distance between the two. The subscript n refers to the component of $U(t)$ normal to the integrating surface, and the subscript r represents the component of $L(t)$ in the direction of r. The subscript $[...]_\tau$ denotes source data evaluated at a retarded time which accounts for the sound propagating from different elements of the discretised integration surface [26]. Therefore, the contribution of a stationary source element at the emission (retarded) time τ will affect pressure signal at a fixed receiver at time

$$t = \tau + \frac{|\mathbf{x} - \mathbf{y}|}{c_0}. \tag{4.15}$$

Accounting for retarded time necessitates interpolating source contributions onto a separate time axis associated with each receiver. Currently this is done by extending the source time axis assuming a fixed time step [26].

In Equation 4.14 U_i and L_i are defined for a stationary control surface as

$$U_i(t) = \frac{\rho' + \rho_0}{\rho_0} u_i(t), \tag{4.16a}$$

$$L_i(t) = P_{ij}(t)\hat{n}_j + \left(\rho' + \rho_0\right) u_i(t) \left(u_i(t) \cdot \hat{n}_i\right), \tag{4.16b}$$

where $\rho'(t)$ is the instantaneous density fluctuation, $P_{ij}(t)$ is the compressive stress tensor and $\hat{n}$ is the normal unit vector to the control surface, S.

The compressive stress tensor can be reduced to the fluctuating pressure component of the field, $P_{ij}(t) \approx p(t) - p_0$ [126] and the density fluctuations will be zero for an incompressible fluid so Equations 4.16 can be re-written as

$$U_i(t) = u_i(t), \tag{4.17a}$$

$$L_i(t) = \left(p(t) - p_0\right) \hat{n}_j + \rho_0 u_i(t) \left(u_i(t) \cdot \hat{n}_i\right). \tag{4.17b}$$

Following [16], by substituting the acoustic variables in Equation 4.17 into Equation 4.14 and again substituting back into Equation 4.13, the total pressure at the receiver can be written as

$$\begin{aligned} 4\pi p'(\mathbf{x},t) = &\underbrace{\int_S \left[\frac{\rho_0 \, \dot{u}_n}{|\mathbf{r}|}\right]_\tau dS\left(\mathbf{y}\right)}_{p'_0} + \underbrace{\int_S \left[\frac{p \, \hat{\mathbf{n}} \cdot \hat{\mathbf{r}}}{|\mathbf{r}|^2}\right]_\tau dS\left(\mathbf{y}\right)}_{p'_1} + \underbrace{\int_S \left[\frac{\rho_0 \, u_n u_r}{|\mathbf{r}|^2}\right]_\tau dS\left(\mathbf{y}\right)}_{p'_2} + \\ &\underbrace{\int_S \left[\frac{\dot{p}\hat{\mathbf{n}} \cdot \hat{\mathbf{r}}}{c_0|\mathbf{r}|}\right]_\tau dS\left(\mathbf{y}\right)}_{p'_3} + \underbrace{\int_S \left[\frac{\rho_0 \left(\dot{u_n} u_r\right)}{c_0|\mathbf{r}|}\right]_\tau dS\left(\mathbf{y}\right)}_{p'_4} + p'_Q(\mathbf{x},t) \end{aligned} \tag{4.18}$$

where p' is the acoustic pressure fluctuation at the receiver location, $\mathbf{x}$, and time, t. The integral is calculated over the surface, S, with elemental source locations, $\mathbf{y}$. The time derivative of pressure is shown by $\dot{p}$, the vector normal to the surface element, $\mathbf{n}$, the vector in the direction of the receiver, $\mathbf{r}$, and the speed of sound in the fluid, c_0. This is the general form of FW-H equation and can be applied to an integration surface which is either coincident with a solid surface, or within the fluid domain.

Following [33], the sound radiation for low Mach number flows considered in this work is

likely to be dominated by the dipole sources as the monopole sources such as cavitation are being neglected and the Mach number scaling effects discussed previously imply the quadrupole sources will not radiate efficiently. The dipoles are caused by the unsteady forces due to the interaction between the fluid and the solid surfaces and act directly on the solid surfaces, as seen in Equation (4.9). This means that the far-field noise can be predicted by sampling the pressure on the solid surfaces, and applying the FW-H analogy to deduce the far-field acoustic pressures.

It can be seen in Equation 4.18 that the integral terms for p'_0, p'_2, and p'_4 go to zero when the integration surface is taken to be coincident with the solid boundary as there can be no flow normal to the solid wall. Furthermore, following [127] and [27] it has been shown that the FW-H analogy in Equation 4.18 in this case can be reduced to

$$4\pi p'(\mathbf{x},t) = \int_S \left[\frac{\dot{p}\hat{\mathbf{n}}\cdot\hat{\mathbf{r}}}{c_0|\mathbf{r}|}\right]_\tau dS\,(\mathbf{y}) \tag{4.19}$$

as the $|\mathbf{r}|^2$ term on the denominator of the p'_1 term implies that this term becomes insignificant as the observer moves to the far-field as $\mathbf{r}$ becomes large.

A schematic representation of the importance of the relative vectors used in this analogy is shown in Figure 4.2. The quadrupole source contribution from the sources distributed in the volume of fluid surrounding the body have been ignored due to the high data storage requirements of saving complete field information at high sampling frequencies.

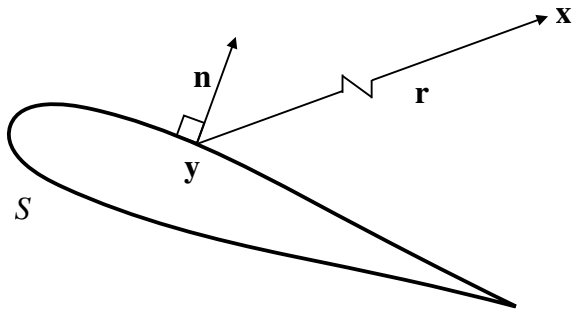

Figure 4.2: Schematic representation of the notation used in the Ffowcs-Williams Hawkings acoustic analogy implemented in this study.

In this work, the stationary control surface has been chosen to be fixed on the solid boundaries of interest in the arrangement. Choosing the control surface to be coincident with the solid boundaries allows the surfaces (called patches in OpenFOAM) to be sampled at a chosen, fixed time step, recording the instantaneous pressure, p and time derivative of pressure, $\dot{p}$, for every face of the respective patches. The analogy is then implemented with the use of a post-processing script which calculates the contribution to the acoustic pressure at each receiver location of each face of each patch, accounting for retarded time, τ. This

methodology is computationally expensive regarding memory usage, by saving the data from every face for every time step and has been verified in its previous implementation [26].

It is also possible to implement a run-time implementation of this analogy, such that the acoustic sources are integrated onto the reciever time axis at each time-step. Calculating the contributions from the sources at every time-step greatly reduces the memory requirements and has been shown to work well in the past [27] and [16]. The disadvantage of this method however, is that the receiver locations need to be selected in advance, and any new receivers require a new simulation. This is the reason the current implementation has been chosen here, to allow flexibility in the post-processing analysis to change receiver locations if required, as well as allowing surface pressure samplings.

The implementation of the FW-H will follow the implementation used by [16], and operates by saving the pressure data from the chosen cell faces at every time step. This implementation was chosen as it allows the author to revisit the data in the future and use a different receiver location, or extract the time series of surface pressure data. The chosen implementation involves creating a new runtime function within `OpenFOAM` which could be given the patch name, as defined during the mesh generation, and the choice of variables to record. Due to the computational expense of these simulations and the computational power available using the IRIDIS High Performance Computing Facility at the University of Southampton, the simulation had to be run on the cluster several times, with the data being concatenated afterwards to create a clean time series of sufficient length to recover the spectral resolution required.

The analogy was implemented using `Python`, and allowed the recorded cells to be further subdivided by location and or orientation, to help provide insight into potential sound source regions. Equation 4.19 is then applied to each of the chosen faces in turn, at each recorded time step in turn, accounting for the effect of retarded time to calculate the time series of the pressure signal contribution at the receiver of each face. These signals are then added together, to produce the far-field pressure signal, as it would appear to an observer.

4.6 Summary

The selected method of numerically modelling the sound radiation in this study will involve using an incompressible LES solver in combination with a Ffowcs Williams-Hawkings acoustic analogy. The LES solver will calculate the fluid flow, resolving the large structures directly and modelling those which are smaller than the local grid resolution. The acoustic source terms will be recorded by saving the instantaneous pressure at each cell face on the solid surfaces of the foil and the boundary surface. Each face acts as a dipole and its radiation to a nominated receiver location is calculated using the acoustic analogy which accounts for

the orientation of the surface with respect to the receiver location, as well as the relative position of all of the individual faces by accounting for the retarded time. The FW-H analogy relies on the acoustic sources being fully captured by the selected solver and so the use of an incompressible solver means that only those sources which can be regarded as acoustically compact will be captured. Mechanisms such as trailing edge noise which rely on the scattering of turbulence will not be captured in the incompressible solver and neither will their influence on the noise production.

Part II

Parametric analysis of a finite aspect ratio foil with zero camber and a rectangular tip

Chapter 5

Tip vortex formation around open tipped foil

5.1 Introduction

To fully understand the effect of a tip gap on the flow around the tip of a finite aspect ratio lifting surface, the unrestricted tip flow must first be investigated and understood. The surface to be used will be a NACA0020 foil, a symmetric foil (zero camber), with the maximum thickness of 20% of the chord (see Figure 1.4). This foil has been chosen as it has been used in experimental research [128] as well as CFD simulations of the same set up [129], and the data from these has been made available by the respective authors for verification. The aim of the experiments was to analyse the performance of a foil in the wake of a propeller, which involved comparison with the free stream performance of the foil, and the freestream set up will be the focus of this investigation. The experimental set up used by [128] can be seen in Figure 5.1.

The NACA0020 was chosen as it represents an approximation for a single propeller blade, while reducing computational complexity by operating in a fixed position, with a simplified geometry. The initial investigation can then be adapted to investigate the change in vortex generation and behaviour with the introduction of a boundary surface near the tip of the foil, allowing a parametric progression towards investigating the interaction between the tip vortex and the duct boundary layer in a marine propulsor.

The experiment included pressure tappings at several spanwise locations on the foil from $7 - 97\,\%$, as well as calculating the lift and drag forces and coefficients. These pressure tappings will not only be used to validate the performance predictions of these simulations but the location near the tip of the foil may help validate the flow regime over the tip of the foil which generates the tip vortex.

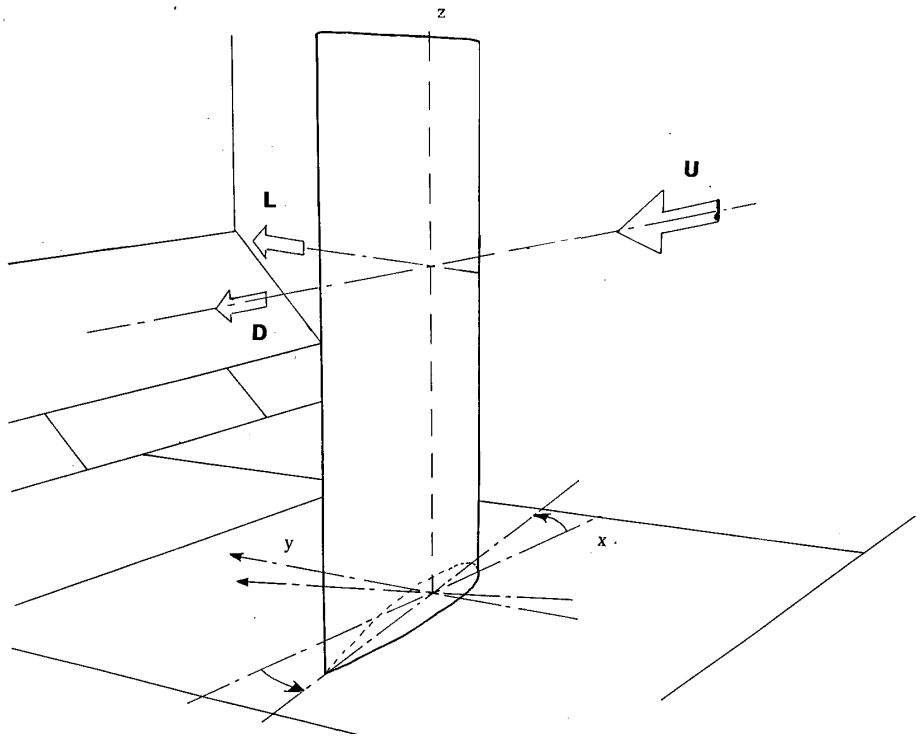

Figure 5.1: Experimental set up used by [128] which was recreated by [129] and will be used in this study to allow close comparison of results.

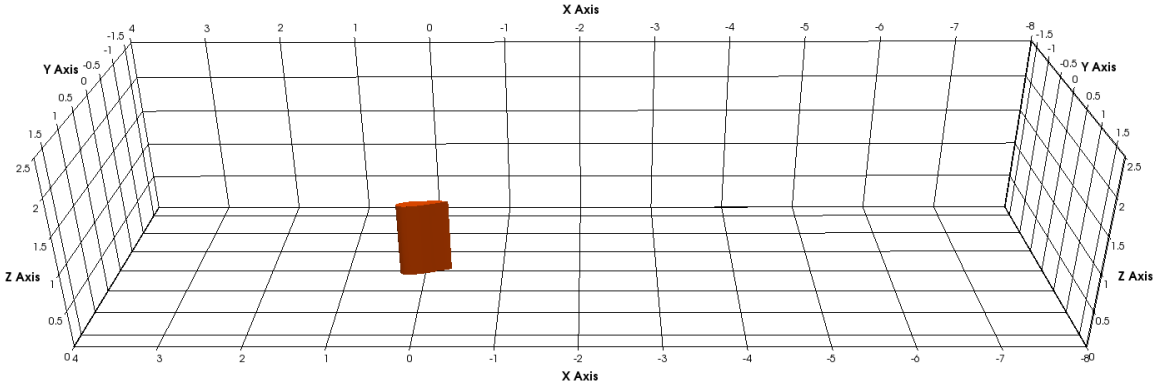

Figure 5.2: Simulation domain for NACA0020 tip vortex investigation. The mid-chord of the root of the foil is located at $(0, 0, 0)$ with flow from left to right.

Table 5.1: Numerical model settings.

Parameter	Badoe et al. [129]	Setting
Mesh Type	Unstructured (Hex)	Unstructured (Hex)
No. of Elements	2.5M	5.9M
y^+	30	ave=1.35 max=15.42
Inlet	Freestream velocity (10m/s)	Freestream velocity (10m/s)
Outlet	Zero gradient	Zero gradient
Tunnel floor/side walls	Slip	Slip
Tunnel roof	Slip	Slip
Foil	No slip	No slip
Turbulence Model	$k-\omega$ SST Turbulence	$k-\omega$ SST Turbulence
Reynolds' Number	4×10^5	4×10^5

5.2 Simulation set-up

The simulation was setup to match the work by Badoe et al. [129], using the same domain dimensions, which match the cross sectional dimensions of the wind tunnel used by Molland and Turnock [128]. The matching of the simulation domain allows direct comparison of results, however the mesh was generated with the aim of capturing the tip vortex and its path as it convects downstream, and so the cell count was considerably higher. Figure 5.2 shows the domain used, with the foil root centre placed at $(0, 0, 0)$. The domain extends 12 chord lengths downstream and 6 chord lengths upstream, with the width of $3.5m$ and height of $2.5m$ or 5.25 and 3.75 chord lengths respectively, similar to the length used by [129] and with height and width equal to that of the R.J. Mitchell wind tunnel at the University of Southampton. The x-axis is positive in the upstream direction, y is positive to the SS of the foil, and z is positive moving along the span of the foil (physically, vertically upwards based on the experimental set up for the foil). The surfaces of the wind tunnel were prescribed a no slip condition, which is not strictly valid because physically they would have a boundary layer in the experiments but the extra computational cost of refining the mesh on all the surfaces would be large, and the effect on the tip vortex would be small. The impact of this assumption is discussed further in Section 5.3.

The foil is set to 9.6 degrees angle of attack, as was used by both previous studies. As this work is only interested in the tip vortex formation, the simulation was not run at other angles of attack. The flow speed was set to $10m/s$, with the chord based Reynolds number set equal to [129] at 4×10^5. This Reynolds number represents a transitional regime such that the boundary layer is likely to be transitioning between a laminar flow which would be observed at smaller speeds and the turbulent boundary layer which would be expected at higher speeds. The model used in the preceding experiments used a trip at 5% chord from the leading edge to ensure a consistent location for transition between the two flow regimes.

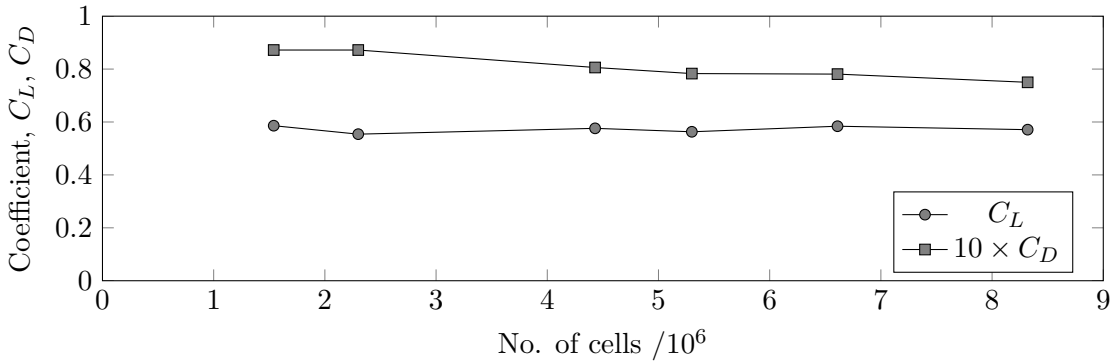

Figure 5.3: Grid convergence study showing grid independence for the present study.

The mesh was constructed using `snappyHexMesh`, an unstructured hexahedral mesh which uses a background mesh, and refinement regions which can be controlled by using solid surfaces (patches) or defined volumes. The mesh was generated to ensure a grid size with $y^+ \approx 30$ on the surface of the foil, with refinement regions located in regions where the flow is expected to be more complex or accelerated. These refinement regions include the leading edge, high refinement along the trailing edge to capture the effects of the bluntness of this surface, and a cylindrical region extending from the trailing edge tip downstream to capture the vortex structure. The simulation was run using the SIMPLE alogrithm using a RANS solver with $k - \omega$ SST turbulence model. Table 5.1 shows the simulation setup compared with the simulations by Badoe et al. [129].

5.3 Comparison with previous experiments

The first goal was to recreate the wind tunnel experiments and corresponding simulations conducted by [128] and [129]. These experiments analysed the lift and drag forces and coefficients, as well as profiles of chordwise pressure distribution at several locations along the span. Initial simulations predicted lift and drag coefficients which agreed with previous studies, and were independent of mesh size. Figure 5.3 shows the lift and drag coefficients for various mesh sizes ranging from 1.5 to 8.5 million cells which indicates $C_L = 0.58$ which is in good agreement with the values from previous works [129]. The C_D value was found to be 0.075 and was therefore over-predicted compared to the experimental study, which is likely to be due to the turbulence model used in this simulation [130]. In this simulation the 3D representation of the experiment may also have affected the drag of the foil. The floor in the simulation was prescribed a slip condition to aid with computational cost as discussed in Section 5.2. However, in reality the floor of the wind tunnel represents a no-slip condition and so the flow at the root of the foil is very complex, which is not being fully captured by the simulation and therefore will be a source of error. The incoming flow at the root of the

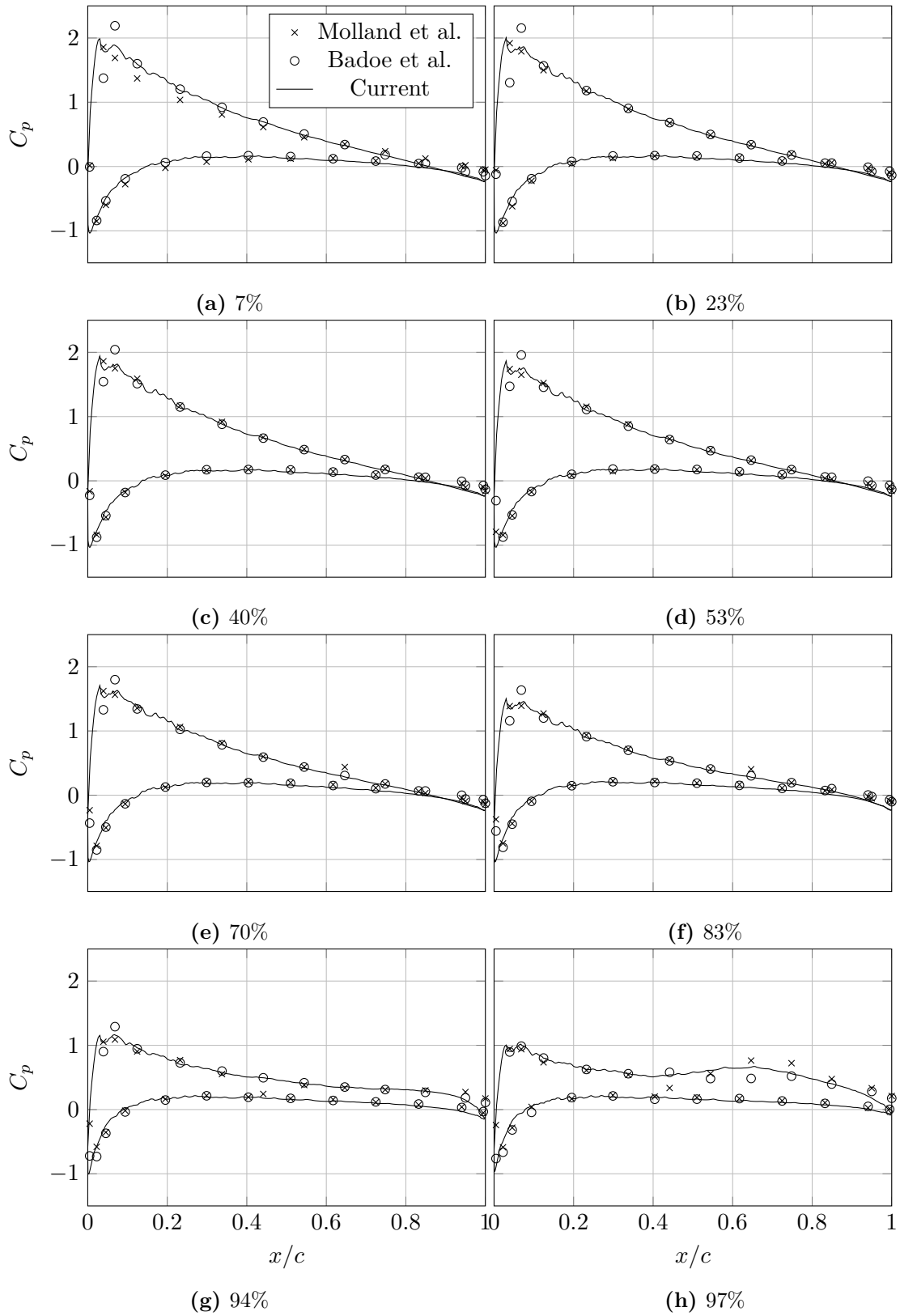

Figure 5.4: Comparison of RANS simulations, shown with a solid line, with Badoe et al. [129] shown with circles and Molland et al.[128] shown with crosses.

foil would be decelerated due to the boundary layer, effectively reducing the mean inflow velocity and so the simulations are likely to predict higher values of C_D when normalised using the same free-stream velocity.

Figure 5.4 shows the chordwise pressure distribution at eight span wise locations to match the experimental and numerical works. The span wise locations we at $z/L = 7\%, 23\%, 40\%, 53\%, 70\%, 83\%, 94\%, 97\%$ where z is the distance from the root and L is the span of the foil. It can be seen that the overall profile of the pressure contour agrees with the experimental data well in most cases. There is an over prediction of C_p at 7% span for $5\% < x/c < 50\%$ which is most likely caused by the use of a slip condition for the floor in the simulation compared to the experiment which would reduce the inflow velocity and therefore lead to an over prediction of C_p. Adding a no-slip condition to the CFD would have greatly increased the computational cost and as the pressure contour along the rest of the span matches the experiment well, it was assumed that this difference near the root would not affect the formation of the tip vortex significantly. Towards the tip of the foil, the secondary pressure peak caused by the tip vortex can be clearly seen in the experimental data, with good agreement from the current CFD study. The simulations by Badoe et al. [129] agree less well, but were not concerned with the tip vortex, and so had a smaller grid size of 2.5 million cells, without specific refinement regions surrounding the tip. The formation of the tip vortex is likely to rely on unsteady flow mechanisms caused by the separation of flow over the sharp edges and so the use of a time-averaged simulation is likely to be responsible for the under prediction of the secondary pressure peak.

5.4 Identifying the tip vortex

As discussed in Section 3.5, it can be difficult to devise an objective definition of a vortex in complex flow. In relatively simple flow, where the vortex path is known, taking the cross-flow velocities can reveal the presence of a vortex and give an indication of the location of its core. This requires the presence of a single vortex which is the only factor influencing the vortex. Figure 5.5 shows the stream-wise sampling locations used in this analysis. The velocity profiles were sampled at 0.75 to 3.75 chord lengths downstream of the foil TE, with the lines extending ± 0.75 chord length from the tip of the TE. The 2-dimensional analysis of the $\lambda_2 - criterion$ was also carried out at the stream-wise locations shown in Figure 5.5.

Figure 5.6 shows the chord-wise and span-wise extents of the sampling lines used, along with the pressure sampled on a slice orthogonal to the mean flow direction at $x/c = -3.75$. The velocity components parallel to the slice have been visualised using arrows, indicating the strong vortical flow generated downstream of the foil. It can be seen that the pressure field responsible for generating lift is large compared with the foil, while the pressure drop at the centre of the tip vortex is relatively small. The importance of this will be discussed

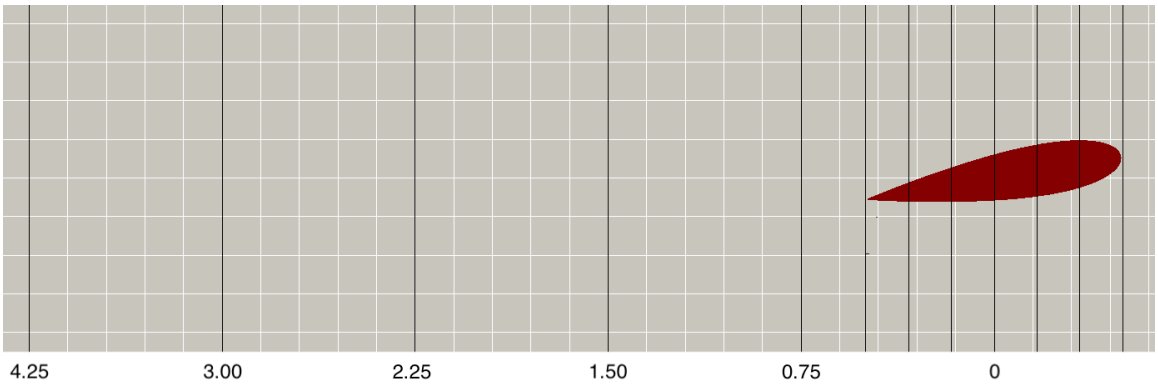

Figure 5.5: Sampling locations used in the velocity profiles at the downstream locations, and the λ_2 criterion analysis at all locations. Dimensions are normalised by chord and grid size is $0.15c$.

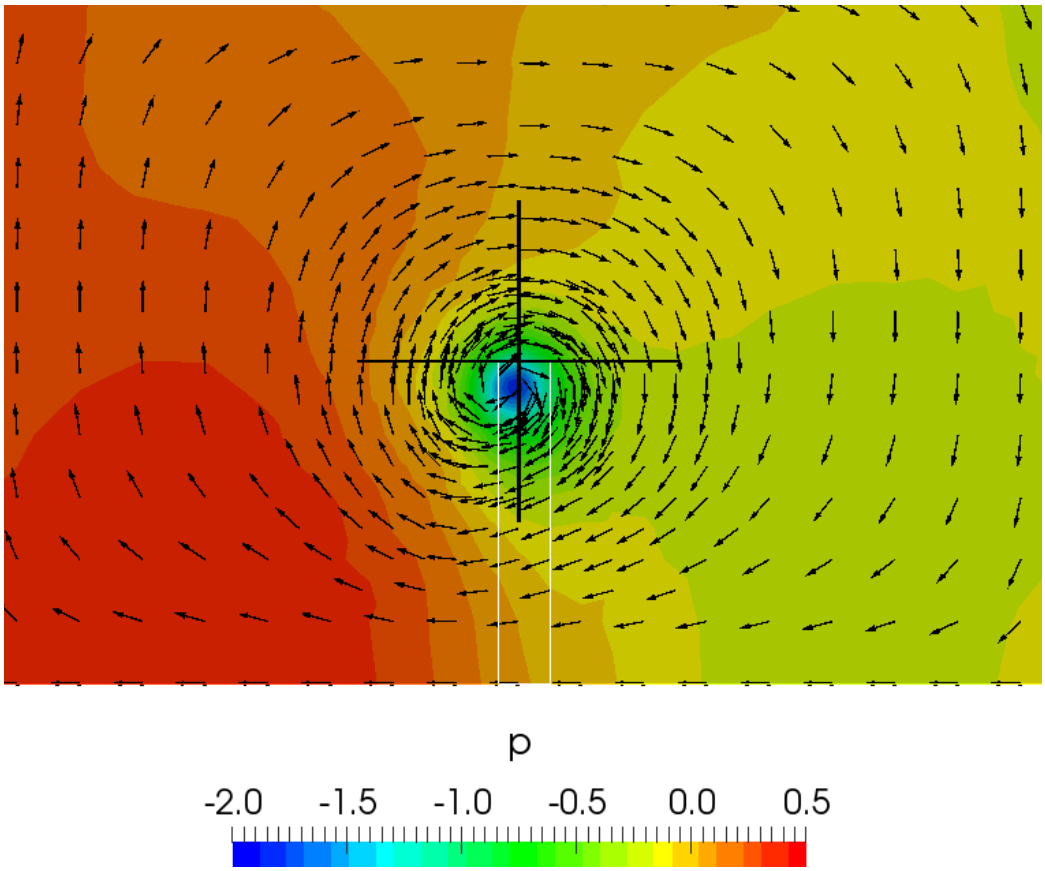

Figure 5.6: A sample plane taken downstream at $x/c = -3.75$, coloured by pressure, with arrows illustrating the velocity vector components parallel to the plane illustrating the strongly vortical nature of the flow in that region. The foil outline is shown in white, with the sampling lines used for the velocities shown in black to illustrate the relative location of the vortex core.

in greater detail in Chapter 6.

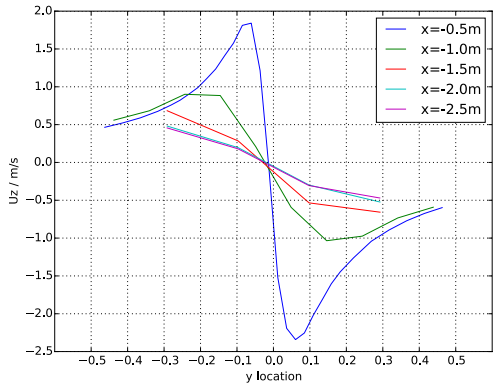

(a) Coarse outer mesh without refinement along vortex path

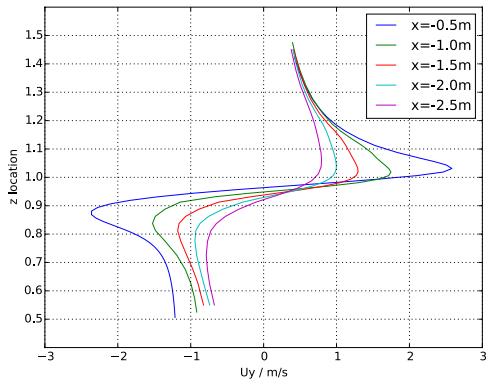

(b) Coarse outer mesh with refinement along vortex path

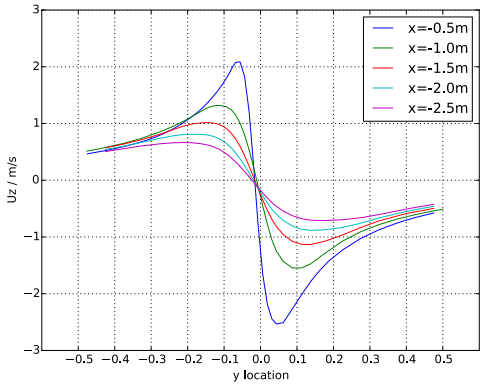

(c) Coarse outer mesh with refinement along vortex path

Figure 5.7: Velocity components reveal the presence of a vortex.

Figure 5.7 shows the y and z velocity components, sampled downstream of the foil at various locations for the different meshes. It can be seen that the refinement along the vortex core has a significant impact on the velocity profile resolution. As discussed in Section 3.5 the velocity is linearly distributed with respect to the radius within the viscous core of the vortex, and inversely proportional to the radius squared outside of the core. This shows the relationship expected of a Rankine vortex velocity gradient through the core gives its rotational speed. By inspecting where the velocity components are zero, the location of the core in each dimension can be calculated, using U_y to find the z coordinate of the core, which shows it contracting towards the root of the foil as it moves downstream, as predicted. This method has revealed the need for mesh refinement along the vortex core however, if more than one vortex is in close proximity, using this method to identify, locate and calculate the strength of them becomes complicated.

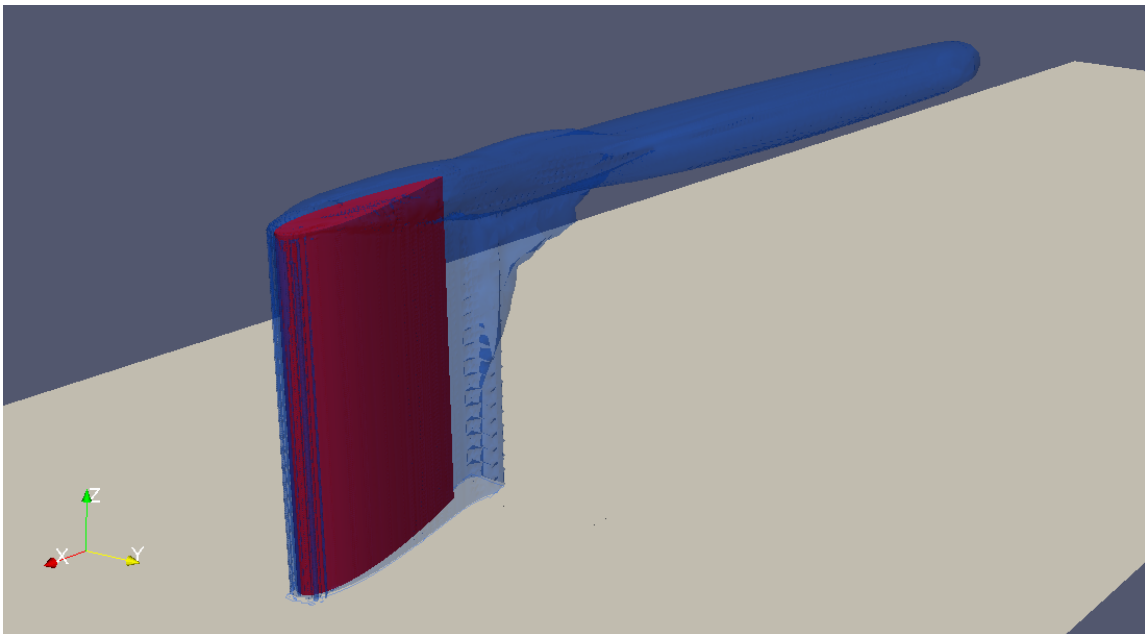

(a) Vorticity magnitude = 10,

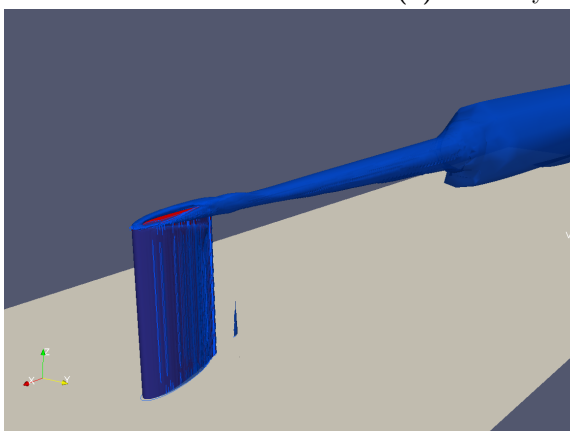

(b) Q-criterion,

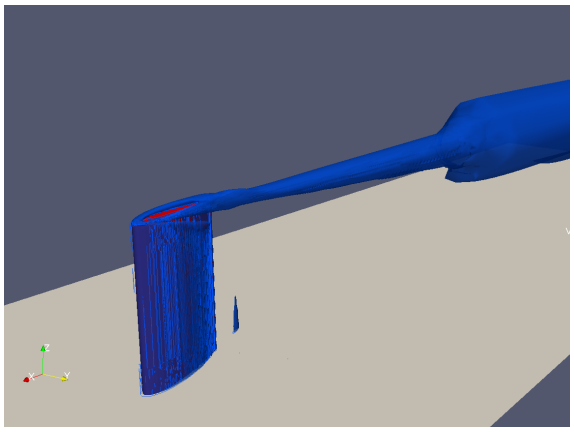

(c) λ_2 criterion,

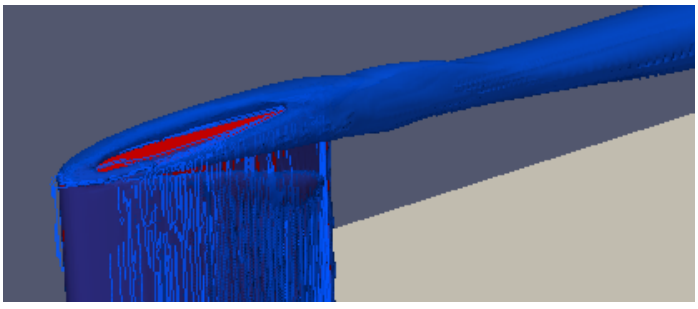

(d) λ_2 criterion at the tip.

Figure 5.8: Comparison of vortex identification methods.

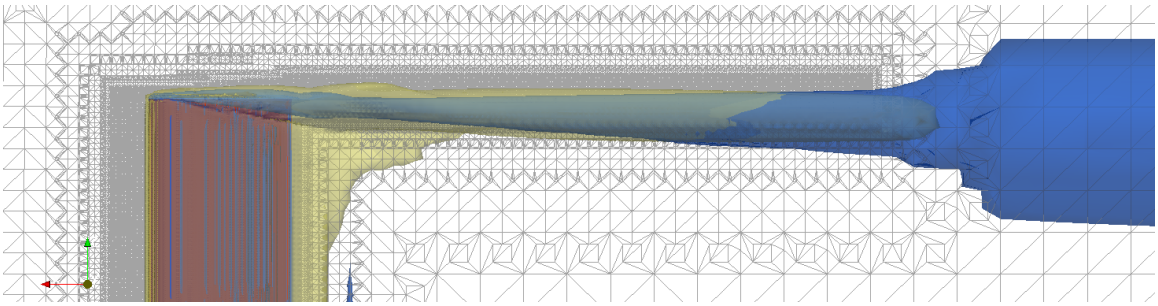

Figure 5.9: Vorticity = 10 (yellow) and $\lambda_2 = 0$ (blue) are plotted over the mesh, with the foil shown in red. The mesh visualised illustrates the need for careful mesh refinement.

Further investigation of the vorticity produced by the foil was carried out by using the velocity vector field to calculate the vorticity vector field, and these were then used to calculate the Q-criterion and λ_2-criterion as scalar fields. This allows each criteria to be plotted as an iso-surface or contour, which in three dimensions gives a good illustration of the vortex formation and structure, and when taken in two dimensional slices through the domain, allows the measurement of the size, location and strength of all of the vortices in the domain. Figure 5.8 shows the vortex as identified by the different criteria. Figure 5.8a shows the vorticity criteria. It has already been discussed how this method is not fully objective in defining a vortex, but it does illustrate the vortex sheet which is expected from the trailing edge of the foil, which rolls up into the tip vortex. However the vortex itself doesn't seem to expand downstream as expected. Figures 5.8b and 5.8c show a very similar vortex from the tip. As this flow is relatively complex, the improved objectivity of the λ_2-criterion suggested by Chong et al. [96] does not seem to have affected the vortex identification. Both the Q-criterion and λ_2-criterion identify the boundary layer as being the core of a vortex which is intuitively incorrect but is due to the high vorticity associated with the boundary layer region.

As there is little difference between the Q-criterion and λ_2-criterion, and both are readily implemented within the existing `OpenFOAM` framework, the λ_2-criterion will be used in the rest of this thesis. Figure 5.8d shows the increased resolution which is achieved using the λ_2-criterion when compared with the used of a vorticity contour, by identifying both vortex structures on the PS edge (far side) and SS edge (near side) of the foil. These two vortices have the same direction of rotation and coalesce as the meet at the trailing edge of the foil.

Figure 5.9 shows a comparison of the vortex identification methods as well as the mesh in the plane of the vortex. Both criteria show that the vortex contracts in the spanwise direction and so the mesh refinement for the vortex core is misaligned downstream. Streamwise sections were analysed to find the path of the vortex in Figures 5.10 and 5.11. The projected frontal area of the foil is shown as a black rectangle, and the local cross-section of the foil where applicable is shown in white, with the PS of the foil on the left and SS on the right.

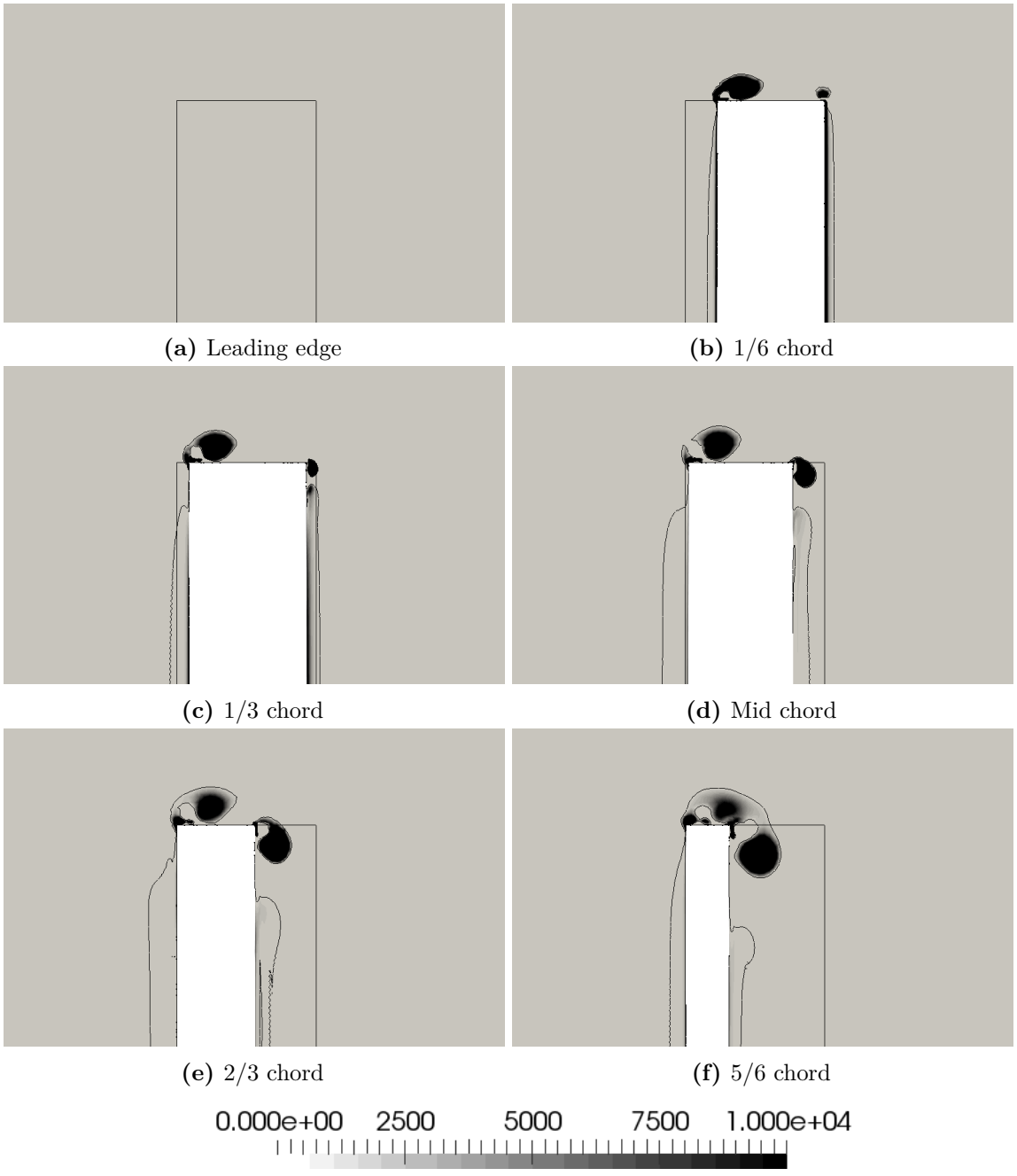

(a) Leading edge

(b) 1/6 chord

(c) 1/3 chord

(d) Mid chord

(e) 2/3 chord

(f) 5/6 chord

(g) λ_2 contour colouring from $0 - 10,000$ in steps of 500

Figure 5.10: Formation of the tip vortex when $\alpha = 9.6°$, with the pressure side on the left and suction side on the right. The projected frontal area of the foil is shown by the black rectangular outline, with the cross-section of the foil shown in white where necessary. The $\lambda_2 = 0$ outline is traced around the areas where a vortex has been identified. The surfaces are coloured by λ_2 from the grey background at $\lambda_2 < 0$ to black for $\lambda_2 = 10,000$.

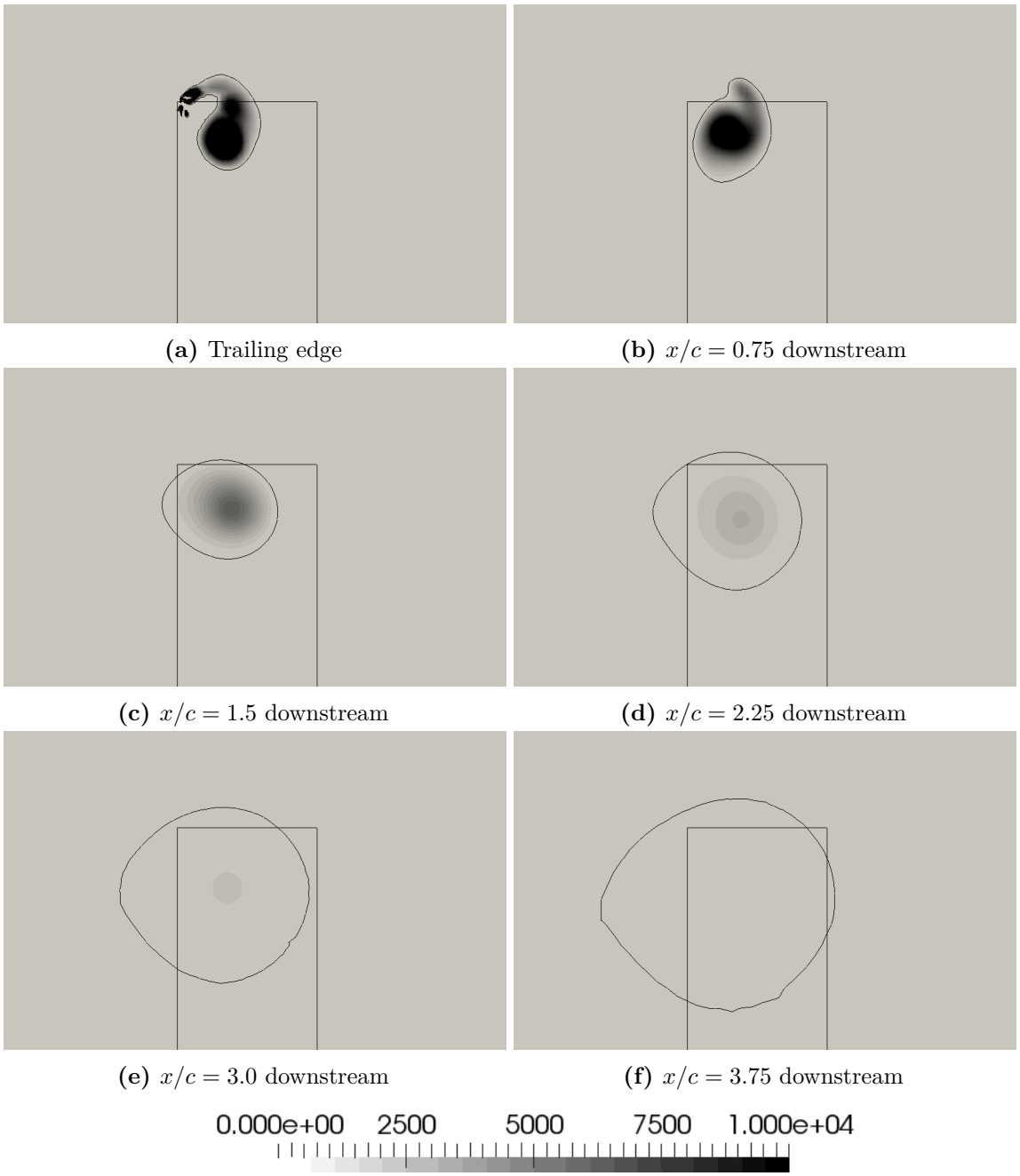

(a) Trailing edge

(b) $x/c = 0.75$ downstream

(c) $x/c = 1.5$ downstream

(d) $x/c = 2.25$ downstream

(e) $x/c = 3.0$ downstream

(f) $x/c = 3.75$ downstream

(g) λ_2 contour colouring from $0 - 10,000$ in steps of 500

Figure 5.11: Formation of the tip vortex when $\alpha = 9.6°$, with the pressure side on the left and suction side on the right. The projected frontal area of the foil is shown by the black rectangular outline, with the cross-section of the foil shown in white where necessary. The $\lambda_2 = 0$ outline is traced around the areas where a vortex has been identified. The surfaces are coloured by λ_2 from the grey background at $\lambda_2 < 0$ to black for $\lambda_2 = 10,000$. Downstream distances are given with reference to the mid chord.

Table 5.2: Summary of the impact of a high resolution surface file on the force coefficients

Coefficient	Chapter 5	High resolution surface	% change
C_L	0.583	0.576	-1.20
C_D	0.626	0.636	1.60

The slices are coloured by the λ_2 criterion with the minimum value set to zero. Regions identified as being outside of the vortex core is therefore shown as a constant grey, with the black outline used to identify the limit of the identified vortex. The λ_2 colour scale was set based on the first downstream location with a maximum value of 10,000. The vortex structures shown around the foil tip can be seen to have well defined black areas, indicating very strong vortex structures. As the figures move after through the foil, the vortex can be seen forming from the PS edge due to the tip leakage flow. A small vortex can also be seen forming on the SS edge but it is less strong as most of the energy in this flow is used building the first vortex. As the figures move further aft the first vortex remains while the second vortex moves down onto the SS and grows in strength. As the foil section gets narrower at 5/6 chord, these vortices can be seen combining such that at the trailing edge there is one large vortex being convected downstream. These structures agree with previous experimental works [131].

The downstream sections show how this vortex grows in size as the energy is dissipated into the surrounding fluid, and the strength of the core can be seen to decrease. These sections also illustrate the spanwise contraction as expected, and the further downstream the vortex travels, the more it highlights the misalignment with the mesh, shown by the irregular shape of the vortex boundary.

5.5 Impact of model geometry

The C_P distribution along the chord of the foil exhibited some small chord-wise variations in all of the simulations, shown in Figure 5.4. Figure 5.12 shows the effect of adjusting the mesh and the simulation settings to improve the pressure distribution to obtain better agreement with experimental results and produce the smooth contour that would be expected for a foil with no roughness. Figure 5.12a shows the original, coarse mesh of 1.5 million cells, Figure 5.12b shows the same mesh with but with a reduced residual criteria, and Figure 5.12c shows the same criteria with a more refined mesh of 5.5 million cells. The residual criteria assesses how well the mass and momentum is conserved in each cell. The residual is calculated as the difference between the flux into and out of a cell for each fluid property. Reducing the criteria to a lower number forces the simulation to carry out more iterations until the criteria is satisfied.

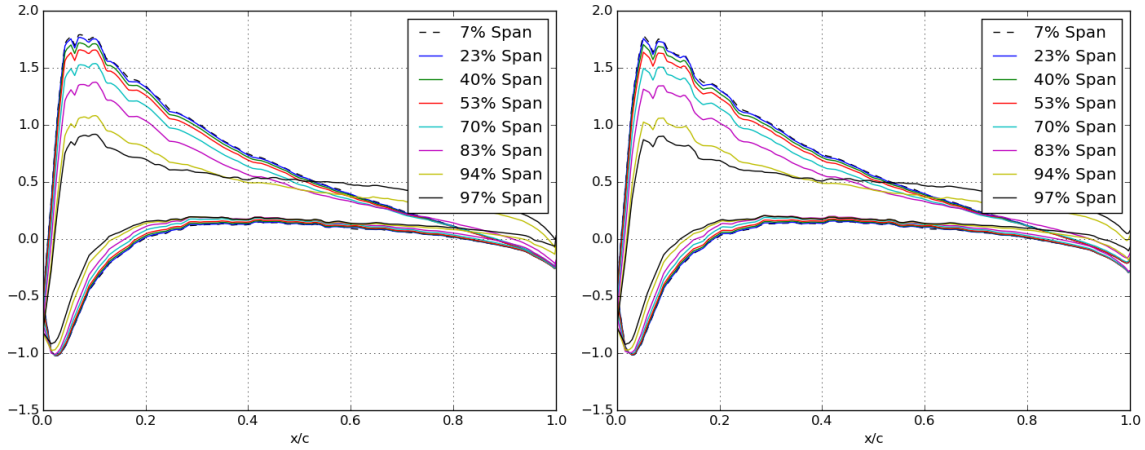

(a) Course Mesh

(b) Reduced residual criteria

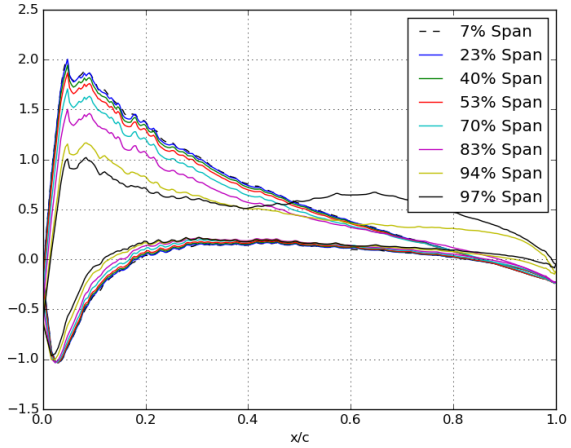

(c) Improved mesh and reduced residual criteria

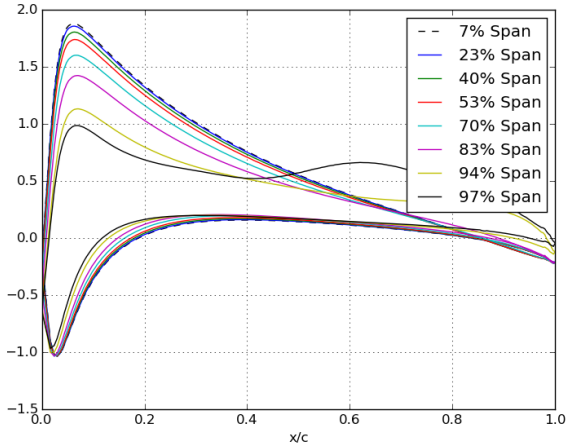

(d) High resolution STL with original settings

Figure 5.12: Adjusting the simulation settings and mesh refinement to improve the pressure distribution. Finally it was found that the original surface file was responsible for the variations in the pressure distribution and a higher resolution model surface resolved the issue.

It can be seen that while all of the figures have small fluctuations in the pressure, the general profile of the distribution improves with each adjustment made. Figures 5.12a to 5.12b the peak pressure near the leading edge can be seen more clearly after the settings were adjusted after the original mesh and settings caused this peak to become more rounded than expected. From Figures 5.12b to 5.12c this peak can be seen even more clearly, while the pressure contour at 97% span can be seen to have a much larger secondary peak towards the trailing edge of the foil. One key improvement in this mesh was the introduction of a refinement zone which follows the tip of the foil, which has had the effect of better capturing the tip leakage flow, and therefore the pressure increase on the SS caused by the formation of the tip vortex.

It is interesting to note that the discontinuities in the pressure distribution occur at the

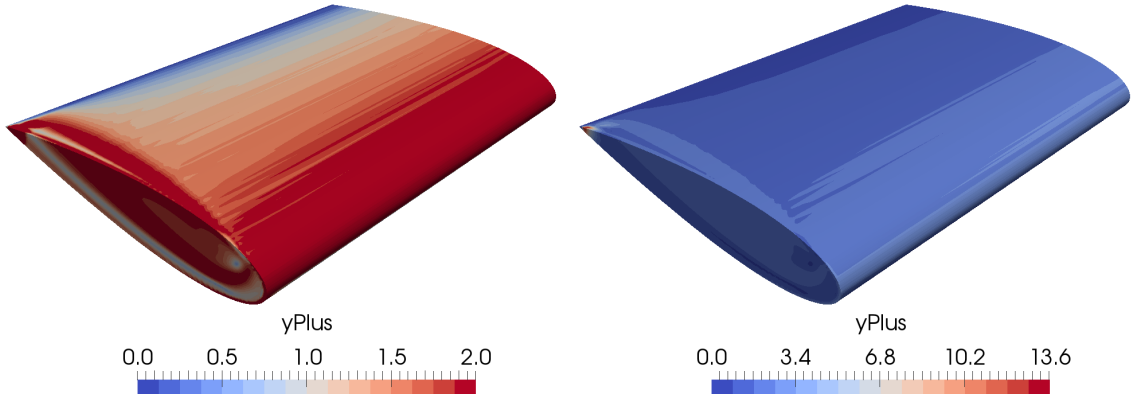

(a) Coloured from $0-2$ to show areas which are in need of improvement.

(b) Coloured by total range, up to 13.6 showing the mesh issues at the TE tip.

Figure 5.13: Distribution of y^+ for NACA0020 foil surface, taken during post-processing, to check the suitability of the local mesh density.

same chord-wise locations for all span-wise sampling lines, leading to the hypothesis that the base shape of the foil may have been at fault. As the surface used in these simulations was the same as provided by Badoe et al. [129] a new surface was produced using a high density spline for the NACA0020 outline. The resulting C_P distribution can be seen in Figure 5.12d which shows the smooth C_P distribution expected from a steady state solution. It is likely that the original surface file did not have sufficient clustering of control points near the leading edge resulting in an abrupt change of curvature, creating the pressure variations. Table 5.2 shows the summary of the force coefficients, confirming that the lift and drag forces were not significantly affected by this.

5.6 Summary

The simulation described in this chapter has shown good agreement with previous simulations and predictions for lift (within $\approx 10\%$) forces as well as pressure distribution over the surface of the foil. The pressure distributions near the tip show the vortex formation affecting the chord wise pressure profile, adding confidence to the accuracy of the tip vortex prediction. It is likely that the under-prediction of the vortex induced secondary peak in the pressure distribution is due to the use of time-averaged simulations to simulate an unsteady flow feature.

Analysing the vorticity sheet propagating from the trailing edge suggests that the mesh downstream of the trailing edge is also in need of further refinement. It has been shown that the surface used to generate the geometry for the foil in the mesh was not of a high enough resolution and this was the cause of the varying chord-wise C_p distribution. The suitability of `snappyHexMesh` for blade geometries has been discussed by Lloyd [27], and the instability

of the layer generation has been discussed in this chapter. The use if an alternative mesh generation software will be presented in Chapter 6.

The formation of the tip vortex has been shown to consist of two distinct vortices forming over the two sharp edges on the square tip of this foil. These vortices coalesce towards the TE of the foil as the width of the tip reduces to the size of the PS edge vortex with neither of the vortices appearing to be dominant as they have comparable size before joining. As the tip gap is introduced it is possible that the PS vortex, which is above the tip, could become stretched as the gap is reduced, potentially with the effect of the vortices coalescing further forwards. As the tip gap reduces it is reasonable to assume that the transverse flow through the gap will increase in a similar way to a contracting channel, and this increased flow may drive the SS vortex to become stronger and more dominant.

Once the vortex is shed it can be seen that the path contracts in the span-wise direction, caused by the down-wash of the foil producing a pressure gradient across the vortex. As the gap is reduced this down-wash is likely to remain and potentially increase in strength as the lift performance of the foil increases. However with the introduction of a boundary surface above the foil tip it is unclear how the span-wise vortex path will be affected by the tip gap.

Chapter 6

Impact of a finite tip gap

6.1 Introduction

The preliminary foil investigation in Chapter 5 will be further developed to investigate the effect of introducing a boundary near the free tip of the foil on the tip flow and vortex generation. The flow through the gap around a foil tip is difficult to investigate experimentally and so the unsteady flow features within the gap are not well documented. The foil case and the range of pressure data available allows for validation of the CFD set-up and therefore gives confidence to the findings made with the adapted arrangement, as shown by the analysis conducted in Chapter 5.

Chapter 2 discussed that ducted propellers are widely known to produce lower noise levels but without a thorough understanding of the mechanisms which are impacted by the presence of the duct. This chapter will focus on investigating the effect of the tip gap by introducing a large test matrix to identify the critical height which causes a significant impact in the tip leakage flow and vortex generation. Time-averaged simulations will be used initially to understand the effect of the tip gap size on the general flow characteristics, before moving to time-resolved simulations to investigate the unsteady flow features in the tip gap region. This understanding will provide a good database to infer the influence of the tip gap on noise generation mechanisms, and also serve as a development of the chosen simulation set up.

Table 6.1: RANS numerical model settings.

Parameter	Unit	Setting
Foil span	m	1
Foil chord	m	0.667
Mesh Type	-	Unstructured (Hex)
No. of Elements	-	$\approx 8-10$m
y^+	-	$\approx 1-2$
Inlet	-	Freestream velocity (10m/s)
Outlet	-	Zero gradient
Tunnel floor/side walls	-	Slip
Tunnel roof	-	Slip
Foil	-	No slip
Duct	-	Slip
Reynolds' Number	-	4×10^5
Turbulence Model	-	$k-\omega$ SST Turbulence
Solver	-	SIMPLE

Table 6.2: Test matrix detailing tip gaps to be investigated, shown in SI units as well as relative to characteristic dimensions.

$h[mm]$	500	400	300	200	100	50	40	30	20	10
$h/c[\%]$	75	60	45	30	15	7.5	6.0	4.5	3.0	1.5

6.2 Time averaged simulations

6.2.1 Test case methodology

The first investigation into the effect of a tip gap is a series of time-averaged RANS simulations, for a variety of tip gap heights and foil thicknesses. There are several reasons for running a wide range of RANS simulations. Firstly because these simulations require less computational time to produce results, whilst at the same time allowing the converged RANS solution to be used as an initial condition when running the LES simulations later. The RANS cases allow predictions to be made about the possibly important conditions regarding noise generation, therefore reducing the number of LES simulations required to capture the more crucial arrangements.

The simulation is set up using very similar conditions to those in Chapter 5 as can be seen by the summary given in Table 6.1. The initial series of tip gaps to be investigated is shown in Table 6.2, with the height given in terms of the absolute distance in mm as well as as a percentage of the chord of the foil.

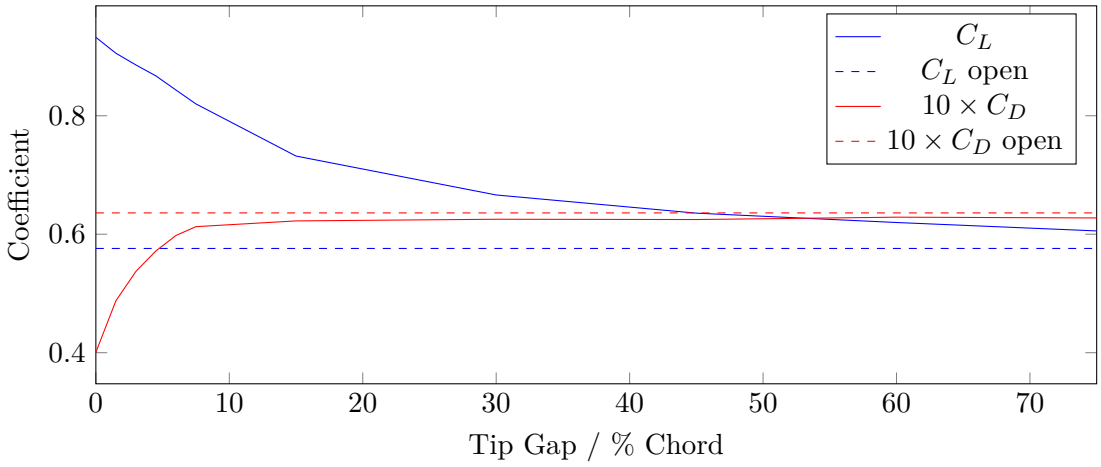

Figure 6.1: Variation of C_L and C_D with varying tip gap.

6.2.2 Grid development

Using the initial refinement regions for the vortex and wake sheet from the open foil simulations the tip gap height, h, was reduced and the vortex path was tracked for each new case. This was carried out using slices through the domain during pos-processing, as in Figures 5.10 and 5.11, and using the centre of the $\lambda_2 = 0$ contour line as the location of the centre of the vortex core. As the tip gap varied, the flow speed increased through the gap which affected the trajectory of the vortex as it moved downstream, as well as the separation point of the vortex from the SS edge. The trajectory of the tip vortex will be discussed at greater depth in Section 6.2.2. Figure 6.3 shows the result of the vortex path analysis. The grids were then individually tailored to have the vortex refinement region follow this path, and the refinement region around the tip was expanded to allow the vortex roll-up and separation from the SS edge to be captured accurately.

Performance comparison

As the tip gap is reduced there are predictable effects that will occur with regard to the lift and drag coefficients, as well as the pressure coefficients distributed along the length of the chord.

Figure 6.1 shows the effect of the tip gap on the lift and drag of the foil. It can be seen that both the lift and drag improves. However, the drag only improves significantly at small tip gap heights, while the lift improves with comparatively large tip gap heights, roughly ten times larger than the critical tip gap height for drag improvements. An aerofoil operates by creating a circulation effect within the flow stream, accelerating the air above the foil, and decelerating the air below it. These relative accelerations create changes in the pressure of the flow, decreasing it where flow is accelerated and increasing it where the flow

is decelerated. The relative pressures lead to the more common references for the sides of the foil, pressure side where the fluid pressure is higher, and suction side where it is lower. In most practical geometries, the foil is of a finite aspect ratio, as is the case here. The tip is therefore open and the two pressure fields meet at the tip forming a pressure gradient, and fluid flows around the tip, often referred to as tip leakage flow. The extent of the pressure field is large, relative to the foil, as was demonstrated in Figure 5.6. When the open tip of the foil is restricted by a boundary surface, it can be seen that even at comparatively large gaps the pressure field is likely to be effected, confirmed by the data shown in Figure 6.1.

The tip leakage flow causes the formation of a vortex on the tip, which is shed as it reaches the trailing edge of the foil, and convects downstream. The centre of a vortex causes a decrease in pressure relative to the surrounding field, and therefore induces a pressure gradient between the downstream and upstream sides of the foil. The net force on the foil in the same direction as the flow is referred to as induced drag and forms a major component of overall drag on any open tipped foil. The physical size of this vortex was presented in Chapter 5. It can be seen in Figure 5.10 that the diameter of this vortex, relative to the thickness of the foil about $^1/_3$. For large tip gaps the structure of the tip vortex is likely to be largely unaffected and so the drag remains fairly constant. However, when the tip gap reaches a critical height, here shown to be $h/c = 7.5\%$, the drag drops, indicating the tip vortex has been weakened by the presence of the boundary surface near the tip. Indeed, $^1/_3$ of the maximum thickness ($^1/_3 \times 667 \times 0.2 \approx 45mm$), corresponds to the critical tip gap height of $50mm$. As the tip gap reduces to this size, the formation of the tip vortex is impeded and its strength is reduced, thereby reducing the pressure drop at its core in turn, and therefore reducing the drag it imparts on the foil. Further discussion of the formation and propagation of the tip vortex is made in the following section.

The effect of the tip gap height on performance agrees with observations in experiments by [132], using a separation between two foils rather than using a bounding wall surface. This represents a similar geometry to these simulations as the duct has not been given a no-slip condition and so behaves in a similar way to a symmetry plane as it does not impede the strength of the vortex by restricting the rotational flow, but limits its position relative to the foil tip.

The reduction in the tip vortex formation implies that the secondary peaks in C_P seen towards trailing edge near the tip in Figure 5.12d will also be reduced. As the gap tends to zero, the foil tends to quasi two-dimensional, bound between two slip surfaces, and the chord-wise C_P distribution would be expected to be the same in all positions along the span. Figure 6.2 shows the C_P distribution along the span for the $h/c = 1.5\%$ case, the smallest gap in the current study. In comparison to Figure 5.12d it shows three key differences. These are:

1. Higher peak C_P due to the reduction in losses in the pressure field around the tip

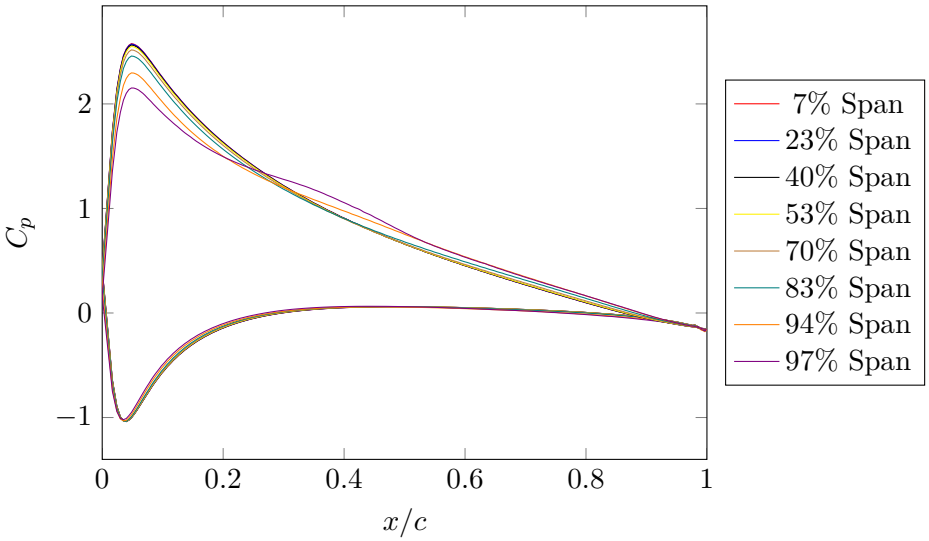

Figure 6.2: Distribution of C_P along span for the NACA0020, $h/c = 1.5\%$ case.

2. More similar profile shapes along the span, again demonstrating the reduced losses in the pressure field

3. Reduced secondary peak in the C_p distribution at 97% Span, suggesting the strength of the vortex is greatly reduced. The location of this peak has also moved towards the LE from $x/c \approx 0.6$ to $x/c \approx 0.4$. The significance of the movement towards the LE will be discussed in the following Section.

Tip vortex path

Figure 6.3 shows the path of the propagating vortex for different tip gaps. In this figure flow is moving from right to left, with the foil location shown for reference. It can be seen that the vortex path in the transverse plane shows strong dependence on the tip gap size. As the gap reduces in size, the trajectory angle can be seen to increase, causing the vortex to deviate from the direction of the mean flow. At $h/c = 7.5\%$ this angle can be seen to be at it's highest, resulting in the largest deflection downstream by nearly $x/c = 0.4$. As the gap reduces further it can be seen that the angle reduces, but that the initial deflection continues to increase. Further analysis will show that the two vortices which were seen in Chapter 5 do not reach the trailing edge with a sufficiently small gap, but instead the vortex on the SS edge becomes dominant and is shed further forwards on the tip. For this reason the vortex path was not plotted forward of $x/c = -0.75$ as in this region there is not a single core to track. As the tip gap reduces further the trajectory angle can be seen to reduce back to a negligible angle, similar to those seen with very large gaps. This behaviour could suggest the existence of a critical gap size, at $\approx 7.5\%$ chord, before reaching a super-critical condition and re-stabilising as the gap reduces further.

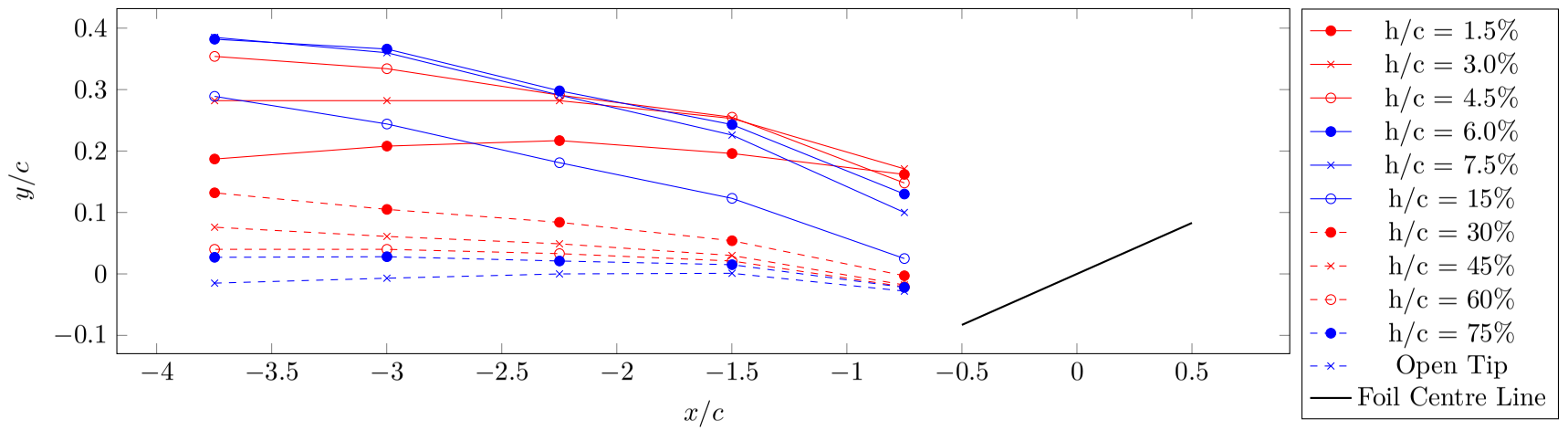

(a) Transverse deflection of vortex path.

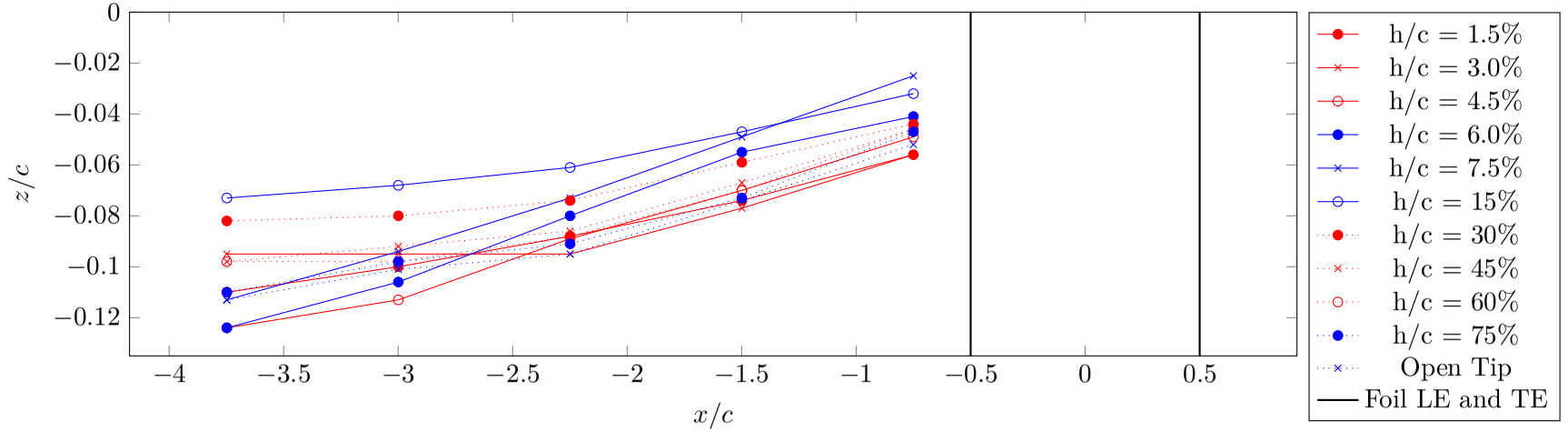

(b) Vertical deflection of vortex path.

Figure 6.3: Effect of the tip gap on the propagation path of the tip vortex downstream.

It can be seen that the variation in the deflection in the vortex path is far greater in the transverse direction than in the vertical direction, by a factor of ≈ 10. Given the radius of the vortex core at $x/c = -0.75$ is ≈ 0.035m, and the variance of the vertical path deflection at that location is a similar size, it is clear that the vortex path in the vertical plane is reasonably independent of the tip gap. Further downstream at $x/c = -3.75$ the vortex radius is ≈ 0.1m, with the difference in the path trajectories only being approximately half of that.

Tip leakage analysis

The separation point of the propagating vortex was also seen to change depending on the tip gap and this was further investigated using the λ_2 criterion to produce a contour of $\lambda_2 = 0$ to illustrate the shape of the vortex core. Using this analysis in Chapter 5 it has been seen that for an open tip foil there are two vortices forming: one by the flow over the PS edge that stays on the tip; and one produced by the tip leakage flow over the SS edge which stays attached to the SS. These two vortices then coalesce to form one vortex that convects downstream from the tip TE. Figure 6.4 shows the same analysis for various tip gap heights. It can be seen that as the tip gap gets smaller the velocity of the cross-flow, U_y, above the tip increases and so the vortex forming on the SS becomes dominant. Furthermore it can be seen that if the gap is small enough, then the tip flow reaches sufficient strength that the vortex is shed forward of the trailing edge, and the position at which it is shed moves further forward as the gap gets smaller. This critical condition seems to occur when the $h/c \approx 7.5\%$. Inspection of the $\lambda_2 = 0$ contour in Figure 6.4f, suggests that this gap is where the tip vortex detaches from the wake sheet and is shed further forward on the foil. As the gap moves reduces further, the λ_2 contour suggests the existence of small vortical structures leaking from the PS edge. It is difficult to infer the physical meaning of these structures, or even to have confidence in their precise shape when the flow in this small gap region is expected to be highly complex. This confirms the difficulties of using a time averaged solution to simulate tip leakage flow discussed in the literature [67].

Figure 6.6 shows the $\lambda_2 = 0$ contour for the NACA0012 and NACA0016 aerofoils with $h/c = 7.5\%$ and $h/c = 1.5\%$. Inspection of the contours with suggests that the reduced thickness has resulted in an increased tendency for the propagating vortex to be shed forward of the trailing edge. At the smallest gap the vortical structures leaking across the tip can still be seen in both the NACA0016 and NACA0012 test cases.

To investigate the effect of the tip gap and foil thickness on the tip leakage velocity component, U_y, a sampling line was placed from the centre of the foil tip, at (0,0,1), which ran vertically to the limit of the domain. As seen in Figure 6.6, the tendency of the tip vortex to shed forward of the trailing edge seems to increase with decreased foil thickness. This is intuitively

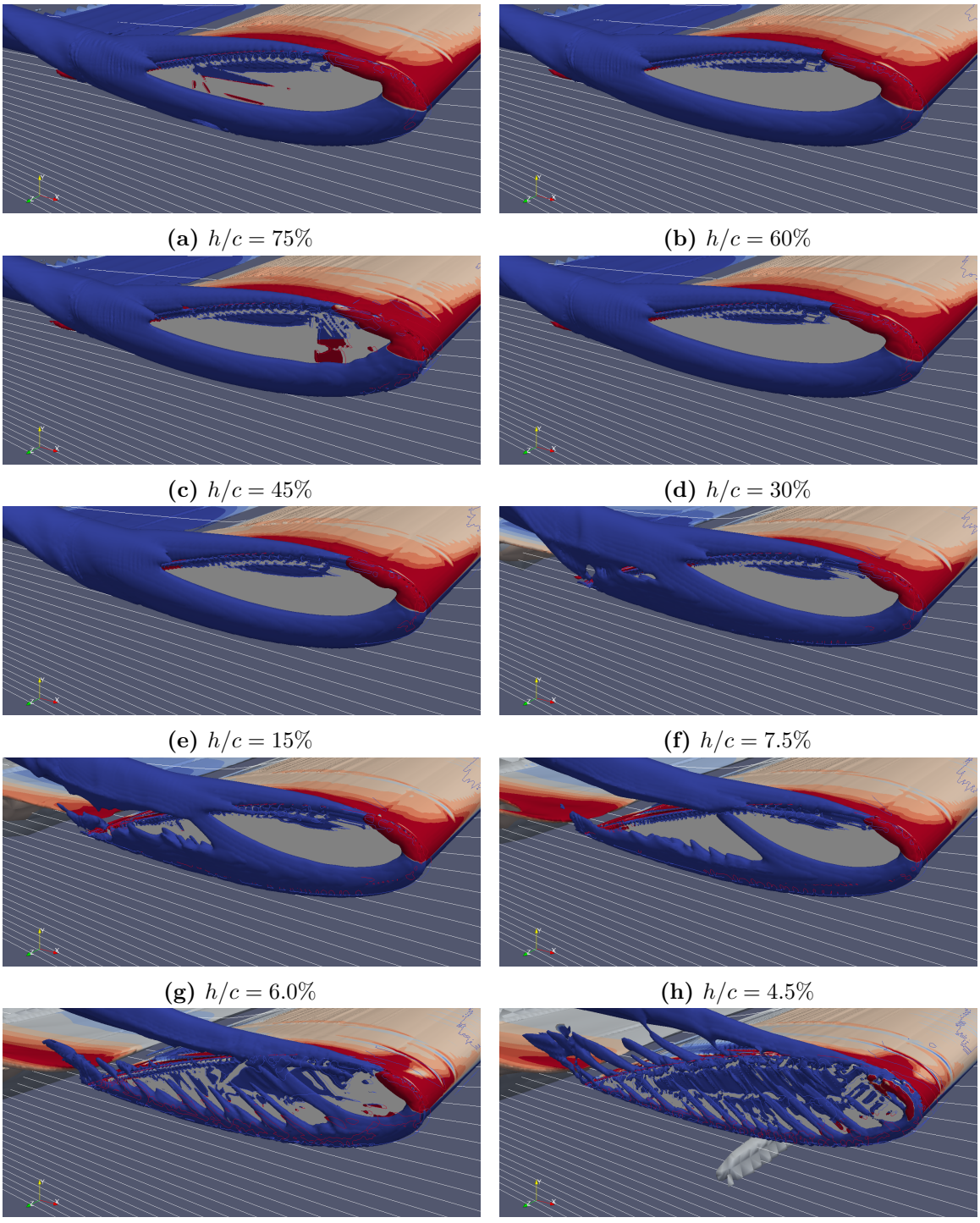

(a) $h/c = 75\%$ **(b)** $h/c = 60\%$

(c) $h/c = 45\%$ **(d)** $h/c = 30\%$

(e) $h/c = 15\%$ **(f)** $h/c = 7.5\%$

(g) $h/c = 6.0\%$ **(h)** $h/c = 4.5\%$

(i) $h/c = 3.0\%$ **(j)** $h/c = 1.5\%$

Figure 6.4: The effect of tip gap size on the formation and propagation of the tip vortex, shown by the contour $\lambda_2 = 0$. Flow is in the $-x$ direction relative to the axes in each figure, and the contour is coloured by vorticity in the x direction to show the direction of rotation of the vortices.

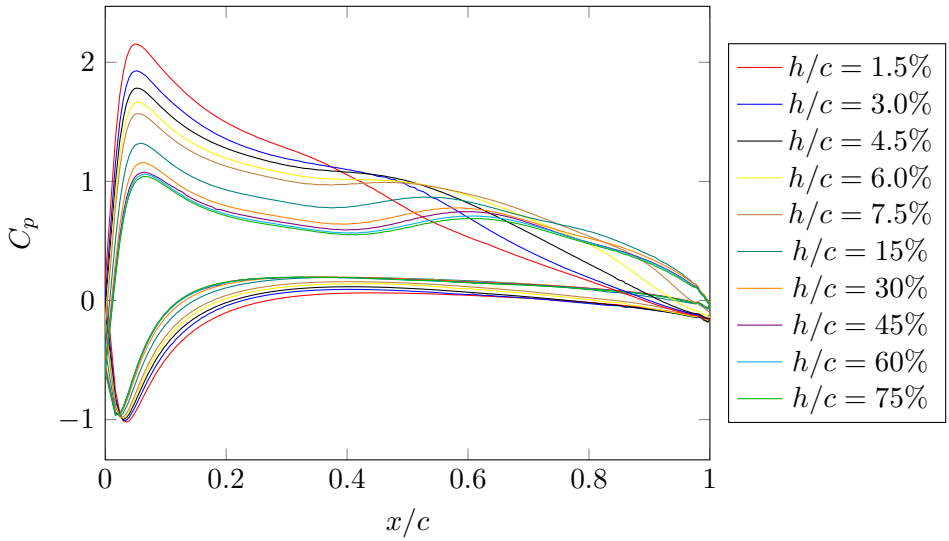

Figure 6.5: Variation of C_P distribution at 97% Span for different tip gap sizes on the NACA0020 foil.

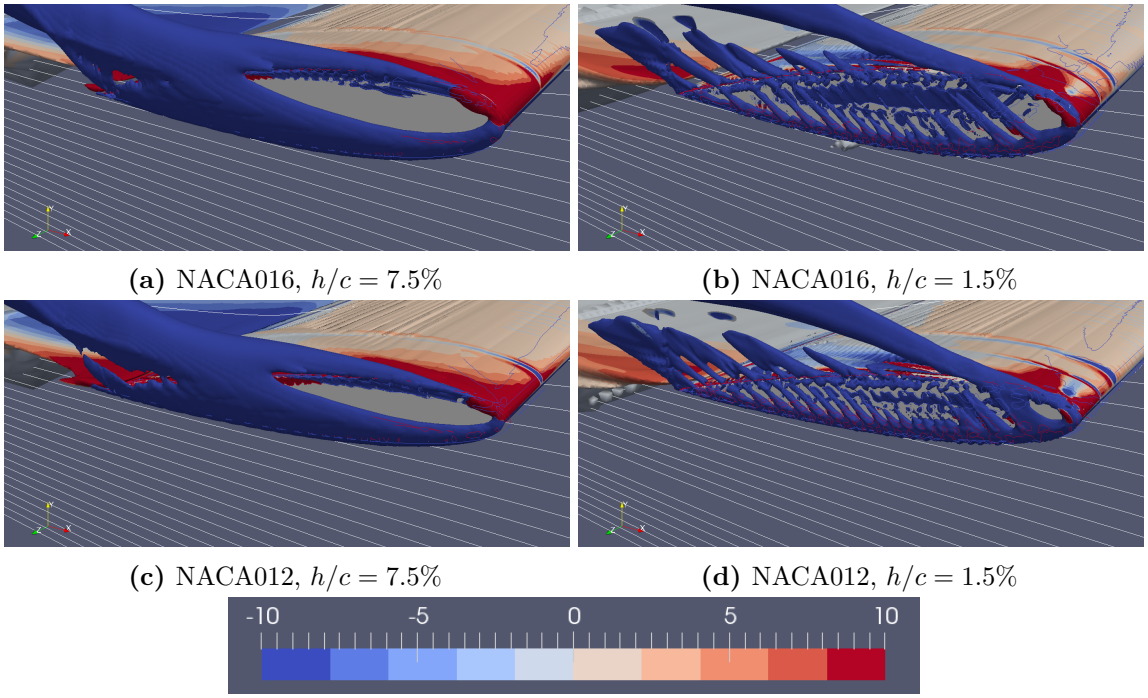

(a) NACA016, $h/c = 7.5\%$

(b) NACA016, $h/c = 1.5\%$

(c) NACA012, $h/c = 7.5\%$

(d) NACA012, $h/c = 1.5\%$

Figure 6.6: The effect of foil thickness and tip gap size on the formation and propagation of the tip vortex, shown by the contour $\lambda_2 = 0$. Flow is in the $-x$ direction relative to the axes in each figure, and the contour is coloured by vorticity in the x direction to show the direction of rotation of the vortices.

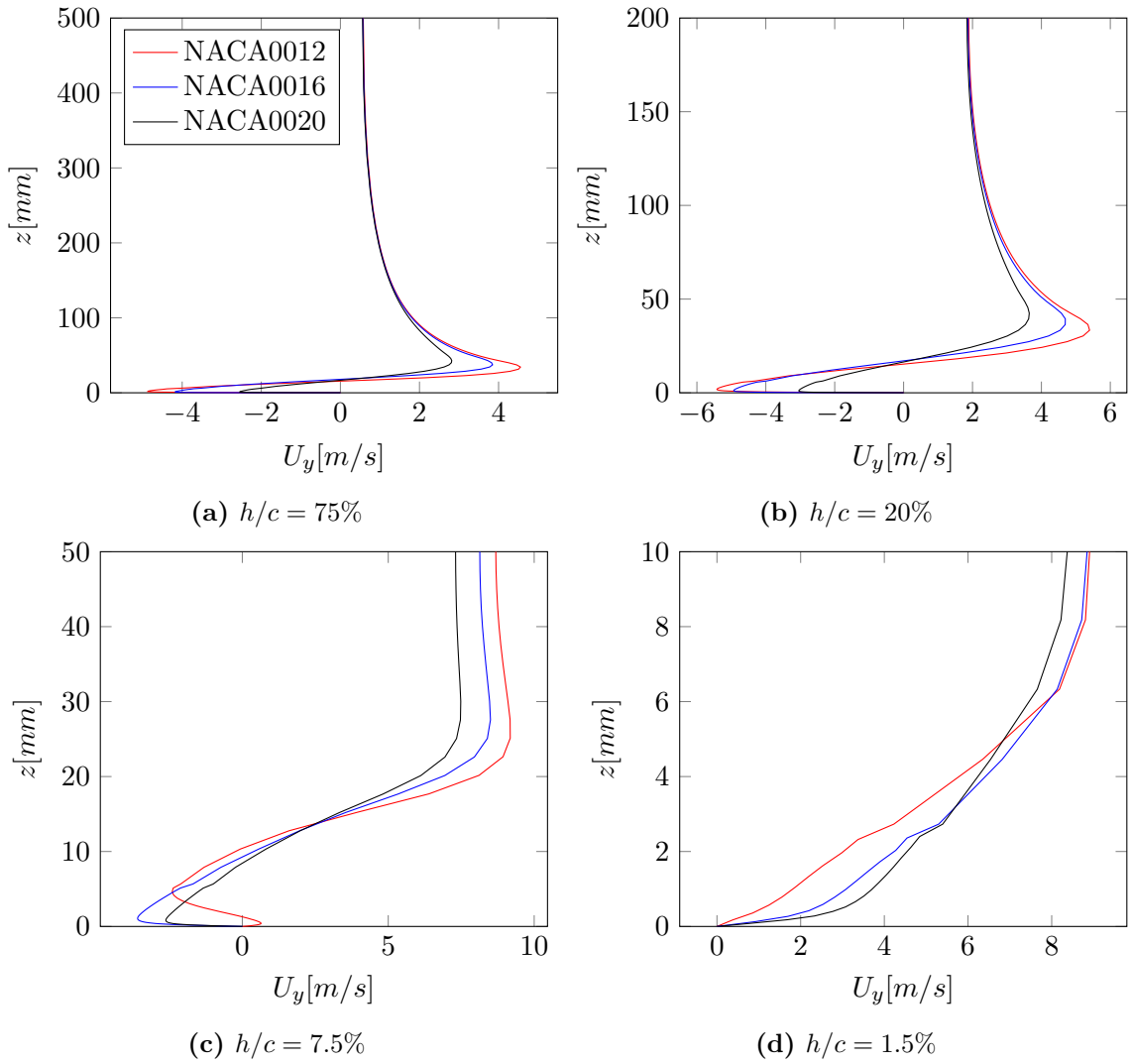

(a) $h/c = 75\%$ **(b)** $h/c = 20\%$

(c) $h/c = 7.5\%$ **(d)** $h/c = 1.5\%$

Figure 6.7: Transverse velocity components in the centre of the tip demonstrating the effect of varying the tip gap.

expected as thin foils will generate more lift for the same angle of attack, and so the tip leakage component is expected to be higher. Thinner foils also present a smaller physical separation of the low and high pressure fields therefore generating a higher pressure gradient across the tip.

Figure 6.7 shows the effect of reducing the gap on the transverse velocity component, U_y. The velocity distributions can be seen to resemble a Rankine vortex distribution, with the tip gap having the effect of increasing the transverse velocity component above the vortex. It can also be seen that the thinner NACA0012 foil produces higher magnitudes of U_y than the thicker foils, supporting the previous analysis. At the smallest gap heights the cross flow velocity resembles that of a regular boundary layer flow with no evidence of any recirculation. At such small tip gap heights the flow through the tip gap is analogous to channel flow with

a forward facing step at the inlet and a backward facing step at the outlet. The higher pressure gradient along this channel produced by the thinner aerofoils is likely to produce stronger separation at the inlet edge and therefore velocity profiles that resemble more turbulent boundary layers, with the magnitude of the velocity gradient at the wall shown in this figure to be inversely proportional to foil thickness.

6.3 Time resolved simulations

6.3.1 Test case description

In order to gain a better understanding of the tip gap flow, unsteady simulations are required as the complexity of the flow has proven to be inadequately modelled using time averaged simulations. As discussed in section 5.3, `snappyHexMesh` has shown some instability in the generation of the boundary layer cells in the mesh, and so for the NACA0020 foil only three cases $h/c = 7.5\%$, $h/c = 30\%$ and $h/c = 60\%$ have suitable meshes to meet the grid density requirements for LES as discussed in Chapter 3. These cases will be the focus of the initial unsteady simulation study, while alternative mesh techniques are analysed and validated.

The simulation setup remained largely the same as given in Table 6.1, with the change to using the PIMPLE algorithm to solve the time-resolved Navier Stokes equations. The turbulence is modelled using LES with the wall adapting local eddy (WALE) viscosity model described in Section 3.2.2. Due to the different ways that LES and RANS deal with the turbulent structures in the flow, the LES simulations need time to re-converge to the LES solution. Convergence in the RANS simulations can be assessed by monitoring the residual data, a measure of the error in the continuity equations. However, as LES flow is unsteady, this residual convergence will need to be achieved at every time step before the simulation can move forward [133]. Convergence instead is measured here by tracking the force coefficients on the foil. While the forces will never be totally steady, they can be seen to shift from their initial values and settle to an oscillating value about a new mean. As discussed in Chapter 5, the force coefficients calculated for the RANS simulations differed from the experimental values found by [128]. The higher fidelity of LES simulations should provide a reduction in the coefficient of drag and an increase in the coefficient of lift.

In Section 6.2 the λ_2 criterion identified the wake sheet as being a vortex core, as well as some regions far away from the foil where coherent vortex structures are not expected to form. Due to the definition of $\lambda_2 = 0$ being at the point where vorticity dominates the shear strain, areas which have very low levels of both quantity sometimes are identified by the criterion which are not of interest to this study. One benefit in the use of λ_2 is that the strength of vorticity found at the limit of the vortex core means that by increasing the value used for the contour, the shape of the main vortex core is still captured well, whilst

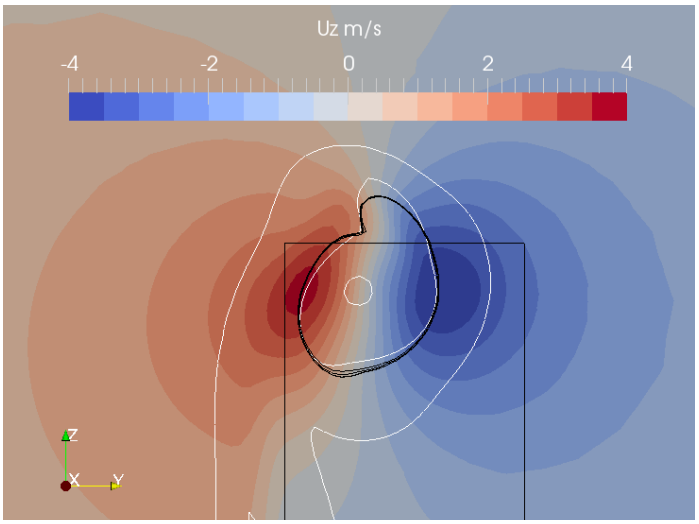

(a) Investigation of the robustness of the λ_2-criterion for vortex identification. White contours are for vorticity values of $|\omega| = 10, 100$ and 250 and black contours show $\lambda_2 = 0, 10, 100$, and 250.

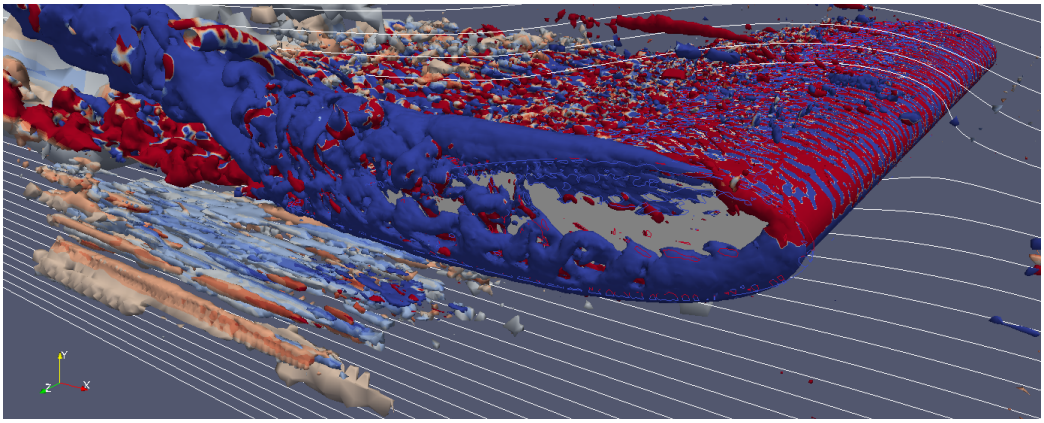

(b) Snapshot of $\lambda_2 = 0$ contour on tip leakage flow for $h/c = 7.5\%$ LES case, coloured by $-10 < \omega_x < 10$, with blue showing negative values and red showing positive values.

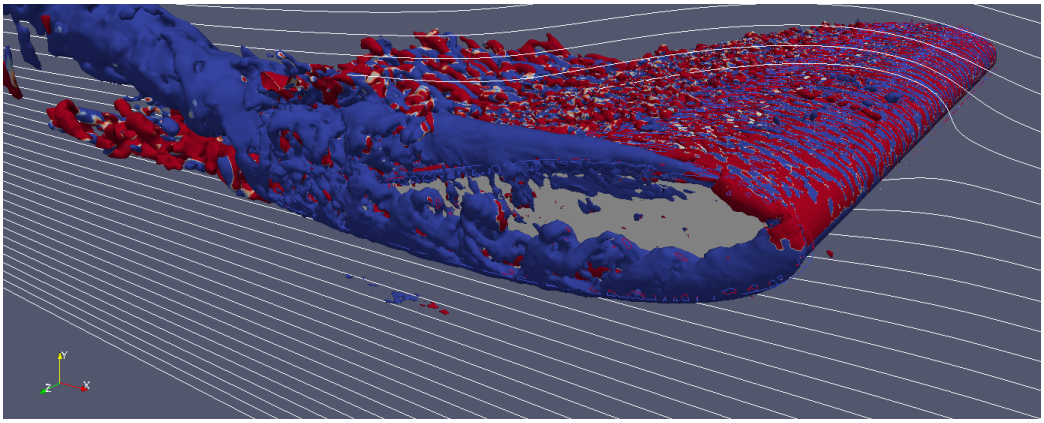

(c) Snapshot of $\lambda_2 = 250$ contour on tip leakage flow for $h/c = 7.5\%$ LES case, coloured by $-10 < \omega_x < 10$, with blue showing negative values and red showing positive values.

Figure 6.8: Demonstration of the robustness of the λ_2-criterion in detecting the edge of strong vortex cores.

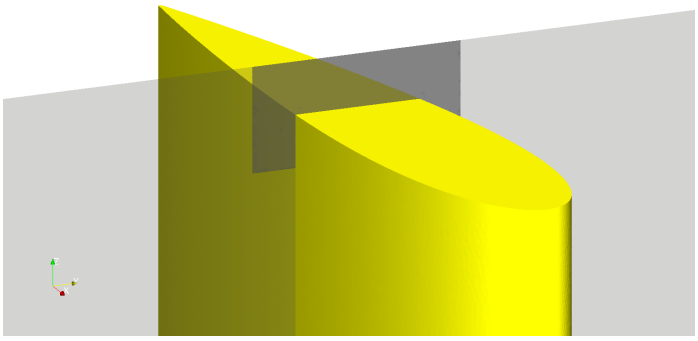

Figure 6.9: Schematic of slice location used to investigate unsteady flow features in the tip gap.

removing areas where vorticity dominates the rate of shear only slightly. This robustness is shown in Figure 6.8a where the four contours of $\lambda_2 = 0, 10, 100$ and 250 all show very close agreement with the peak in the vertical velocity component U_z expected at the edge of the vortex core. Figures 6.8b and 6.8c show the effect of increasing the value used for the contour from 0 to 250. It can be seen that qualitatively, the flow structures on the tip are unaffected, while the structures which are further downstream in the wake and other parts of the domain are not shown by the higher criterion value. Note that the leading edge of the foil has been identified by this value of the criterion. This is because the vorticity is so high in this region due to the extremely thin profile of the boundary layer that the criterion incorrectly identifies it as being a coherent vortex.

6.3.2 Unsteady flow features in the tip gap region

Figure 6.8c shows a snapshot of the $h/c = 7.5\%$ simulation results using a $\lambda_2 = 250$ contour, coloured by vorticity about the x-axis, ω_x to show the directionality of the vortical structures. This surface suggests the vortex seen on the PS edge in the RANS simulations is an unsteady structure which lost definition due to the time-averaging process. However the vortex on the SS edge seems much more stable as it convects towards the TE. Further analysis of the transverse flow through the tip gap region is achieved by taking a transverse slice through the mid-chord of the foil as shown in Figure 6.9. The dark grey area shows the flow visualised in Figure 6.10.

Figure 6.10 shows snapshots from an animation using this analysis for the three cases. These figures are orientated with the x-axis, as indicated by the axes shown. The grey area shows the foil cross-section at this location. The SS is on the right of the figure, and the PS is on the left, so the mean tip leakage flow is from left to right, in the positive y-direction. The upper limit of the figure is $50mm$ above the foil tip, i.e. at the edge of the domain for the

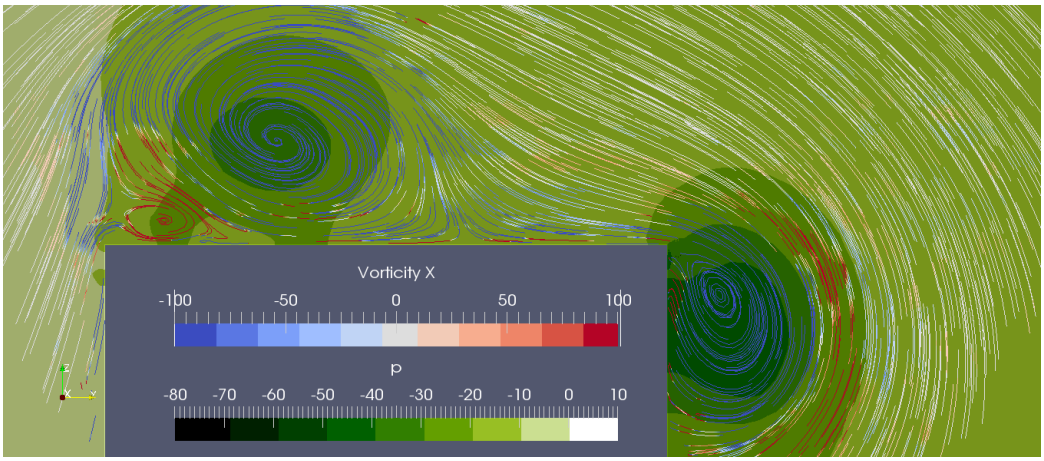

(a) $h/c = 60\%$

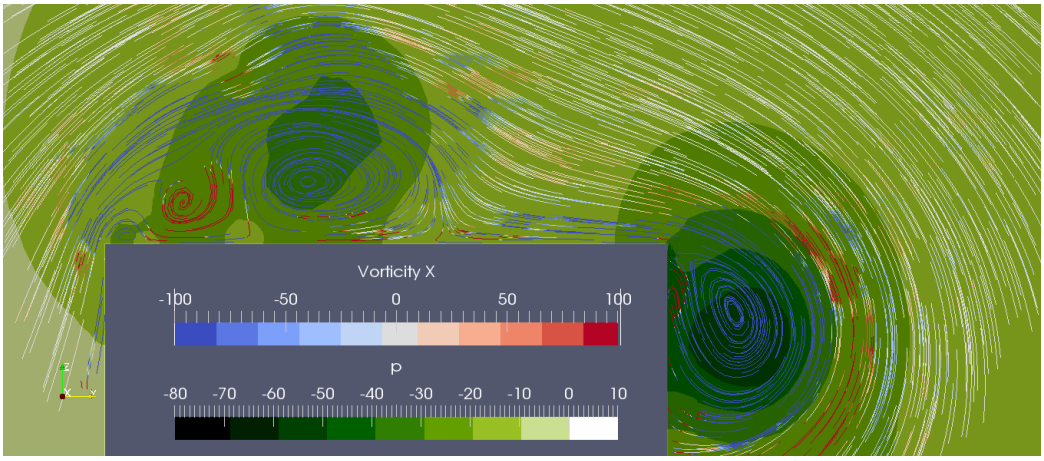

(b) $h/c = 30\%$

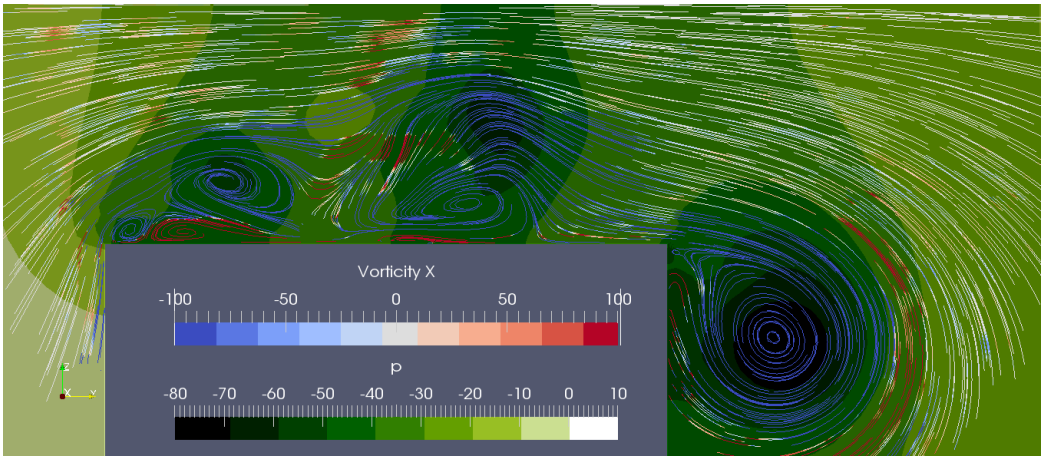

(c) $h/c = 7.5\%$

Figure 6.10: Snapshots of transverse velocity component stream lines for initial LES analysis. Streamlines are coloured by ω_x and the slice is coloured by relative pressure.

$h/c = 7.5\%$ case. The slice has been coloured by relative pressure to show the pressure drop caused by the complex flow, and the stream vectors have been coloured by vorticity ω_x to indicate the direction of rotation.

In all three cases the vortex on the SS edge was observed to remain highly stable throughout the animation. The formation of this vortex is due to the total tip leakage flow, which remains stable in the y-direction due to the pressure gradient between the two sides of the foil. However as the tip gap reduces and the tip flow velocity increases it can be seen that this vortex increases in strength, shown by the larger pressure drop observed for a smaller tip gap.

The vortices on the top of the foil showed more complex behaviour with the stability of these formations decreasing with decreasing tip gap. The animation of the $h/c = 60\%$ case showed low frequency shedding of this vortex, which occurred as the vortex reached a critical size as shown by Figure 6.10a. It can be seen that a counter-rotating vortex is present between the large vortex and the PS edge which experienced a similar shedding frequency to the larger vortex.

The vortices on the tip of the $h/c = 30\%$ case exhibited a similar behaviour and the instantaneous flow-field image has been generated just before shedding of the large vortex, again with its partner counter-rotating vortex. Note also the presence of a third, even smaller vortex attached to the PS edge. The periodicity of this shedding was slightly higher for this case that the $h/c = 60\%$ case.

Figure 6.10c shows the regions of low pressure being shed from the PS edge along with the associated vortex structures for the $h/c = 7.5\%$ case. This case exhibited oscillating vortices of contrary directions shedding from the PS edge, similar a to Von Karman vortex street observed in the wake of a cylinder.

These vortices can also be seen to cause much greater pressure drops than the larger tip gaps which could have two consequences. This work is neglecting the effects of cavitation, but large pressure drops would increase the likelihood of cavitation and the associated monopole source. A large pressure drop could also imply that the pressure fluctuations are of a larger amplitude in the $h/c = 7.5\%$ case, which would imply a louder dipole source of noise present on the tip surface.

6.3.3 Potential noise sources

The final stage of the initial investigation is to attempt to predict the potential noise source locations which are dependent on the tip vortex, and in turn on the size of the tip gap. It is emphasised here that this is an attempt to infer the acoustic sources from the incompressible flow solution. It has long been recognised that an essential mechanism in the

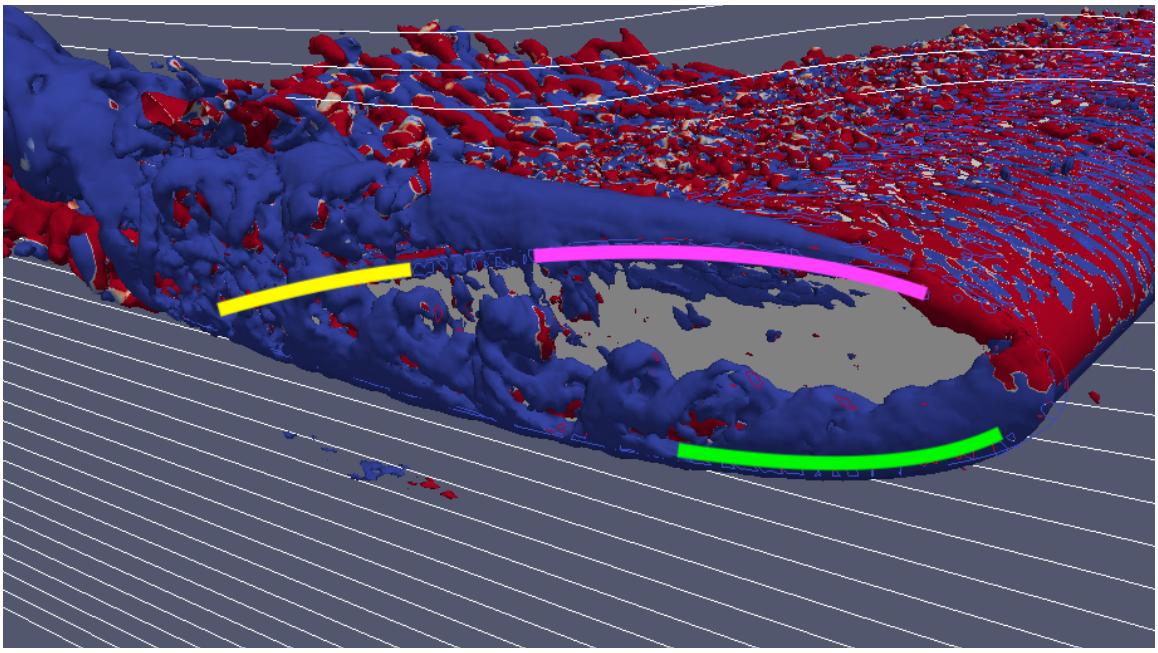

Figure 6.11: Snapshot of LES simulation with predicted noise source locations illustrated. The green line shows the location where the helical vortex structure is shed from, before it convects through the tip gap and is shed over the opposite edge near the TE shown by the yellow line. The pink line illustrates the building of the steady vortex on the suction side edge.

generation of noise due to turbulent flow passing over an edge is scattering of its vorticity into sound, which of course is absent from the incompressible flow solution computed here. Subsonically convecting turbulent flow in the absence of an edge is intrinsically an inefficient radiator, generating only a non-propagating, hydrodynamic near field. Nevertheless, once this limitation is recognised it is possible to speculate on the possible sources of acoustic noise from the behaviour and characteristics of the unsteady flow near and around the tip gap. As discussed, the existence of monopole sources in this flow is being neglected by assuming that the depth of operation is deep enough to suppress cavitation and so only dipoles and quadrupoles will be considered here.

Figure 6.11 shows the three key regions which could be identified as potential contributors to noise. The green line illustrates the forward part of the pressure side edge of the tip which initiates the unsteady vortical structures in the tip gap region. These highly unsteady structures could be quadrupole sources of noise themselves, although due to the low Mach numbers involved are unlikely to propagate to the far-field, as previously discussed. As these structures are driven through the tip gap by the cross flow they are then shed over the suction side edge of the tip, shown by the yellow line. This area is likely therefore to be a dipole noise source, caused by the unsteady pressure fluctuations on the solid surface.

The noise generation mechanism due to unsteady flow passing over an edge has some

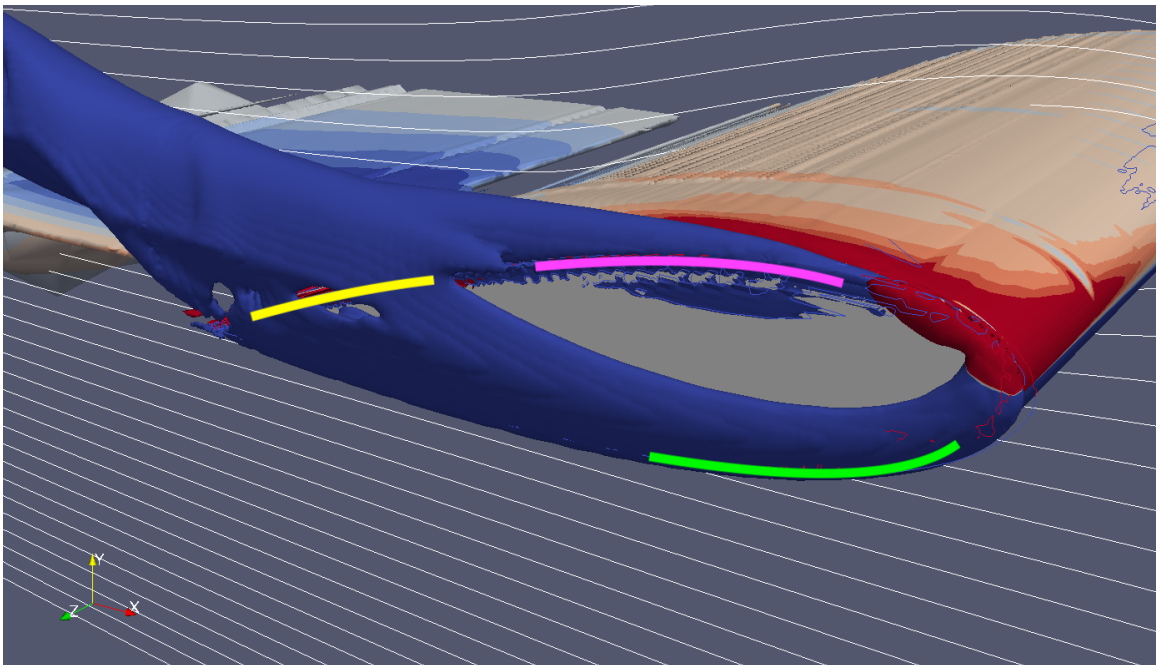

Figure 6.12: RANS simulation with predicted noise source locations from LES analysis. The coloured lines follow those in figure 6.11.

similarities to flow passing over a backward facing step. It is unclear how, or how efficiently, the unsteady pressure hydrodynamic pressure along the suction side edge then radiates as sound to the far field. It is clear, however, that this vortex is the essential source of unsteadiness which then drives the acoustic field. The level of acoustic far field radiation will be clearly dependent on the magnitude of pressure, the effective convection speed of the flow as it passes over the edge, and the coherence of the pressure along the edge. It is well known that pressure disturbances that effectively convect faster than the sound speed are efficient sources of sound while subsonic disturbances do not radiate to the far field.

The pink line is the forward part of the suction side of the tip, where the steady vortex structure initiates and grows as it is driven by the cross flow. As this vortex builds in strength and is shed downstream it will inevitably become unstable and the vortex structures will break up, potentially leading to another quadrupole source, as well as producing increased inflow turbulence for any solid surfaces which may be downstream. This mechanism has been presented in the literature and is of interest in the aviation industry when the Mach number of the tips of fan blades is sometimes supersonic. However the quadrupole noise source generated by the breakdown of vortices in the free-flow is unlikely to be a dominant source of noise in a marine context with $M < 0.03$.

In the interest of establishing this methodology as a viable option during the design cycle for noise mitigating propulsors, it is interesting to compare the noise sources identified by the LES simulations with the results of the RANS simulations already conducted. RANS

simulations require far less computational expense as discussed earlier and therefore are more affordable to be used to assist design. Figure 6.12 shows the same locations drawn on the RANS simulation results of the same test case. It is interesting to note that despite the concerns of the efficacy of the λ_2-criterion to highlight coherent structures in time-averaged simulations, it has predicted the key regions of interest accurately. This is of particular interest as the computational effort required to carry out the RANS simulation is significantly less than that of the LES simulations and so could lead to a practicable design methodology.

6.4 Transition to tetrahedral mesh methodology

It has been discussed earlier in this and the preceding chapter that the `snappyHexMesh` mesh generator presented a number of issues regarding the growth of cell layers near the sharp edges of the tip of the foil. As this study is focussed on investigating the flow in this region it was decided to use a different mesh generation software called `Pointwise`. `Pointwise` can be used as a structured or unstructured grid generator and will be used here to produce unstructured grids. The grids are generated by first producing triangular surface meshes for all of the boundaries of the domain. The surface meshes are produced by defining the spacing of points along the lines which mark the edges of the solid surfaces. This allows the cells to be clustered on different parts of the surfaces, such as near sharp edge or areas of high curvature, without having to rely solely on the refinement regions used in `snappyHexMesh`. The surface mesh can then be extruded into a layer of prismatic cells from selected boundaries, such as those where the no-slip condition is to be enforced and therefore require the resolution to capture the boundary layer profile. Once the extruded cells reach isotropy, established when the lengths of each of the cell edges are close to being equal, the remainder of the volume is populated with tetrahedral cells. The domain can include the use of refinement zones to cluster cells within certain regions by specifying the maximum edge length of the cells generated there. The increased resolution control on the surfaces combined with refinement regions in the fluid allows greater overall control of the domain resolution. For this reason `Pointwise` was used to generate the meshes for the rest of this thesis.

Figure 6.13 shows the surface mesh on the tip for the two different generators along with the instantaneous pressure field from an LES solution. In Figures 6.13a and 6.13b it can be seen that there is a significant increase in the number of cells on the tip surface, despite the total cell count for each domain remaining similar (within $\approx 5\%$). It can be seen that the cells are also clustered on the edges of the tip towards the trailing edge which is likely to be a critical region in the future studies in this work.

Figures 6.13c and 6.13d show the instantaneous pressure on the tip surface for the two different mesh generators. Here it can be seen that the general shape of the pressure

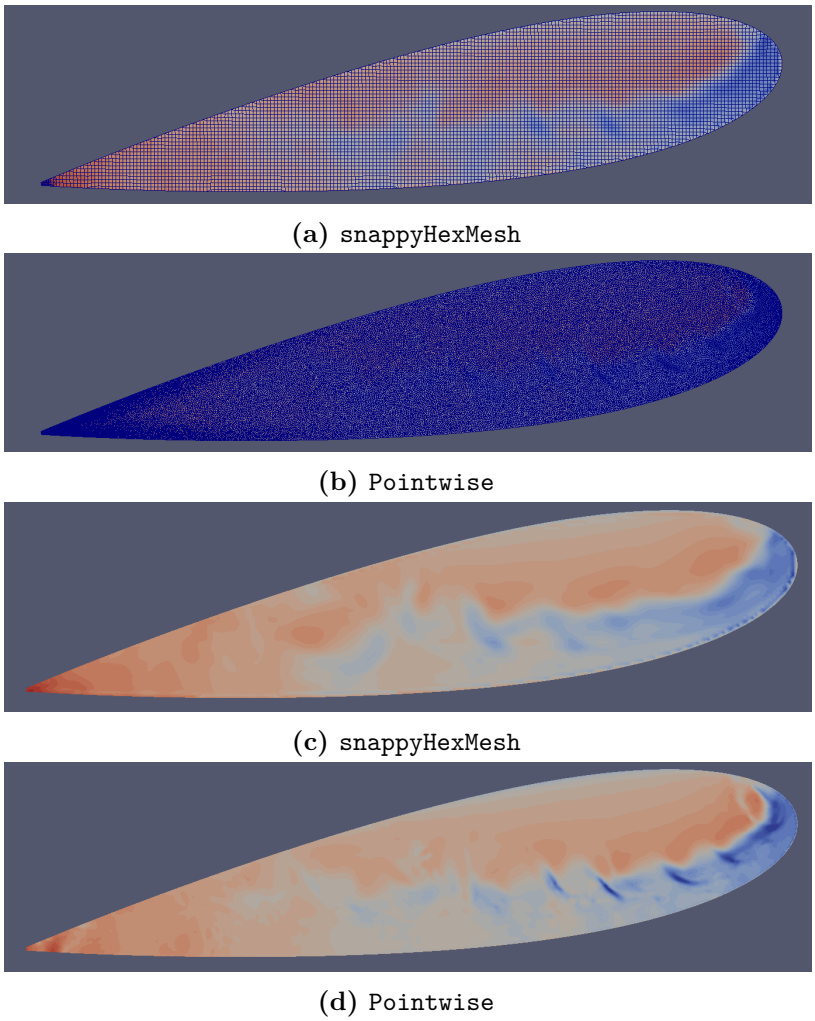

(a) `snappyHexMesh`

(b) `Pointwise`

(c) `snappyHexMesh`

(d) `Pointwise`

Figure 6.13: Comparing the mesh on the tip of the foil using `Pointwise` and `snappyHexMesh` software, and the qualitative impact this has on the surface pressure fluctuations captured.

fluctuations is similar, caused by the tip separation vortex which is strongest near the point of separation and then breaks down further downstream. However, the mesh generated using `Pointwise` captures a significantly greater number of small structures, due to the higher localised resolution.

Figure 6.14 shows the PSD of the surface pressure spectra sampled on the chord-line of the tip surface of the foil at $x/c = 70\%$ for both `snappyHexMesh` and `Pointwise` meshes. It can be seen that while maximum pressures are comparable, with a characteristic peak shown at $\approx 700Hz$, the spectra produced by the `snappyHexMesh` mesh experience a sharper drop-off than those from the `Pointwise` grid. It is proposed that the difference in the capturing of small scale structures by the different meshes, visible in Figure 6.13, is responsible for the higher pressure levels in the mid frequencies from the `Pointwise` mesh. The PSD

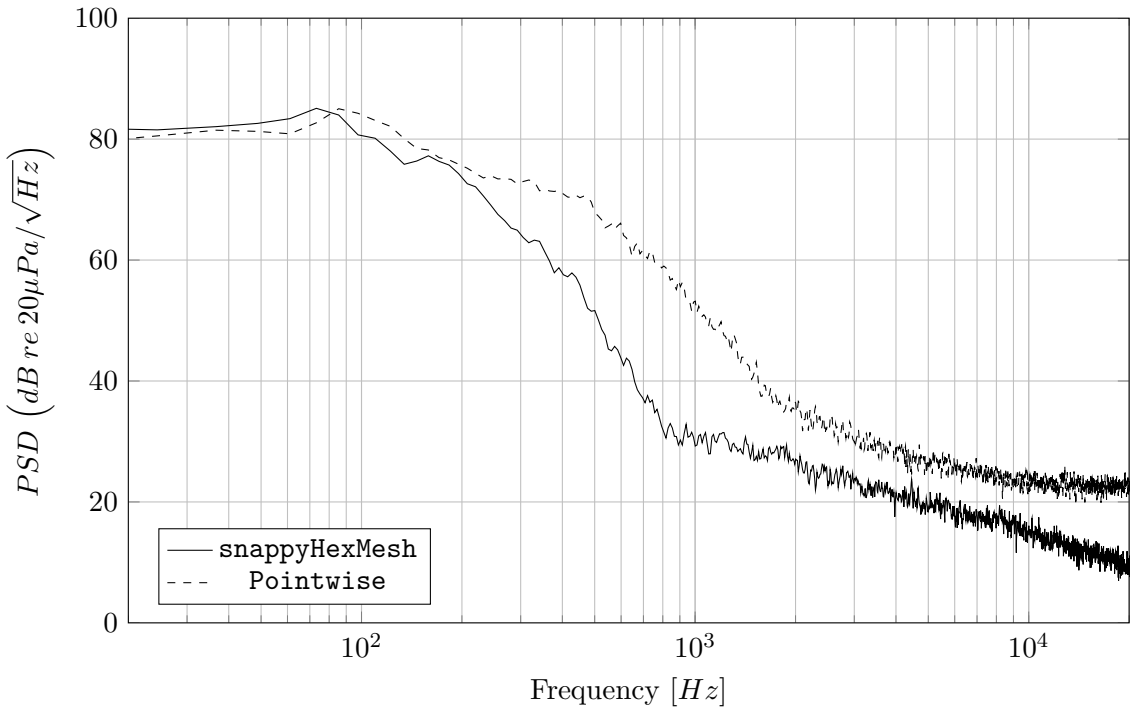

Figure 6.14: Comparing different meshes produced by `Pointwise` and `snappyHexMesh`, and the impact this has on the frequency content of the surface pressure fluctuations on the tip surface sampled on the chord-line at $x/c = 70\%$.

produced by the `Pointwise` mesh compares better than those from `snappyHexMesh` with surface pressure spectra experimentally observed in the tip gap of a NACA5510 foil in previous works [9].

Figure 6.15 shows the different meshes which were produced using pointwise to verify the grid independence of the results. It can be seen that, as with the `snappyHexMesh` grid independence study, the results show little variation, within $\approx 3\%$ of each other. The mesh resolution used here is approaching the limit of what is practicable given the computational capability available, hence the prooritised refinement in the tip region to ensure that the capture of the tip leakage flow is as accurate as possible. In order to verify that the mesh provides sufficient accuracy in LES, a series of tip gap cases were run in both RANS and LES and the resulting force coefficients can be seen in Figure 6.16 and it can be seen that the LES simulations predicts a higher lift and lower drag than the RANS simulations for the equivalent arrangements. It is understood that RANS models of aerofoils have a tendency to under predict lift and over predict drag, which agrees with the results shown [134]. The relatively constant offset in these coefficients suggests that the influence of the varying tip gap is being well captured in the LES, and therefore that the grid is sufficiently dense.

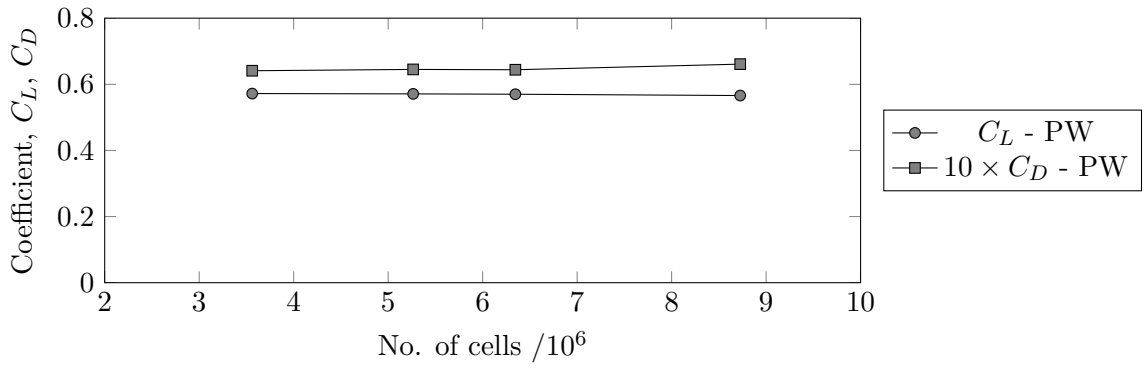

Figure 6.15: Grid convergence study showing grid independence for the present study.

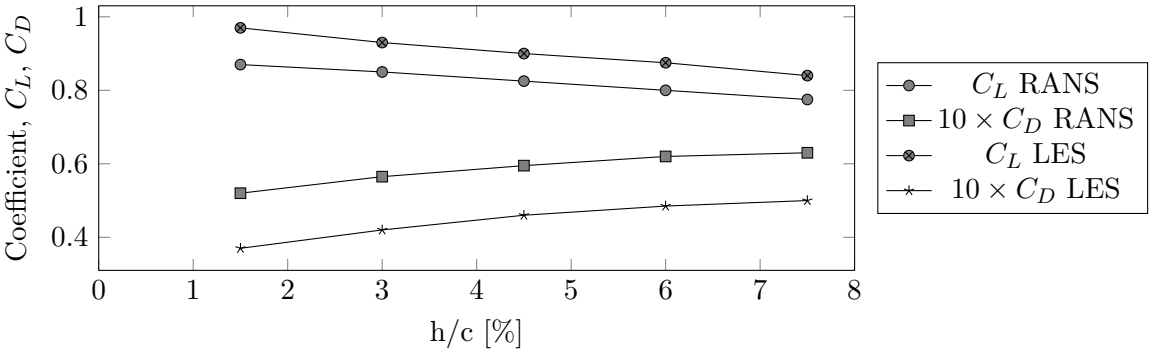

Figure 6.16: Grid independence study for the present case, showing the comparison between RANS and LES results.

6.5 Summary

This chapter has presented the simulations used in the preliminary tip gap investigation. Time-averaged RANS simulations were used to assess a large variety of cases, with three different foils and ten different gap sizes. These results have identified the potential existence of critical a gap size, whilst also developing simulation settings and analysing mesh resolution dependence. The inconsistency of `snappyHexMesh` has limited the number of simulations currently carried out using LES, and training has been undertaken using `Pointwise` to develop meshes to be tested using RANS which have been presented and the use of `Pointwise` will replace `snappyHexMesh`.

Time-resolved LES simulations have been carried out on the NACA0020 foil and have produced insightful results. The presented unsteady simulations have revealed flow features within the tip gap with greater detail than the RANS simulations as expected, and have given implications as to the potential noise sources from the vortices being shed from the foil tip edge. The scale of these structures is much smaller than the tip vortex as a whole and has revealed some complex behaviour which has not been covered in the literature.

Part III

Case study of cambered foil with reduced tip gap and realistic boundary conditions

Chapter 7

Parametric analysis of NACA5510

7.1 Introduction

The simulations presented in Part II did not model the no slip condition on the boundary surface above the foil, and therefore also did not take into account the boundary layer velocity profile on this surface. This chapter aims to move towards a more realistic test case by including the no slip condition, while modelling the development of the boundary layer by prescribing it at the inlet and the use of a cambered foil as would be more representative of a propeller blade. This case was chosen as a premilinary study into the far-field noise prediction for comparison against the experimental work conducted by [49]. This study also investigates the effect of the tip gap size. The inlet boundary layer profile was chosen to be parabolic, with an inlet thickness of $\delta = 5\%$ chord. This value was chosen so that as the boundary layer developed it reached a thickenss of $\delta \approx 10\%$ at the leading edge of the foil and so was similar to the measured boundary layer from the experimental work mentioned. The angle of attack, $\alpha = 10^{\circ}$ was chosen to create a strong lift force and therefore strong tip leakage flow. The inflow velocity, $U_{\infty} = 10m/s$, was chosen to allow continuity with previous results, whilst increasing the Reynolds number to closer match the realistic case of a marine propeller. The numerical settings used in these simulations are given in Table 7.1. In this series of investigations, the reference case will be at an angle of attack of 10°, with a tip gap of 10mm, or 1% chord, and an inflow freestream velocity of $10m/s$, giving a Reynolds number of 6.6×10^5. This Reynolds number was chosen to be within the range of realistic Reynolds numbers for the tips of submarine propellers [135].

Table 7.1: Numerical model settings for LES of NACA5510 case.

Parameter	Unit	Setting
Section span	m	1
Foil chord	m	1
Gap height	m	$1\%c$
Mesh Type	-	Unstructured
No. of Elements	-	$\approx$ 10M
y^+_{max}(Foil, Boundary surface)	-	(< 1, ≈ 15)
Inlet	-	BL Profile ($U_\infty = 10m/s$, $\delta = 5\%c$)
Outlet	-	Zero gradient
Boundary surface (foil root)	-	Slip
Boundary surface (foil tip) roof	-	Slip
Domain side walls	-	Slip
Foil	-	No slip
Reynolds' Number	-	6.6×10^5
Angle of Attack	deg	10
SGS Model	-	WALE
Solver	-	PIMPLE

7.2 Simulation setup

The implementation of the boundary surface mesh, required to implement the no slip condition, is computationally expensive, even with the use of wall functions so it is important to establish whether it is necessary to include it in the simulations. These factors will be considered by analysing the performance characteristics, using the λ_2-criterion to identify key flow features and by investigating the pressure fluctuations on the solid surfaces. The far-field noise predictions are made using the FW-H analogy.

The simulations presented in this part are set up with the origin, $(0, 0, 0)$ in the computational domain at the centre of the chord-line of the foil, on the lower boundary surface. The domain is C-shaped and extends for 20 chord lengths, c, laterally and downstream, beyond the constant span of the section of the domain, as shown in Figure 7.1.There is a unit span between the boundary surfaces which is held constant. The foil is of a unit chord and the span is adjusted to produce the desired gap, h between the tip of the foil and the lower surface. Therefore the root of the foil is flush with the upper surface of the domain, with the mid point of the chord line located at $(0, 0, 1)$. The boundary surface extends $2c$, downstream of the foil, $2.5\,c$ to either side, and $5\,c$ lengths up stream to the inlet as shown in Figure 7.2. Figure 7.1 shows the location of the four receivers used for the far-field acoustic prediction: upstream (UP), downstream (DN), and on the suction side (SS) and pressure side (PS) relative to the foil. It can be seen that the upstream receiver is outside of the computational domain which is one of the benefits of using an acoustic analogy, as discussed in Chapter 4.

This topology is used to investigate a range of tip gap sizes from $h/c = 5\%$ to $h/c = 0.5\%$

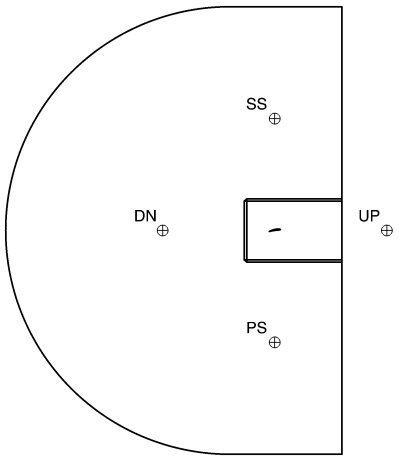

Figure 7.1: C-Shaped domain topology used in NACA5510 investigation, with the inlet on the right and semi-circular outlet on the left. The receiver locations used in the FW-H analysis are included, named by their position relative to the foil and mean flow direction.

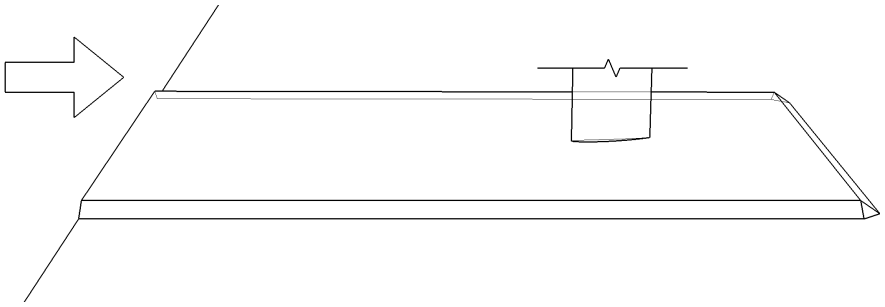

Figure 7.2: A zoomed in schematic showing the arrangement of the foil above the boundary surface. The edge of the boundary surface has a chamfer connecting it to the lower limit of the domain, and the inlet can be seen on the left. The gap, h is between the boundary surface and the foil shown. The upper extent of the domain is flush with the root of the foil (no gap) and has not been shown.

with attention paid to the performance coefficients to infer the potential implications for noise production. One case is then chosen to investigate in detail with the aim of establishing a link between the far-field noise observed and its relationship with the gap flow. The fluctuating surface pressures are inspected on the solid surfaces to infer the regions which may be responsible for noise production. The λ_2-criterion is then used to locate the coherent vortex structures within the fluid. Finally the FW-H analogy is used to predict the radiated noise into the far-field for four receiver locations located 10 chord lengths from the foil directly up and down stream and to the suction and pressure sides as shown in Figure 7.1. The aim of this analysis is to attempt to link the far-field noise to the flow features observed in the tip gap, and therefore make an estimation of the sources of noise in the tip gap region, in order to produce effective noise mitigating designs. The sampling surfaces used in the

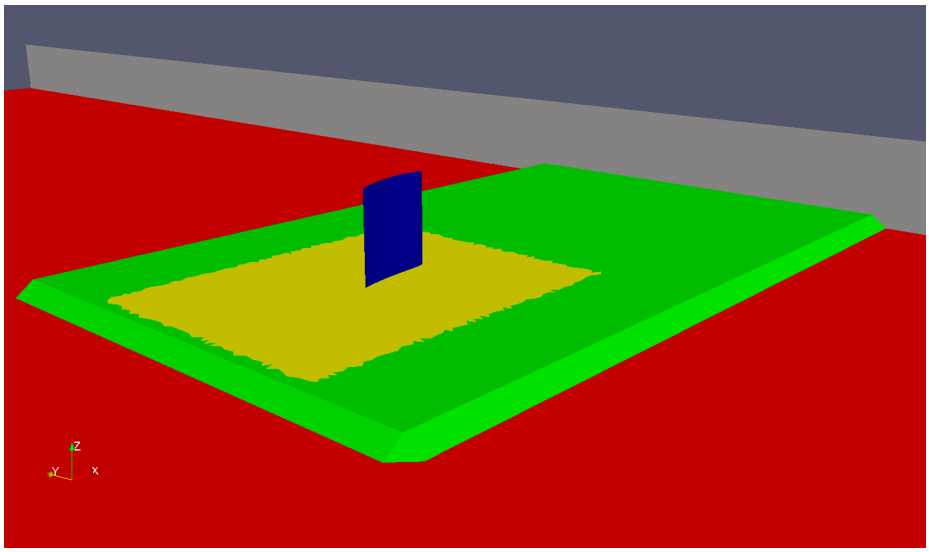

Figure 7.3: The sampling patches within the domain used for the FW-H analogy shown in blue (foil) and yellow (boundary surface). This view of the domain shows the inlet in light grey on the right, with flow from top right to bottom left. The remainder of the boundary surface which was not used for the FW-H source is shown in green and the lower limit of the domain is shown in red.

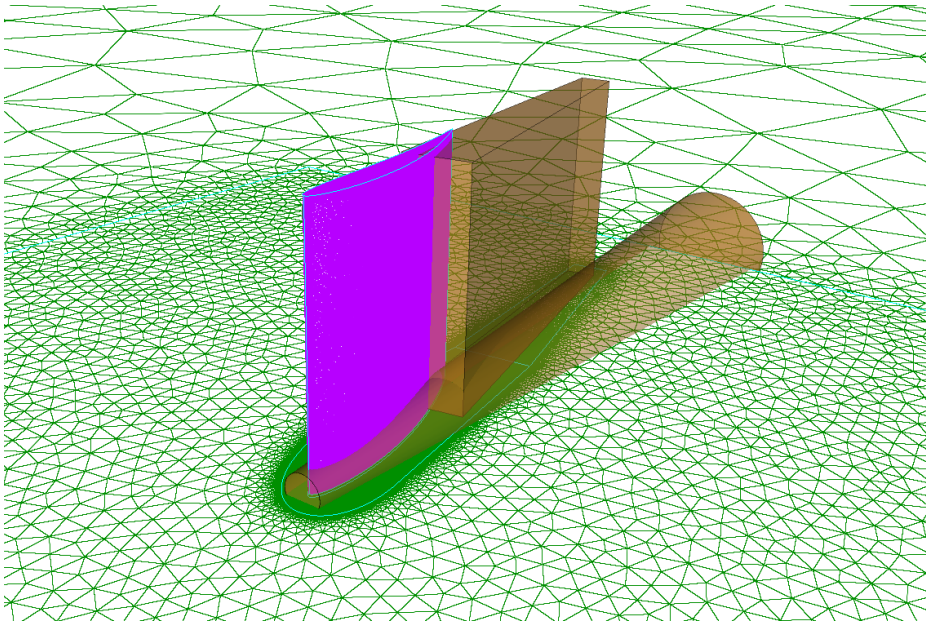

Figure 7.4: Schematic representation of the meshing methodology. The foil surface mesh is shown in pink, with the boundary surface and outer domain surface meshes shown in green and the volumetric refinement zones are shown in orange. The tip of the foil is at the bottom in this figure, hence the high refinement shown on the boundary surface mesh in that region.

FW-H analysis can be seen in Figure 7.3, showing the foil in blue, and the boundary surface

in green with a small gap present between the two. It can be seen that the sampling patch used on the boundary surface has been selected to avoid the sharp edges found at the limit of the boundary surface so that any noise sources generated by the flow interacting with this edge are not captured as this study is focussed on the noise sources within the tip gap.

In order to allow the discretised equations of motion of the fluid to be solved, the volume surrounding the geometries was divided to form a volumetric mesh using proprietary `Pointwise` software. First, solid surfaces of the foil and boundary surface were triangulated and the surface triangles were extruded to yield a prismatic boundary layer mesh. Particular care was devoted to the region between the tip and the boundary surface where poor quality cells had to be avoided to yield a high-quality solution. The remaining volume was then further triangulated to form a tetrahedral mesh with additional refinement around the wake of the foils. The combination of these techniques can be seen in Figure 7.4 for the NACA5510 case.

The convergence of the time-resolved simulations in this part is judged by monitoring the global force coefficients. The simulations are allowed time to reach a steady state where the coefficients vary around a slowly varying mean value. This is assessed by monitoring the mean of each of the coefficients in the three Cartesian directions over the previous 2000 time steps. The time scales for unsteady simulations are typically normalised by using the number of 'flow-throughs', N, given by the characteristic length divided by the mean flow velocity, such that the $N = L/U_\infty$. In practical terms this is akin to the number of characteristic lengths that an object would move through a stationary fluid. The time taken for the simulations to converge in this part was typically of the order of $N \approx 10 - 15$. The sampling time was then limited to $N \approx 3$, such that $t \approx 0.3$s to limit the memory requirements and post-processing time taken, whilst still obtaining enough resolution in the lower frequencies during the frequency domain analysis.

7.3 Flow features

Previous experimental works have included PIV measurements from within the tip gap region to capture the velocity contour and highlight the tip leakage component. Figure 7.5 shows a similar plane taken through the tip gap for the $h/c = 5.0\%$ case coloured by velocity magnitude with flow from right to left, and tip leakage flow due to angle of attack and camber in the upwards direction. Figure 7 from Jacob et al. [49] shows good agreement with both the instantaneous and mean velocities in the gap, giving confidence that the simulations presented are capturing the behaviour of the tip gap flow accurately.

The λ_2-criterion has been used to investigate the flow features in the tip region, and infer the effect of implementing the no slip condition on the boundary surface. Figure 7.6 shows

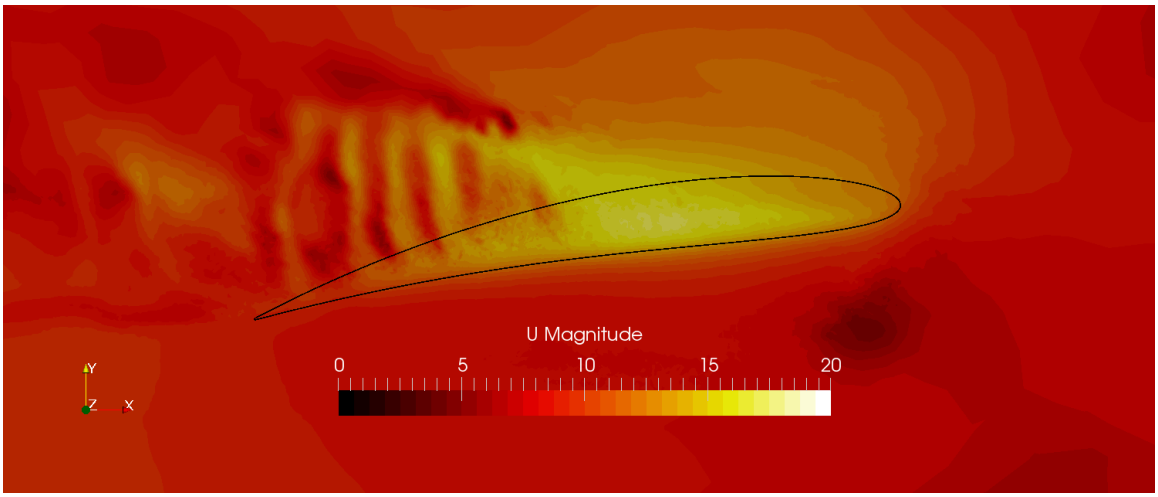

(a) Instantaneous velocity magnitude

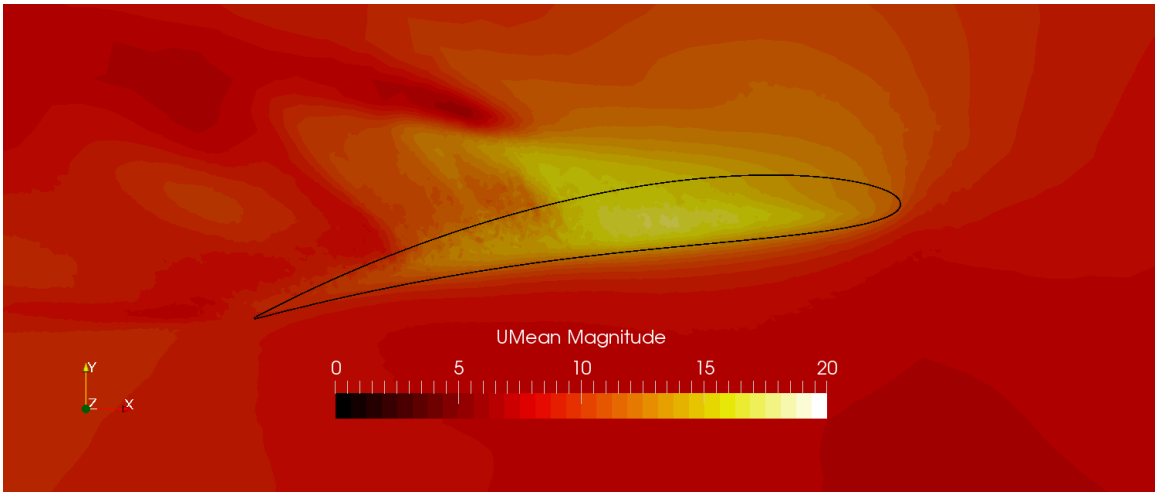

(b) Mean velocity magnitude

Figure 7.5: Velocity magnitude within the tip gap showing good agreement with similar experimental studies [49]

as snapshot from an LES simulation of the $h/c = 1\%$ case, with the contour coloured by vorticity about the x-axis, ω_x to indicate the direction of rotation of the coherent vortices.

It can be seen that the implementation of the no-slip condition on the boundary surface has had a significant impact on the flow features when compared with the study in Part II. The suction side vortex, driven by the tip leakage jet, can be seen forming in red, which in turn generates a counter vortex in blue alongside it. As these vortices convect downstream they can be seen to become unstable and break down. Furthermore, due to the small size of the tip gap, the interaction between the foil and the boundary surface induces a series of horse shoe vortices and countervortices upstream of the leading edge.

Figure 7.7 shows the view of the tip of the foil with the boundary surface is removed along with a schematic representation illustrating the key flow features. The leading edge of the

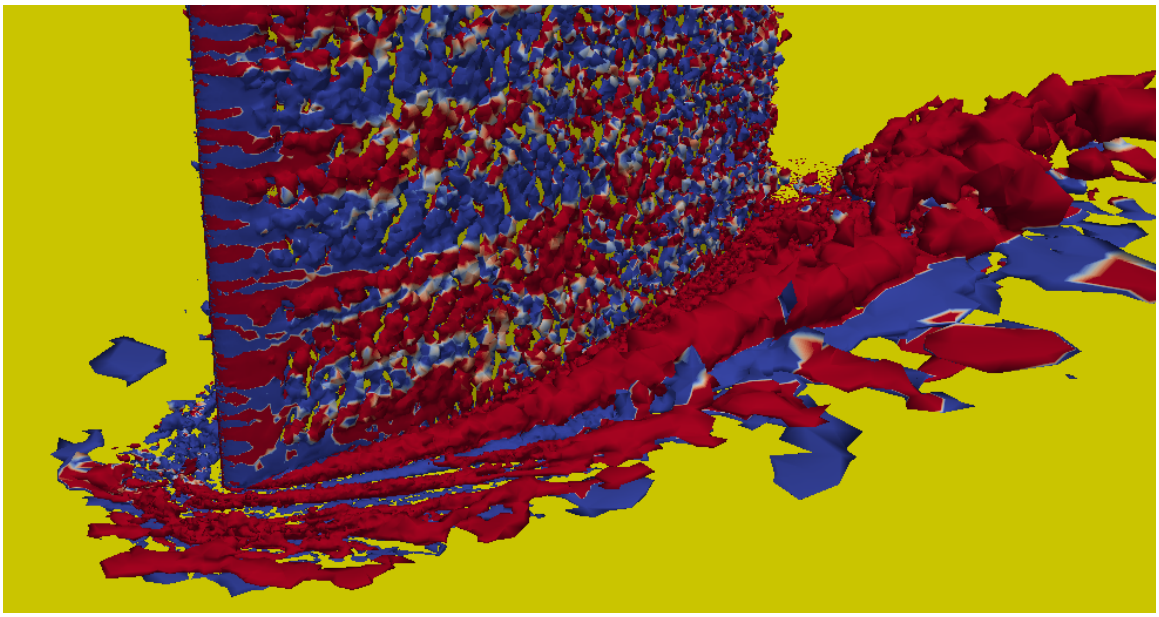

(a) View of the suction side of the foil from the leading edge looking aft illustrating horseshoe vortex system and the formation of the tip leakage vortex.

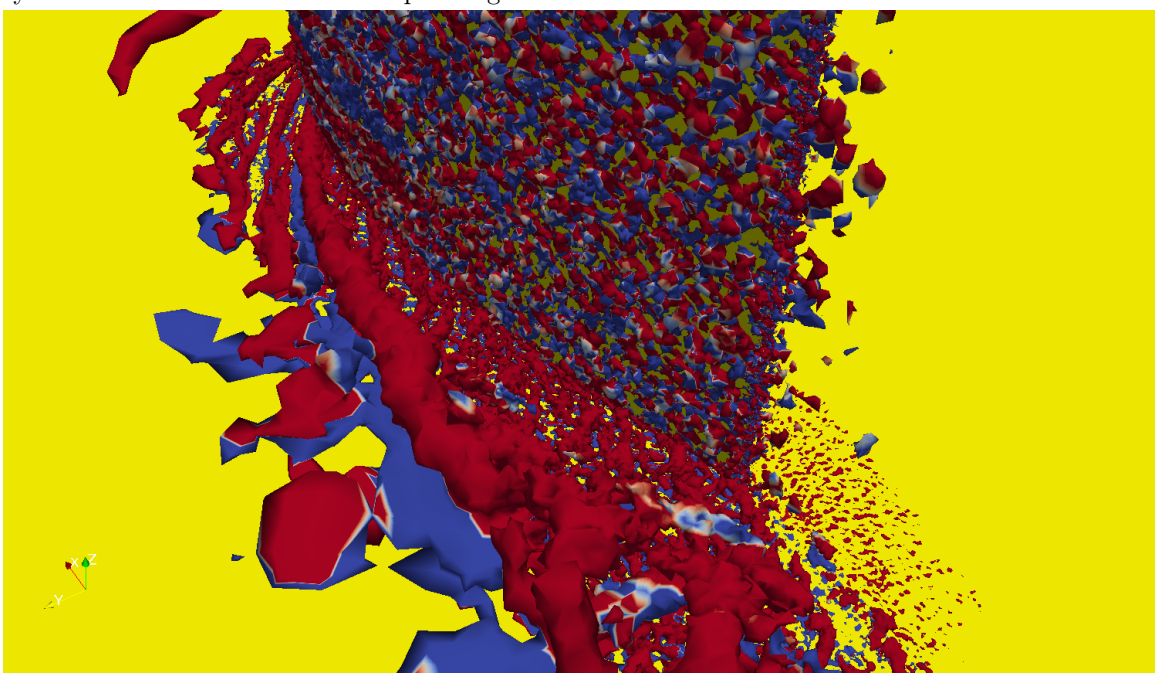

(b) View of the suction side of the foil from the trailing edge looking forward showing the breakdown of the stable tip leakage vortex.

Figure 7.6: Coherent vortical structures produced by the interaction between the tip gap jet and the boundary surface boundary layer illustrated by a contour of λ_2.

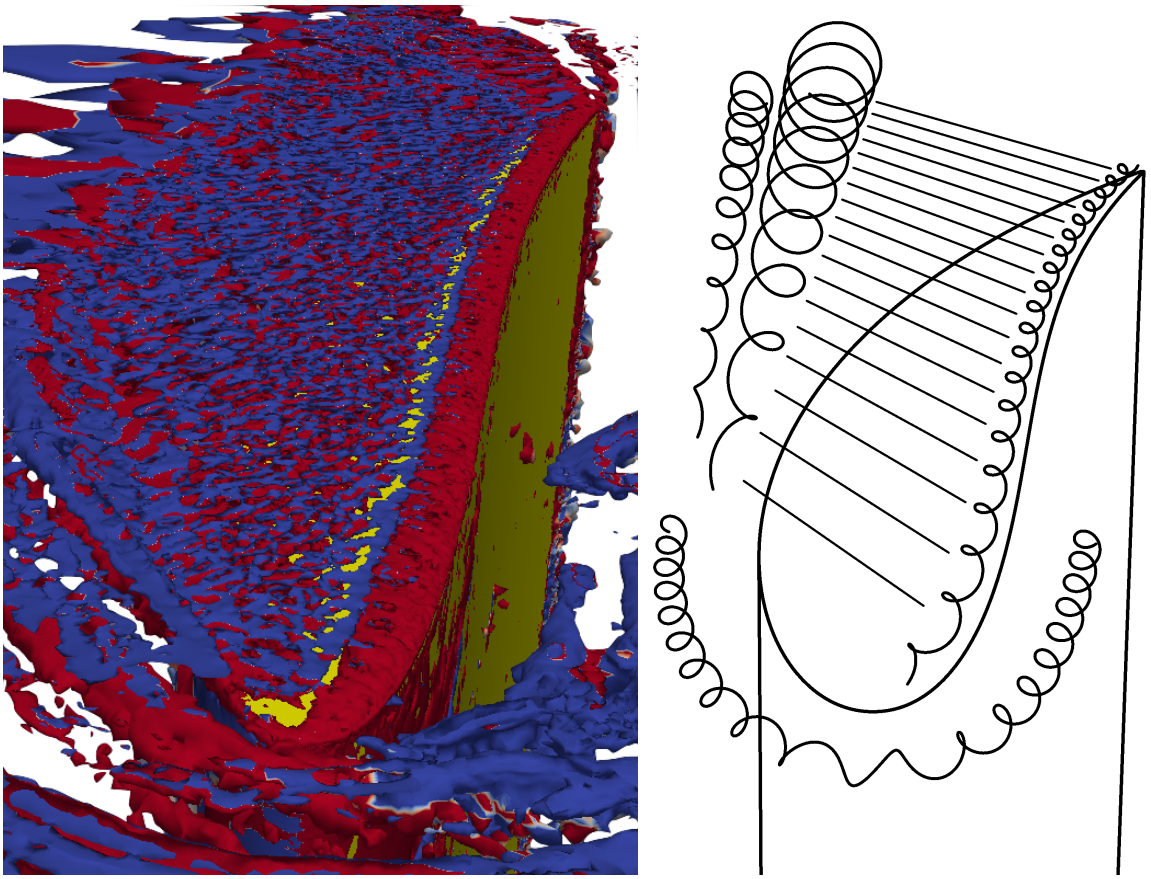

(a) Tip gap flow with iso-contour of λ_2 **(b)** Schematic sketch of flow features

Figure 7.7: Schematic representation of the flow features within the tip gap region of the aerofoil, looking towards the leading edge and into the tip gap, as in Figure 7.7a. The pressure side is on the right, the suction side on the left, with flow into the page, causing tip leakage from right to left, over the tip of the foil.

foil is in the foreground at the bottom of the image, with the trailing edge in the background at the top. The concave camber of the pressure side of the foil can be seen on the right, along with the vortex caused by its sharp edge at the tip. It can be seen that this vortex has a fairly constant size, and appears stable along the chord of the foil. As the flow moves through the gap (from right to left in the image) there is a strong sheet of vorticity, which in turn creates counter vorticity by interacting with the boundary surface. This behaviour is illustrated by the mix of red and blue colouring in Figure 7.7a. It is expected that in these regions where there are strong vortex structures close to a solid surface, as illustrated by the λ_2 contour, that strong pressure fluctuations will be present on that surface.

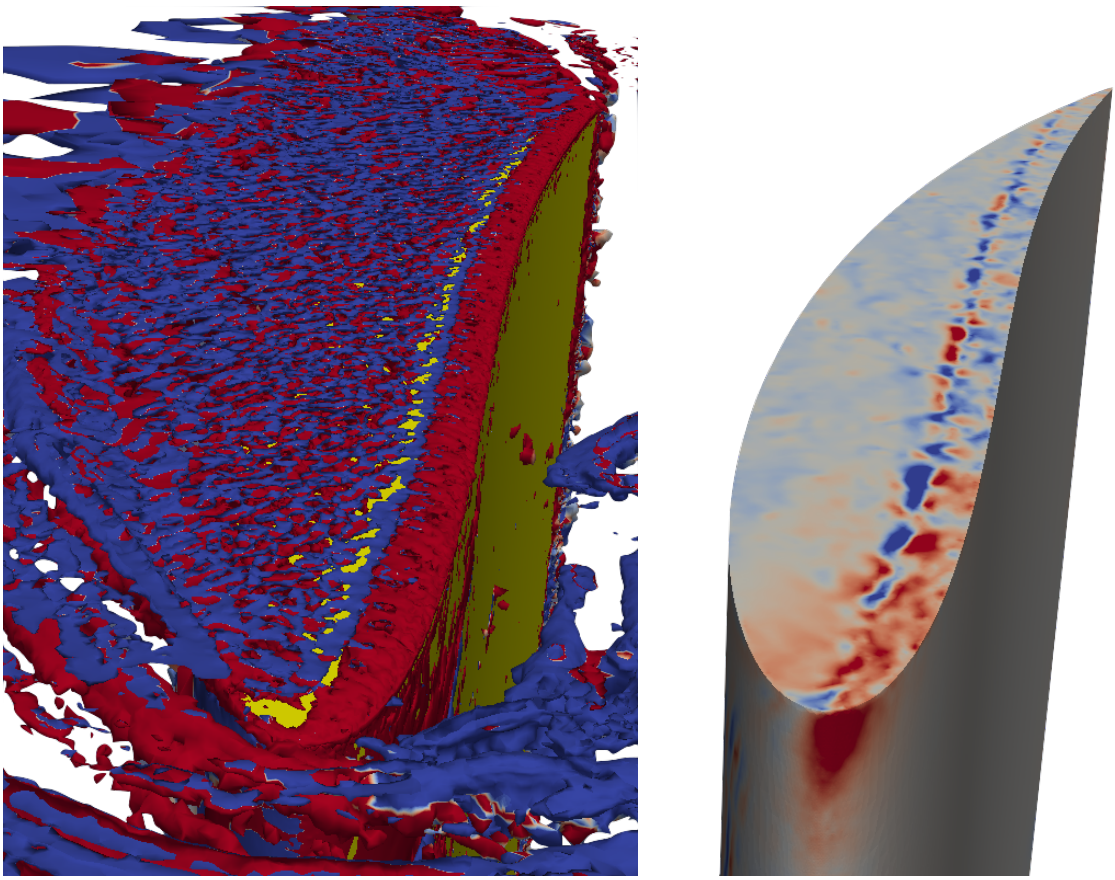

(a) Tip gap flow with iso-contour of λ_2

(b) Fluctuating pressure component p' on the foil tip

Figure 7.8: Fluctuating pressure, p' on the tip of the foil showing similar patterns to the coherent structures identified by the λ_2 contour.

7.4 Surface pressure fluctuations

Following Equation 4.4a, the fluctuating pressure on the surface of the solid faces can be visualised by subtracting the mean pressure, p_0, from the instantaneous pressure, p, on each face of each surface.

The colouring for this analysis, shown in Figures 7.8 and 7.9, is limited to ± 10 Pa so that areas with very small fluctuating amplitude show as grey to highlight the high amplitude fluctuations. Figure 7.8 shows this visualisation from the same angle as Figure 7.7a and it can be seen that the stable vortex which forms on the tip near the pressure side edge causes strong surface pressure fluctuations. The sheet vorticity can be seen to also cause fluctuating pressures on the surface but at a lower amplitude, indicated by the light shades of colour.

Similarly, Figure 7.9 shows the same view angle as Figure 7.6 with strong pressure fluctuations

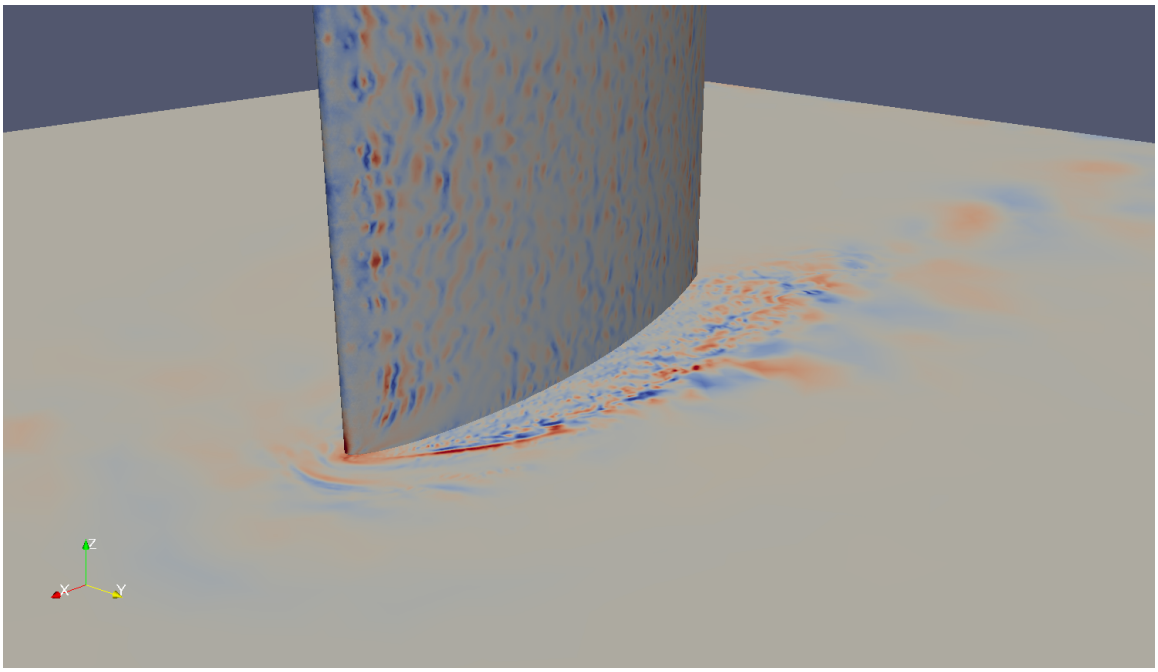

(a) View of the suction side of the foil from the leading edge looking aft illustrating horseshoe vortex system and the formation of the tip leakage vortex.

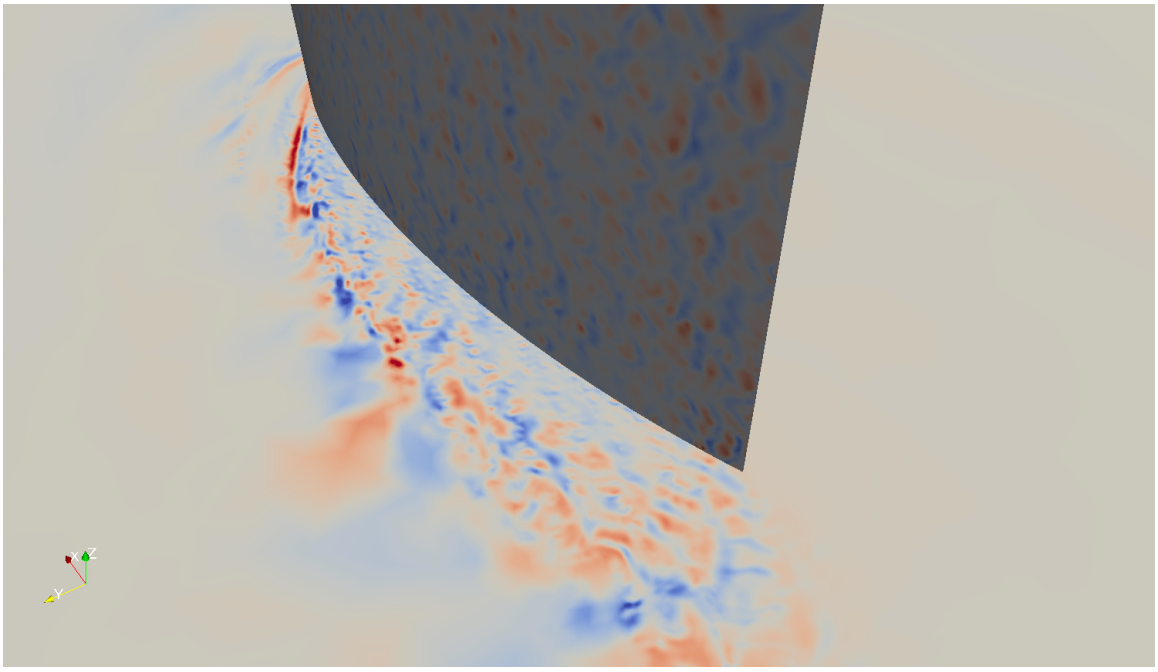

(b) View of the suction side of the foil from the trailing edge looking forward showing the breakdown of the stable tip leakage vortex.

Figure 7.9: Coherent vortical structures produced by the interaction between the tip gap jet and the boundary surface boundary layer illustrated by a contour of λ_2.

seen on the surfaces where the λ_2 contours occur. The strongest of these pressure fluctuations can be seen on the boundary surface near the leading edge of the foil, where the vortex is

smallest and most concentrated. As the vortex moves downstream it can be seen to grow in size, fed by the tip leakage jet, and eventually become unstable and brake up. This behaviour can be seen in the fluctuating surface pressure as they become more dispersed and reduce in amplitude further downstream.

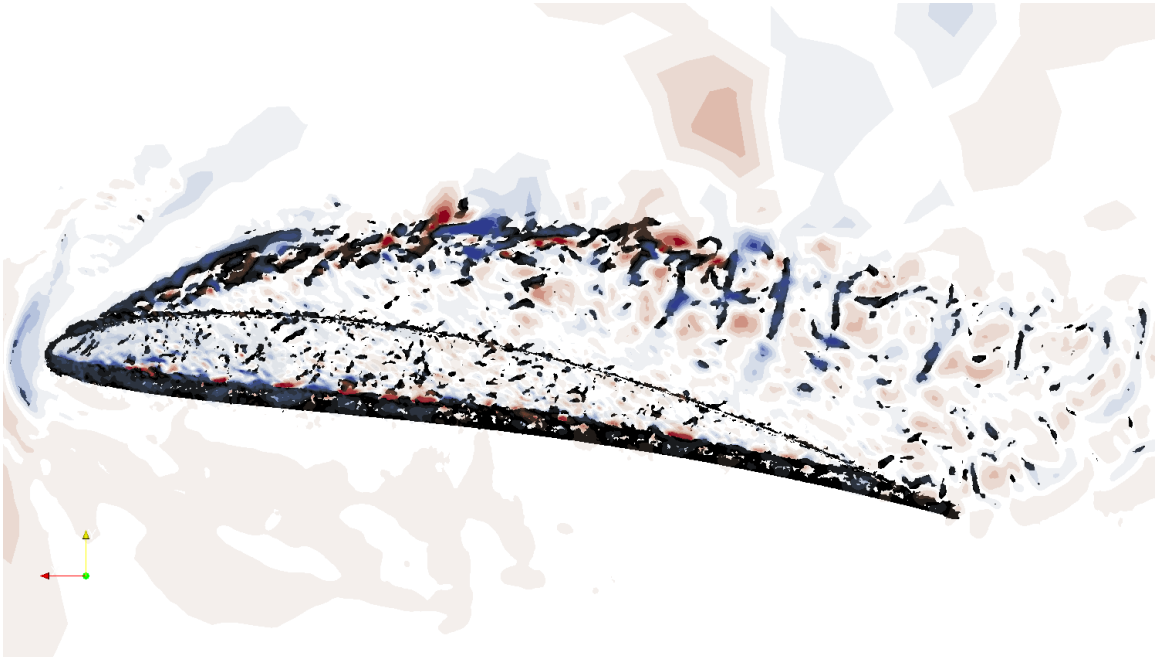

Figure 7.10: Pressure fluctuations, p' with coherent vortex structures shown by λ_2 contour in black.

If the λ_2-criterion and the p' analyses are combined it can be seen that the areas which experience the strongest pressure fluctuations are those nearest the strongest vortex structures, as in Figure 7.10. This visualisation is achieved by making the small amplitude pressure fluctuations transparent for the p' analysis on the boundary surface, allowing a view through the boundary surface, into the gap. The λ_2 contour is set to a higher value of 10^5 and made opaque and black, which can be seen forming on the pressure side edge of the foil tip surface, as well being ejected from the gap by the tip gap jet. The same transparent p' analysis is used on the foil, which can be seen behind the black contour, and the high amplitude pressure fluctuations can be seen to follow the outline shape of that contour.

7.5 Far-field acoustic predictions

The Ffowcs-Williams Hawkings (FW-H) acoustic analogy was used to predict the far-field noise based on the assumption that the incompressible flow solutions are directly the sources of sound and that edge scattering, such as that which occurs for trailing edge noise, is not a significant factor. The integration surfaces, S, chosen were on the solid surfaces of the

foil and table. For this analysis they were investigated separately to infer their individual contribution to the overall far-field noise.

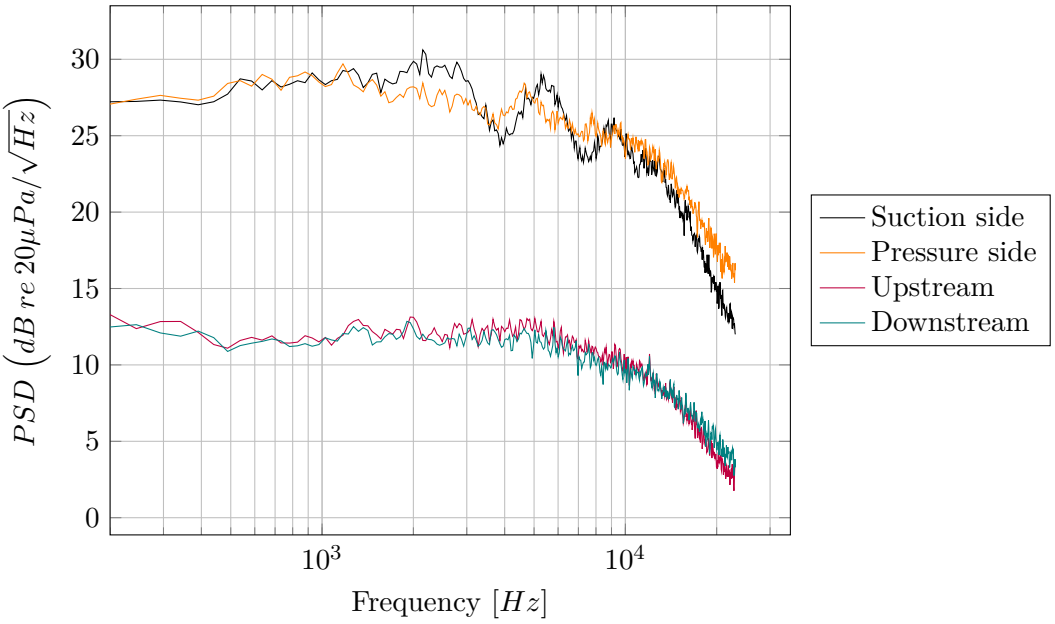

Figure 7.11: Farfield PSD from the foil only, for all receiver locations.

Figure 7.11 shows the power spectral density (PSD) for the four receivers with contributions from the foil surface only. It can be seen that the pressures of the transverse receivers are much greater than those receivers in the stream-wise direction. This is to be expected due to the directionality of a dipole source, with the angle between the radiation vector and the surface normal being much smaller for transverse receivers.

Figure 7.12 shows the PSD for the four receivers with contributions from the boundary surface only. It can be seen that the pressure are similar for all receivers, and is far lower than the power contribution from the foil surface. Again, considering the directivity of the dipole, with the angle of the receiver and normal vector nearing 90°, it is expected for the contributions from the boundary surface to these receivers to be very small. It is suggested that the higher frequency components, $f > 3\,kHz$ in Figure 7.12, are likely to be due to numerical noise as the pressure fluctuations at the receiver become small enough to be dominated by numerical precision.

Further investigation of the foil surfaces can be achieved by applying the FW-H analogy to a subset of the faces on the patch. This subdivides the foil patch into two discrete elements, comprising of the square tip surface, and the lifting surfaces and trailing edge. This subdivision splits the foil into elements which had normal-directions in the same plane as the receivers (the lifting surfaces and trailing edge) and those with normal-directions which are nearly orthogonal to the receivers (the tip surface).

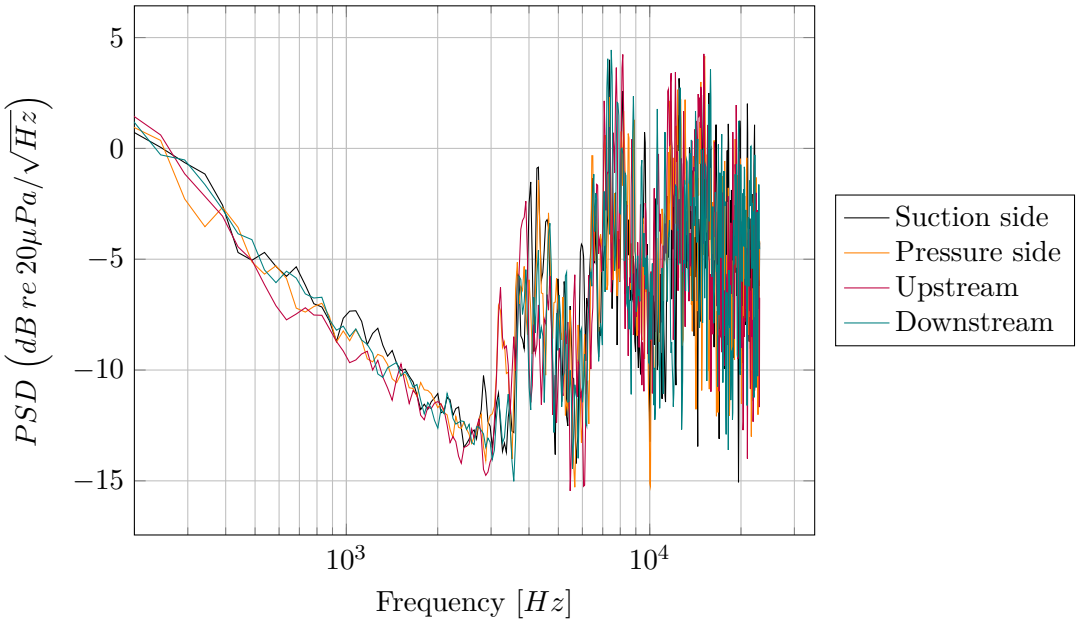

Figure 7.12: Farfield PSD from the boundary surface only, for all receiver locations.

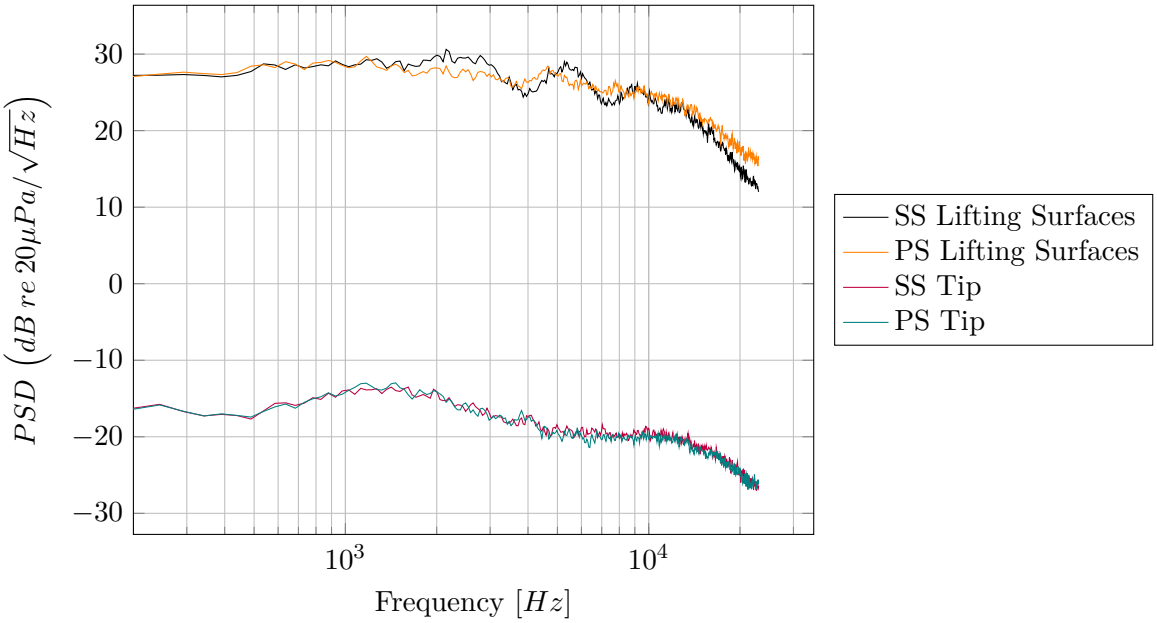

Figure 7.13: Farfield PSD from different parts of the foil, for all receiver location.

Figure 7.13 shows the far-field acoustic PSD for the transverse receivers for this split patch analysis. It can be seen that the square tip surface has little contribution to the far-field due again to the directivity of the dipole source. It can be seen that the other surfaces of the foil, whose normal directions are in the same plane as the receivers contribute much higher power levels to the acoustic pressures observed in the far-field.

7.6 Effect of varying tip gap height

7.6.1 Performance characteristics

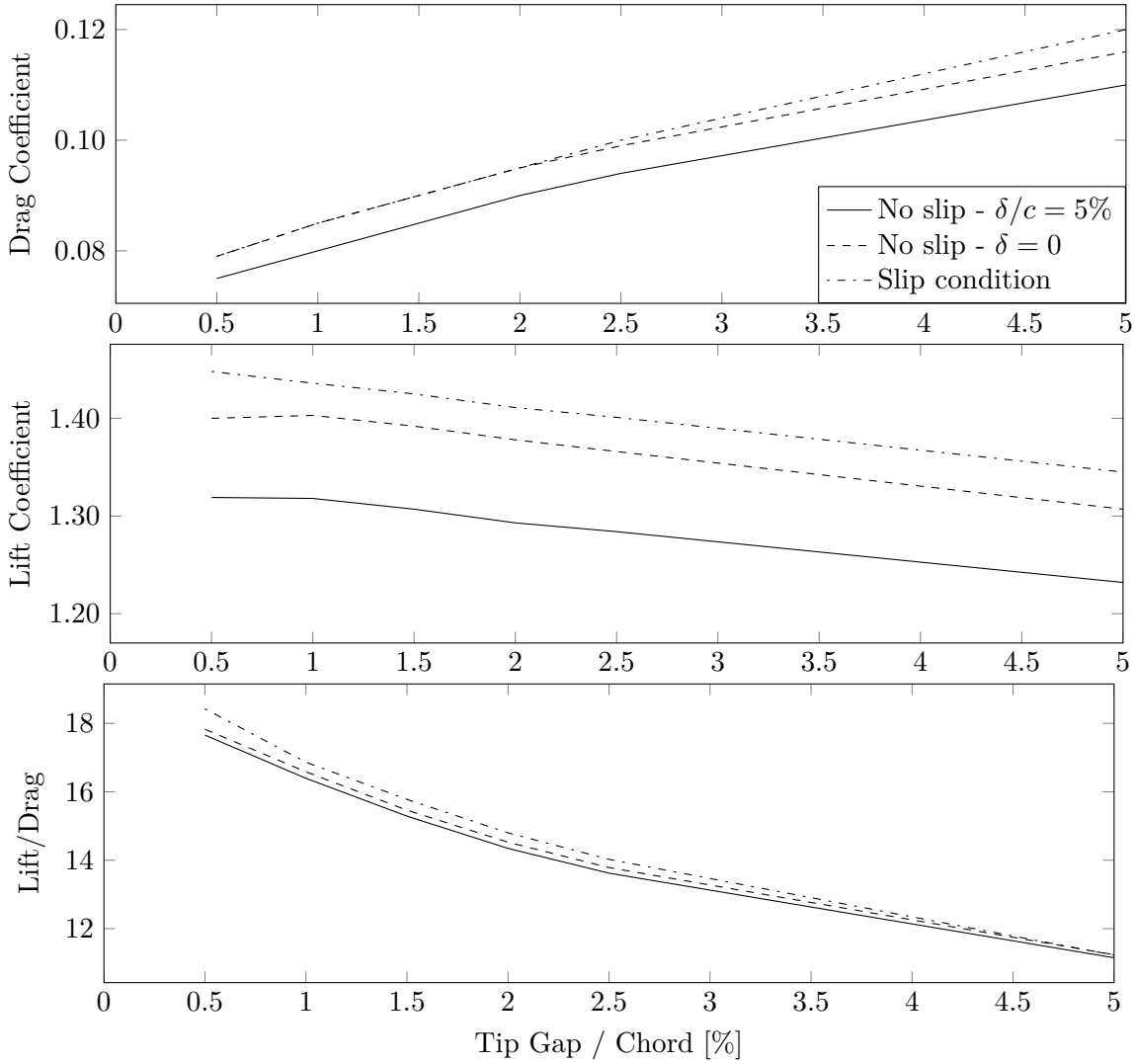

Figure 7.14: Variation of performance coefficients with tip gap on NACA5510 foil for various simulation conditions.

Figure 7.14 shows the lift and drag performance of the foil with varying tip gap. It can be seen that both performance attributes are improved by the reducing tip gap, but C_L seems to have reached a limit of improvement at 0.5% when a no-slip condition is implemented on the boundary surface. This is likely due to the reduction in the strength of the tip vortex on the suction side of the foil, which therefore reduces vortex induced lift. This effect is occurring at all tip gaps investigated, and it seems the loss of vortex induced lift begins to dominate the increase in lift from the overall pressure field at this gap size.

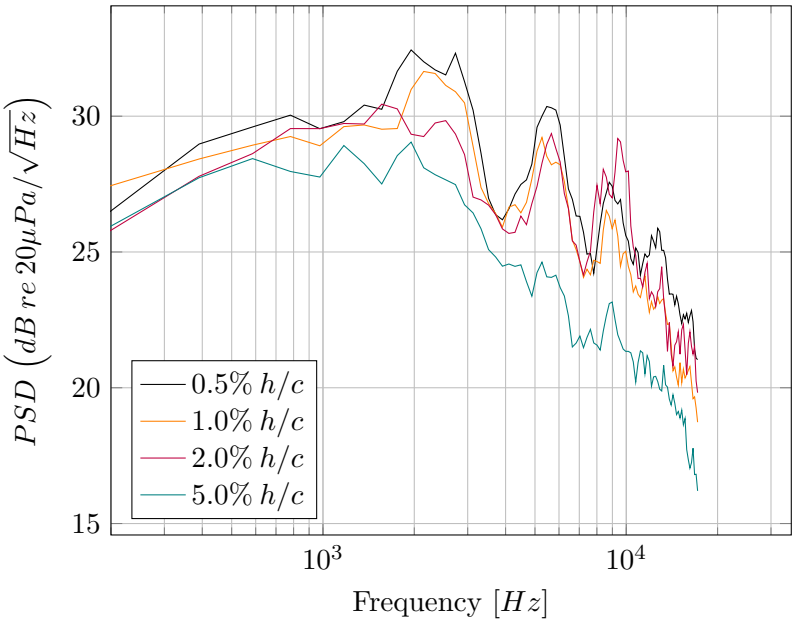

Figure 7.15: Effect on far-field acoustic radiations of varying tip gap.

For C_D it can be seen that at the larger gap sizes there is a difference between all three cases, however at smaller gap sizes, $h/c < 2\%$, C_D is roughly equal for the slip condition and the no-slip without the boundary layer prescribed. For C_L it can be seen that at large tip gaps the gradient is similar but has a constant offset caused by the implementation of the no-slip condition.

The introduction of the boundary layer profile for the boundary surface on the inlet can be seen to produce a constant offset in both lift and drag when compared with the no-slip case without the boundary layer profile prescribed. This is caused by reducing the effective span of the foil due to the reduced inflow velocity over the tip region of the foil which is immersed in the boundary layer of the boundary surface.

7.6.2 Acoustic radiation

The FW-H analogy was used to make predictions of the far-field radiated noise produced by the four different tip gap arrangements under investigation. This analysis used the foil surfaces only, and the receiver location was chosen to be on the suction side, following the analysis in the previous sections showing that this had the highest pressure levels and strongest characteristic peaks.

Figure 7.15 shows the PSDs of the pressure spectra at the suction side far-field receiver. It can be seen that the peak shown at $f \approx 2 - 3kHz$ is seen to increase in strength with a reducing tip gap size. This appears counter intuitive following the literature which suggests

that smaller tip gap sizes are beneficial regarding far-field noise. In order to identify the source regions which were responsible for the peak and explain its relationship with tip gap size, the foil was further subdivided within the post-processing analysis and it became clear that this peak was not caused by the tip region of the foil but the whole span. Chapter 8 discusses this analysis in depth, along with a thorough investigation into the potential noise sources, and Chapter 9 investigates the influence of the tip gap height on these sources.

7.7 Summary

This chapter has presented the use of a more realistic arrangement than used in the intial study in Part II. This development has included the effects of a no-slip condition being implemented on the boundary surface, increased foil camber and decreased foil thickness, and smaller tip gap sizes. The implementation of the no-slip condition on the boundary surface has been shown to:

- increase the complexity of the tip gap flow by causing extra vorticity as the unsteady structures interact with the boundary layer
- produce a horseshoe vortex at the leading edge of the foil as the tip gap is reduced which combines with the tip leakage vortex to form a large unsteady region which convects downstream
- reduce the effective tip gap size by limiting the volume flow rate through the gap and this is reflected in the lift and drag coefficients.

With the reduction in tip gap size from previous simulations in Chapter 6 and the inclusion of the no-slip condition on the boundary surface, the behaviour of the vortex which forms over the pressure side edge is seen to change. The flow over the pressure side edge has been shown to remain attached and convect along the tip edge downstream. As more energy is fed into the pressure side edge vortex smaller structures are shed through the tip gap, producing strong pressure fluctuations on the tip surface. The reduced tip gap causes the shedding of the tip leakage vortex towards the leading edge of the foil as predicted in Chapter 6 and therefore stopping it from causing increased trailing edge noise.

Chapter 8

Noise source mechanisms

8.1 Introduction

The previous chapter revealed that a reduction in tip gap produced an increase in the far-field radiated acoustic pressures, and revealed details of the unsteady flow structures within the tip gap region. This chapter will present further analysis on the far-field radiated pressures by subdividing the foil surfaces to infer the most important regions of the foil regarding noise generation. The flow features will be investigated and a taxonomy of noise sources in the tip gap region is proposed, highlighting the mechanisms which are hypothesised to be responsible for noise generation. This chapter will focus on the reference case discussed in Chapter 7, in which $\alpha = 10°$, $h = 10$ mm, $U_\infty = 10$ m/s and Re=6.6×10^5.

8.2 Noise source identification

In order to infer the regions of the aerofoil responsible for the far-field noise, the surfaces, S, used for the acoustic analogy in Equation 4.19 were further subdivided during post-processing. The analogy is applied to each individual section to predict the individual contributions to the far-field pressure. This is a legitimate approach if the sources are essentially incompressible such as in the case of localised turbulent flow which cannot scatter at boundaries to produce sound. In this case, the surface of computation may be sub-divided as long as the individual integration surfaces are not smaller than the turbulence length-scale of the flow [107]. This was done in both the span-wise and chord-wise directions and a schematic representation of these divisions is shown in Figure 8.1.

Figure 8.2a shows the contributions to the overall noise spectra of the span-wise subdivisions of the aerofoil. The aerofoil was split into 10 equal sections from root to tip. It can be seen that the tip section has the highest contribution, but with $< 4dB$ difference between it and

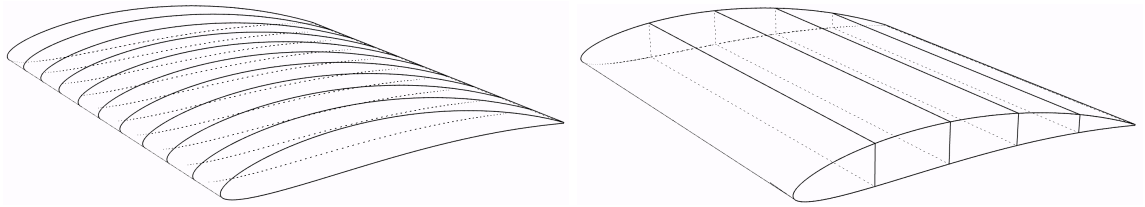

(a) Ten span-wise sections **(b)** Five chord-wise sections

Figure 8.1: Schematic representation of the subdivision of the foil surface in the span-wise and chord-wise direction.

the other sections of the foil. This implies that while the tip gap region provides a higher acoustic radiation than the other sections individually, for this case the noise of the whole foil is more significant that the noise from the tip region. The increase observed for the tip section is likely caused by the formation of the tip leakage vortex, as well as the interaction between the tip region and the no slip condition on the boundary surface resulting in the formation of a horseshoe vortex as seen in Chapter 7. Both tip-flow features cause increased pressure fluctuations on the surface of the foil in that region. excerpt

Figure 8.2b shows the far-field acoustic pressure contributions from five equal chord-wise subdivisions of the aerofoil. It can be seen that the front two sections contribute the most to the far-field acoustic pressure, with section 2, i.e. $20 - 40\%$ chord, providing the more characteristic humps seen in Figure 7.11. This result is counter-intuitive as it would be expected for the trailing edge to be the dominant noise region, especially given the minor difference between the tip section and other span-wise subdivisions. This confirms the recommendations made by Glegg and Devenport [107] that noise mechanisms such as trailing edge noise can not be predicted using incompressible solvers as the scattering mechanism requires compressibility to be accounted for.

Trailing edge noise is generated when a turbulent boundary layer passes over a sharp, straight trailing edge. The turbulence in the boundary layer causes a scattering of the vorticity into coherent surface pressure fluctuations which propagate efficiently to the far-field. This scattering mechanism relies on the compressibility of the fluid to propagate the acoustic wave upstream. The flow speed is of a very low Mach number ($M \approx 0.03$) and so incompressibility can be assumed for solving the fluid flow, however, the scattering mechanism still relies on the compressibility [107]. There are methods which can predict trailing edge noise based on the hydrostatic pressure fluctuations close to the trailing edge [122]. This is done using a transfer function to account for the scattering mechanism and infer the far-field radiation of the noise. However these methods are based on semi-infinite flat plates with trailing edges which are perpendicular to the flow. The current geometry shows turbulence being shed from a sharp edge which is curved and at an angle to the incoming flow, meaning empirical and analytical models are unlikely to be able to predict the scattering accurately.

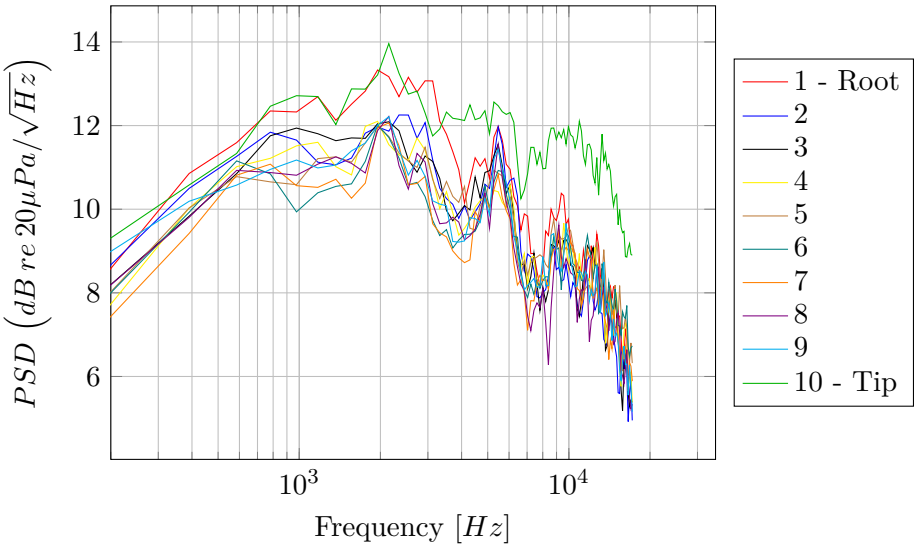

(a) Span-wise sections

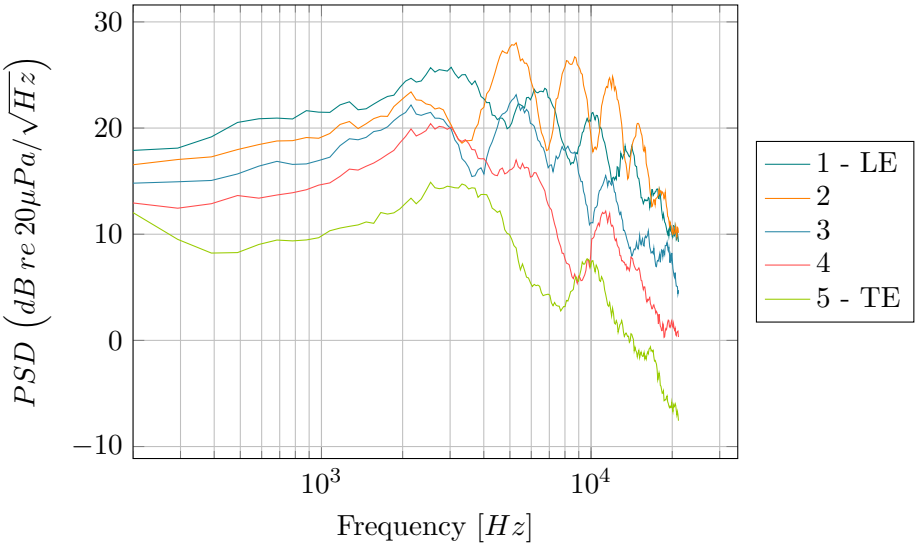

(b) Chord-wise sections

Figure 8.2: Results of the acoustic analogy used on different subsections of the foil.

The combination of incompressible solver with an acoustic analogy adopted here will not be sufficient to capture trailing edge noise as discussed in Chapter 4. The front 40% of the foil is shown to be responsible for the highest contributions to far-field noise. The high pressure fluctuations at the front of the foil are likely caused by the transition of the boundary layer from laminar to turbulent which occurs near the leading edge. Due to the straight leading edge this transition occurs at the same location along the span, increasing span-wise coherence in the pressure fluctuations, meaning they propagate more efficiently than other areas of the foil where the turbulence is more fully developed and less coherent. The location of this transition can be seen by the λ_2 visualisations in Figure 7.6, and the

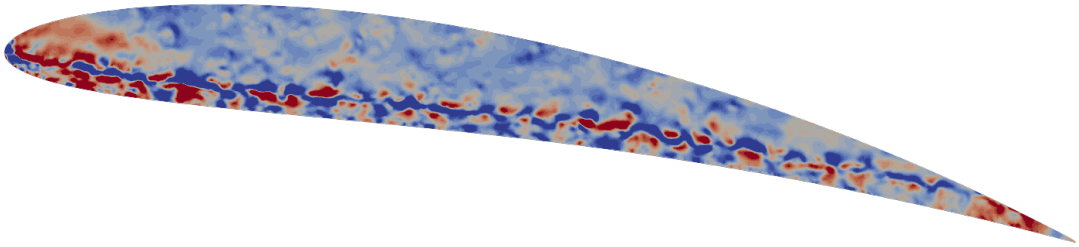

Figure 8.3: Instantaneous surface pressure fluctuations on the tip of the foil which may experience a scattering effect, similar to those at the trailing edge, as they are shed over the suction side edge.

effect this has on surface pressure fluctuations can be seen in the p' analysis in Figure 7.9.

Investigation of the flow features using the surface pressure fluctuations and λ_2 analysis presented here leads to the hypothesis that the noise production mechanisms in the tip gap region are similar to those at the trailing edge, involving the scattering of turbulent structures by the tip edge. The scattering mechanism on the tip edge is likely to create acoustic waves which travel along the suction surface of the foil, creating a source which is not acoustically compact and therefore will not be captured by the incompressible solver.

8.3 Taxonomy of suspected noise source mechanisms

Figure 8.3 shows the instantaneous pressure fluctuations on the tip of the aerofoil, while Figure 8.4a shows the flow features in this region using the λ_2 criterion and Figure 8.4b shows a schematic sketch of the critical features. The sketch shows four distinct mechanisms which may contribute to the noise generated by the foil in the tip gap region:

1. The vortex which forms over the pressure side edge of the tip is stable in its position, and convects down stream along the tip edge towards the trailing edge of the foil. Figure 8.3 shows the strong pressure fluctuations associated with this vortex, which are eventually shed over the suction side edge of the tip, near the trailing edge of the foil. It would be expected for these structures to scatter over the suction side edge of the foil generating an efficient noise source which may propagate to the far-field.

2. In the presence of small tip gaps, such as the 1% gap presented, the physical size of the pressure side edge vortex is limited. As more energy is fed into the vortex by the tip leakage flow, it sheds smaller vortex structures through the tip gap, similar to a sheet of vorticity, before shedding over the suction side edge. It would be expected for scattering of these structures to occur over this edge and generate noise, similar to flows over backward facing steps [136] [137] [138] [139] [140]. Typically the backward

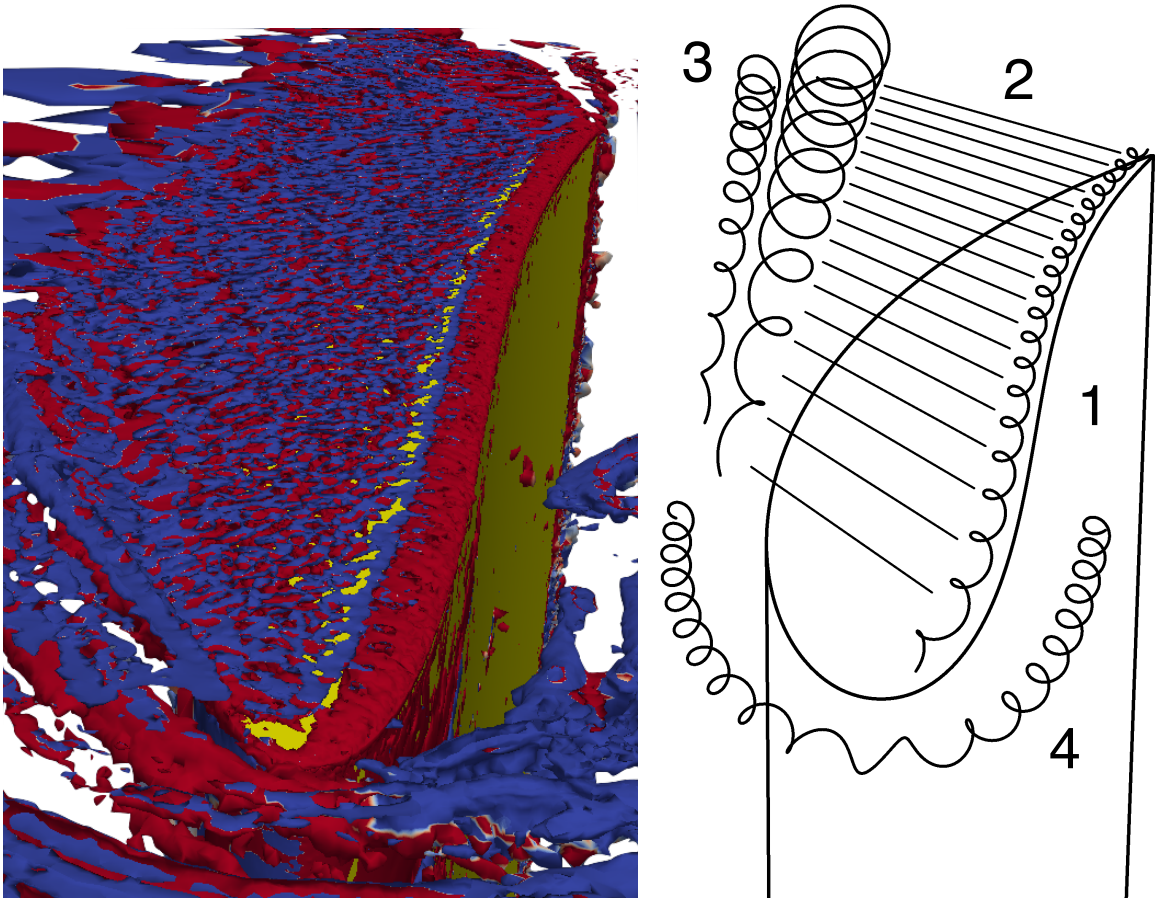

(a) Tip gap flow **(b)** Schematic sketch

Figure 8.4: Schematic representation of the flow features within the tip gap region of the aerofoil, looking towards the leading edge and into the tip gap, as in Figure 7.7a. The pressure side is on the right, the suction side on the left, with flow into the page, causing tip leakage from right to left, over the tip of the foil.

facing steps investigated in the literature have an aspect ratio close to 1, such that their depth is roughly equal to their height, and there is typically no surface restricting the flow above the step. The flow structures which form over the top of the step are therefore large compared with the step size, and the back face of the step is small. In the current arrangement the length ratios involved are quite different, with small gap height compared to step depth and large back face compared to the gap height. This presents a large surface over which the acoustic waves can be scattered. The scattering of vorticity over large backward facing steps such as this has not been covered in the literature.

3. The tip leakage flow drives a stable tip leakage vortex (TLV), which in turn generates a counter vortex due to the no-slip condition of the boundary surface. These structures are consistant with similar invesitgations of aerofoils with small tip gaps carried out

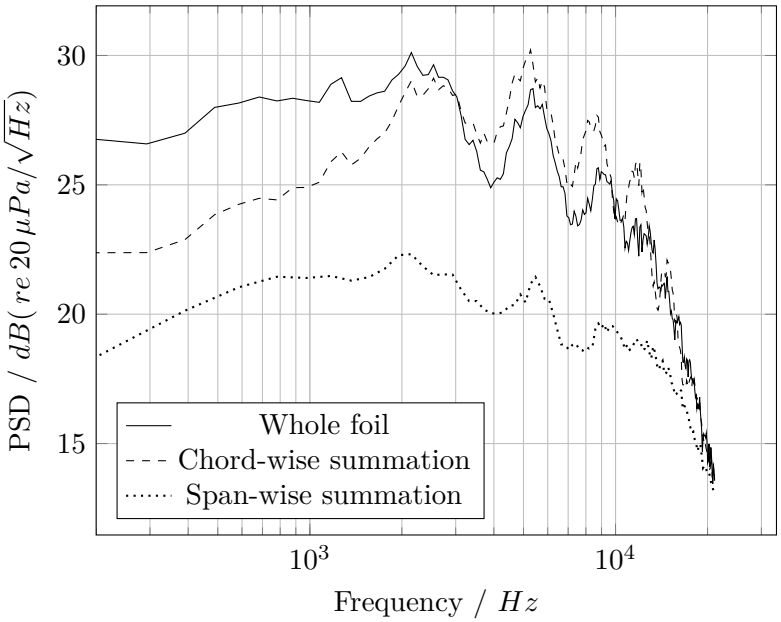

Figure 8.5: Summation of the strips used in the FW-H analysis suggests that a span-wise coherence exists, illustrated by the much lower pressure levels of the sum of the strips compared with the whole foil. The similarity between the summed chord-wise strips and the whole foil confirms that the trailing edge noise caused by acoustic scattering is not being captured.

by [9], [20] [14]. The TLV interacts with the duct boundary layer and produces a large region of strong vorticity and therefore likely quadrupole sources [56]. However, the very low Mach numbers of interest in the marine environment suggest that this is unlikely to be an efficient source for far-field propagation. These structures will have implications for any solid boundaries downstream such as stator blades, causing turbulence interaction noise, and the trailing edge of the duct in a ducted propeller, causing increased trailing edge noise from the duct. These considerations are beyond the scope of this investigation and so have not been investigated further.

4. If the tip gap is reduced sufficiently a horseshoe or necklace vortex forms due to the interaction between the orthogonal wall and blade surfaces. On the pressure side of the foil this vortex becomes part of the system of vortices driven by the tip leakage flow and therefore away from the foil. On the suction side this vortex is broken down and drawn through the gap by the tip leakage flow potentially having a limited impact on the noise production of the foil as it interacts with the tip edges.

Due to the limitations in the incompressible solver in capturing the vorticity scattering mechanism, the noise generated by these tip flow features will not be adequately captured, and so the far-field noise predictions may be significantly under predicted.

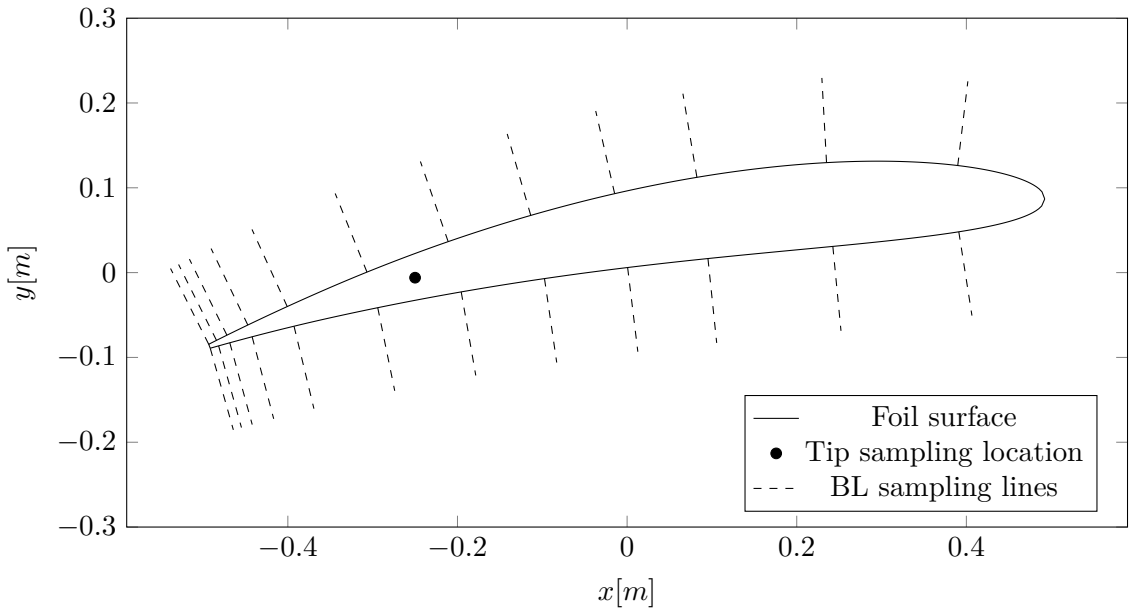

Figure 8.6: Boundary layer sampling locations.

8.4 Noise sources captured by present implementation

As discussed in previous sections in this Chapter, the current implementation of an incompressible solver is not capable of capturing the scattering mechanisms which might dominate in the aerofoil configuration here with turbulent flows being shed over sharp edges. The far-field acoustic pressures were found to contain peaks in the pressure spectra, and the frequencies of these peaks varied for different chord-wise sections of the foil. This further confirms that the far-field pressures are unlikely to be caused by scattered turbulence, as this causes the scattered acoustic wave to radiate from the entire foil surface, and so dividing the foil into distinct sections would be unlikely to show different characteristic frequencies from different regions of the foil.

Figure 8.5 shows the comparison of the summations of the far-field pressure spectra of the chord-wise and span-wise sections of the foil with the far-field pressure spectra radiated from the whole foil surface. It can be seen that the summation of the chord-wise strips shows good agreement with the far-field noise predictions made when the whole foil was used. This suggests that there is little chord-wise coherence on the foil surface, confirming that acoustic waves scattered upstream by the trailing edge are not present. The pressure spectra given by the span-wise summation can be seen to be significantly lower than that of the whole foil, suggesting that there is coherence in the span-wise direction.

If the scattering of turbulence is not being captured then the acoustic radiation predicted by the FW-H analogy relies on the hydrodynamic surface pressure fluctuations which are dependent on the turbulent boundary layer properties. It has been discussed in Chapter

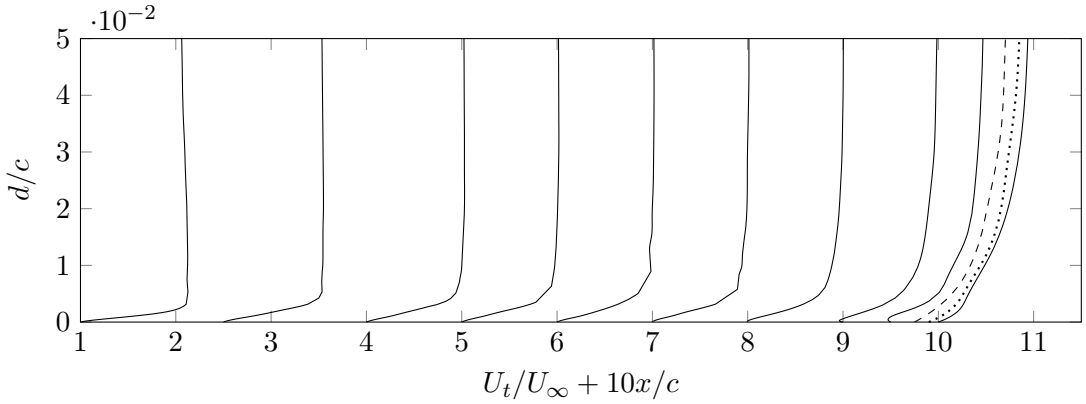

Figure 8.7: Boundary layer profile development along the suction surface of the foil at mid-span for $h/c = 1.0\%$.

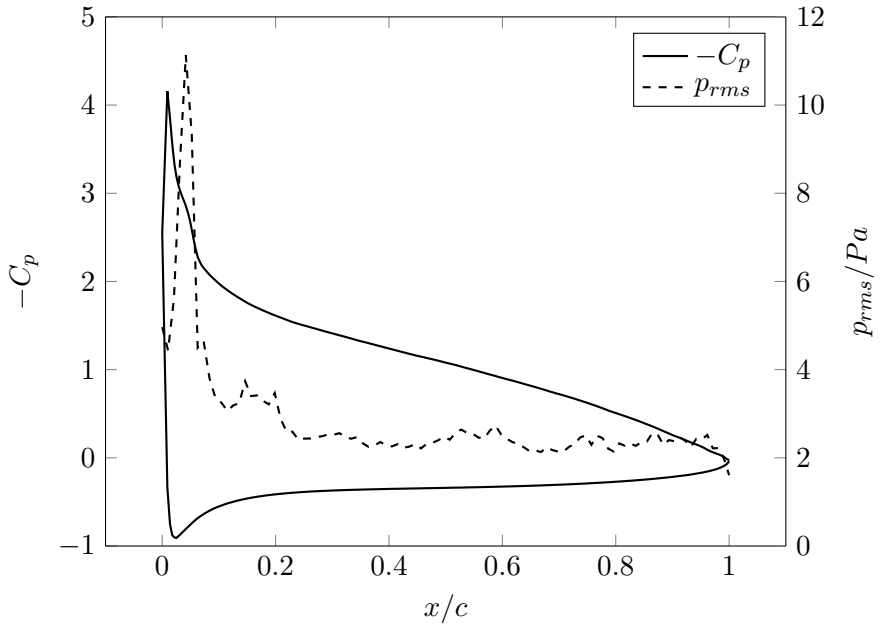

Figure 8.8: Comparison of C_p distribution and p_{rms} at midspan for $h/c = 1\%$ case.

3 that the accurate simulation of turbulent boundary layer transition using LES is very difficult and would require significantly increased resolution of the mesh on the foil surface. Capturing transition is not the primary objective in the current work and so the mesh was designed to prioritise the tip gap resolution to maintain computational affordability, which has also been discussed in Chapter 3. The result is that the accuracy of the frequency content of the turbulent boundary layer in the presented simulations is likely to be limited.

To assess the development of the boundary layer over the surface of the foil, the mean velocity was sampled along the chord at midspan with the sampling locations following Greschner et al. [13] at $x/c = 10$, 25, 40, 50, 60, 70, 80, 90, 95, 97.5, 99 and 100 % as shown in figure 8.6. Figure 8.6 also shows the point on the tip surface where the pressure was sampled to assess

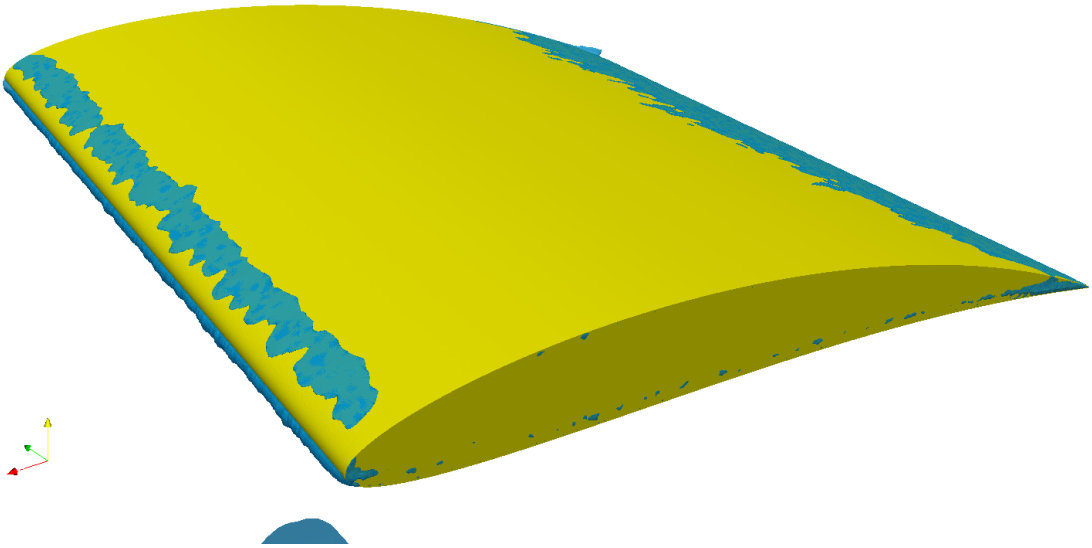

Figure 8.9: Areas of localised flow separation shown using a contour of $U_x = 10^{-5}\ m/s$, shown in blue, to identify regions with an upstream flow velocity.

the frequency content of the surface pressure fluctuations in the tip gap. The impact which the tip gap has on the surface pressure fluctuations on the tip will be discussed in detail in Chapter 9. It can be seen that the sampling lines are perpendicular to the foil surface and the mean velocity was sampled perpendicular to these lines, i.e. tangentially to the surface of the foil. This velocity will be given the subscript t to identify this. The mean boundary layer velocities shown in Figure 8.7 correspond well with previous numerical simulations of similar arrangements [13].

Figure 8.8 shows the chord-wise distribution of pressure coefficient, C_p, and root mean square, rms, pressure, sampled at mid span of the foil. The pressure coefficient is sampled on both the pressure side and suction side of the foil and the rms pressure is sampled on the suction side only. Inspection of the pressure distribution shows a secondary hump at $x/c \approx 4\%$, suggesting the presence of a laminar separation bubble. The reattachment of this bubble is likely to cause the transition from a laminar to a turbulent boundary layer, and the peak shown in the p_{rms} plot show that the combination of these events is causing strong rms pressure fluctuations. The separation near the leading edge is shown in Figure 8.9 which uses an iso-contour surface of $U_x = 10^{-5}\ m/s$ to illustrate areas of recirculating flow caused by the separation bubble.

8.5 Summary

Splitting the foil into several sections showed only a minor increase in the contribution to far-field noise from the tip region. Due to the use of an incompressible solver any noise mechanisms which rely on the scattering of turbulence are not captured. A taxonomy of important unsteady flow features has been presented and the likely importance of the different mechanisms discussed. It is suggested that the primary noise source mechanism in the tip gap region of ducted propellers is likely to be due to the vorticity in the tip leakage flow being scattered as it interacts with the tip edge. The flow through a tip gap is analogous to that of a forward-backward facing step, however the proportions in the current study differ greatly from those investigated in the literature.

The noise sources captured by the incompressible solver for use with the acoustic analogy are likely to be dominated by hydrodynamic pressure fluctuations due to the solver not being capable of capturing the scattering mechanism. It has been discussed that the far-field noise predictions are likely to be dominated by the unsteady pressure fluctuations within the boundary layer on the suction surface of the foil.

The tip leakage vortex is shown to interact with the horseshoe vortex as well as the tip leakage flow and convect downstream. The breakup of this vortex is hypothesised in the literature to be an important noise source in aerodynamic arrangements. It has been discussed that in the marine environment the Mach numbers of interest are significantly lower, $M < 0.03$, and therefore the the breakdown of vorticity in the free fluid is unlikely to be a dominant noise source in water.

Chapter 9

Noise source sensitivity to the tip gap

9.1 Introduction

In chapter 7 it was shown that the far-field radiated noise was affected by the varying tip gap height, and that the far-field noise increased with reducing tip gap height. Chapter 8 discussed the pressure fluctuations which are being radiated are likely to be purely hydrodynamic i.e. not capturing the scattering of turbulent structures over sharp edges. The noise sources responsible for the predicted far-field pressure fluctuations have been discussed including the chord-wise distribution of rms pressure and static pressure coefficient, C_p. This revealed the presence of a small laminar separation bubble near the leading edge which was confirmed by highlighting areas of recirculating flow in post-processing. A taxonomy of likely noise source mechanisms in the tip region has been proposed using the flow features to predict the most likely locations for turbulence scattering noise mechanisms. This chapter continues the analysis from Chapter 8 and investigates the sensitivity of each of the mechanisms discussed on the size of the tip gap height, when h/c is 0.5%, 1.0%, 2.0% and 5.0%. If the behaviour of the suggested noise mechanisms can be shown to follow the same trend in the far-field noise found in the literature this will strengthen the hypothesis made whilst giving indications towards making progressive design changes.

9.2 Far-field noise radiation from different source regions

Using the post-processing technique of generating a subset of surface faces to use as the integration surface, the FW-H analysis was carried out on the tip region of the foil, to compare with the far-field radiations from the total foil. This region was set up to be 10%

of the length of the span of the foil for the $h/c = 1\%$ case, i.e. the span of the integration surface is $99\,mm$. This span was then used for the subsequent subsections to ensure that an equal integration surface area was used in each case. Figure 9.1 shows the prediction of the noise using this tip region as the integration surface compared with the use of the remainder of the foil and the whole foil. Note that Figure 9.1a is the same as Figure 7.15.

It can be seen that while the use of the whole foil as the integration surface in Figure 9.1a produces a hump at $f \approx 5\,kHz$, the use of the tip region in Figure 9.1b shows that the reducing tip gap produces reduced far-field acoustic radiations from that region. This relationship between the tip gap and the far-field noise intuitively follows the expectation found in the literature, however it is the reverse of the trend shown when the whole foil is used as the integration surface. This infers that the tip gap has an impact on the noise generated by the rest of the foil, as is shown in Figure 9.1c, which uses the remaining part of the foil which was not used for the tip section analysis. It can be seen that the remaining section of the foil follows the same trend as the whole foil, with a hump at $f \approx 5\,kHz$.

9.3 Pressure distribution

It has been shown that the surface pressure fluctuations captured in the FW-H analysis are hydrodynamic in origin. However, note that the tip gap plays a significant role in the fluid behaviour over the whole foil. It has been shown that the strongest contributions to the far-field noise appear to be due to the transition at the leading edge, where the boundary layer changes from laminar to turbulent.

Figure 9.2 shows the C_p distrbutions at mid-span for the four different tip gaps. It can be seen that as the tip gap height is reduced, the low pressure hump on the suction side near the leading edge increases, confirming the increase in lift performance seen previously in Figure 7.14. The increased strength of this spike causes an increase in the magnitude of the adverse pressure gradient, moving further downstream on the foil and so could trigger a more aggressive transition, causing the increased noise seen in the far-field predictions. Furthermore, it can be seen that the C_p distribution has a second, smaller peak, just downstream of the initial peak. The second peak in C_p is indicative of a laminar separation bubble, caused by the strong adverse pressure gradient, as discussed in Chapter 8.

Figure 9.3 shows the pressure coefficient C_p over the whole suction surface of the foil. In these figures the root of the blade is at the top, with the tip, and therefore the tip gap, shown at the bottom. The leading edge is to the left and the trailing edge is on the right. At the largest tip gap the influence of the strong tip leakage vortex can be seen in the bubble of low pressure near the tip caused by the pressure drop in the core of the TLV. This is seen to decrease in size and strength with decreasing tip gap height. The magnitude of the

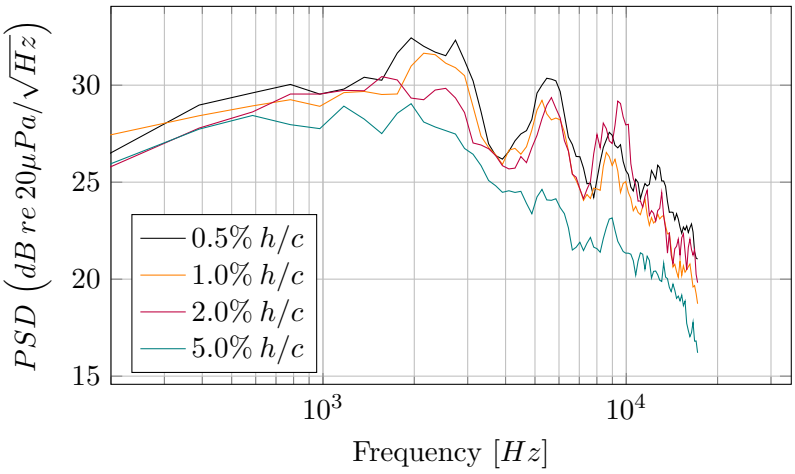

(a) Whole foil

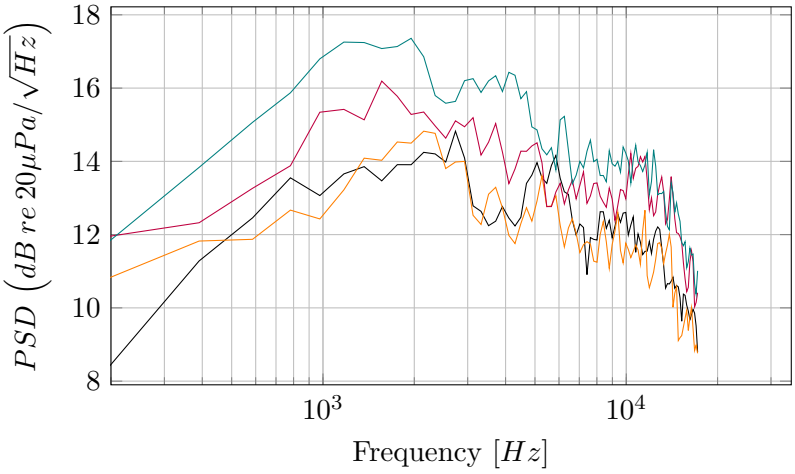

(b) Tip region only

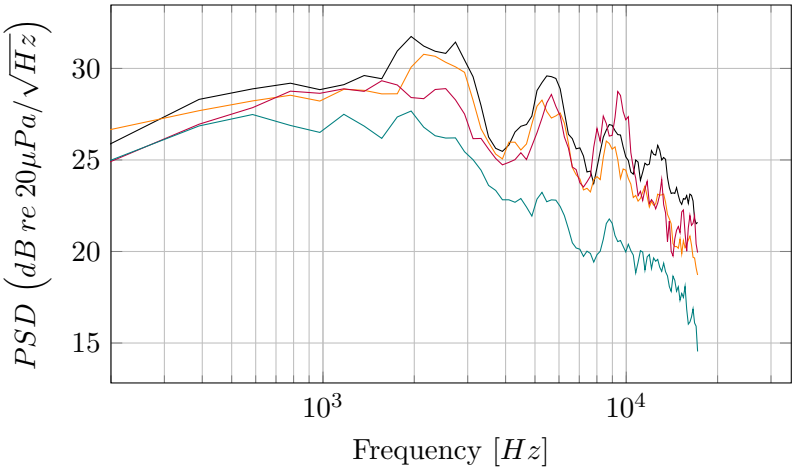

(c) Remaining region only

Figure 9.1: Effect on far-field acoustic radiations from different regions of the foil for various tip gaps.

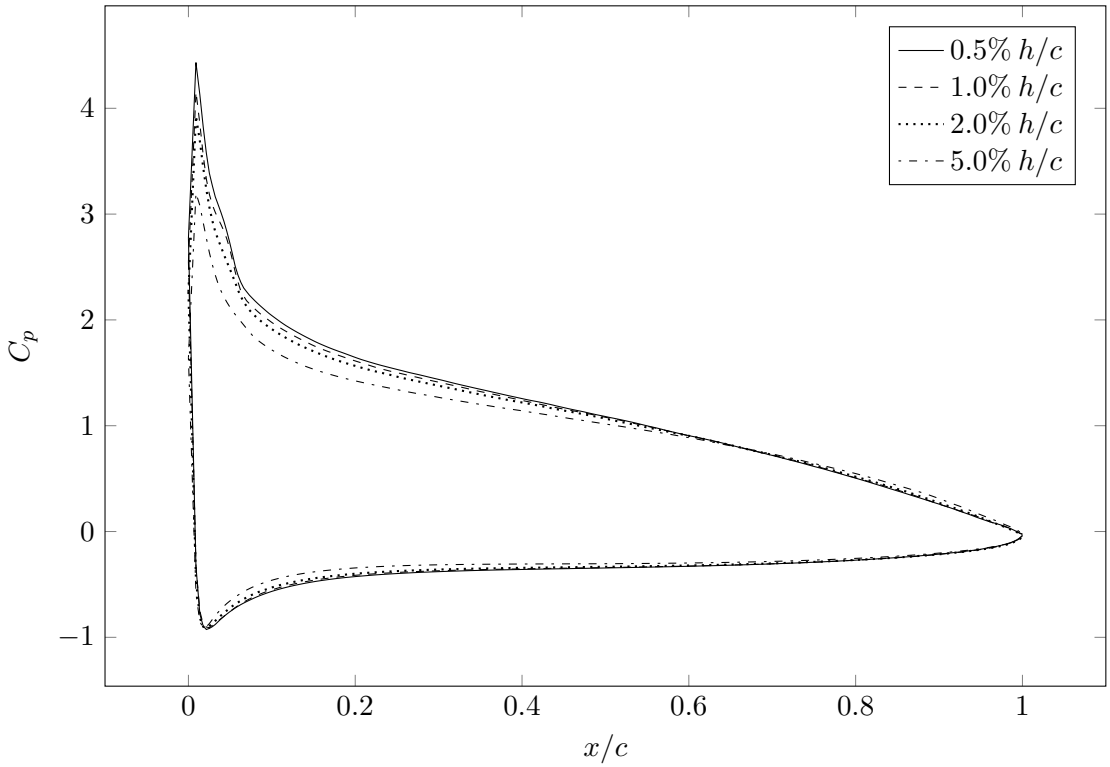

Figure 9.2: C_p distribution at mid span for different tip gap heights.

pressure coefficient can be seen to increase as the tip gap height decreases, shown by the darker colours towards the leading edge, as observed at mid span in Figure 9.2.

Figure 9.4 shows the regions of separation on the foil for the four cases. This contour was produced using the x-component of the mean flow velocity such that $U_x = 1 \times 10^{-5} m/s$ to identify regions with an upstream flow component. It can be seen that in the configuration with the largest tip gap height there is little separation occurring at the leading edge, but as the tip gap is reduced, the area of separation near the leading edge increases. The increasing separation region follows the variation in the pressure distribution as shown in Figures 9.2 and 9.3 which demonstrated a higher magnitude of pressure coefficient, resulting in a more severe adverse pressure gradient, and a secondary hump can be seen in Figure 9.2 for the smaller tip gap heights.

9.4 Boundary layer development

It has been suggested in the previous sections that the increased adverse pressure gradient may be responsible for a more severe tripping of the boundary layer and so the impact of the tip gap height on the development of the boundary layer has been analysed here. Figure 9.5 shows the boundary layer profiles at two key locations, $x/c = 40\%$ and $x/c = 90\%$. These

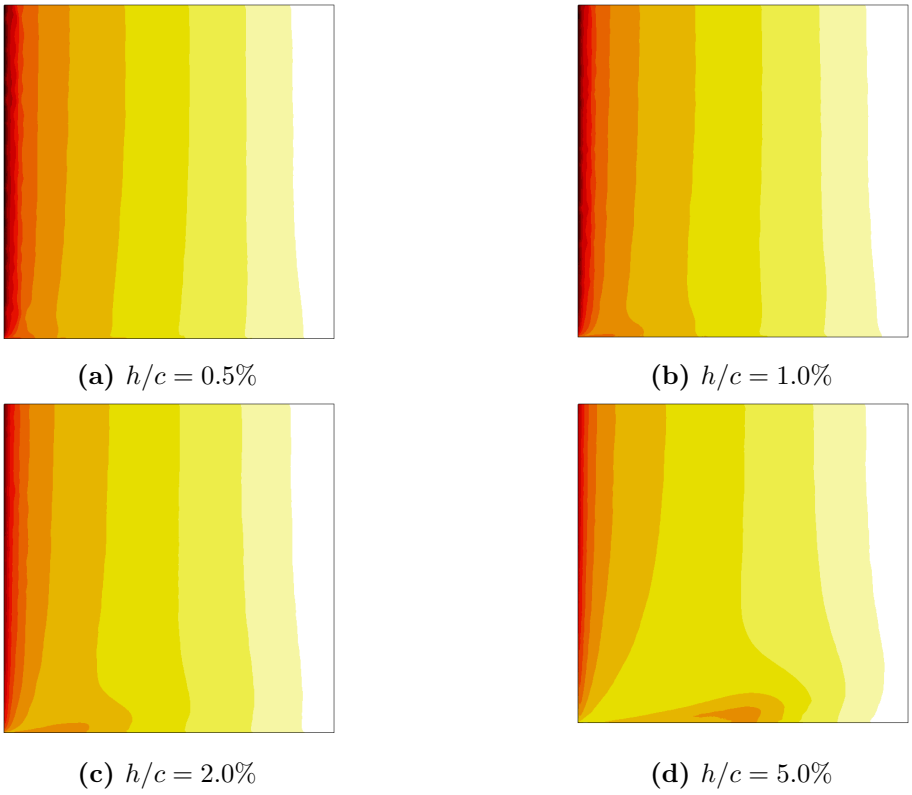

(a) $h/c = 0.5\%$ **(b)** $h/c = 1.0\%$

(c) $h/c = 2.0\%$ **(d)** $h/c = 5.0\%$

Figure 9.3: Pressure coefficient, C_p plotted over the suction side of the foil. The leading edge is on the left, trailing edge on the right, root is at the top and the tip and gap are at the bottom of each figure. The colouring is $0 \leq -C_p \leq 5$ where 0 is white and 5 is black.

sampling locations where selected by the results from the divided FW-H analysis shown in Figure 8.2b, which suggests that the $20\% - 40\%$ section produced the strongest far-field radiated pressures and the most distinct characteristic frequencies.

From Figure 9.5a it can be seen that the boundary layer thickness has an inverse relationship to the tip gap height agreeing with the previous discussion that the transition is more aggressive for the reduced tip gap cases. Furthermore, Figure 9.5b shows that this increase in boundary layer thickness continues to the trailing edge of the foil, which will impact the strength of the trailing edge noise generation, implying that trailing edge noise may be increased by reducing the tip gap. The development of the boundary layer for all four cases is shown in Figure 9.6.

9.5 Unsteady pressure distribution

Figure 9.7 shows the *rms* pressure distribution over the suction side of the foil in the form of a contour plot, illustrating the high pressure fluctuations which occur near the leading edge. In this figure the leading edge is to the left, with the trailing edge to the right, the

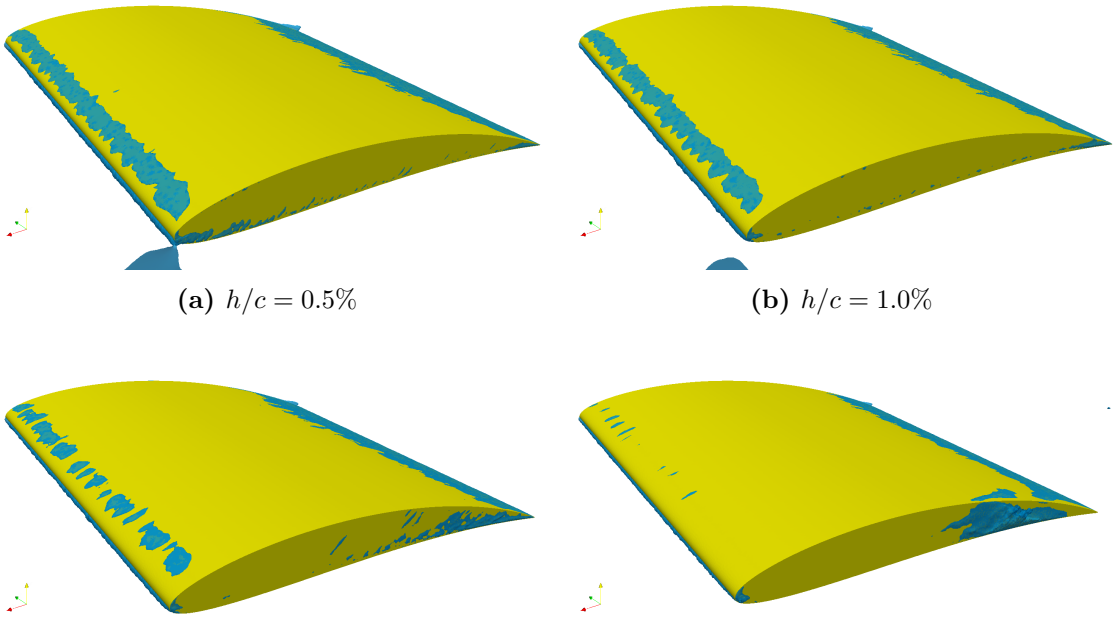

(a) $h/c = 0.5\%$ **(b)** $h/c = 1.0\%$

(c) $h/c = 2.0\%$ **(d)** $h/c = 5.0\%$

Figure 9.4: Areas of localised flow separation shown using a contour of $U_x = 10^{-5}\, m/s$ to identify regions with an upstream flow velocity.

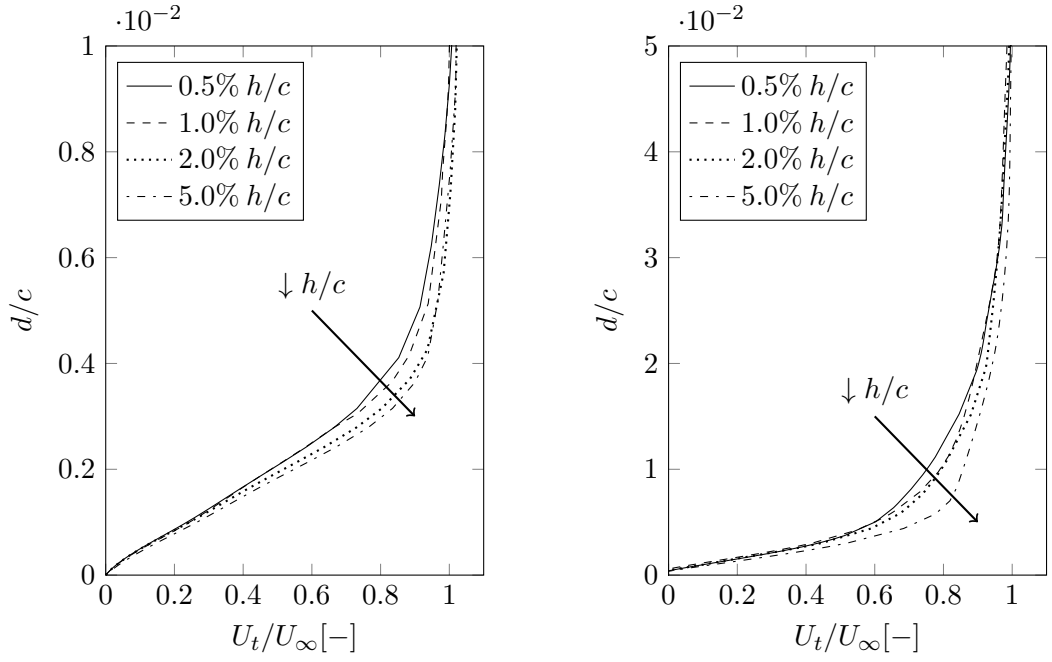

(a) $x/c = 40\%$ **(b)** $x/c = 90\%$

Figure 9.5: Mid-span boundary layer profiles at key chord-wise locations for varying tip gap heights illustrating the impact that the tip gap height has on the the entire foil.

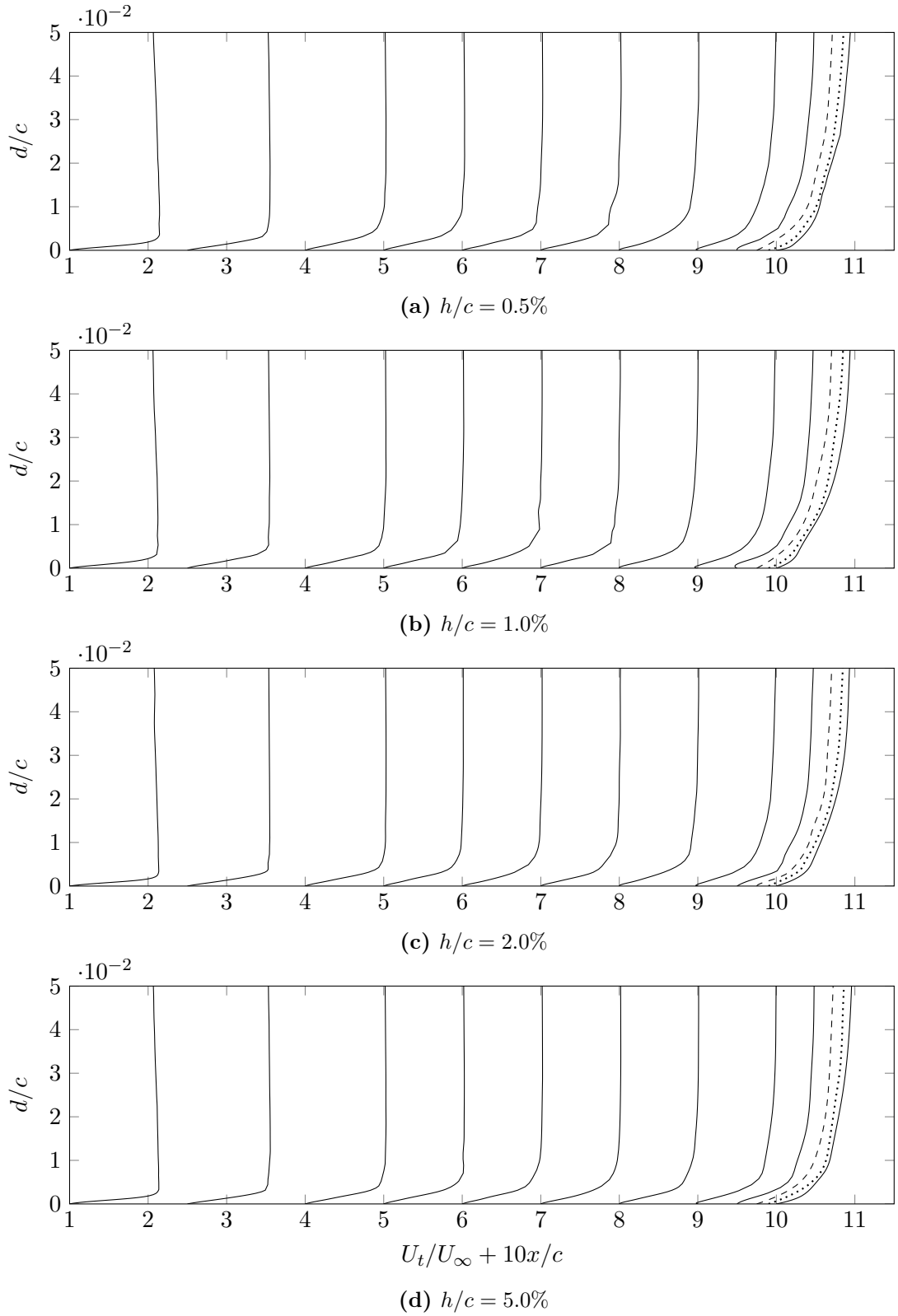

(a) $h/c = 0.5\%$

(b) $h/c = 1.0\%$

(c) $h/c = 2.0\%$

(d) $h/c = 5.0\%$

Figure 9.6: Boundary layer profile development along the suction surface of the foil at mid-span for various tip gap heights using the sampling locations shown in Figure 8.6 following Greschner et al. [13].

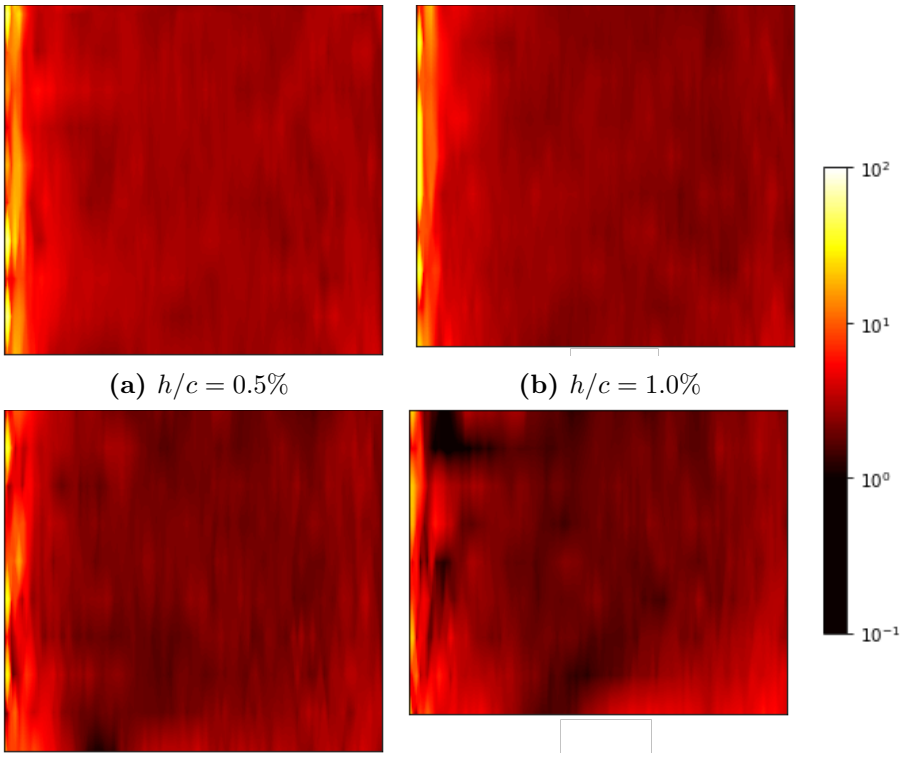

(a) $h/c = 0.5\%$ **(b)** $h/c = 1.0\%$

(c) $h/c = 2.0\%$ **(d)** $h/c = 5.0\%$

Figure 9.7: Effect on surface *rms* pressure of varying tip gap height.

root is at the top and the tip and gap are at the bottom. It can be seen that at the larger tip gaps, the strong tip leakage vortex causes a "shadow" shown by the reduction in *rms* pressure at the location of the TLV being shed from the tip gap and drawing energy out of the boundary layer nearby.

The location of this region of decreased surface pressure fluctuations can be seen to move further forwards on the foil as the gap reduces from 5% to 2%, and then seems to be removed completely at the small tip gap heights. This is in agreement with the analysis of the flow features throughout this thesis which have observed the shedding of the TLV occurring further towards the leading edge as the tip gap is reduced. This phenomenon will be discussed further later in this chapter.

9.6 Coherent vortex structures in the gap

Figure 9.8 shows the instantaneous iso-contour surfaces of $\lambda_2 = 10^5$ obtained from LES simulations to demonstrate the difference in the coherent vortex structures generated by different tip gaps, along with the instantaneous fluctuating component of surface pressure, p'. It can be seen that at the largest tip gap, $h/c = 5.0\%$, there are strong vortical structures

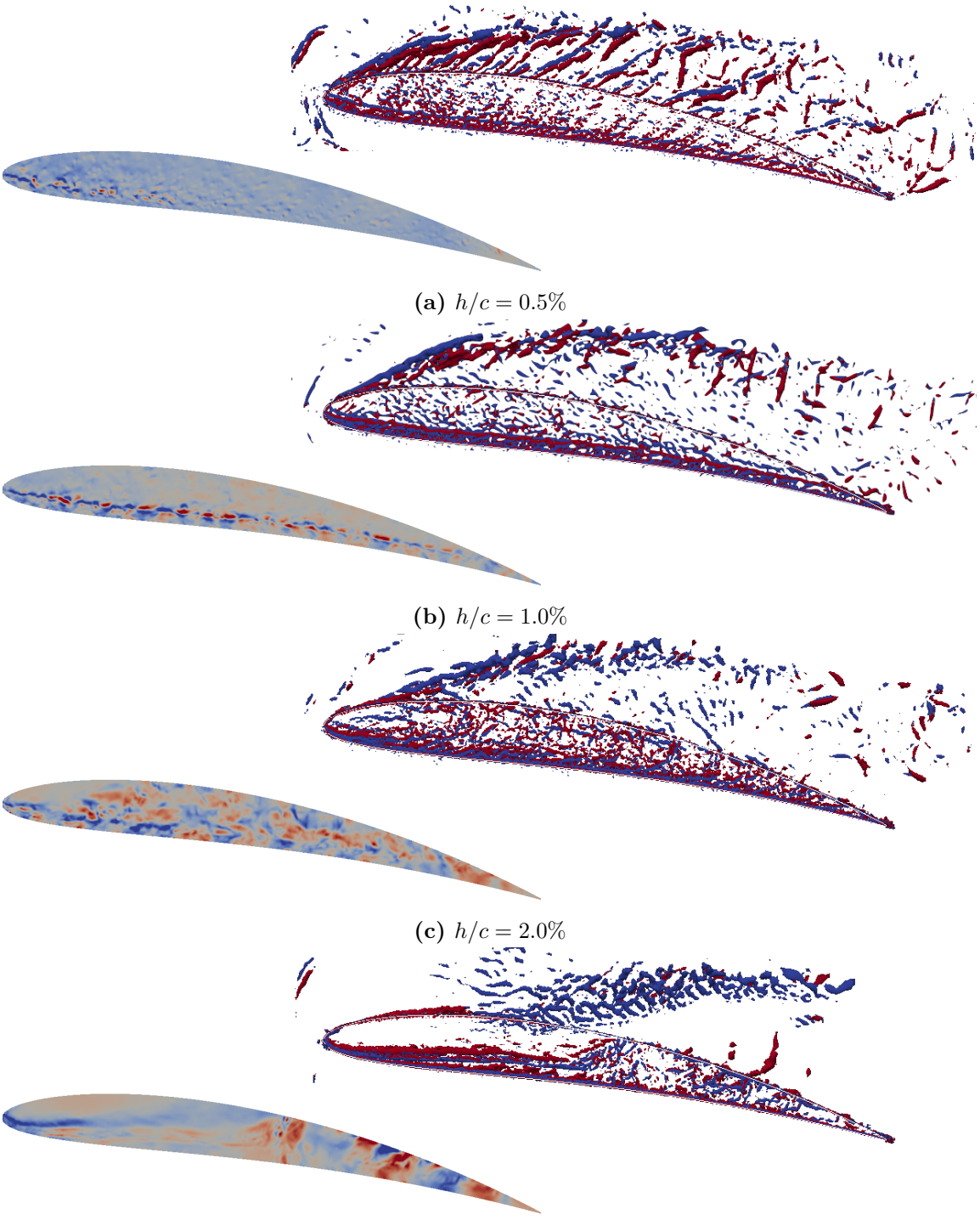

(a) $h/c = 0.5\%$

(b) $h/c = 1.0\%$

(c) $h/c = 2.0\%$

(d) $h/c = 5.0\%$

Figure 9.8: The right hand figures show the instantaneous iso-contour surfaces of $\lambda_2 = 10^5$ from LES simulations to demonstrate the difference in the coherent vortex structures generated by different tip gap heights. Contours are coloured by ω_x to show vorticity direction in the stream-wise direction. The left hand figures show the instantaneous fluctuating component of the surface pressure, $-10 \leq p' \leq 10$ Pa.

formed within the tip gap near the leading edge caused by the tip leakage flow over the pressure side edge. These structures are shed through the gap at between $x/c \approx 20 - 40\%$ where the strong tip leakage vortex causes counter vortices to be generated against the boundary surface above the tip. These can be seen in blue on the suction side of the foil. Further downstream within the tip gap other large structures can be seen to be generated over the pressure side edge of the foil and are shed through the gap. These structures occur in the same location as the instantaneous fluctuating components of the surface pressure and it can be seen that, at this tip gap, the front half of the foil tip experiences relatively weak surface pressure fluctuations. Closer to the trailing edge the surface pressure fluctuations can be seen to increase, qualitatively appearing to be maximum near the suction side edge of the foil tip where they are shed into the free fluid. This area of the tip edge is likely to be the dominant cause of noise in the tip region as these structures are scattered by the sharp edge.

As the gap reduces to 2.0% it can be seen that the vortex which is formed over the pressure side edge is physically restricted by the tip gap and the tip leakage flow is not strong enough to detach it from the foil tip surface. Instead it remains attached to the pressure side edge and as energy is fed into it by the tip leakage flow, it sheds smaller structures through the tip gap. It can be seen that the size restriction of the tip gap results in smaller vortex structures which reduces the magnitude of the surface pressure fluctuations and creating a more homogeneous distribution across the foil tip before being drawn through the gap by the tip leakage flow and shed over the suction side edge.

As the tip gap is reduced further it can be seen that the vortex which forms over the pressure side edge remains, and also stays attached to the edge. However, the vortex is reduced in strength by the physical restriction placed on the size of the vortex. Consequently, the surface pressure fluctuations are also seen to reduce, both along the length of the PS vortex, and in the strength of the structures which are shed through the gap. At $h/c = 1.0\%$ the PS vortex remains attached and convects along the edge as previously discussed, along with the strong pressure fluctuations associated with it. At $h/c = 0.5\%$ the pressure fluctuations caused by the PS vortex are seen to be mostly suppressed by the size of the gap.

9.7 Surface pressure fluctuations on the foil tip

In order to assess the impact of the tip gap on the frequency content of the surface pressure fluctuations a sampling point was extracted from the recorded pressures on the foil tip at 75% chord from the leading edge and on the mean camber line as shown in Figure 8.6. Figure 9.9a shows the surface pressure spectra sampled from this point. This point has been chosen as it is similar to the sampling point, B, used in [9], [49], and [76]. The frequencies of the pressure spectra can be non-dimensionalised using the Strouhal number of the flow:

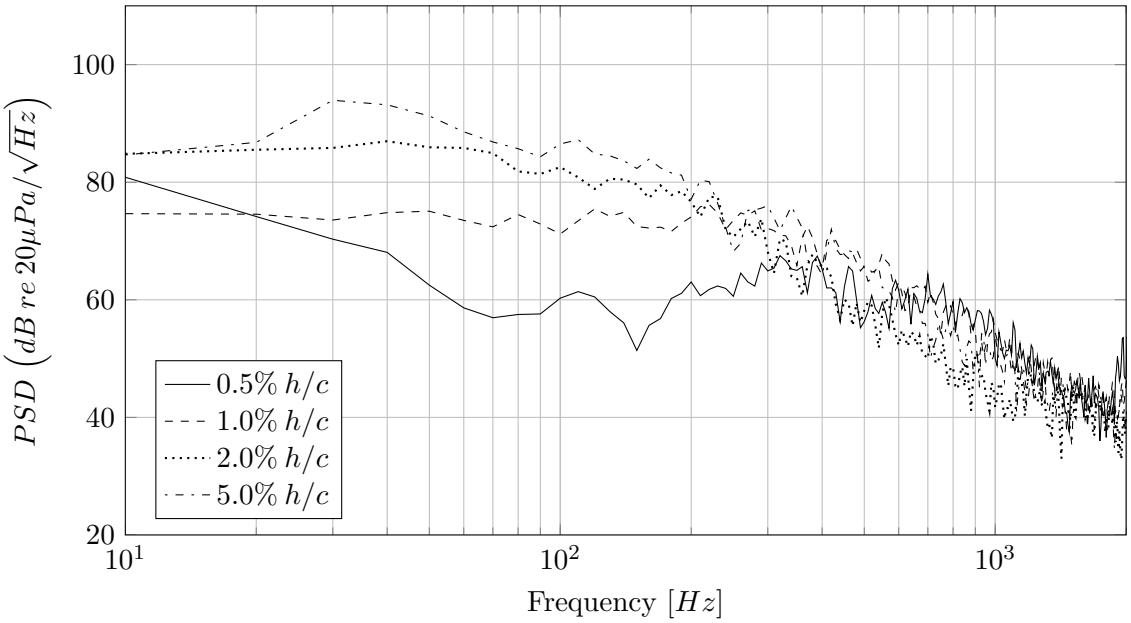

(a) PSD vs frequency

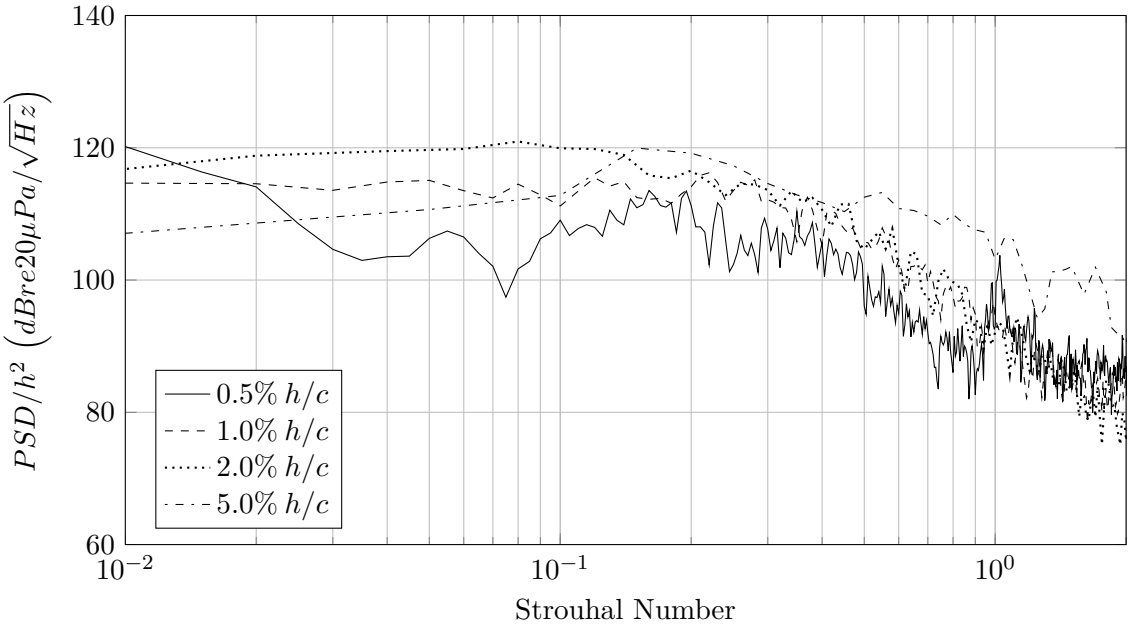

(b) PSD normalised by $1/h^2$ vs Strouhal Number

Figure 9.9: Surface pressure spectra on the tip of the foil for various tip gaps.

$$St = \frac{fL}{U} \tag{9.1}$$

where f is the frequency, L is the characteristic length and U is the flow speed. For this analysis, L was taken to be the tip gap, h and the mean flow speed was $10m/s$ as prescribed at the inlet of the domain. The magnitude of the pressure spectra was found to be

approximately proportional to the tip gap height squared. Figure 9.9 shows the comparison of the spectra both with and without the normalisation. It can be seen that the surface pressure fluctuations at this location exhibit a peak at $0.15 \leq St \leq 0.2$ which is in agreement with the experimental works [76]. It is noteworthy that the Strouhal number of 0.2 is typical for Von Karman vortex shedding in the wake of a cylinder. Similar flow structures were observed in the initial tip gap studies in this work, presented in Chapter 6, which found the $h/c = 7.5\%$ case to demonstrate a critical gap height which caused the onset of periodic, oscillating vortex shedding over the pressure side edge.

It can be seen that the magnitude of the pressure fluctuations are roughly proportional to the tip gap height squared. It has been discussed in Section 9.6 that the tip gap height places a physical limit on the size of the vortex structures which can occur in the gap, and it has been shown that these structures are directly responsible for the surface pressure fluctuations in this region, which in turn will correspond to the strength of the scattered waves when the structures are shed over the suction side edge of the foil.

9.8 Summary

Varying the tip gap has been shown to impact flow features over the whole foil surface. The reduction in flow through the tip gap increases the pressure difference between different sides of the foil leading to higher peak C_p values and instigating flow separation at the leading edge. The reduction in the tip gap has the effect of increasing the effective angle of attack and therefore, in a practical design, the pitch of propeller blades should be adjusted along with the tip gap to avoid cavitation caused by the stronger pressure drop on the suction surface.

The increased C_p peak has been shown to create a stronger adverse pressure gradient and therefore thicker boundary layer profile across the suction side of the foil. The unsteady pressure fluctuations on the suction surface are likely to be the dominant source of noise captured by the present implementation of the acoustic analogy, and the increased boundary layer thickness with reduced tip gap matches the trend of increased noise predicted in the far-field. The frequency content of the boundary layer is unlikely to be accurately captured in the presented simulations as the focus of the study is on the tip flow and so the use of increased resolution in the boundary layer has been avoided, due to computational limitations.

The presented analysis of the tip gap flow features suggests that the complex structures inside the tip gap are being captured well by the chosen meshing methodology. Furthermore, the tip surface pressure frequency spectra show good agreement with preceding experimental and numerical works and provides confirmation that the frequency content of the unsteady

flow features in the tip gap are well represented. By prioritising the tip region resolution the simulations remained computationally affordable, allowing the study of several different arrangements whilst capturing the unsteady flow mechanisms in the tip gap accurately.

The reduction in tip gap size has been shown to reduce the size of the coherent structures within the tip gap and reduce the magnitude of the pressure fluctuations on the tip surface. The surface pressure spectra on the tip has been shown to be roughly proportional to the tip gap squared which agrees with the accepted trend found in the literature that reduced tip gap sizes produces lower tip vortex noise.

Part IV

Recommendations and conclusions

Chapter 10

Recommended design modifications

10.1 Introduction

As discussed in Chapter 8, it is suggested that the mechanism by which noise is generated in the tip gap region is similar to that of trailing edge noise, such that strong turbulent structures are scattered as they pass over the suction side edge of the tip. It is further suggested that in order to improve the behaviour of the tip with regard to noise, these structures must be reduced in their strength, or in the strength of the scattering interaction. It was observed in Chapter 7 that the smaller tip gaps used caused the pressure side vortex to become bound to the edge of the tip and break down into a sheet of vorticity which quickly forms coherent structures, which are drawn through the tip gap by the tip leakage flow.

This chapter will discuss a number of potential modifications that could be applied to the foil to reduce the noise mechanisms which have been hypothesised. The individual merits of each modification will be discussed, along with their ease of design and implementation, both for new designs and for retro-fitting to existing propellers.

10.2 Suggested modifications

As discussed in the early chapters in this thesis, the aviation industry has been paying close attention to tip gap generated noise for longer than the marine industry due to pressures over reducing noise for residents near airports and passengers on board. The reduction of the tip gap suppresses the size and strength of the turbulent structures in the gap, as well as reducing the strength of the tip leakage vortex in order to reduce the noise produced. Due

to the rotational speed of turbo fan engines, the tip speed can often have a Mach number an order of magnitude higher than that of a marine propeller and so the TLV and the associated quadrupole sources can have a significant contribution to far-field noise.

The use of ever decreasing tip gaps is not feasible in marine propellers due to the increased likelihood of cavitation caused by the pressure drop in the tip gap region. In ducted fan design, such as for HVAC systems, other tip modifications have to be made in order to reduce noise using larger tip gap heights. These modifications are likely to have greater similarity to the requirements of the marine propeller industry and the proposed design improvements from the literature have been discussed in Chapter 2.

Based on the suggested improvements found in the literature and the hypothesised noise sources located within the tip gap, several potential design improvements are discussed here. One design modification will be selected to analyse using the same CFD set-up as in the preceding chapters to assess its effectiveness at eliminating the hypothesised noise generation mechanisms.

Filleted tip edges

The taxonomy of noise sources in Chapter 8 suggests that the primary mechanism is likely to be caused by either the tip separation vortex being scattered over the suction side edge of the foil near the trailing edge, or when the gap is sufficiently small, the strong turbulent structures which are shed from this vortex being scattered as they interact with the sharp suction side edge. The introduction of a fillet on the pressure side edge could remove the tip separation vortex and therefore create a smooth inflow for the tip leakage flow, removing the strongest of the turbulent structures within the tip gap.

This has potential drawbacks regarding the lift and drag performance of the foil as the smoothed inflow conditions are likely to allow for an increased tip leakage flow rate which in turn is likely to produce a stronger tip leakage vortex. This could displace the vortex further from the suction surface of the foil causing a reduction in vortex induced lift, while the increased strength could cause a stronger pressure drop downstream of the foil, therefore increasing the vortex induced drag.

Filleting the pressure side edge of the foil tip has some advantages in its simplicity:

- using a fillet to smooth the inflow should not require a complex design to achieve the goal of smoothing the inflow, it simply needs to be large enough to remove the tip separation vortex
- numerically this arrangement should be straight forward to recreate and analyse, allowing good comparison with the base case

- the manufacture of such a modification should be simple as the exact profile of the fillet is not likely to be critical to the flow, and so can be retrofitted to existing propellers.

Use of a winglet or tip end plate

Taking inspiration from wings of commercial aircraft and high performance cars, winglets and end plates can be used to control the formation strength and position of tip vortices. In this discussion a winglet is referring to a continuation of the lifting surface which bends along the span resulting in the tip surface being aligned with the direction of lift, thus the tip surface is not generating any useful lift and so the camber and angle of attack in this area is removed. An end-plate is referring to a flat plat which is orthogonal to the lifting surface of the foil, applied across the tip and separates the high and low pressure side of the lifting surface. The general principle is that the winglet or end plate is generating very little lift and therefore the pressure gradient across its tip is comparatively weaker than it would be over a simple flat lifting surface and therefore the strength of the tip vortex is reduced. These devices have been proposed in the past for use in the marine industry to improve the propulsive performance of the propeller but as the load on each blade of a marine propeller is high, they are usually cast from single pieces of metal before the surface is ground into shape, making the formation of complicated winglets difficult. It has been suggested that the tip vortex forms a strong acoustic source as it interacts with the trailing edge of the foil and so shedding the TLV away from the trailing edge using a winglet could improve the acoustics, however, it has been shown throughout this work that in a ducted arrangement the TLV is shed by the tip leakage flow and does not interact with the trailing edge.

As technology improves these designs may become feasible in the marine industry, for example with access to large scale 3D printers for the production of moulds for metal casting or using improved composite manufacturing techniques. In the HVAC and turbomachine industry tip end plates have been studied to improve aerodynamic performance [141], as well as acoustic performance [142] [143], and winglets have been investigated regarding their aeroacoustic impact [44] [45]. These studies agree that the use of well designed tip treatments can control the formation of tip vortices and reduce the emitted noise, however, the mechanism by which they reduce noise is not understood.

This work will not focus on the use of winglets or end plates as they require complex geometries causing more difficult flow comparisons with the current study, as well as limited transferability to the marine industry for the reasons discussed here.

Trailing edge noise treatments

It has been discussed that the proposed primary noise mechanism shares similarities with trailing edge noise which suggests that similar treatments could be useful to the current case by applying the edge treatment to the suction side edge of the tip to reduce the scattering effect predicted there. Two popular current areas of study regarding trailing edge noise use trailing edge serrations [144] [145] [146] and perforated trailing edges [147] [148]. The use of a serrated trailing edge reduces the span-wise coherence of the scattering process and therefore reduces the efficiency of the source for radiating noise to the far-field, as well as causing destructive interference between waves propagating from different points on the trailing edge, reducing their strength. Trailing edge perforations reduce the strength of surface pressure fluctuations before they reach the trailing edge and thus reduce the noise source strength. The use of perforations in the tip has previously been suggested for use in turbofan engines [149]. In a marine context the use of a porous material in the tip is likely to instigate cavitation caused by localised pressure drops, however, the use of a serrated edge could be feasible and relatively simple to manufacture.

Trailing edges reduce noise radiation by creating destructive interference by scattering the turbulence at different stream-wise locations, thereby creating a phase lag between different regions of the trailing edge. In order to design a serrated trailing edge which effectively reduces edge interaction noise the shape and size of the serrations need to be carefully designed. The assessment of their effectiveness relies on the far-field radiated noise which has been shown not to be feasible in the current set up with the available computational power. For this reason this modification will not be investigated here.

Use of rotating shroud to remove tip gap

The final modification to be discussed here is the use of a rotating shroud to remove the tip gap all together and therefore remove all tip leakage flow and the associated noise mechanisms. The aviation industry makes use of shrouded blades in compressors by including a shroud on the tip of each blade which then link together to form a continuous shroud, as well as in smaller axial fans where a ring shroud is part of the whole propeller [150]. In the marine industry there has been a rise in the use of Rim Driven Thrusters (RDTs) which use electromagnetic induction to drive the rim of the propeller [151] [152]. These often have the open tip of the propeller blade in the center where the hub would usually be, but can incorporate a rotating hub to remove the presence of an open blade tip. In the context of a full scale marine propeller the shroud required would constitute a significant increase in mass of the propeller, which is located far away from the axis of rotation and therefore impacting the torque required. This can be offset somewhat by the fact that the propeller blades are now supported at both ends and so the blade itself can be made thinner, lighter

and therefore more efficient.

This modification would remove the noise source mechanisms proposed in this work but would become a rather trivial case if investigated compared with the current set-up as the blade would become quasi 2-dimensional, bound between flat plates. This would likely increase the strength of the horseshoe vortex around the tip and it would no longer be driven away from the foil by the tip leakage flow. The horseshoe vortex would be likely to remain attached to the suction surface and impact the trailing edge noise as it is shed from the foil. The introduction of a rim which is installed within a channel in the duct creates a complex flow in the fluid between the surfaces similar to that of a Taylor Couette flow [153] [154], with unknown impacts on the noise generation. Therefore an assessment of the effectiveness of this design modification would require the prediction of the trailing edge noise. Furthermore, this would be a major design modification with many other factors to be considered as discussed and so the rotating shroud will not be investigated here.

10.3 Comparison of a modified tip with the base case

10.3.1 Chosen design modification

This study has chosen to investigate the influence of introducing a fillet on the pressure side edge of the tip in an effort to reduce the turbulence in the tip gap region. This modification has been chosen as it is the most practical to retrofit to real propellers, as well as being practical to implement using the current simulation methodology. It also has the benefit of retaining a flat surface along the mean camber line of the blade tip, allowing direct comparison of surface pressure taken from the same sampling location spectra as used in Chapter 9. It is suggested that by filleting the pressure side edge of the foil tip, the vortex seen on that edge in the case study can be reduced in strength, or given a sufficient fillet radius, removed completely. If this vortex can be removed then the tip leakage flow should be much smoother, with lower turbulence strengths and fewer and weaker coherent structures being drawn through the tip gap. To use the trailing edge comparison, this would have the effect of creating a much thinner boundary layer passing over the sharp tip edge on the suction side, in turn reducing the scattering of these structures and therefore the radiated noise to the far-field.

There are also potential negative effects of filleting the pressure side edge of the tip. The smoother tip leakage flow will likely lead to higher flow velocities and therefore volumetric flow rates through the tip gap. This will inevitably cause an increase in the strength of the TLV. The increased tip leakage flow may also cause earlier separation of the TLV from the foil, and drive it further away from the suction surface of the foil. It is expected that regarding the noise produced this will have little effect, but may impact the performance of

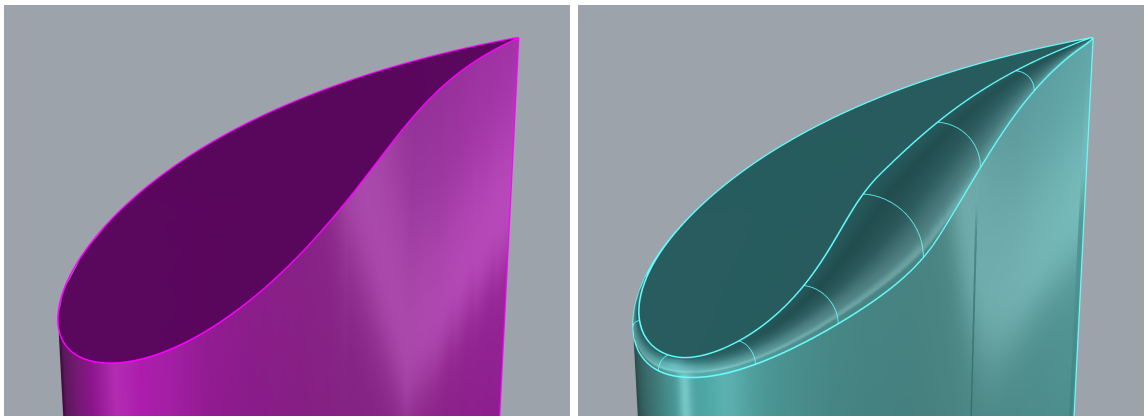

(a) Base case - square edges **(b)** Modified case - filleted pressure side edge

Figure 10.1: Comparison of the original and modified foil tip geometry.

the foil. The increased TLV strength could see an increased pressure drop at its core, and thus impart a higher drag on the foil. Moving the trajectory of the TLV further from the suction surface may reduce the vortex induced lift experienced by the foil, however, given the increase in vortex strength, it is hard to speculate whether the lift will be positively or negatively impacted.

It is recommended that further investigation should be carried out using a parametric process to assess the required fillet size to achieve the desired reduction in the turbulent structures within the tip gap. However, this study will focus on one modification, using a relatively large fillet with a maximum radius of 30 % of the foil thickness (i.e. 30 mm). Figure 10.1 shows the geometry of the variable fillet used on this foil. To avoid any difficulties regarding meshing the fillet was continued over the entire tip edge with the radius for the suction side set to 0.5 mm, effectively making it a sharp edge given the grid size long the edge has a maximum edge length of $\approx 0.3\,mm$. This radius was gradually increased in the last 10 % chord before the leading edge, where it was set to 5 mm. The radius was set to its maximum dimension of 30 mm at the location of the maximum thickness of the foil, before reducing back down to 0.5 mm at the trailing edge.

10.3.2 Comparison methodology

The comparison was made between the two chosen designs using the realistic reference case used in Chapter 7 in both time averaged and time resolved simulations. The modified foil was inserted into the same meshing domain used previously, with a 1% tip gap height, 10° angle of attack. Due to the fillets on the tip of the foil the mesh resolution on the tip had to be increased to capture the curvature smoothly. As before, the filleted foil was run using a RANS solver initially, to provide a good approximation from which to initiate the LES analysis. This RANS analysis will also be presented as the results of the RANS simulations

Table 10.1: Performance comparison of modified and original tip design.

Parameter	Unit	RANS			LES		
		Square	Filleted	Change [%]	Square	Filleted	Change [%]
C_D	[-]	0.080	0.083	2.8	0.067	0.074	10.1
C_L	[-]	1.318	1.329	0.8	1.488	1.457	-2.1
Lift:Drag	[-]	16.39	16.07	-2.0	21.70	19.69	-11.0

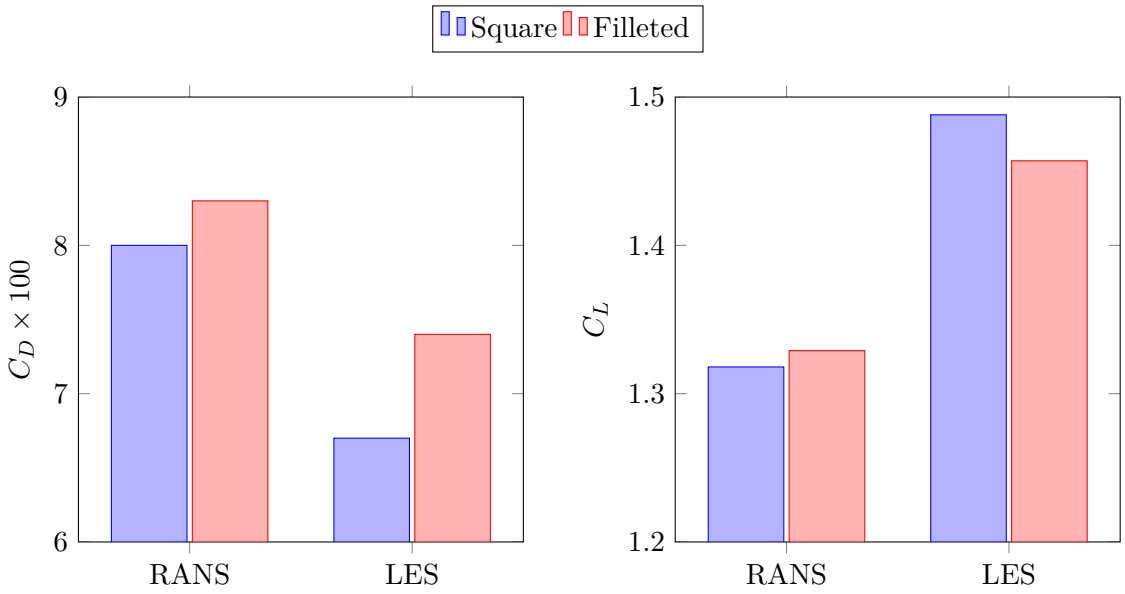

Figure 10.2: Comparison of the performance coefficients for the original and modified tip designs using both RANS and LES solutions.

have been shown in previous chapters to offer a good initial insight into the generation of large vortical structures, and therefore can be used as an initial design methodology.

10.3.3 Performance

Due to the importance of the tip vortex in the lift and drag performance of the foil, as discussed in Chapter 6, it is expected that the filleted pressure side edge of the tip will have an impact on the performance of the foil with regards to force coefficients as well as noise. Table 10.1 shows the effect of the modified tip shape on the forces of the foil for the RANS and LES studies.

It can be seen that for both steady and unsteady simulations the drag increases for the filleted foil compared to the square tipped foil. This is to be expected as the filleted pressure side edge provides less resistance to the tip leakage flow, meaning the TLV in the filleted case is expected to be stronger and therefore cause increased drag. It can be seen that for

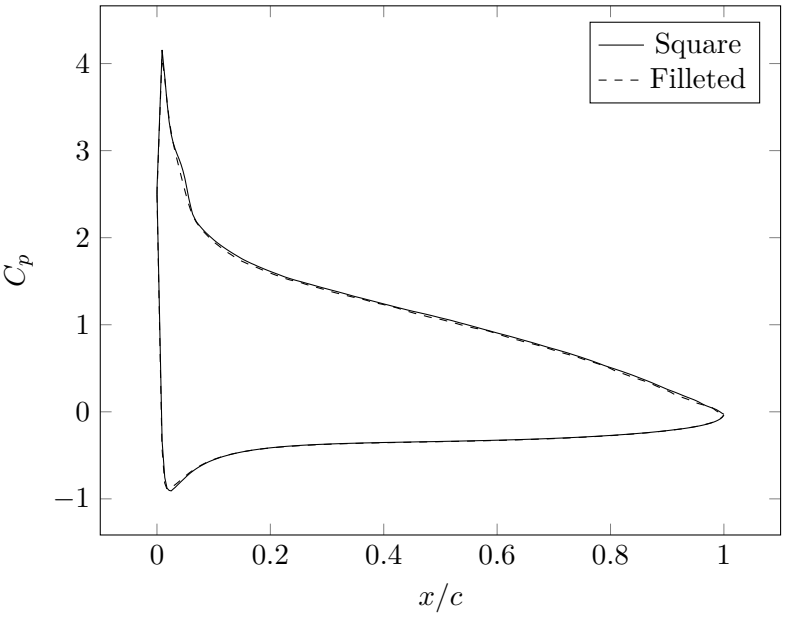

Figure 10.3: C_p distribution at mid span for original and modified tip designs, calculated using mean pressures from the LES simulations.

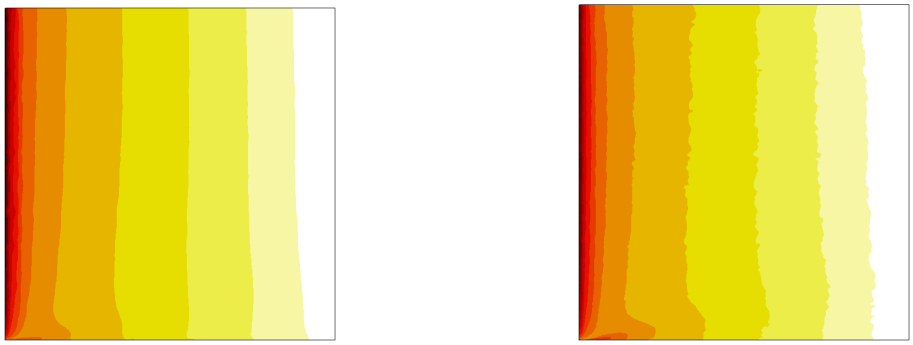

(a) Original - square tip **(b)** Modified - filleted tip

Figure 10.4: Pressure coefficient, C_p plotted over the suction side of the foil. The leading edge is on the left, trailing edge on the right, root is at the top and the tip and gap are at the bottom of each figure. The colouring is $0 \leq -C_p \leq 5$ where 0 is white and 5 is black.

both tip designs the drag is lower in the LES solutions than those computed using RANS which is expected as RANS often over predicts the drag of aerofoils, as discussed in Chapter 5.

It can be seen that the RANS analysis predicts a slight improvement of lift for the modified tip, while the LES simulations predict a reduction in lift. It has been discussed in Chapter 6 as well as presented in the literature [67] that RANS solvers are likely to find great difficulty in modelling the complex turbulence found in tip clearance flows such as this. It is expected for the lift performance of the foil to decrease with the modified tip as the tip leakage flow

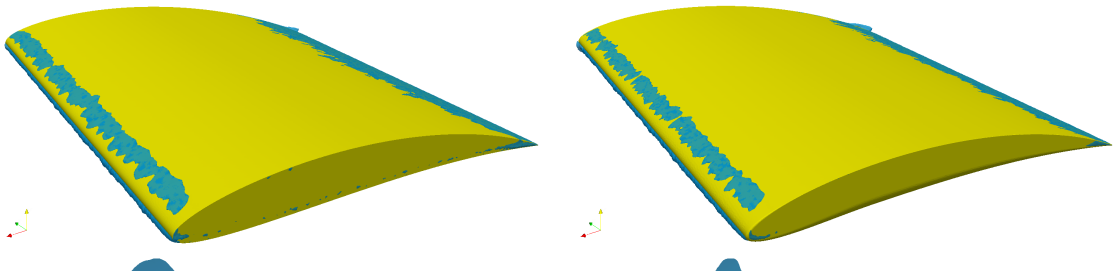

(a) Original - square tip **(b)** Modified - filleted tip

Figure 10.5: Areas of localised flow separation shown using a contour of $U_x = 10^{-5}\, m/s$ to identify regions with an upstream flow velocity.

is less restricted and therefore the pressure difference between the two sides of the foil is reduced. This can be seen in Figure 10.3 as the magnitude of the pressure coefficient for the modified tip is slightly reduced over the whole chord.

The fillet in this test case was chosen to be as large as practicable without causing other discontinuities around the tip edge and so the maximum radius is $\approx 30\%$ of the maximum thickness of the foil. The loss of aerodynamic performance observed in these results could be reduced by optimizing the radius of the fillet around the foil, such that the separation vortex on the pressure side edge is removed, whilst minimizing losses due to excess tip leakage flow.

10.3.4 Tip gap flow

Figure 10.6 shows the comparison of the original foil design against a foil with a large fillet on the pressure side edge, using the iso-contour of $\lambda_2 = 10^5$ to define the presence of strong vortex structures in the tip gap region, along with the instantaneous surface pressure fluctuations coloured nominally between $\pm 10Pa$ by subtracting the mean surface pressure from the instantaneous surface pressure at each face on the surface.

For the square tipped foil in Figure 10.6a, as discussed in Chapter 7 it can be seen that the pressure side edge generates a small vortex which is held close to the edge. This vortex is limited in size by the tip gap height and so as it reaches its physical limitation, the additional energy being supplied by the tip leakage flow causes this vortex to break down into a sheet of distinct structure which are drawn through the tip gap and feed the TLV. This TLV can be seen to shed from the foil near the leading edge and quickly breaks down into a group of structures which swirl within a larger vortex system. It should be noted for both figures in Figure 10.6 that the criteria for the isocontour has been set deliberately high to only capture the strongest vortex cores and the TLV remains present in both cases. It was hypothesised in Chapter 7 that the key noise mechanisms in the tip gap region are due to the sheet of

vortex structures as well as the pressure side edge vortex propagating along the edge and being shed over the suction side edge near the trailing edge.

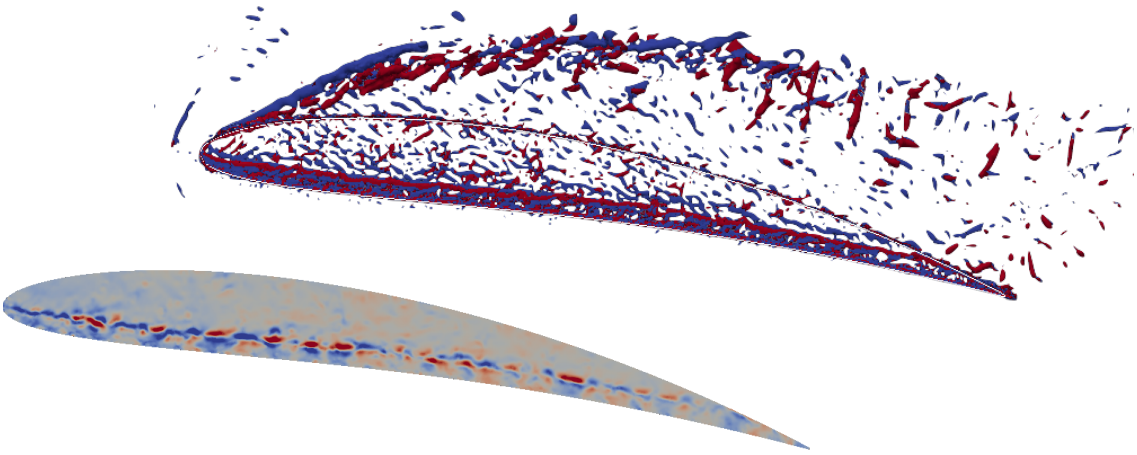

(a) Original - square tip

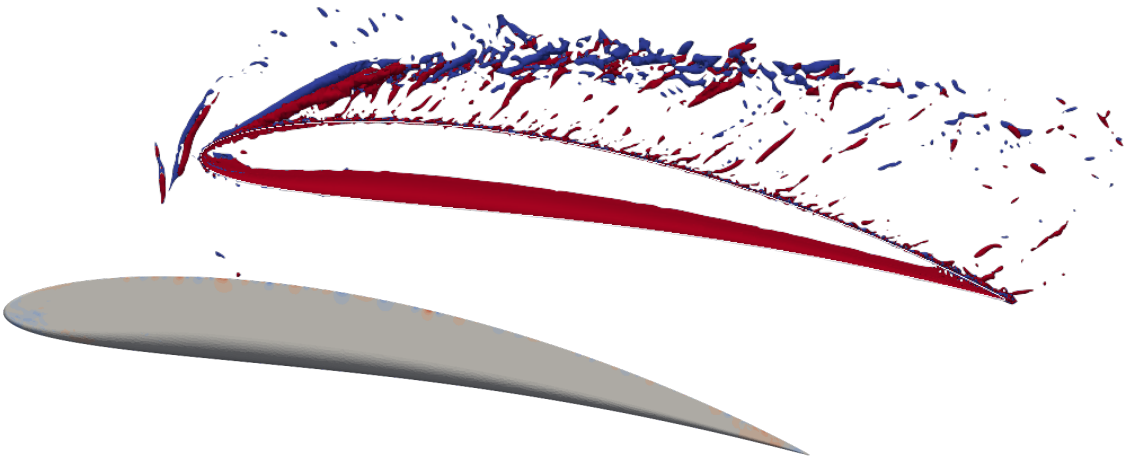

(b) Modified - filleted tip

Figure 10.6: The right hand figures show the instantaneous iso-contour surfaces of $\lambda_2 = 10^5$ from LES simulations to demonstrate the difference in the coherent vortex structures generated by different tip gap heights. Contours are coloured by ω_x to show vorticity direction in the stream-wise direction. The left hand figures show the instantaneous fluctuating component of the surface pressure, $-10 \leq p' \leq 10$ Pa.

It can bee seen that the pressure side edge vortex discussed produces significant pressure fluctuations, which convect along the edge towards the trailing edge of the tip. These pressure fluctuations can be seen to eventually be shed over the suction side edge. The effect of the shedding of other vortex structures through the tip gap can also be seen by the colouring of the rest of the tip surface. These structures are drawn through the gap and shed over the suction side edge, likely involving some scattering effects as they interact with

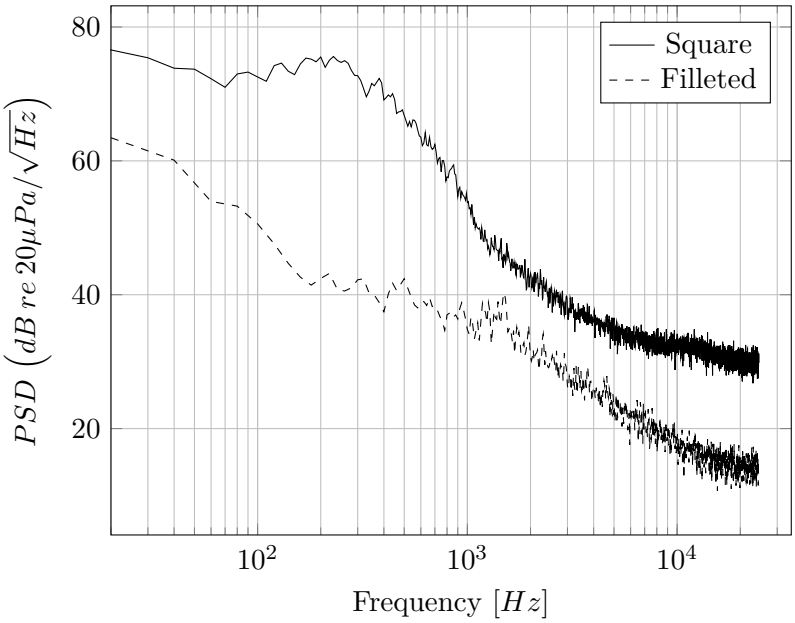

Figure 10.7: Comparison of surface pressure fluctuations for original and modified tip geometries.

the edge.

The effect of the filleted pressure side edge can be seen in Figure 10.6b, showing the absence of any coherent vortex structures within the gap. The λ_2 contour has shown the high level of vorticity in the boundary layer over the fillet, similarly to the boundary layer being identified on the leading edge of the foil as discussed in Chapter 6. The lack of structures within the tip gap region is indicative of the steadiness of the tip leakage flow for the filleted case compared with the square tipped case. This smoothed inflow through the tip gap is the reason the TLV is seen to be stronger and more stable near the leading edge. Crucially, the stable vortex on the pressure side edge is not present along with the absence of the vortex structures in the tip leakage flow. The use of the filleted edge has removed the two features thought responsible for noise generation in the tip gap region. The smoothing of the tip gap inflow can be seen to have a significant impact on the pressure fluctuations observed on the tip surface using the same colour scaling and post-processing technique as the square tipped foil. This in turn implies that the pressure fluctuations which are shed over the suction side edge are reduced, directly reducing the strength of any scattering mechanism which occurs there.

Figure 10.7 shows the PSD of the surface pressure fluctuations on the tip surface, sampled on the mean camber line at $x/c = 75\%$, the same location used in Chapter 9 as well as in similar experimental works [9] [76]. It shows that the magnitude of the surface pressure fluctuations is significantly decreased across all frequencies by $\approx 10dB$, and the characteristic peak is removed completely with a maximum reduction of $> 30dB$.

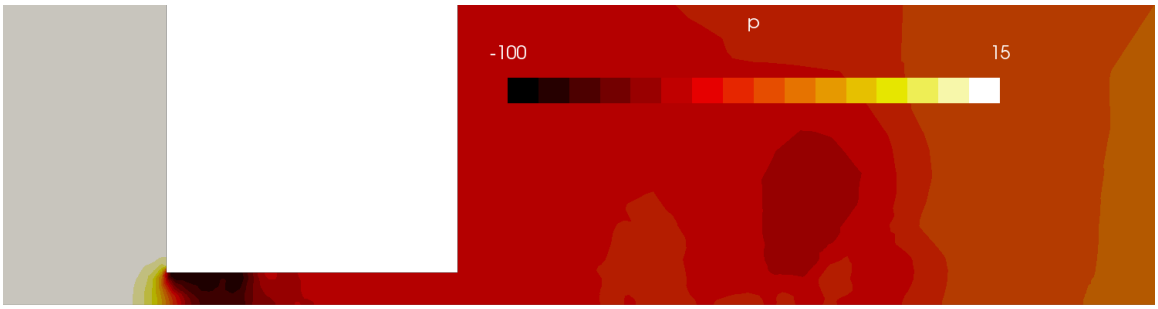

(a) Original - pressure contour only

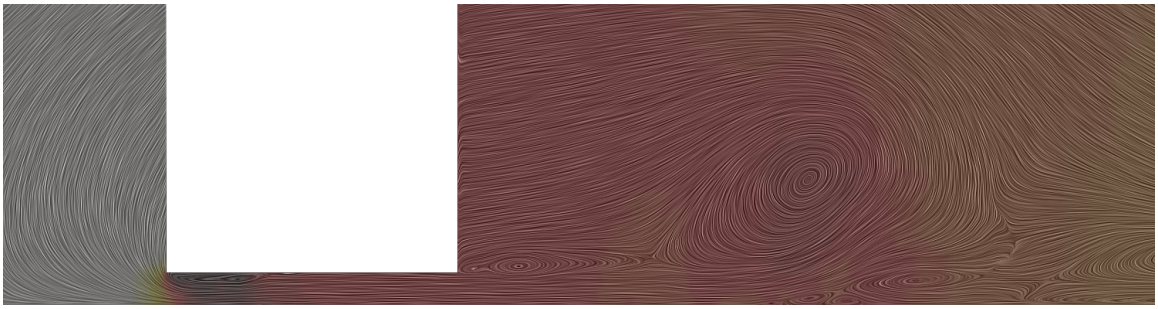

(b) Original - pressure contour overlayed with streamlines of planar velocity components

(c) Modified - pressure contour only

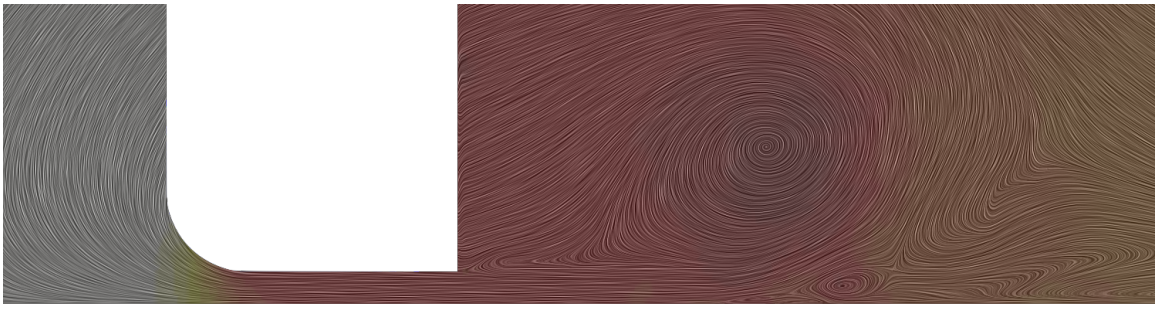

(d) Modified - pressure contour overlayed with streamlines of planar velocity components

Figure 10.8: Comparison of the relative pressure drop around the tip for the original and modified tip along with streamlines of planar velocity components to illustrate the areas of separated flow and large vortices.

Figure 10.8 shows the result of taking a slice through the domain in the yz-plane, orthogonal to the mean flow direction, similarly to the analysis used in Figure 6.10. In this figure the mean flow is directed into the page, with the pressure side of the foil on the left and suction

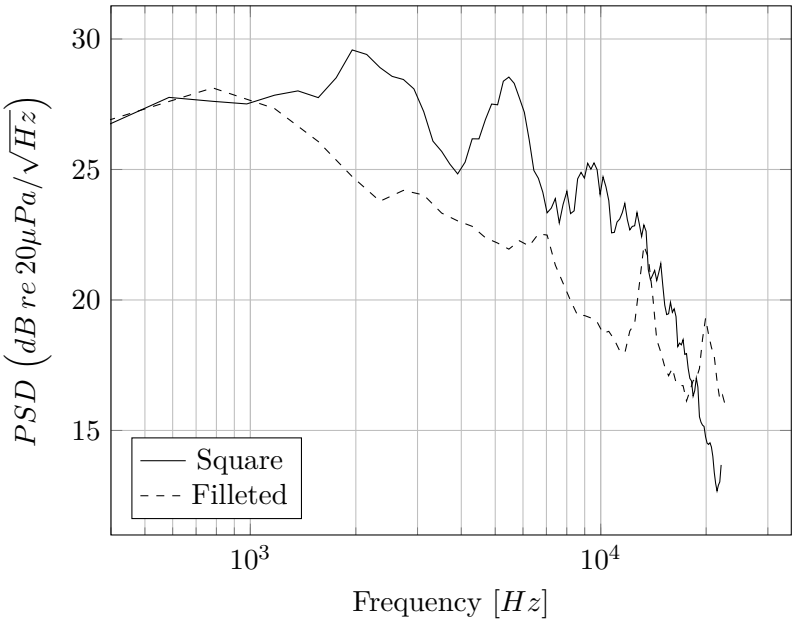

Figure 10.9: Comparison of far-field noise predictions for original and modified foil tip geometry.

side on the right, therefore, tip leakage flow is from left to right. The slices are all coloured by relative pressure $-100 \leq p \leq 15$ Pa as shown by the legend in Figure 10.8a, with Figures 10.8a and 10.8c showing only the pressure contour on the surface and Figures 10.8b and 10.8d also showing the streamlines based on velocity components parallel to the slice. It can be seen that for the square tip foil, the pressure side vortex causes a significant localised pressure drop at its core where the filleted edge allows for a smoother inflow and, therefore, no formation of a vortex structure and no localised pressure drop. The pressure side vortex effectively reduces the tip gap height with regard to the tip flow velocity and reduces the strength of the TLV, confirmed by the reduced pressure drop in the TLV core for the square case compared with the filleted foil which sees a higher pressure drop in the TLV core.

It has been discussed that this work is neglecting the effects of cavitation, however, in practice it is a phenomenon which always needs to be considered and the impacts of the suggested design modifications will be briefly discussed here. In the introduction of this thesis Figure 1.2 illustrated the issue of cavitation causing a limit on the operability based on local hydrostatic pressure. Figure 10.8 shows that changing the tip of a propeller to include a fillet on the pressure side edge could delay the onset of cavitation by reducing the maximum pressure drop. The improvements shown regarding the suggested noise source mechanisms as well as the benefits to cavitation risk would need to be balanced against the demonstrated loss in propulsive performance discussed in this chapter. The implication of smoothing the inflow is that the tip gap can be reduced even further without increasing the risk of cavitation and regaining some of the lost performance. This is an interesting

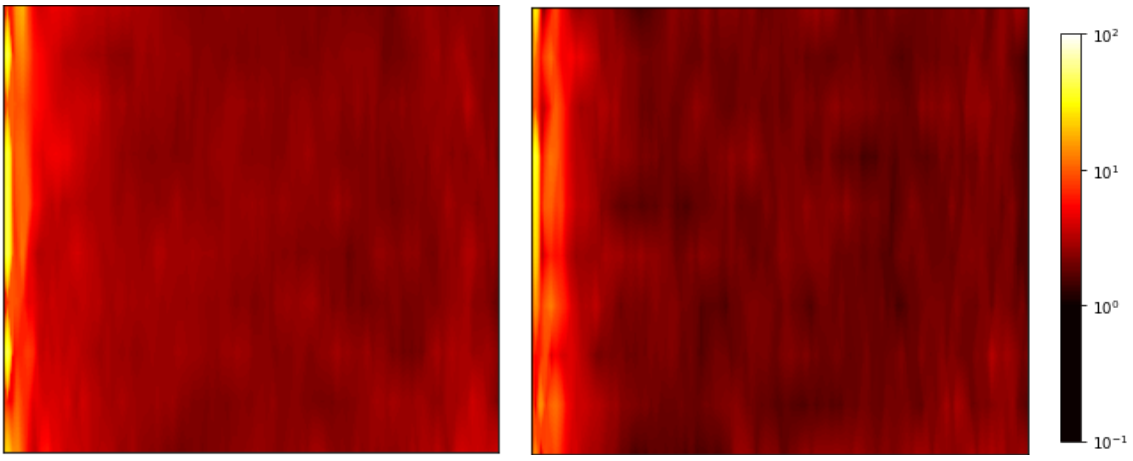

(a) Original tip **(b)** Modified tip

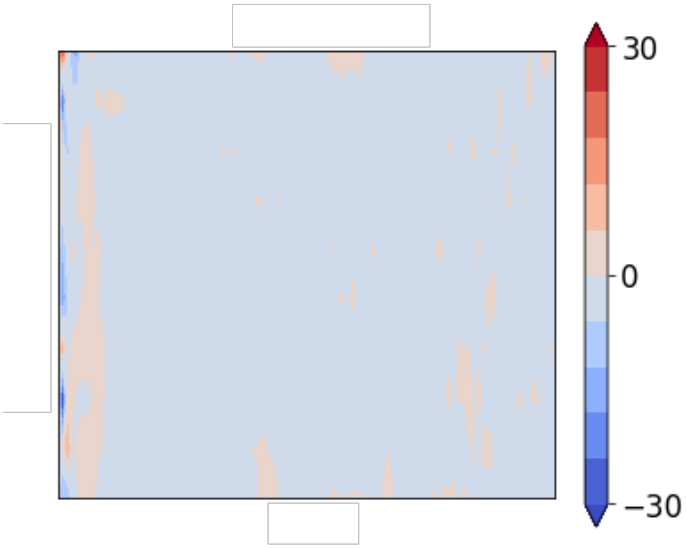

(c) Difference in surface pressure fluctuations on the suction surface between modified and original tip designs. Negative values show a reduction in surface pressure fluctuations due to the tip design change.

Figure 10.10: Change in *rms* pressures on the suction surface due to the modified tip.

topic which would require further study and would ideally account for variables such as manufacturing tolerances for marine propellers which may limit the reduction of the tip gap.

10.3.5 Far-field noise predictions

The far-field noise predictions generated using the FW-H analogy are shown in Figure 10.9 for the original and modified foil tips. It can be seen that for the modified tip case the low frequencies show good agreement but the humps which were seen in the square tip case have been removed. This could be due to the increase in tip gap flow and subsequent strengthening

of the TLV drawing energy out of the boundary layer and reducing the strength of the surface pressure fluctuations. Figure 10.10 shows the rms pressures on the suction surface for the two cases along with the difference between the two designs. By taking the rms pressures sampled from the modified tip surfaces and subtracting those from the original foil reveals the effect of the tip design. Negative values therefore show areas with reduced rms pressure due to the design modification.

10.4 Summary

A variety of potential design improvements have been suggested following inspiration from literature for reducing trailing edge noise, as well as intuitive developments to reduce the strength of the unsteady structures in the tip gap. A simple design modification was chosen by introducing a fillet onto the pressure side edge and has been shown to remove the unsteady structures in the gap along with the associated pressure fluctuations on the tip surface. The filleted edge was chosen because it represented a case which allows direct comparison with studies in previous chapters, it is easy to implement within the current methodology and would be easy to retrofit to full scale propellers if necessary.

The comparison between the original and modified tip design showed a decrease in aerodynamic performance, as would be expected due to increased tip leakage flow. The coherent vortical structures in the gap were removed and the magnitude of the pressure fluctuations on the tip surface were greatly reduced. The pressure spectra revealed a reduction of $> 30dB$ at the key frequency found in the previous chapter and previous studies found in the literature. The removal of the coherent vortical structures in the tip gap also reduced the magnitude of the pressure drop significantly, improving the cavitation performance.

The simple design modification presented has shown promise and is worthy of further investigation to optimise the geometry and tip gap, such that lift and drag performance losses are minimised while retaining the reductions in likely noise mechanisms.

Chapter 11

Conclusions and future work

11.1 Conclusions

Noise mechanisms due to unsteady flow features

The flow in the tip gap region has been shown to contain features that are analogous to trailing edge and forward-backward facing steps, both of which are known to be efficient sources of noise. It has been discussed that in a marine environment the Mach number of the tip of a propeller is very low, $M \approx 0.03$, therefore, the Mach number scaling of different multi-pole sources implies that quadrupole sources such as those caused by the strong tip leakage vortex and its interaction with the turbulent boundary layer are unlikely to be dominant.

This is contrary to the proposed sources found in literature which focus on the breakdown of vorticity in the free stream causing quadrupole sources [9] [49] [74]. The reason for the different proposed noise mechanisms is in part due to the significance of the Mach number scaling, as the literature is mainly focused on the noise generation of aerodynamic fans where the flow speeds are higher and the sound speed is lower than the marine applications of interest in this work.

Assuming that monopole sources are excluded due to the operational depth of the propellers this investigation is based upon implies that the dipole sources caused by the scattering of turbulent structures around solid surfaces is likely to dominate the far-field noise radiation. In particular it is proposed that the strong turbulent structures observed in detail in this work are likely to cause efficient scattering from the suction side edge. The varying of the tip gap height varies the location that strongest structures are shed from which agrees with the far-field measurements taken by Schneider et al. [74].

Furthermore, the reduction in the tip gap height was found to impact the whole span of

the foil due to the reduced leakage flow. These effects included the generation of a thicker boundary layer due to a higher adverse pressure gradient near the leading edge. This is likely to impact the strength of the trailing edge noise which has been shown to increase in strength with increased boundary layer thickness. In a marine context the increase pressure drop observed on the suction side will affect the onset of cavitation.

In the case of an open propeller, it is likely that the tip vortex causes increased trailing edge noise as it remains attached to the foil surface and is shed over the trailing edge. The increased tip leakage flow observed even at relatively large gaps has been shown to drive this vortex away from the foil surface and it is likely to be inconsequential regarding trailing edge noise at practical tip gap sizes in ducted propellers.

Design modifications

The chosen design modification of introducing a fillet to the pressure side edge was shown to completely remove the separation vortex which was observed on the pressure side edge of the square tipped foil. The removal of this feature subsequently removed all of the coherent vortex structures within the gap and therefore the surface pressure fluctuations on the tip surface were greatly reduced, with the pressure spectra showing a reduction of > 30dB at the characteristic frequency corresponding to a Strouhal number of ≈ 0.2. The reduction of the surface pressure fluctuations observed on the tip indicate the reduction in strength of the turbulence passing over the suction side edge of the foil, therefore, reducing the strength of the scattered acoustic waves which are likely to occur at that edge.

The modification was shown to have a negative impact on the lift and drag performance of the foil which indicates a reduction in propulsive performance when considering the foil being used in a ducted propeller. This was due to the reduced impingement of the tip leakage flow by smoothing the inflow conditions, reducing the pressure difference between the pressure and suction sides of the foil which reduced the lift by $\approx 2\%$ and strengthening the tip leakage vortex which increased the drag by $\approx 10\%$, thus decreasing the lift to drag ration by $\approx 11\%$.

The removal of the vortex structures from within the tip gap has been shown to significantly reduce the localised pressure drops in that area, therefore reducing the likelihood of cavitation. A combination of a reduced fillet radius, along with a further reduced tip gap height could reduce the performance lost whilst maintaining the reduced strength of the noise sources.

Including no-slip boundary condition on the boundary surface

Chapter 7 introduced the use of the no-slip boundary condition on the surface above the foil tip. It was shown that at the smaller tip gaps the drag coefficient seemed unaffected by the

use of the no slip condition and with a constant offset in the lift coefficient at all but the smallest gaps. However, Chapter 8 showed that the strong vortical structures in the tip gap region produced in turn produced counter rotating structures due to the no-slip condition on the boundary surface. It is concluded that the increased computational expense of including the no slip condition on this surface is crucial to understanding the unsteady flow in the tip gap region.

Suitability of incompressible flow solver for tip gap noise estimates

It has been shown that the far-field noise predictions made using the combination of incompressible flow solver and acoustic analogy do not accurately capture the noise source mechanisms proposed in this thesis. Furthermore, the literature has presented studies which use this combination of techniques to try and predict noise generated by scattering mechanisms such as trailing edge noise and leading edge noise due to turbulence ingestion and compare specific design improvements. This technique should be used with caution for the development of improved designs due to its limitations at high frequencies.

Noise mechanisms neglected in this study

In order to carry out this study a number of noise mechanisms which would be present in realistic geometries have been neglected, as discussed in Chapter 1. It is therefore worthwhile to revisit those neglected mechanisms and attempt to infer the impact that the recommended design modifications may have on them.

Cavitation has been considered throughout despite the base assumption that the operating depth of any realistic design would be sufficient to suppress its presence. However, it was found that the suggested design modification was in fact likely to improve the cavitation performance when compared with square tipped blades which are often found in ducted propulsors.

Ducted propulsors require structural elements to support the duct which surrounds the propeller. The necessary presence of these structures is often utilised in the form of stator blades which generate lift using the swirling wake of the propeller to augment the total thrust of the unit. This means that the inflow to the stators is highly turbulent and so turbulence ingestion noise is inevitable on these blades. The proposed design modification was found to increase the strength of the tip leakage vortex which will in turn increase the turbulence which is ingested by the stators. The impacts of this should be considered along side any benefits found in the reduction of noise from the propeller.

11.2 Summary of contributions

Peer reviewed conference and journal articles

- A. Higgens, A. Lidtke, P. Joseph, S. Turnock, *Investigation into the Tip Gap Flow and its Influence on Ducted Propeller Tip Gap Noise Using Acoustic Analogies*, In Journal of Ship Research (under review) [1]
- A. Higgens, A. Lidtke, P. Joseph, S. Turnock, *Investigation into the Tip Gap Flow and its Influence on Ducted Propeller Tip Gap Noise Using Acoustic Analogies*, In Proceedings of the 32nd Symposium on Naval Hydrodynamics (2018) [3]

Conference proceedings

- A. Higgens, P. Joseph, S. Turnock, *Improvements in the Methodology for Identifying Noise Sources in Ducted Marine Propellers*, In Proceedings of the 21st Numerical Towing Tank Symposium - NuTTS '18 [2]
- A. Higgens, P. Joseph, S. Turnock, *Investigation into the Tip Gap Flow and its Influence on Ducted Propeller Tip Gap Noise Using CFD*, In Proceedings of the 20th Numerical Towing Tank Symposium - NuTTS '17 [4]

11.3 Future Work

The most important hypothesised noise mechanism in this work involves the scattering of turbulence from the suction side edge of the foil in a similar mechanism to trailing edge noise. It is possible to use a transfer function to use the surface pressure fluctuations near the trailing edge to predict the far-field radiated noise accounting for the scattering mechanism. This leads on naturally to a number of further studies:

Parametric analysis of tip gap height and foil fillet radius

Following on directly from Chapter 10, it has been shown that using a large fillet with a maximum radius of $\approx 30\%$ of the thickness of the foil removes the turbulent structures from the tip gap and consequently dampens the surface pressure fluctuations on the foil tip. The use of such a large fillet has found a drop in the aerodynamic performance of the foil of $\approx 11\%$ combined with a reduced pressure drop in the tip gap region implying that with a filleted edge the tip gap can be further reduced without impact the operability of the propeller with regard to cavitation. A worthwhile further study would be the optimisation

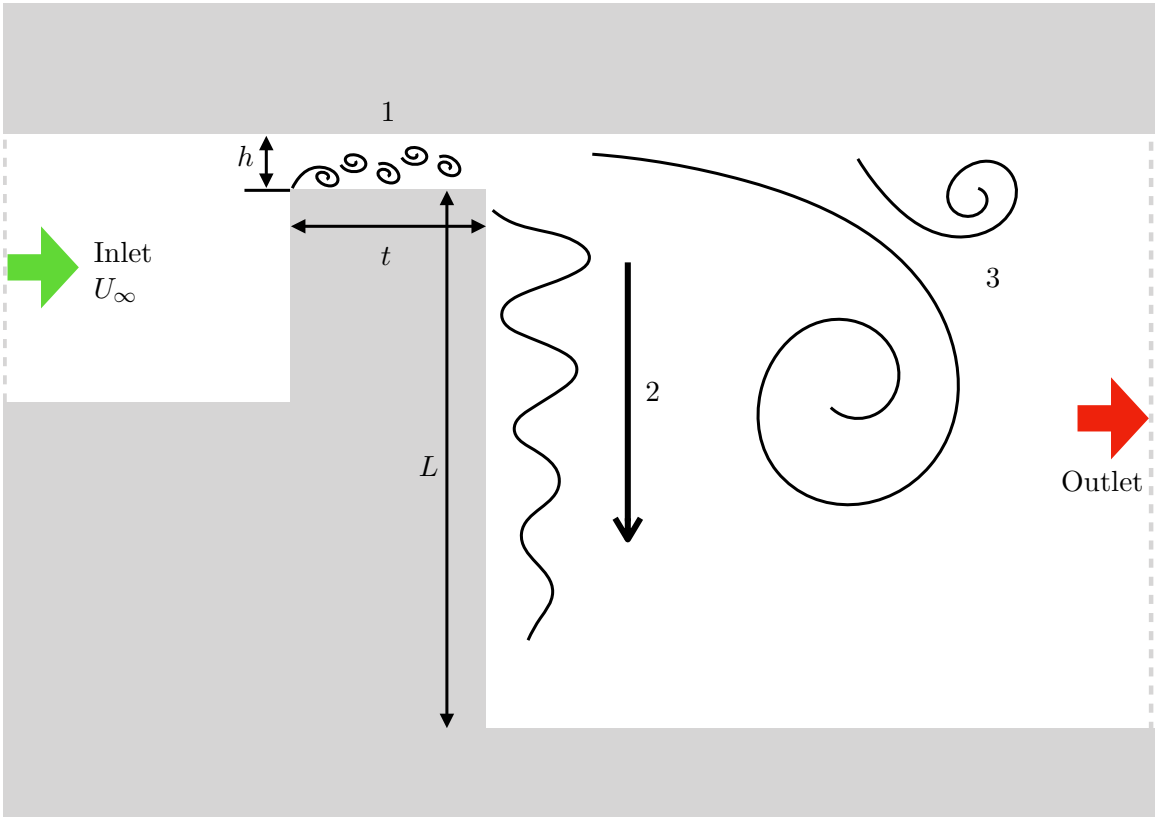

Figure 11.1: Suggested numerical domain for future study of simplified tip leakage noise source highlighting the key dimensions which differentiate it from current forward-backward facing step studies and important flow features to capture and investigate.

of the foil fillet radius and tip gap height to find a combination which results in the desired reduction in noise source features with a minimal impact on the aerodynamic performance.

Compressible analysis of current geometry

The natural progression from the study in Chapter 9 would be to repeat the simulations in a fully compressible solver. This would require a substantial increase in the mesh resolution and could provide far-field noise predictions using the FW-H acoustic analogy, with close attention paid to the noise mechanisms proposed in this work. This level of resolution is still prohibitive compared with the computational power available to many and so a simplified model may be the best first step in further anaylsis.

High resolution investigation of proposed noise mechanism

Figure 11.1 illustrates a simplified domain which could be used to numerically study the primary noise source which has been hypothesised by this study where the grey areas show

solid walls and the white is occupied by the fluid. The green arrow denotes the inlet and the red arrow the outlet of the domain. Key dimensions are given by t, h and L, representing the thickness of the foil, the tip gap height and the span of the foil respectively. Feature 1 is the shedding of a separation vortex over the sharp edge which breaks into discrete structures due to the restriction in the tip gap height. Feature 2 is the scattering of the turbulent structures over the sharp edge of the backward facing step as acoustic waves. Feature 3 is the tip leakage vortex and corresponding counter vortices.

The study of forward-backward facing steps currently focuses on steps with an aspect ratio close to 1, where the height and length of the step are relatively equal and with unconstrained flow above the step allowing large vortex structures to form relative to the geometry of the step. The tip leakage flow around a propeller blade with a small tip gap near a boundary surface presents a case with much higher aspect ratios than those presented in the literature, as the span is roughly equal to the chord and, therefore, could be susceptible to acoustic scattering down the back face of the step. Using the geometries used in the simulations presented in Part III of this thesis, the ratios of the dimensions presented in Figure 11.1 would be $L/t \approx 10$ and $L/h \approx 100$. This arrangement allows for a reduced chord to be investigated, further reducing the size of the domain and allowing a higher resolution of computation to be applied such as wall resolved compressible LES or full DNS calculations to investigate the relationship between the surface pressure fluctuations in the tip gap and the far-field radiated noise.

A parametric variation of this geometry could be relatively easily implemented, varying the length ratios discussed, as well as varying the angle of the edge to the incoming flow as the tip gap flow is seldom orthogonal to the edges over which the turbulence is generated and subsequently scattered.

References

[1] A. D. Higgens, A. K. Lidtke, P. F. Joseph and S. R. Turnock, *Investigation into the Tip Gap Flow and its Influence on Ducted Propeller Tip Gap Noise Using Acoustic Analogies*, *Journal of Ship Research* (2018) .

[2] A. D. Higgens, P. F. Joseph and S. R. Turnock, *Improvements in the Methodology for Identifying Noise Sources in Ducted Marine Propellers*, in *21st Numerical Towing Tank Symposium*, 2018.

[3] A. D. Higgens, A. K. Lidtke, P. F. Joseph and S. R. Turnock, *Investigation into the Tip Gap Flow and its Influence on Ducted Propeller Tip Gap Noise Using Acoustic Analogies*, in *32nd Symposium on Naval Hydrodynamics*, (Hamburg), 2018.

[4] A. D. Higgens, A. K. Lidtke, P. F. Joseph and S. R. Turnock, *Investigation into the Tip Gap Flow and its Influence on Ducted Propeller Tip Gap Noise Using Acoustic Analogies*, in *20th Numerical Towing Tank Symposium*, 2017.

[5] D. Wittekind, *The increasing noise level in the sea – a challenge for ship technology?*, *104 th Congress of the German Society for Maritime Technology* **104th** (2009) 8.

[6] *EU FP7. AQUO Project.*, 2014.

[7] *EU FP7. SONIC Project.*, 2014.

[8] International Maritime Organisation (IMO), *Guidelines for the reduction of underwater noise from commercial shipping to address adverse impacts on marine life*, Tech. Rep. April, 2014.

[9] J. Grilliat, E. Jondeau and M. C. Jacob, *Aerodynamic and acoustic measurements of a Tip Leakage Flow*, *Proceedings of the 8th International Symposium on Experimental and Computational Aerothermodynamics of Internal Flows* (2007) .

[10] D. You, R. Mittal, M. Wang and P. Moin, *Computational Methodology for Large-Eddy Simulation of Tip-Clearance Flows*, *AIAA Journal* **42** (2008) 271–279.

[11] V. John, A. Kindl and C. Suciu, *Finite element LES and VMS methods on tetrahedral meshes*, *Journal of Computational and Applied Mathematics* **233** (2010) 3095–3102.

[12] A. John, N. Qin and S. Shahpar, *The Impact of Realistic Casing Geometries and Clearances on Fan Blade Tip Aerodynamics (GT2017-64403)*, in *Proceedings of ASME Turbo Expo 2017: Turbomachinery Technical Conference and Exposition*, no. June, (Charlotte), 2017. DOI.

[13] B. Greschner, J. Grilliat, M. Jacob and F. Thiele, *Measurements and wall Modeled LES Simulation of Trailing Edge Noise Caused by a Turbulent Boundary Layer*, *International Journal of Aeroacoustics* **9** (2010) 329–355.

[14] A. Mann, M. Kim, J. Wu, F. Perot, J. Grilliat, M. C. Jacob et al., *Airfoil Tip Leakage Aeroacoustics Predictions using a Lattice Boltzmann Based Method*, *22nd AIAA/CEAS Aeroacoustics Conference* (2016) 1–17.

[15] E. J. Foeth, C. W. Van Doorne, T. Van Terwisga and B. Wieneke, *Time resolved PIV and flow visualization of 3D sheet cavitation*, *Experiments in Fluids* **40** (2006) 503–513.

[16] A. K. Lidtke, *Predicting radiated noise of marine propellers using acoustic analogies and hybrid Eulerian-Lagrangian cavitation models*. PhD thesis, University of Southampton, Southampton, 2017.

[17] J. Zhong, S. Han, H. Lu and X. Kan, *Effect of tip geometry and tip clearance on aerodynamic performance of a linear compressor cascade*, *Chinese Journal of Aeronautics* **26** (2013) 583–593.

[18] S. A. Sjolander and K. K. Amrud, *Effects of Tip Clearance on Blade Loading in a Planar Cascade of Turbine Blades*, *Journal of Turbomachinery* **109** (1987) 237.

[19] R. Ma and W. J. Devenport, *Unsteady Periodic Behavior of a Disturbed Tip-Leakage Flow*, *AIAA Journal* **44** (2006) 1073–1086.

[20] R. Ma and W. J. Devenport, *Tip Gap Effects on the Unsteady Behavior of a Tip Leakage Vortex*, *AIAA Journal* **45** (2007) 1713–1724.

[21] R. Ma and W. J. Devenport, *Unsteady Aperiodic Behavior of a Periodically Disturbed Tip-Leakage Vortex*, *AIAA Journal* **46** (2008) 1025–1038.

[22] J. Carlton, *Marine Propellers and Propulsion*. Butterworth-Heinemann, 2012.

[23] A. F. Molland, S. R. Turnock and D. A. Hudson, *Ship Resistance and Propulsion: Practical Estimation of Ship Propulsive Power*. Camberidge University Press, 2011.

[24] S. Caloni, S. Shahpar and J. D. Coull, *Numerical investigations of different tip designs for shroudless turbine blades*, *Proceedings of the Institution of Mechanical Engineers, Part A: Journal of Power and Energy* **230** (2016) 709–720.

[25] A. John, N. Qin and S. Shahpar, *Understanding fan blade tip aerodynamics*, *12th European Conference on Turbomachinery Fluid Dynamics and Thermodynamics, ETC 2017* (2017) 1–13.

[26] A. K. Lidtke, S. R. Turnock and V. F. Humphrey, *Characterisation of sheet cavity noise of a hydrofoil using the Ffowcs Williams-Hawkings acoustic analogy*, *Computers and Fluids* **130** (2016) 8–23.

[27] T. P. Lloyd, *Large eddy simulations of inflow turbulence noise: application to tidal turbines*. PhD thesis, University of Southampton, 2013.

[28] G. K. Batchelor, *An Introduction to Fluid Dynamics*. Cambridge University Press, 1967, 10.1063/1.3060769.

[29] A. Kolmogorov, *The local structure of turbulence in incompressible viscous fluid for very large Reynolds numberst*, *Proc. R. Soc.* **434** (1991) 9–13.

[30] A. Kolmogorov, *A refinement of previous hypotheses concerning the local structure of turbulence*, *J. Fluid. Mech* **13** (1962) 83–85.

[31] M. Lighthill, *On sound generated aerodynamically. I. General theory*, *Proceedings of the Royal Society of London. Series A. Mathematical and Physical Sciences* **211** (1952) 564 LP – 587.

[32] M. Lighthill, *On soudn generated aerodynamically. II. Turbulence as a source of sound*, *Proceedings of the Royal Society of London. Series A. Mathematical and Physical Sciences* **222** (1952) 1 LP –32.

[33] N. Curle, *The influence of solid boundaries upon aerodynamic sound*, *Proceedings of the Royal Society of London. Series A. Mathematical and Physical Sciences* **231** (1955) 505 LP – 514.

[34] A. Patri and Y. Patnaik, *Random forest and stochastic gradient tree boosting based approach for the prediction of airfoil self-noise*, *Procedia Computer Science* **46** (2015) 109–121.

[35] R. Bensow and M. Liefvendahl, *An acoustic analogy and scale-resolving flow simulation methodology for the prediction of propeller radiated noise*, in *Proceedings of the 31st Symposium on Naval Hydrodynamics*, (Monterey, CA, USA.), pp. 11–16, 2016.

[36] A. K. Lidtke, S. R. Turnock and V. F. Humphrey, *Use of acoustic analogy for marine propeller noise characterisation*, *Proceedings of the 4th Symposium on Marine Propulsors* (2015) .

[37] T. P. Lloyd, D. R. Rijpkema and E. van Wijngaarden, *Propeller acoustic modelling:*

comparing CFD results with an acoustic analogy approach, *Proceedings of the 4th International Symposium on Marine Propulsors* (2015) .

[38] R. Berdanier, *Literature review : On the acoustics of the presence of tip clearances in axial fans and compressors*, *AIAA* (2011) .

[39] A. R. George and S.-T. Chou, *Broardband Rotor Noise Analyses*, *NASA Contractor Report* **3797** (1984) .

[40] D. Quinlan and P. Bent, *High frequency noise generation in small axial flow fans*, *Journal of Sound and Vibration* **218** (1998) 177–204.

[41] J. H. Dittmar, D. M. Elliott and B. Fite, *The noise of a forward swept fan*, .

[42] T. Fukano and C. M. Jang, *Tip clearance noise of axial flow fans operating at design and off-design condition*, *Journal of Sound and Vibration* **275** (2004) 1027–1050.

[43] S. Bianchi, a. Corsini, F. Rispoli and a. G. Sheard, *Detection of aerodynamic noise sources in low-speed axial fans with tip end-plates*, *Proceedings of the Institution of Mechanical Engineers, Part C: Journal of Mechanical Engineering Science* **223** (2009) 1379–1392.

[44] M. Milavec, B. Širok, D. Vidal de Ventos and M. Hočevar, *Influence of the shape of the blade tip on the emitted noise in the air-gap between the rotor and the housing of an axial fan*, *Forschung im Ingenieurwesen* **78** (2014) 107–119.

[45] M. Milavec, B. Širok, D. Vidal de Ventos and M. Hočevar, *Identification of noise generation and flow kinematics in the air gap for two different blade tip designs of an axial fan*, *Forschung im Ingenieurwesen/Engineering Research* **79** (2015) 29–39.

[46] B. Bizjan, M. Milavec, B. Širok, F. Trenc and M. Hočevar, *Energy dissipation in the blade tip region of an axial fan*, *Journal of Sound and Vibration* **382** (2016) 63–72.

[47] R. C. Dunne and M. S. Howe, *Wall-bounded blade-tip vortex interaction noise*, *Journal of Sound and Vibration* **202** (1997) 605–618.

[48] D. A. Bies, *An experimental investigation of Curle's theory of aerodynamic noise generation by a stationary body in a turbulent air stream*, *Journal of Sound and Vibration* **278** (2004) 581–587.

[49] M. C. Jacob, J. Grilliat, R. Camussi and G. C. Gennaro, *Aeroacoustic investigation of a single airfoil tip leakage flow*, *International Journal of Aeroacoustics, Multi-Science Publishing* **9** (2010) 253–272.

[50] J. Liu, F. Holste and W. Neise, *On the azimuthal mode structure of rotating blade flow instabilities in axial turbomachines*, *2nd AIAA and CEAS Aeroacoustics Conference* (1996) .

[51] B. Pardowitz, A. Moreau, U. Tapken and L. Enghardt, *Experimental identification of rotating instability of an axial fan with shrouded rotor*, *Proceedings of the Institution of Mechanical Engineers, Part A: Journal of Power and Energy* **229** (2015) 520–528.

[52] K. C. San and Y. F. Fei, *Characteristic flow patterns and aerodynamic performance on a forward-swept wing*, *Journal of Mechanical Science and Technology* **26** (2012) 3103–3110.

[53] R. Repp, D. Gentile, D. Hanson, S. Chunduru and H. Engines, *Design and Test of Fan/Nacelle Models Quiet High-Speed Fan Design*, *Contract* (2003) .

[54] C. Pashias, *Propeller tip vortex simulation using adaptive grid refinement based on flow feature identification*. PhD thesis, University of Southampton, 2005.

[55] F. Kameier and W. Neise, *Rotating blade flow instability as a source of noise in axial turbomachines*, *Journal of Sound and Vibration* **203** (jun, 1997) 833–853.

[56] S. Glegg, *The state of the art of broadband rotor noise prediction*, Tech. Rep. 84/14, 1984.

[57] U. W. Ganz, P. D. Joppa, T. J. Patten, D. F. Scharpf, B. Commercial and A. Group, *Boeing 18-Inch Fan Rig Broadband Noise Test*, *Nasa* (1998) .

[58] S. Ianniello, R. Muscari and A. Di Mascio, *Ship underwater noise assessment by the acoustic analogy. Part I: Nonlinear analysis of a marine propeller in a uniform flow*, *Journal of Marine Science and Technology (Japan)* **18** (2013) 547–570.

[59] T. Lloyd, F. H. Lafeber and J. Bosschers, *Investigation and validation of procedures for cavitation noise prediction from model-scale measurements*, *Proceedings of 32nd Symposium on Naval Hydrodynamics* (2018) 5–10.

[60] W. Devenport, J. Österlund, C. Bak, K. Brown, A. Borgoltz and P. Davidsson, *Design and Operation of Hybrid Aeroacoustic Wind Tunnels*, .

[61] W. Devenport, K. Brown, A. Borgoltz, E. Paterson, C. Bak, N. Sørensen et al., *Advanced Wind Tunnel Boundary Simulation for Kevlar Wall Aeroacoustic Wind Tunnels*, .

[62] R. E. Bensow and M. Liefvendahl, *Implicit and explicit subgrid modeling in les applied to a marine propeller*, *Fluid Dynamics Conference* (2008) 1–12.

[63] S. Ianniello, R. Muscari and A. Di Mascio, *Ship underwater noise assessment by the acoustic analogy. Part III: Measurements versus numerical predictions on a full-scale ship*, *Journal of Marine Science and Technology (Japan)* **19** (2014) 125–142.

[64] S. Ianniello, R. Muscari and A. Di Mascio, *Ship underwater noise assessment by the*

acoustic analogy. Part II: Hydroacoustic analysis of a ship scaled model, *Journal of Marine Science and Technology (Japan)* **19** (2014) 52–74.

[65] S. Ianniello, *The Ffowcs Williams-Hawkings equation for hydroacoustic analysis of rotating blades. Part 1. the rotpole*, *Journal of Fluid Mechanics* **797** (2016) 345–388.

[66] V. M. Viitanen, A. Hynninen, T. Sipilä and T. Siikonen, *DDES of Wetted and Cavitating Marine Propeller for CHA Underwater Noise Assessment*, *Journal of Marine Science and Engineering* **6** (2018) 1–26.

[67] Y. Li, H. Chen and J. Katz, *Challenges in Modeling of Turbulence in the Tip Region of Axial Turbomachines*, in *Proceedings of 32nd Symposium on Naval Hydrodynamics*, 2018.

[68] W. E. Zorumski, *Aircraft noise prediction program theoretical manual, part 1*, tech. rep., NASA Langley Research Center; Hampton, VA, United States, 1982.

[69] C. Ventres, M. Theobald and W. Mark, *Turbofan noise generation. Volume 1: Analysis*, *NASA STI/Recon Technical Report N* **1** (1982) .

[70] M. Nallasamy and E. Envia, *Computation of rotor wake turbulence noise*, *Journal of Sound and Vibration* **282** (2005) 649–678.

[71] E. Envia, D. L. Tweedt, R. P. Woodward, D. M. Elliott, E. B. Fite, C. E. Hughes et al., *An Assessment of Current Fan Noise Prediction Capability*. No. October. 2008.

[72] J. De Laborderie and S. Moreau, *Prediction of tonal ducted fan noise*, *Journal of Sound and Vibration* **372** (2016) 105–132.

[73] D. You, R. Mittal, M. Wang and P. Moin, *Study of Rotor Tip-Clearance Flow Using Large-Eddy Simulation*, *41st Aerospace Sciences Meeting and Exhibit* (2003) 0838.

[74] M. Schneider and A. Lucius, *Investigation of axial fan tip noise mechanisms by means of CAA and beamforming technique*, .

[75] J. Decaix, G. Balarac, M. Dreyer, M. Farhat and C. Münch, *RANS and les computations of the tip-leakage vortex for different gap widths*, *Journal of Turbulence* **16** (2015) 309–341.

[76] M. C. Jacob, E. Jondeau, B. Li and J. C. Boudet, *Tip Leakage Flow: Advanced Measurements and Analysis*, *22nd AIAA/CEAS Aeroacoustics Conference, Aeroacoustics Conferences, (AIAA 2016-2823)* (2016) .

[77] J. Boudet, J. Caro, B. Li, E. Jondeau and M. C. Jacob, *Zonal large-eddy simulation of a tip leakage flow*, *International Journal of Aeroacoustics* **15** (2016) 646–661.

[78] J. Boudet, E. Jondeau, B. Li, J. Caro and M. C. Jacob, *Wavelet Analysis of a Blade Tip-Leakage Flow*, *AIAA Journal* **56** (2018) 3332–3336.

[79] F. R. Menter, *Improved two-equation k-omega turbulence models for aerodynamic flows*, Tech. Rep. 103978, 1992. 10.2514/6.1993-2906.

[80] F. Ducros, F. Nicoud and T. Poinsot, *Wall-adapting local eddy-viscosity models for simulations in complex geometries*, *Conference on Numerical Methods in Fluid Dynamics* (1998) 1–7.

[81] F. Piscaglia, a. Montorfano, a. Onorati and F. Brusiani, *Boundary Conditions and SGS Models for LES of Wall-Bounded Separated Flows: An Application to Engine-Like Geometries*, *Oil & Gas Science and Technology – Revue d'IFP Energies nouvelles* **69** (2013) 11–27.

[82] M. Weickert, G. Teike, O. Schmidt and M. Sommerfeld, *Investigation of the LES WALE turbulence model within the lattice Boltzmann framework*, *Computers and Mathematics with Applications* **59** (2010) 2200–2214.

[83] I. Yilmaz and L. Davidson, *Comparison of SGS Models in Large - Eddy Simulation for Transition to Turbulence in Taylor-Green Flow*, *The 16th International Conference on Fluid Flow Technologies* (2015) .

[84] C. Y. Lee and S. Cant, *Assessment of LES Subgrid-scale Models and Investigation of Hydrodynamic Behaviour for an Axisymmetrical Bluff Body Flow*, *Flow, Turbulence and Combustion* **98** (2017) 155–176.

[85] O. Ben-Nasr, A. Hadjadj, A. Chaudhuri and M. S. Shadloo, *Assessment of subgrid-scale modeling for large-eddy simulation of a spatially-evolving compressible turbulent boundary layer*, *Computers and Fluids* **151** (2017) 144–158.

[86] H. Choi and P. Moin, *Grid-point requirements for large eddy simulation: Chapman's estimates revisited*, *Physics of Fluids* **24** (2012) 1–6.

[87] U. Piomelli and E. Balaras, *Wall Layer Models for Large Eddy Simulations*, *Annual Review of Fluid Mechanics* **34** (2002) 349–374.

[88] W. Cabot and P. Moin, *Approximate Wall Boundary Conditions in the Large-Eddy Simulation of High {R}Eynolds Number Flow*, *Flow, Turbulence and Combustion* **63** (2000) 269–291.

[89] L. S. Caretto, A. D. Gosman, S. V. Patankar and D. B. Spalding, *Two calculation procedures for steady, three-dimensional flows with recirculation*, in *Proceedings of the Third International Conference on Numerical Methods in Fluid Mechanics* (H. Cabannes and R. Temam, eds.), (Berlin, Heidelberg), pp. 60–68, Springer Berlin Heidelberg, 1973.

[90] R. Issa, *Solution of the Implicitly Discretised Fluid Flow Equations by Operator-Splitting*, *Journal of Computational Physics* **62** (1985) 40–65.

[91] OpenFOAM, *OpenFOAM programmer's guide.* 2015.

[92] D. B. Giaiotti and F. Stel, *The Rankine Vortex Model*, *October* (2006) 1–14.

[93] J. C. R. Hunt, a. a. Wray and P. Moin, *Eddies, streams, and convergence zones in turbulent flows*, *Center for Turbulence Research, Proceedings of the Summer Program* (1988) 193–208.

[94] J. Jeong and F. Hussain, *On the indentification of a Vortex*, *Journal of Fluid Mechanics* **285** (1995) 69–94.

[95] G. Haller, *An objective definition of a vortex*, *Journal of Fluid Mechanics* **525** (2005) 1–26.

[96] M. S. Chong, A. E. Perry and B. J. Cantwell, *A general classification of three-dimensional flow fields*, *Physics of Fluids A: Fluid Dynamics* **2** (1990) 765.

[97] M. S. Howe, *Acoustics of Fluid-Structure Interactions.* Cambridge University Press, Cambridge, Massachusetts & London, England, 1998.

[98] M. Wang, J. B. Freund and S. K. Lele, *Computational Prediction of Flow-Generated Sound*, *Annual Review of Fluid Mechanics* **38** (2006) 483–512.

[99] D. Crighton, *Basic Principles of Aerodynamic Noise Generation*, *Progress in Aerospace Sciences* **16** (1975) 31–96.

[100] A. A. Oberai, F. Roknaldin and T. J. R. Hughes, *Computational procedures for determining structural-acoustic response due to hydrodynamic sources*, .

[101] C. Bogey, C. Bailly and D. Juve, *Noise Investigation of a High Subsonic,Moderate-Reynolds-Number Jet Using Compressible LES*, *Theoretical and Computational Fluid Dynamics* **16** (2003) 273–297.

[102] D. J. Bodony and S. K. Lele, *On using large-eddy simulation for the prediction of noise from cold and heated turbulent jets*, *Physics of Fluids* **17** (2005) 1–20.

[103] R. D. Sandberg, L. E. Jones, N. D. Sandham and P. F. Joseph, *Direct numerical simulations of tonal noise generated by laminar flow past airfoils*, *Journal of Sound and Vibration* **320** (2009) 838–858.

[104] D. R. Chapman, *Computational aerodynamics development and outlook*, *AIAA Journal* **17** (1979) 1293–1313.

[105] J. Schmalz and W. Kowalczyk, *Implementation of Acoustic Analogies in OpenFOAM for Computation of Sound Fields*, *Open Jurnal of Acoustics* **5** (2015) 29–44.

[106] C. Bailly, C. Bogey and X. Gloerfelt, *Some useful hybrid approaches for predicting aerodynamic noise*, *Comptes Rendus Mécanique* **333** (2005) 666–675.

[107] S. Glegg and W. Devenport, *Aeroacoustics of low mach number flows: Fundamentals, analysis, and measurement*. 2017.

[108] J. E. Ffowcs Williams and D. L. Hawkings, *Sound Generation by Turbulence and Surfaces in Arbitrary Motion*, *Philosophical Transactions of the Royal Society of London. Series A, Mathematical and Physical Sciences* **264** (1969) 321–342.

[109] M. L. Shur, P. R. Spalart, M. K. Strelets and A. K. Travin, *Towards the prediction of noise from jet engines*, *International Journal of Heat and Fluid Flow* **24** (2003) 551–561.

[110] G. Rahier, J. Prieur, F. Vuillot, N. Lupoglazoff and A. Biancherin, *Investigation of integral surface formulations for acoustic post-processing of unsteady aerodynamic jet simulations*, *Aerospace Science and Technology* **8** (2004) 453–467.

[111] S. Mendez, M. Shoeybi, S. K. Lele and P. Moin, *On the use of the Ffowcs Williams-Hawkings equation to predict far-field jet noise from large-eddy simulations*, *International Journal of Aeroacoustics* **12** (2013) 1–20.

[112] J. Casper and F. Farassat, *Broadband trailing edge noise predictions in the time domain*, *Journal of Sound and Vibration* (2003) .

[113] E. Manoha, B. Troff and P. Sagaut, *Trailing-Edge Noise Prediction Using Large-Eddy Simulation and Acoustic Analogy*, *AIAA Journal* **38** (2000) 575–583.

[114] W. R. Wolf and S. K. Lele, *Trailing-Edge Noise Predictions Using Compressible Large-Eddy Simulation and Acoustic Analogy*, *AIAA Journal* **50** (2012) 2423–2434.

[115] J. C. Hardin and D. S. Pope, *An Acoustic / Viscous Splitting Technique for Computational Aeroacoustics*, *Theoretical and Computational Fluid Dynamics* **6** (1994) 323–340.

[116] Y. Moon and Seo, *A splitting method for aeroacoustic noise prediction of low Mach number viscous flows*, *International Journal of Aeroacoustics* **4** (2005) 21–36.

[117] R. Ewert, M. Meinke and W. Schröder, *Computation of Aeroacoustic Sound Via Hybrid CFD/CAA-Method*, *RTO AVT Symposium* **079** (2001) 8–11.

[118] M. Farshchi, S. K. Hannani and M. Ebrahimi, *Linearized and non-linear acoustic/viscous splitting techniques for low Mach number ows*, *International Journal for Numerical Methods in Fluids* **1072** (2003) 1059–1072.

[119] T. H. Zheng, S. K. Tang and W. Z. Shen, *Simulation of vortex sound using the*

viscous/acoustic splitting approach, *Transactions of the Canadian Society for Mechanical Engineering* **35** (2011) 39–56.

[120] C. J. Doolan, D. Moreau, E. Arcondoulis and C. Albarracin, *Trailing Edge Noise Production, Prediction and Control*, .

[121] M. Roger, S. Moreau, M. Roger, S. M. Extensions, M. Roger and S. Moreau, *Extensions and limitations of analytical airfoil broadband noise models To cite this version : HAL Id : hal-00566057 airfoil broadband noise models*, .

[122] R. K. Amiet, *Noise due to turbulent flow past a trailing edge*, *Journal of Sound and Vibration* **47** (1976) 387–393.

[123] M. S. Howe, *A Review of the Theory of Trailing Edge Noise*, Tech. Rep. June, 1978.

[124] T. F. Brooks, S. Pope and M. A. Marcolini, *Airfoil Self-Noise and Prediction*, *NASA Reference Publication 1218* (1989) 1–142.

[125] A. R. G. Harwood, *NUMERICAL EVALUATION OF ACOUSTIC GREEN ' S FUNCTIONS*. PhD thesis, The University of Manchester, 2014.

[126] A. S. Lyrintzis, *Surface integral methods in computational aeroacoustics - from the (CFD) near-field to the (acoustic) far-field*, *International Journal of Aeroacoustics* **2** (2003) 95–128.

[127] H. Reese and T. H. Carolus, *Axial fan noise: towards sound prediction based on numerical unsteady flow data - a case study*, *Acoustics'08 Paris* **123** (2008) 4069–4074.

[128] A. F. Molland and S. Turnock, *Wind tunnel investigation of the influence of propeller loading on ship rudder performance*, tech. rep., University of Southampton, 1991.

[129] C. Badoe, A. Phillips and S. Turnock, *Numerical propeller rudder interaction studies to assist fuel efficient shipping*, in *Numerical Towing Tank Symposium*, 2012.

[130] J. C. Date and S. R. Turnock, *A study into the techniques needed to accurately predict skin friction using RANS solvers with validation against Froude's historical flat plate experimental data*, tech. rep., 1999.

[131] M. Giuni and R. B. Green, *Vortex formation on squared and rounded tip*, *Aerospace Science and Technology* **29** (2013) 191–199.

[132] B. Lakshminarayana and J. Horlock, *Tip-Clearance Flow and Losses for an Isolated Compressor Blade Tip-Clearance Flow and Losses for an Isolated Compressor Blade*, *Technical Report R&M 3316* (1963) .

[133] L. Eça and M. Hoekstra, *A procedure for the estimation of the numerical uncertainty*

of CFD calculations based on grid refinement studies, *Journal of Computational Physics* **262** (2014) 104–130.

[134] H. Xu, W. Shen, W. Zhu, H. Yang and C. Liu, *Aerodynamic analysis of trailing edge enlarged wind turbine airfoils*, *Journal of Physics: Conference Series* **524** (2014) .

[135] R. Leung, *Private communications*, 2019.

[136] M. C. Jacob, A. Louisot, D. Juvé and S. Guerrand, *Experimental Study of Sound Generated by Backward-Facing Steps Under Wall Jet*, *AIAA Journal* **39** (2001) 1254–1260.

[137] Y. Addad, D. Laurence, C. Talotte and M. C. Jacob, *Large eddy simulation of a forward-backward facing step for acoustic source identification*, *International Journal of Heat and Fluid Flow* **24** (2003) 562–571.

[138] M. R. Catlett and R. L. Simpson, *Flow Induced Noise from Turbulent Flow over Steps and Gaps*. PhD thesis, Virginia Polytechnic Institute and State University, 2010.

[139] X. Mao, *Effects of base flow modifications on noise amplifications: Flow past a backward-facing step*, *Journal of Fluid Mechanics* **771** (2015) 229–263.

[140] M. Springer, C. Scheit and S. Becker, *Flow-Induced Noise of a Forward-Backward Facing Step*, in *New results in numerical and experimental fluid mechanics X. Notes on Numerical Fluid Mechanics and Multidisciplinary Design*, vol. 132, 2016. DOI.

[141] S. Han and J. Zhong, *Effect of blade tip winglet on the performance of a highly loaded transonic compressor rotor*, *Chinese Journal of Aeronautics* **29** (2016) 653–661.

[142] A. Corsini, F. Rispoli and A. G. Sheard, *Development of improved blade tip endplate concepts for low-noise operation in industrial fans*, *Proceedings of the Institution of Mechanical Engineers, Part A: Journal of Power and Energy* **221** (2007) 669–681.

[143] A. Corsini and A. G. Sheard, *End-plate for noise-by-flow control in axial fans*, *Periodica Polytechnica Mechanical Engineering* **57** (2013) 3–16.

[144] R. D. Sandberg and L. E. Jones, *Direct numerical simulations of low Reynolds number flow over airfoils with trailing-edge serrations*, *Journal of Sound and Vibration* **330** (2011) 3818–3831.

[145] M. Gruber, *Airfoil noise reduction by edge treatments*. PhD thesis, University of Southampton, 2012.

[146] O. Jianu, M. A. Rosen and G. Naterer, *Noise pollution prevention in wind turbines: Status and recent advances*, *Sustainability* **4** (2012) 1104–1117.

[147] B. W. Fassmann, C. Rautmann, R. Ewert and J. Delfs, *Prediction of Porous Trailing Edge Noise Reduction via Acoustic Perturbation Equations and Volume Averaging*, .

[148] Y. Bae and Y. J. Moon, *Effect of passive porous surface on the trailing-edge noise*, *Physics of Fluids* **23** (2011) .

[149] M. R. Khorrami, L. Fei and C. Meelan, *A Novel Approach for Reducing Rotor Tip-Clearance Induced Noise In Turbofan Engines*, in *7th AIAA/CEAS Aeroacoustics Conference*, 2001.

[150] E. Canepa, A. Cattanei, F. Mazzocut Zecchin, G. Milanese and D. Parodi, *An experimental investigation on the tip leakage noise in axial-flow fans with rotating shroud*, *Journal of Sound and Vibration* **375** (2016) 115–131.

[151] S. Abu Sharkh, S. R. Turnock and A. Hughes, *Design and performance of an electric tip-driven thruster*, in *Proceedings of the Institution of Mechanical Engineers, Part M: Journal of Engineering for the Maritime Environment*, vol. 217, pp. 133–147, 2003.

[152] A. Santoso, I. S. Arief and A. T. Kurniawan, *Performance Analysis Rim Driven Propeller as a Propulsor using Open Water Test*, *International Journal of Marine Engineering Innovation and Research* **2** (2017) .

[153] W. M. Batten, N. W. Bressloff and S. R. Turnock, *Numerical simulations of the evolution of Taylor cells from a growing boundary layer on the inner cylinder of a high radius ratio Taylor-Couette system*, *Physical Review E - Statistical Physics, Plasmas, Fluids, and Related Interdisciplinary Topics* **66** (2002) 5.

[154] W. M. Batten, S. R. Turnock, N. W. Bressloff and S. M. Abu-Sharkh, *Turbulent Taylor-Couette vortex flow between large radius ratio concentric cylinders*, *Experiments in Fluids* **36** (2004) 419–421.